

**Electrochemical Passivation of Ni-Fe-Cr-Mn-Co Multi-Principal
Element Alloy: An Evaluation of the Fate of Alloying Elements
During Aqueous Oxidation**

A Dissertation

Presented to the Faculty of the School of Engineering and Applied Science

University of Virginia

In Partial Fulfillment
Of the Requirements for the Degree of

Doctor of Philosophy

By

Angela Yu Gerard

May 2023

APPROVAL SHEET

This
Dissertation
is submitted in partial fulfillment of the requirements
for the degree of
Doctor of Philosophy

Author: Angela Yu Gerard

This Dissertation has been read and approved by the examining committee:

Advisor: Dr. John R. Scully

Advisor:

Committee Member: Dr. Robert G. Kelly

Committee Member: Dr. Bi-Cheng Zhou


Committee Member: Dr. James M. Fitz-Gerald

Committee Member: Dr. Joseph Poon

Committee Member:

Committee Member:

Accepted for the School of Engineering and Applied Science:



Jennifer L. West, School of Engineering and Applied Science

May 2023

Dissertation Abstract

The effects of alloying elements on protective oxide formation are well understood for conventional corrosion resistant alloys (CRAs) containing a limited number of major and minor alloying elements. However, little is understood regarding protective oxides formed upon exposure to aqueous solutions in the case of multiple principal element alloys (MPEAs), also known as, high entropy alloys (HEAs), and compositionally complex alloys (CCAs). These materials can contain more than 5 principal alloying elements. A limited number of MPEAs have been studied to determine the corrosion resistance and connect these properties to surface oxide passive films which regulate corrosion. Many of these studies focus on the overall corrosion behavior with few details on the MPEAs passive film which mediate oxidation and provide protection. Many merely report alloying elements found in the oxide and typically lack passivity analyses and/or oxide characterization using surface sensitive films and molecular scale interpretations. Moreover, there are few systematic studies that track the fate of each alloying element. Furthermore, incremental variations in passivating elements above and below threshold concentration for passivity without change in metallurgical phases in the underlying substrate is often not possible.

The research presented herein focused on the study of electrochemically formed passive films on $\text{Ni}_{38}\text{Fe}_{20}\text{Cr}_x\text{Mn}_{21-0.5x}\text{Co}_{21-0.5x}$ MPEAs ($x = 22, 14, 10, 6$ at. % - i.e., Cr_x -MPEAs) in acidified and alkaline chloride solutions. These alloys were designed as a part of a broader Energy Frontier Research Center from DOE using intuition, CALPHAD, and emerging data science methods. Binary Fe-Cr, Co-Cr, and Ni-Cr alloys were used to examine whether third element effects were activated in NiFeCrMnCo alloys. Various in-situ and ex-situ characterization techniques were utilized to investigate the electrochemical passivation behavior, dissolution behavior, and the chemical make-up of potentiostatically formed passive films on MPEA surfaces.

When polarized in acidic chloride electrolytes, Cr-MPEAs with Cr contents above the critical threshold concentration of typical binary Cr containing alloys exhibited passivity and formed a protective passive film enriched in Cr(III) species and trace amounts of Ni(II), Fe(II) (IV), Mn(II), and Co(II) cations. Ni enrichment was observed at the oxide/metal interface. Ni, Fe, and Co dissolved into solution during potentiostatic passivation resulting in Cr enrichment

and not assisting in passivation. An in-depth analysis of Cr enrichment and depletion was conducted on passive films formed on both Cr-MPEAs and binary Cr alloys. Correlations between electrochemical passive properties, bulk Cr concentration, and Cr enrichment within the passive film were made. Notably, the Cr10-MPEA exhibited the highest Cr(III) enrichment and was found to exhibit depletion of Cr at the oxide/metal interface suggesting that enrichment is limited by diffusion of Cr through the altered zone. Trends in Cr enrichment with bulk Cr content observed in binary alloys was similar to those observed in MPEAs. Cr hydroxides were the dominate molecular species in all passive films but a small fraction of Cr spinels were detected in the Cr-MPEA passive films. Spinel were not detected in passive films formed on binary alloy surfaces.

The electrochemical passive behavior of the Cr-MPEAs in alkaline chloride solution was investigated using the same techniques discussed for acidic conditions. Passive films formed on the Cr-MPEA surfaces in alkaline conditions were all enriched with Ni and Cr and contained higher concentrations of Fe and Co cations compared to films formed in pH 4 electrolyte.

The influence of exposure time in an acidic Cl^- environment on passive film formation on Cr22-and Cr14-MPEA surfaces was investigated at 100 s, 1 ks, 10 ks, and 86.4 ks and compared to Ni-24Cr binary alloy. All Cr-MPEA passive films were enriched in Cr(III) cations at all exposure times aided by chemical dissolution of Mn(II), Ni(II), Fe(II) in acidified chloride solution. As exposure time increased, the concentration of Fe(II) and Mn(II) cations increased within the Cr-MPEA passive films. The Cr22-MPEA passive film was enriched in Co(II) cations at early exposure times but became depleted at longer times of 10 ks and 86.4 ks. Passive films formed on Cr14-MPEA surface were enriched in Cr(III) and Co(II) cations at all exposure times within the bulk of the film. At longer exposure times Cr spinels began to form eventually becoming the dominant oxide species at exposure time of 86.4 ks. No spinels were detected in Ni-24Cr passive films at any exposure time. Passive films formed at exposure times of 10 ks and 86.4 ks exhibited better passivity than freshly grown passive films at similar film thickness suggesting annealing of point defects and resistance to morphological roughening.

This dissertation provides an improved testing protocol for understanding complex MPEAs as well as understanding on how alloying elements effect MPEAs passivity, what atomistic characteristics contribute to forming protective passive films, as well as, the attributes

that provide better corrosion protection. The analysis presented provides a path forward for determining if a given third alloying element alters the enrichment of a strong passivator like Cr in a solvent such as Ni. Newly acquired information provides further insights into the fate of each principal alloying element during aqueous passivation and how each contribute to the passivation mechanism. Additionally, this improved understanding can help guide potential advancements in designing CRAs.

Table of Contents

Dissertation Abstract.....	3
Table of Contents.....	6
Acknowledgements.....	9
Bibliography	10
List of Tables	12
List of Figures.....	13
List of Abbreviations and Symbols.....	22
1. Introduction.....	24
1.1 Motivation	24
1.2 Background	29
1.3 Critical Unresolved Issues.....	36
1.4 Overall Objective	37
1.5 Organization of Dissertation	37
1.6 References	39
2 Aqueous Passivation of Multi-Principal Element Alloy Ni ₃₈ Fe ₂₀ Cr ₂₂ Mn ₁₀ Co ₁₀ : Unexpected High Cr Enrichment within the Passive Film	47
2.1 Abstract.....	47
2.2 Introduction.....	47
2.3 Experimental.....	51
2.4 Results.....	60
2.4.1 Electrochemical Passivation	60
2.4.2 Oxide Growth and Breakdown at Applied Potentials of -0.25 V _{SCE} and 0.0 V _{SCE}	63
2.4.3 Real-time Solution Analyses for all Cations during a Fixed Potential Hold	66
2.4.4 Oxide Valence State and Local Environment Identified by XPS	69
2.4.5 Surface Oxide and Interface Compositions from Atom Probe Tomography	73
2.4.6 Surface Enrichment and Depletion Factors for Alloying Elements.....	74
2.5 Discussion.....	76
2.5.1 Passive Film Chemical Identity and Composition.....	76
2.5.2 Fate of the Alloying Elements during Aqueous Passivation	77
2.5.3 Factors Contributing to High Cr Enrichment.....	78

2.6 Conclusion	79
2.7 References.....	79
3. The Role of Chromium Content on Aqueous Passivation of Non-Equiatomic Ni ₃₈ Fe ₂₀ Cr _x Mn _{21-0.5x} Co _{21-0.5x} Multi-Principal Element Alloy (x = 22, 14, 10, 6 at. %) in Acidic Chloride Solution	86
3.1 Abstract.....	86
3.2 Introduction.....	87
3.3 Experimental.....	90
3.4 Results.....	106
3.4.1 Electrochemical Passivation Behavior of Cr-MPEAs	106
3.4.2 Aqueous Oxidation at an Applied Passive Potential of 0.0 V _{SCE}	111
3.4.3 AESEC during 10 ks Potentiostatic Hold at 0.0 VSCE for Co-20Cr	116
3.4.4 Oxide Valence State and Cation Fractions Identified by XPS	117
3.4.5 Passive Film and Interface Compositions from APT	121
3.4.6 Passive Film and Altered Zone Alloying Element Enrichment and Depletion Factors	122
3.5 Discussion.....	126
3.5.1 Thermodynamics and Kinetics of Aqueous Passivation of Cr-MPEAs and Binary Alloys.....	126
3.5.2 Other Factors Controlling Cr Enrichment and Depletion.....	129
3.6 Conclusions.....	131
3.7 References.....	132
4. Aqueous Passivation of Non-Equiatomic Ni ₃₈ Fe ₂₀ Cr _x Mn _{21-0.5x} Co _{21-0.5x} Multi-Principal Element Alloy (x = 22, 14, 10, 6 at. %) in an Alkaline Chloride Solution	137
4.1 Abstract.....	137
4.2 Introduction.....	137
4.3 Experimental.....	140
4.4 Results.....	143
4.4.1 Electrochemical Passivation Behavior.....	143
4.4.2 Aqueous Passivation at an Applied Passive Potential of -0.25 V _{SCE}	148
4.4.3 Passive Film Cation Fractions and Valence State Identified by XPS.....	151
4.4.4 AESEC During 10 ks Potentiostatic hold at -0.25VSCE for Cr22-MPEA in deaerated 0.1 M NaCl + NaOH pH 10.....	159
4.5 Discussion.....	160
4.5.1 Aqueous Passivation in Acidic versus Basic Conditions.....	160

4.5.2 Aqueous Passivation of Binary Alloys versus MPEAs	163
4.6 Conclusions.....	164
4.7 References.....	165
5. Evolution of Multi-Principal Element Alloy $\text{Ni}_{38}\text{Fe}_{20}\text{Cr}_x\text{Mn}_{21-0.5x}\text{Co}_{21-0.5x}$ ($x = 22, 14$ at. %) passive film as a function of exposure time in acidified chloride solution.....	170
5.1 Abstract.....	170
5.2 Introduction.....	171
5.3 Experimental.....	174
5.4 Results.....	177
5.4.1 Aqueous Oxidation at an Applied Passive Potential of $-0.25 \text{ V}_{\text{SCE}}$	177
5.4.2 Electrochemical Behavior of Passive Films Formed During Aqueous Oxidation	180
5.4.3 Oxide Valence and Cation Fraction Identified by AR-XPS	182
5.4.4 Passive Film and Altered Zone Enrichment and Depletion Term	190
5.5 Discussion.....	198
5.5.1 What is Known About Oxide Exposure Aging.....	198
5.5.2 Observations in this Study	198
5.5.3 Kinetic versus Thermodynamic Factors	199
5.5.4 Ramifications Towards Corrosion Protection.....	203
5.5 Conclusion	203
5.6 References.....	204
6. Conclusions.....	208
7. Suggested Future Work.....	211
8. Appendix: Thermal oxidation of Multi-Principal Element Alloy $\text{Ni}_{38}\text{Fe}_{20}\text{Cr}_{22}\text{Mn}_{10}\text{Co}_{10}$ and the Nature of its Passive Film: Phase Separated versus Solid Solution Oxides.	214
8.1 Introduction.....	214
8.2 Experimental.....	215
8.3 Results.....	221
8.3.1 APT cation and elemental distribution within oxide and altered zone	221
8.3.2 Oxide Valence, Cation, and Elemental Fraction Identified by AR-XPS.....	222
8.3.3 Theoretical XPS Models of Phase Separated and Solid Solution Oxides	224
8.4 References.....	226

Acknowledgements

Firstly, I would like to thank my family for your unwavering support, motivation, and love, especially from my ~~soon-to-be~~ husband Timothy Dylan Ashely. Without them I would not have been able to accomplish the things I have done throughout my academic career.

I would like to thank my advisor Dr. Scully, for giving me an opportunity to pursue a PhD in material science engineering, especially when I had limited knowledge about MSE and was mainly a chemistry nerd. Thank you to my committee, Dr. Robert Kelly, Dr. Zhou Bi-Cheng, Dr. James Fitz-Gerald, Dr. Joseph Poon, for your guidance and taking the time to test my knowledge. I am extremely thankful for the many collaborators I was given the opportunity to work with in WastePD. A special thank you to Dr. Dan Schreiber and Dr. Elizabeth Kautz for their impeccable passive film characterization and invaluable input. Thank you to Dr. Stephen McDonnell and Ms. Catherine Dukes for your XPS teachings and your willingness to help. I am greatly appreciative of the MSE staff and their kind hearts, the impact you had on my graduate life is immeasurable: Kimberly Fitzhugh, Kari Werres, Jeannie Reese, Tonya Reynolds, Sherri Sullivan, Bryana Amador, Richard White, and Joe Thompson. I would also like to thank the Scully group for their moral support and great banter.

I am grateful of the many academic monitors I have had; your teachings have stuck with me throughout these years and helped guide me through my PhD journey: Coach Kendell Warren, Coach Sarah Owens, Mr. Levi Owens, Coach Roy York, Dr. Cindy Burkhardt, and Dr. Francis Webster. There are many other individuals that have helped me throughout my journey in graduate school and I would like to thank you all for your great friendship and support: Dr. Junsoo Han, Marlene Wartenberg, Dr. Carol Glover, Dr. Kateryna Gusieva, Dr. Rachel Guarriello, Kristen Z Raney aka “KZ”, Raheim Turner, Allegra Turner, Dominique Turner, Adam Harris, and Brianna N. Victor. Lastly, I want to thank the MSE department for giving me an opportunity to further my intelligence and for all the lessons I learned in class and in research. I will take these lessons with me in life but in the words of Mark Twain, “I’m glad I did it partly because it was worth it, but mostly because I shall never have to do it again”.

Bibliography

Publications that resulted from this dissertation and other relevant work are listed below:

1. A.Y. Gerard, J. Han, S.J. McDonnell, K. Ogle, E.J. Kautz, D.K. Schreiber, P. Lu, J.E. Saal, G.S. Frankel, J.R. Scully, Aqueous passivation of multi-principal element alloy Ni₃₈Fe₂₀Cr₂₂Mn₁₀Co₁₀: Unexpected high Cr enrichment within the passive film, *Acta Materialia*, 198 (2020) 121-133.
2. A.Y. Gerard, K. Lutton, A. Lucente, G.S. Frankel, J.R. Scully, Progress in Understanding the Origins of Excellent Corrosion Resistance in Metallic Alloys: From Binary Polycrystalline Alloys to Metallic Glasses and High Entropy Alloys, *CORROSION*, 76 (2020) 485-499.
3. A.Y. Gerard, E.J. Kautz, D.K. Schreiber, J. Han, S. McDonnell, K. Ogle, P. Lu, J.E. Saal, G.S. Frankel, J.R. Scully, The role of chromium content in aqueous passivation of a non-equiatomic Ni₃₈Fe₂₀Cr_xMn_{21-0.5x}Co_{21-0.5x} multi-principal element alloy (x = 22, 14, 10, 6 at%) in acidic chloride solution, *Acta Materialia*, 245 (2023) 118607.
4. P. Lu, J.E. Saal, G.B. Olson, T.S. Li, O.J. Swanson, G.S. Frankel, A.Y. Gerard, K.F. Quiambao, J.R. Scully, Computational materials design of a corrosion resistant high entropy alloy for harsh environments, *Scripta Materialia*, 153 (2018) 19-22.
5. P. Lu, J.E. Saal, G.B. Olson, T. Li, S. Sahu, O.J. Swanson, G.S. Frankel, A.Y. Gerard, J.R. Scully, Computational design and initial corrosion assessment of a series of non-equimolar high entropy alloys, *Scripta Materialia*, 172 (2019) 12-16.
6. K.F. Quiambao, S.J. McDonnell, D.K. Schreiber, A.Y. Gerard, K.M. Freedy, P. Lu, J.E. Saal, G.S. Frankel, J.R. Scully, Passivation of a corrosion resistant high entropy alloy in non-oxidizing sulfate solutions, *Acta Materialia*, 164 (2019) 362-376.
7. T. Li, O.J. Swanson, G.S. Frankel, A.Y. Gerard, P. Lu, J.E. Saal, J.R. Scully, Localized corrosion behavior of a single-phase non-equimolar high entropy alloy, *Electrochimica Acta*, 306 (2019) 71-84.
8. K. Lutton Cwalina, C.R. Demarest, A.Y. Gerard, J.R. Scully, Revisiting the effects of molybdenum and tungsten alloying on corrosion behavior of nickel-chromium alloys in aqueous corrosion, *Current Opinion in Solid State and Materials Science*, 23 (2019) 129-141.
9. S. Sahu, O.J. Swanson, T. Li, A.Y. Gerard, J.R. Scully, G.S. Frankel, Localized Corrosion Behavior of Non-Equiatomic NiFeCrMnCo Multi-Principal Element Alloys, *Electrochimica Acta*, 354 (2020) 136749.

10. J.R. Scully, S.B. Inman, A.Y. Gerard, C.D. Taylor, W. Windl, D.K. Schreiber, P. Lu, J.E. Saal, G.S. Frankel, Controlling the corrosion resistance of multi-principal element alloys, *Scripta Materialia*, 188 (2020) 96-101.
11. K. Wang, J. Han, A.Y. Gerard, J.R. Scully, B.-C. Zhou, Potential-pH diagrams considering complex oxide solution phases for understanding aqueous corrosion of multi-principal element alloys, *npj Materials Degradation*, 4 (2020) 35.
12. C. Nyby, X. Guo, J.E. Saal, S.-C. Chien, A.Y. Gerard, H. Ke, T. Li, P. Lu, C. Oberdorfer, S. Sahu, S. Li, C.D. Taylor, W. Windl, J.R. Scully, G.S. Frankel, Electrochemical metrics for corrosion resistant alloys, *Scientific Data*, 8 (2021) 58.
13. J. Han, X. Li, A.Y. Gerard, P. Lu, J.E. Saal, G.S. Frankel, K. Ogle, J.R. Scully, Potential Dependent Mn Oxidation and Its Role in Passivation of Ni₃₈Fe₂₀Cr₂₂Mn₁₀Co₁₀ Multi-Principal Element Alloy Using Multi-Element Resolved Atomic Emission Spectroelectrochemistry, *Journal of The Electrochemical Society*, 168 (2021) 051508.
14. E.J. Kautz, S.V. Lamberts, D.E. Perea, A.Y. Gerard, J. Han, J.R. Scully, J.E. Saal, D.K. Schreiber, Element redistributions during early stages of oxidation in a Ni₃₈Cr₂₂Fe₂₀Mn₁₀Co₁₀ multi-principal element alloy, *Scripta Materialia*, 194 (2021) 113609.
15. D.K. Schreiber, E.J. Kautz, M.J. Olszta, K. Kruska, A.Y. Gerard, K.F. Quiambao-Tomko, J.R. Scully, Revealing the complexity of high temperature oxide formation in a 38Ni-21Cr-20Fe-13Ru-6Mo-2W (at. %) multi-principal element alloy, *Scripta Materialia*, 210 (2022) 114419.
16. J. Han, A.Y. Gerard, P. Lu, J.E. Saal, K. Ogle, J.R. Scully, Elementally Resolved Dissolution Kinetics of a Ni-Fe-Cr-Mn-Co Multi-Principal Element Alloy in Sulfuric Acid Using AESEC-EIS, *Journal of The Electrochemical Society*, 169 (2022) 081507.
17. A.Y. Gerard, J. Han, S, K. Ogle, K. Wang, B.-C. Zhou, P. Lu, J.E. Saal, G.S. Frankel, J.R. Scully, Aqueous passivation of Non-Equiatomic Ni₃₈Fe₂₀Cr_xMn_{21-0.5x}Co_{21-0.5x} Multi-Principal Element Alloy in (x = 22, 14, 10, 6 at. %) an Alkaline Chloride – In Progress.
18. A.Y. Gerard, J. Han, S, K. Ogle, P. Lu, J.E. Saal, G.S. Frankel, J.R. Scully, Evolution of Multi-Principal Element Alloy Ni₃₈Fe₂₀Cr_xMn_{21-0.5x}Co_{21-0.5x} (x = 22, 14 at. %) passive film as a function of exposure time in Acidified Chloride Solution – In Progress.

List of Tables

Table 2. 1. Model Multi-Principal Element Alloy and Binary Alloy Compositions	51
Table 2. 2. Elemental Fractions in $\text{Ni}_{38}\text{Fe}_{20}\text{Cr}_{22}\text{Mn}_{10}\text{Co}_{10}$ Bulk Material and Electrochemical Passive Film after 10 ks at $-0.25 V_{\text{SCE}}$	70
Table 2. 3. Elemental Fractions in $\text{Ni}_{76}\text{Cr}_{24}$ Bulk Material and Electrochemical Passive Film after 10 ks at $-0.25 V_{\text{SCE}}$	70
Table 2. 4. Binding energy (eV) of XPS Spectra used for passive film analysis.....	71
Table 2. 5. Surface Enrichment Model Parameters for $\text{Ni}_{38}\text{Fe}_{20}\text{Cr}_{22}\text{Mn}_{10}\text{Co}_{10}$	75
Table 2. 6. Surface Enrichment Model Parameters for $\text{Ni}_{76}\text{Cr}_{24}$	75
Table 3. 1. Multiple-Principal Element Alloys and Binary Alloys Composition	91
Table 3. 2. Fitted EIS parameters obtained from model circuit fit for Cr22-, Cr14-, Cr10-MPEA, Fe-20Cr, Co-30Cr, Co-20Cr, Ni-24Cr, and Ni-12Cr.....	93
Table 3. 3. Oxides detected by XPS and their molar mass, density, electrons, and dielectric constant.	94
Table 3. 4. Deconvoluted oxides from XPS and their corresponding fractions.....	95
Table 3. 5. Definitions used for defining the isoconcentration surfaces and interfaces in the APT reconstructions.	100
Table 3. 6. All cation and elemental fractions detected by XPS for passive films formed at $0.0 V_{\text{SCE}}$ for 10 ks in 1 mM NaCl + HCl pH 4 $\text{N}_{2(\text{g})}$ deaerated solution and within the altered zone.	118
Table 4. 1. Multiple-Principal Element Alloys and Binary Alloys Nominal Composition	141
Table 4. 2. All cation and elemental fractions detected by XPS for passive films formed at $-0.25 V_{\text{SCE}}$ for 10ks in 0.1 M NaCl + NaOH pH 10 $\text{N}_{2(\text{g})}$ deaerated solution.	153
Table 4. 3. Predicted Oxides from XPS and their corresponding fraction for passive films formed at $-0.25 V_{\text{SCE}}$ for 10ks in 0.1 M NaCl + NaOH pH 10 $\text{N}_{2(\text{g})}$ deaerated solution.	154
Table 5. 1. Multiple-Principal Element Alloys and Binary Alloy Nominal Composition	175
Table 5. 2. All cation and elemental fractions detected by AR-XPS for passive films formed at $-0.25 V_{\text{SCE}}$ in 0.1 M NaCl + HCl pH 4 $\text{N}_{2(\text{g})}$ deaerated solution for Cr22-MPEA, Cr14-MPEA, and Ni-24Cr binary alloy.	184
Table 8. 1. EALS for elements in Cr_2O_3 , NiO, and Fe_2O_3 oxides obtained from NIST 219	

List of Figures

Fig 1. 1. Breakdown potential as a function of PREN (&Cr+2.5%Mo) for Type 444 Stainless Steels. Dowling, et. al., CORROSION 55 (1999): pp. 187–199	26
Fig 1. 2. Pitting resistance equivalency numbers for a number of model Ni-22Cr (wt. %) alloys and the indicated commercial alloys according to the relationship indicated taking into account Cr, Mo, and W. A.Y. Gerard, et. al., CORROSION, 76 (2020) 485-499.....	27
Fig 1. 3. A schematic of the broad classification for MPEAs, HEAs, and CCAs. N. Birbilis, et. al., npj Materials Degradation, 5 (2021) 14.....	28
Fig 1. 4. (a) Oxide formation energy as a function of cohesive energy. Elements are listed either as passivity promotor (high negative free energy – easily passivate) or dissolution blockers (high cohesive energy). (b)E-pH stability diagram for Ni ₃₈ Cr ₂₁ Fe ₂₀ Ru ₁₃ Mo ₆ in 1 kg H ₂ O at 25 C and 1 atm calculated by CALPHAD. Green regions are correlated to Cr ₂ O ₃ , Blue is Fe-Ni and Ni-Cr Spinel (XY ₂ O ₄), and orange are other oxides. (a) C.D. Taylor, et. al., npj Materials Degradation, 2 (2018) 6. (b) P. Lu, et. al., Scripta Materialia, 153 (2018) 19-22.	28
Fig 1. 5. Passive current density as a function of Bulk Cr concentration for (a) Fe-Cr binary alloys in H ₂ SO ₄ and (b) Ni-Cr binary alloys in 1 N H ₂ SO ₄ . (a) P.F. King, et. al., The Journal of Physical Chemistry, 63 (1959) 2026-2032. (b) .A.P. Bond, et. al., Journal	31
Fig 1. 6. (a) Model for passive films formed on Ni-Cr alloys. At acidic pH levels Cr-rich films form and at alkaline pH levels Ni-rich films form. Cation fraction as a function of exposure time for Potentiostatically formed passive films at 0.2V _{SCE} on Ni-Cr alloys in 0.1 M NaCl (b) pH 4 and (c) pH 10. (a) T. Jabs, et. al., Journal of The Electrochemical Society, 144 (1997) 1231-1243 and (b,c) K.L. Cwalina, et. al., Journal of The Electrochemical Society, 166 (2019) C3241-C3253.....	33
Fig 1. 7. E-pH stability diagram in water at 25 °C for (a) Pure Cr and (b) Pure Ni. M. Pourbaix, National Association of Corrosion Engineers, Houston, TX, 1974.....	34
Fig 1. 8. APT concentration profiles and their corresponding 3D reconstruction of Ni ₃₈ Cr ₂₁ Fe ₂₀ Ru ₁₃ Mo ₆ W ₂ MPEA (a) passive film electrochemically formed at 0.617 VSCE in H ₂ SO ₄ persulfate pH 4 for 10 ks and (b) passive film formed by Air oxidation at 600 °C for 1080 mins.....	35
<i>Fig. 2. 1. APT characterization of the passive film formed on a MPEA after 10,000 seconds exposure at -0.25 VSCE in an aqueous solution of 0.1 molar NaCl (pH 4), and the adjacent base alloy. The concentration profile above gives concentration of all elements across a 6 at% O isocomposition surface, where uncertainties shown as error bars represent 1σ. Bin width for proximity histogram analysis is 0.4 nm. Nominal concentration determined via APT is given by horizontal lines.....</i>	59
Fig. 2. 2. Ranging criteria for atom probe tomography mass spectrum analysis for the base alloy and corrosion film. The mass spectrum is normalized to the peak with the maximum count (⁵⁶ Fe ⁺²).	60
Fig. 2. 3. Anodic polarization behavior in deaerated 0.1 M NaCl + HCl at pH 4 with different surface pretreatments: (1) after initial cathodic reduction at -1.3 VSCE for 10 mins and (2) after initial open circuit hold for 30 mins for (a) Ni ₃₈ Fe ₂₀ Cr ₂₂ Mn ₁₀ Co ₁₀ MPEA and (b) Ni ₇₆ Cr ₂₄ binary alloy	62

Fig. 2. 4. Comparison of anodic potentiodynamic polarization data comparing Ni₃₈Fe₂₀Cr₂₂Mn₁₀Co₁₀ and Ni₇₆Cr₂₄ in deaerated 0.1 M NaCl + HCl at pH 4. (a) Upward polarization with dotted lines at -0.25 V_{SCE} and 0 V_{SCE} indicating passive potentials and current densities used for 10 ks oxide growth. (b) Potential vs. high frequency Imaginary component of impedance (-Z'') during upward polarization displaying regions of active-to-passive transitions, passivity, and breakdown. 63

Fig. 2. 5. Measured electrochemical passive current density during potentiostatic oxide growth for 10 ks of Ni₃₈Fe₂₀Cr₂₂Mn₁₀Co₁₀ and Ni₇₆Cr₂₄ in Deaerated 0.1 M NaCl + HCl at pH 4 at (a) -0.25 V_{SCE} and (b) 0 V_{SCE} 64

Fig. 2. 6. Bode plot of (a) Ni₃₈Fe₂₀Cr₂₂Mn₁₀Co₁₀ MPEA (b) Ni₇₆Cr₂₄ in deaerated 0.1 M NaCl + HCl pH 4 after 10 ks oxide growth at -0.25 V_{SCE}. Experimental Z_{mod} and Z_{phz} were fit to an equivalent circuit yielding a film constant phase element exponential of 0.90 for both alloys. HEA Fitting Parameters: CPE_f = 3.8 x 10⁻⁵ S•sec^α•cm⁻², α_{film} = 0.90, R_f = 1.7 x 10⁵ Ω•cm², W_f = 8.9 x 10⁻⁶ S•sec^{1/2}, CPE_{f_{le}} = 2.2 x 10⁻⁷ S•sec^α•cm⁻², α_{f_{le}} = 0.79, R_{f_{le}} = 36.2 Ω•cm², and R_s = 46.8 Ω•cm². Ni₇₆Cr₂₄ Fitting Parameters: CPE_f = 1.9 x 10⁻⁴ S•sec^α•cm⁻², α_{film} = 0.90, R_f = 4.8 x 10⁴ Ω•cm², W_f = 1.1 x 10⁻⁵ S•sec^{1/2}, CPE_{f_{le}} = 1.4 x 10⁻⁴ S•sec^α•cm⁻², α_{f_{le}} = 0.87, R_{f_{le}} = 1.6 x 10⁴ Ω•cm², and R_s = 43.1 Ω•cm² - utilizing circuit model shown by [Tianshu doi.org/10.1016/j.electacta.2019.03.104]. 65

Fig. 2. 7. In situ measurement of oxide thickness (l_{ox}) as a function of time for Ni₃₈Fe₂₀Cr₂₂Mn₁₀Co₁₀ MPEA and Ni₇₆Cr₂₄ during 10 ks oxide growth at -0.25 V_{SCE} in deaerated 0.1 M NaCl + HCl pH 4. Utilizing 1 Hz CPE component of impedance data, the MPEA's final oxide thickness was ~3 nm. AESEC estimations showed l_{ox} is 3.7 nm and XPS oxide thickness analysis indicated a slightly thinner oxide of ≤ 2 nm. 66

Fig. 2. 8. AESEC elemental dissolution rate vs. time behavior for Ni₃₈Fe₂₀Cr₂₂Mn₁₀Co₁₀ MPEA exposed at -0.25 V_{SCE} in 0.1 M NaCl + HCl pH 4, deaerated electrolyte. The horizontal lines are the detection limit of each alloy element. The elemental dissolution rates are shown as equivalent elemental current densities, i_M. The i_M is normalized (i_M') based on the bulk composition utilizing Eq. 2.9. Dashed lines indicate i_{Ni}^{exp} to determine congruent dissolution of each element. 67

Fig. 2. 9. Comparison between i_{Ni}^{exp} and; (a) i_{Cr}' and (b) i_{Mn}' at E_{app} = -0.25 V_{SCE} based on data from Fig. 6. The highlighted light-yellow area indicates the surface enriched amount of oxidized Cr (a) or Mn(b), calculated from Eqs. 2.10 and 2.11. 68

Fig. 2. 10. Surface cation fractions for Ni₃₈Fe₂₀Cr₂₂Mn₁₀Co₁₀ MPEA based on (a) The mass density per unit area of an alloying element collected on surface (Θ_M), (b) Cation fractions derived from the density per unit area of an element (line) and from XPS calculation (symbol) during at -0.25 V_{SCE} potentiostatic hold in 0.1 M NaCl + HCl pH 4.0, N₂ deaerated electrolyte 69

Fig. 2. 11. XPS spectral analysis and deconvolution of the Ni 2p_{3/2} core level of (a) Ni₃₈Fe₂₀Cr₂₂Mn₁₀Co₁₀ and (b) Ni₇₆Cr₂₄ passive film grown at -0.25 V_{SCE} for 10 ks in deaerated 0.1 M NaCl + HCl pH 4. 72

Fig. 2. 12. XPS spectral analysis and deconvolution of the Cr 2p_{3/2} core level of (a) Ni₃₈Fe₂₀Cr₂₂Mn₁₀Co₁₀ and (b) Ni₇₆Cr₂₄ passive film grown at -0.25 V_{SCE} for 10 ks in deaerated 0.1 M NaCl + HCl pH 4. 72

Fig. 2. 13. XPS spectral analysis and deconvolution of the O1s core level of Ni ₁₃₈ Fe ₂₀ Cr ₂₂ Mn ₁₀ Co ₁₀ passive film grown at -0.25 V _{SCE} for 10 ks in deaerated 0.1 M NaCl + HCl pH 4.....	73
Fig. 2. 14. APT characterization of the corrosion film formed on a MPEA after 10,000 seconds exposure in an aqueous solution of 0.1 M NaCl (pH 4), and the adjacent base alloy. (a) Three dimensional ion maps for all alloying elements and oxide molecular peaks, and (b) concentration of cations across the 6 at% O iso-concentration surface given in (a). Uncertainties shown as error bars represent 1σ from standard counting error. The nominal base alloy composition as determined by APT is given by horizontal lines to the left of the concentration profile.....	74
Fig. 3. 1. Ranging criteria for APT mass spectrum analysis for the base alloy, passive film, and Cr capping layer for Cr-10 and Cr22 MPEAs.	97
Fig. 3. 2. Ranging criteria for APT mass spectrum analysis for the base alloy, passive film, and Cr capping layer for the Fe-20Cr alloy.	98
Fig. 3. 3. Ranging criteria for APT mass spectrum analysis for the base alloy, passive film, and Cr capping layer for the Co-20Cr (at. %) alloy.	99
Fig. 3. 4. (a,b) APT concentration profiles and (c) element distribution maps of the Cr10-MPEA. The passive film was formed electrochemically during step-potentiostatic oxide growth at 0.0 V _{SCE} for 10 ks in deaerated 1 mM NaCl + HCl pH 4. The concentration profile in (a) was determined using a proximity histogram across a 20 at. % O isoconcentration surface with a bin width of 0.2 nm. The concentration profile in (b) shows only element fraction of principal alloying elements, and was calculated from (a). The 3D element distribution maps given in (c) show elemental and corresponding molecular species present in the film and base alloy. All maps are for a 10 nm thick region of interest through the center of the reconstructed volume.	101
Fig. 3. 5. (a,b) APT concentration profiles and (c) element distribution maps of the Cr22-MPEA. The passive film was formed electrochemically during step-potentiostatic oxide growth at 0.0 V _{SCE} for 10 ks in deaerated 1 mM NaCl + HCl pH 4. The concentration profile in (a) was determined using a proximity histogram across a 20 at. % O isoconcentration surface with a bin width of 0.2 nm. The concentration profile in (b) shows only element fraction of principal alloying elements, and was calculated from (a). The 3D element distribution maps given in (c) show elemental and corresponding molecular species present in the film and base alloy. All maps are for a 10 nm thick region of interest through the center of the reconstructed volume.	102
Fig. 3. 6. (a,b) APT concentration profiles and (c) element distribution maps of the Fe-20Cr alloy. The passive film was formed electrochemically during step-potentiostatic oxide growth at 0.0 V _{SCE} for 10 ks in deaerated 1 mM NaCl + HCl pH 4. The concentration profile in (a) was determined using a proximity histogram across a 13 at. % O isoconcentration surface with a bin width of 0.2 nm. The concentration profile in (b) shows only element fraction of principal alloying elements, and was calculated from (a). (c) The 3D element distribution maps given in (c) show elemental and corresponding molecular species present in the film and base alloy. All maps are for a 10 nm thick region of interest through the center of the reconstructed volume.	103
Fig. 3. 7. (a,b) APT concentration profiles and (c) element distribution maps of the Co-20Cr alloy. The passive film was formed electrochemically during step-potentiostatic oxide growth at 0.0 V _{SCE} for 10 ks in deaerated 1 mM NaCl + HCl pH 4. The concentration profile in (a) was determined using a proximity histogram across a 20 at. % O isoconcentration surface with a bin	

width of 0.2 nm. The concentration profile in (b) shows only element fraction of principal alloying elements, and was calculated from (a). (c) The 3D element distribution maps given in (c) show elemental and corresponding molecular species present in the film and base alloy. All maps are for a 10 nm thick region of interest through the center of the reconstructed volume. 104

Fig. 3. 8. Linear sweep voltammetry in $N_{2(g)}$ deaerated 1 mM NaCl + HCl electrolyte at pH 4 after initial cathodic reduction at $-1.3 V_{SCE}$ for 600 s for (a) Cr-MPEAs, (b) Ni-xCr binary alloys ($x = 30, 20, 24, 12, 10, 5$ Cr atomic %), (c) Fe-xCr binary alloys and (d) Co-xCr binary alloys. Where $x = 30, 20, 10, 5$ Cr at. %. 106

Fig. 3. 9. Linear sweep voltammetry in $N_{2(g)}$ deaerated 0.1 M NaCl + HCl at pH 4 after initial cathodic reduction at $-1.3 V_{SCE}$ for 600 s for (a) Cr-MPEAs, (b) Ni-xCr binary alloys ($x = 30, 20, 24, 12, 10, 5$ Cr atomic %), (c) Fe-xCr binary alloys and (d) Co-xCr binary alloys. Where $x = 30, 20, 10, 5$ Cr at. %. 107

Fig. 3. 10. Potential vs. imaginary component of impedance ($-Z''$) at $f = Hz$ during LSV with $0.5 mV s^{-1}$ scan rate in $N_{2(g)}$ deaerated 1 mM NaCl + HCl at pH 4 after initial cathodic reduction at $-1.3V_{SCE}$ for 600 s for (a) Cr22-MPEA versus Ni-24Cr, and (b) Cr6-MPEA versus Ni-5Cr..... 109

Fig. 3. 11. Linear sweep voltammetry in $N_{2(g)}$ deaerated 1 mM NaCl + HCl at pH 4 after initial cathodic reduction at $-1.3 V_{SCE}$ for 10 mins for Cr22-MPEA, Cr14-MPEA, Cr10-MPEA, Ni-24Cr, Ni-12Cr, Fe-20Cr, Co-30Cr, and Co-20Cr. Horizontal dotted lines indicate potentials in which various oxides are predicted to be stable at pH 4. Oxide formation potentials were obtained from potential-pH stability diagrams retrieved from Wang et al. doi: 10.1038/s41529-020-00141-6. 109

Fig. 3. 12. Comparison of current density versus bulk alloy Cr concentration at $0.0 V_{SCE}$ acquired from linear sweep voltammetry for Cr-MPEAs, Ni-Cr, Fe-Cr, and Co-Cr alloys in (a) $N_{2(g)}$ deaerated 1 mM NaCl + HCl at pH 4 and (b) $N_{2(g)}$ deaerated 0.1 M NaCl + HCl at pH 4. Standard errors bars were computed from repeated experiments. 110

Fig. 3. 13. Measured electrochemical current density during potentiostatic hold at $0.0 V_{SCE}$ for 10 ks 4 after initial cathodic reduction at $-1.3V_{SCE}$ for 600 s in deaerated 1 mM NaCl + HCl at pH 4 of Cr22-MPEA, Cr14-MPEA, Cr10-MPEA, Ni-24Cr, Ni-12Cr, Ni-10Cr, Fe-20Cr, Co-30Cr, and Co-20Cr. 112

Fig. 3. 14. Measured electrochemical current density during potentiostatic hold at $0.0 V_{SCE}$ for 10 ks 4 after initial cathodic reduction at $-1.3V_{SCE}$ for 600 s in deaerated 1 mM NaCl + HCl at pH 4 of Cr6-MPEA and Co-10Cr. 112

Fig. 3. 15. Bode plot of Cr22-MPEA, Cr14-MPEA, Cr10-MPEA, Ni-24Cr, Ni-12Cr, Ni-10Cr, Fe-20Cr, Co-30Cr, and Co-20Cr in deaerated 1 mM NaCl + HCl at pH 4 after potentiostatic hold at $0.0 V_{SCE}$ for 10 ks..... 113

Fig. 3. 16. In-situ estimation of oxide thickness for Cr22-MPEA, Cr14-MPEA, Cr10-MPEA, Ni-24Cr, Ni-12Cr, Fe-20Cr, Co-30Cr, and Co-20Cr during potentiostatic hold at $0.0 V_{SCE}$ for 10 ks in deaerated 1 mM NaCl + HCl at pH 4 114

Fig. 3. 17. (a) Total electrochemical charge, (b) ion ejection charge, and (c) efficiency of passive films formed on Cr22-MPEA, Cr14-MPEA, Cr10-MPEA, Ni-24Cr, Ni-12Cr, Fe-20Cr, Co-30Cr, and Co-20Cr during potentiostatic hold at $0.0 V_{SCE}$ for 10 ks in deaerated 1 mM NaCl + HCl at pH 4. Values were estimated from measured current density and oxide thickness as a function of time. 115

Fig. 3. 18. Atomic emission spectroelectrochemistry of Co-20Cr during potentiostatic hold at 0.0 V_{SCE} for 10 ks in deaerated 1 mM NaCl + HCl at pH 4 after initial cathodic reduction at -1.3 V_{SCE} for 600 s.....	116
Fig. 3. 19. XPS spectral deconvolution of O 1s, Ni 2p _{3/2} , and Cr 2p _{3/2} core level for the passive films formed during step-potentiostatic oxide growth at 0.0 V_{SCE} for 10 ks in deaerated 1 mM NaCl + HCl at pH 4 on Cr22-, Cr14-, Cr10-MPEA, Ni-24Cr, Ni-12Cr, Fe-20Cr, Co-30Cr, and Co-20Cr.....	119
Fig. 3. 20. (a) APT concentration profile and (b) element distribution maps of the Cr10-MPEA electrochemically formed passive film during potentiostatic hold at 0.0 V_{SCE} for 10 ks in deaerated 1 mM NaCl + HCl pH 4. The concentration profile in (a) was determined using a proximity histogram across a 20 at.% O isoconcentration surface with a bin width of 0.2 nm. The 3D element distribution maps given in (b) show elemental and corresponding molecular species (e.g., Ni, NiO) present in the film and base alloy. All maps are for a 10 nm thick region of interest through the center of the reconstructed volume.....	122
Fig. 3. 21. XPS Cr enrichment/depletion factor (f_{Cr}) for both Cr cations within the passive film ($f_{Cr,ox}$) and elemental Cr within the altered zone ($f_{Cr,az}$) (i.e., metal/oxide interface).....	123
Fig. 3. 22. Enrichment and depletion predictions for Cr in the altered zone and passive films formed on Ni ₃₈ Fe ₂₀ Cr _x Mn _{21-0.5x} Co _{21-0.5x} , where x = 22, 14, and 10. The black dotted line is the ideal condition in which the Cr oxide concentrations is equal to the bulk Cr concentration ($X^{ox} = X^S$). Above this dotted line Cr is to be enriched and below Cr is depleted. Hypothetical enrichment and depletion curves were based from experimental XPS and APT Cr enrichment terms obtained using Castle's method	124
Fig. 3. 23. Hypothetical depletion zone considering conservation of mass using experimental XPS data and bulk elemental concentrations.	125
Fig. 3. 24. Schematic of passive film and altered zone at or below the metal/film interface as a function of charge efficiency for Cr10-MPEA. Passive film enrichment and depletion within the inner and outer regions were correlated to the APT concentration profile for the Cr10-MPEA electrochemically formed passive film during potentiostatic hold at 0.0 V_{SCE} for 10 ks in deaerated 1 mM NaCl + HCl pH 4.	125
Fig. 3. 25. Linear sweep voltammetry in N _{2(g)} deaerated 1 mM NaCl + HCl electrolyte at pH 4 after initial cathodic reduction at -1.3 V_{SCE} for 600 s for Pure Ni, Fe, Cr, Mn, and Co.....	129
Fig. 4. 1.. Linear sweep voltammetry in N _{2(g)} deaerated 0.1 M NaCl + HCl electrolyte at pH 4 after an initial cathodic reduction at -1.3 V_{SCE} for 600 s for (a) xCr-MPEAs, (b) Ni-yCr, (c) Fe-uCr, and (d) Co-uCr. Where x = 22, 14, 10, 6 at. % , y = 24, 12, 5 at. %, and u = 20, 10, 5 at.%. alloys (x = 30, 20, 24, 12, 10, 5 Cr atomic %), (c) Fe-xCr binary alloys and (d) Co-xCr binary alloys. Where x = 30, 20, 10, 5 Cr at. %.	144
Fig. 4. 2. Linear sweep voltammetry in N _{2(g)} deaerated 0.1 M NaCl + NaOH electrolyte at pH 10 after an initial cathodic reduction at -1.3 V_{SCE} for 600 s for (a) xCr-MPEAs, (b) Ni-yCr, (c) Fe-uCr, and (d) Co-uCr. Where x = 22, 14, 10, 6 at. % , y = 24, 12, 5 at. %, and u = 20, 10, 5 at.%.	146
Fig. 4. 3. Comparison of current density versus bulk alloy Cr concentration from linear sweep voltammetry at -0.25 V_{SCE} in N _{2(g)} deaerated 0.1 M NaCl + HCl or NaOH electrolyte at (a) pH 4	

<i>and (b) pH 10 for xCr-MPEAs, Ni-yCr, Fe-uCr, and Co-uCr. Where x = 22, 14, 10, 6 at. %, y = 24, 12, 5 at. %, and u = 20, 10, 5 at.%.</i>	147
Fig. 4. 4. Comparison of current density versus bulk alloy Cr concentration from linear sweep voltammetry at $-0.40 V_{SCE}$ in $N_{2(g)}$ deaerated 0.1 M NaCl + HCl or NaOH electrolyte at (a) pH 4 and (b) pH 10 for xCr-MPEAs, Ni-yCr, Fe-uCr, and Co-uCr. Where x = 22, 14, 10, 6 at. %, y = 24, 12, 5 at. %, and u = 20, 10, 5 at.%.	147
Fig. 4. 5. Measured electrochemical current density during potentiostatic hold at $-0.25 V_{SCE}$ for 10 ks after initial cathodic reduction at $-1.3V_{SCE}$ for 600 s in deaerated 0.1 M NaCl + NaOH at pH 10 of xCr-MPEAs, Ni-yCr, Fe-uCr, Co-uCr. Where x = 22, 14, 10, 6 at. %, y = 24, 12, 5 at. %, and u = 20, 10, 5 at.%.	148
Fig. 4. 6. Bode plot of xCr-MPEAs, Ni-yCr, Fe-20Cr, Co-uCr. in deaerated 0.1 M NaCl + NaOH at pH 10 after potentiostatic hold at $-0.25 V_{SCE}$ for 10 ks. Where x = 22, 14, 10 at. %, y = 24, 12 at. %, and u = 20, 10 at.%.	149
Fig. 4. 7. In-situ estimation of oxide (passive film) thickness for xCr-MPEAs, Ni-yCr, Fe-20Cr, Co-uCr during potentiostatic hold at $-0.25 V_{SCE}$ for 10 ks in deaerated 0.1 M NaCl + NaOH at pH 10. Where x = 22, 14, 10 at. %, y = 24, 12 at. %, and u = 20, 10 at.%.	150
Fig. 4. 8. (a) Total electrochemical charge, (b) ion ejection charge, and (c) efficiency of passive films formed on Cr22-MPEA, Cr14-MPEA, Cr10-MPEA, Ni-24Cr, Ni-12Cr, Fe-20Cr, Co-20Cr, and Co-10Cr during potentiostatic hold at $-0.25 V_{SCE}$ for 10 ks in deaerated 0.1 M NaCl + NaOH at pH 10. Values were estimated from measured current density and passive film (oxide) thickness as a function of time.	151
Fig. 4. 9. XPS spectral deconvolution of O 1s, Ni 2p _{3/2} , Fe2p _{1/2} , and Cr 2p _{3/2} core level for the passive films formed during step-potentiostatic oxide growth at $-0.25 V_{SCE}$ for 10 ks in deaerated 0.1 M NaCl + NaOH at pH 10 on xCr-MPEAs. Where x = 22, 14, 10 at. %.	154
Fig. 4. 10. XPS spectral deconvolution of O 1s, Ni 2p _{3/2} , and Cr 2p _{3/2} core level for the passive films formed during step-potentiostatic oxide growth at $-0.25 V_{SCE}$ for 10 ks in deaerated 0.1 M NaCl + NaOH at pH 10 on Ni-yCr. Where x = 24, 12 at. %	155
Fig. 4. 11. XPS spectral deconvolution of O 1s, Fe 2p _{3/2} , and Cr 2p _{3/2} core level for the passive films formed during step-potentiostatic oxide growth at $-0.25 V_{SCE}$ for 10 ks in deaerated 0.1 M NaCl + NaOH at pH 10 on Fe-20Cr.	155
Fig. 4. 12. XPS spectral deconvolution of O 1s, Co 2p _{3/2} , and Cr 2p _{3/2} core level for the passive films formed during step-potentiostatic oxide growth at $-0.25 V_{SCE}$ for 10 ks in deaerated 0.1 M NaCl + NaOH at pH 10 on Co-uCr. Where u = 20, 10 at. %.	156
Fig. 4. 13. Cr (III) cation % versus Bulk Cr at. % for the passive films formed during step-potentiostatic oxide growth at 10 ks in deaerated (a) 1 mM NaCl + HCl at pH 4 at $-0.0 V_{SCE}$ and (b) 0.1 M NaCl + NaOH at pH 10 at $-0.25 V_{SCE}$ on xCr-MPEAs, Ni-yCr, Fe-20Cr, Co-uCr. Where x = 22, 14, 10 at. %, y = 24, 12 at. %, and u = 20, 10 at.%.	157
Fig. 4. 14. Cr (III) Oxide % versus Bulk Cr at. % for the passive films formed during step-potentiostatic oxide growth at $-0.25 V_{SCE}$ for 10 ks in deaerated (a) 1 mM NaCl + HCl at pH 4 and (b) 0.1 M NaCl + NaOH at pH 10 on xCr-MPEAs, Ni-yCr, Fe-20Cr, Co-uCr. Where x = 22, 14, 10 at. %, y = 24, 12 at. %, and u = 20, 10 at.%.	158

Fig. 4. 15. Cr (III) + M (II) cation % versus Bulk Cr at. % for the passive films formed during step-potentiostatic oxide growth at $-0.25 V_{SCE}$ for 10 ks in deaerated (a) 1 mM NaCl + HCl at pH 4 and (b) 0.1 M NaCl + NaOH at pH 10 on xCr-MPEAs. Where x = 22, 14, 10 at. %	159
Fig. 4. 16. Atomic emission spectroelectrochemistry of Cr22-MPEA during potentiostatic hold at $-0.25 V_{SCE}$ for 10 ks in deaerated 0.1 M NaCl + NaOH at pH 10 after initial cathodic reduction at $-1.3 V_{SCE}$ for 600 s.	160
Fig. 4. 17. Linear sweep voltammetry in $N_{2(g)}$ deaerated 0.1 M NaCl + NaOH electrolyte at pH 10 after an initial cathodic reduction at $-1.3 V_{SCE}$ for 600 s for Pure Ni, Fe, Cr, Mn, and Co.	161
Fig. 4. 18. Ion molality versus potential and phase molality versus potential for the Cr22-MPEA at pH 10. Ion molality refers to reaction products that are dissolved species and phase molality refers to reaction products that are stable solid phase (i.e., precipitate).	163
Fig. 5. 1. Measured electrochemical current density during potentiostatic hold at $-0.25 V_{SCE}$ for 100 s, 1ks, 10 ks, and 86.4 ks (24 h) after initial cathodic reduction at $-1.3V_{SCE}$ for 600 s in deaerated 0.1 M NaCl + HCl at pH 4 of (a) Cr22-MPEA, (b) Cr14-MPEA, and (c) Ni-24Cr. Time outside the parathesis is the nominal time and the time within parathesis is the total time held at $-0.25V_{SCE}$ (SFEIS time + EIS time).	178
Fig. 5. 2. Bode plot of Cr22-MPEA, Cr14-MPEA, and Ni-24Cr in deaerated 0.1 M NaCl + HCl at pH 4 after potentiostatic hold at $-0.25 V_{SCE}$ for 100s, 1ks, 10 ks, and 86.4 ks (24 h). Time outside the parathesis is the nominal time and the time within parathesis is the total time held at $-0.25V_{SCE}$ (SFEIS time + EIS time).	180
Fig. 5. 3. Cr22-MPEA, Cr14-MPEA, and Ni-24 Cr (a) Linear sweep voltammetry and (b) potential vs. imaginary component of impedance ($-Z''$) at $f = 1 \text{ Hz}$ during LSV with 0.5 mV s^{-1} scan rate in $N_{2(g)}$ deaerated 0.1 M NaCl + HCl at pH 4 after initial cathodic reduction at $-1.3 V_{SCE}$ for 600 s and potentiostatic hold at $-0.25 V_{SCE}$ at each exposure time. Time outside the parathesis is the nominal time and the time within parathesis is the total time held at $-0.25V_{SCE}$ (SFEIS time + EIS time).	182
Fig. 5. 4. Cation fractions detected by AR-XPS at 45° and 90° take-off angle for (a) Cr22-MPEA and (b) Cr14-MPEA passive films potentiostatically formed at $-0.25 V_{SCE}$ for 100 s, 1ks, 10 ks, and 86.4 ks (24 h) after initial cathodic reduction at $-1.3V_{SCE}$ for 600 s in deaerated 0.1 M NaCl + HCl at pH 4. The bulk atomic fraction for each alloying element is indicated by the horizontal dashed lines. Native air oxide XPS cation fraction is shown on the y-axis. Cation fractions of Cr22-MPEA and Ni-24Cr cathodically pretreated surface is indicated by the colored outline data points at time = 30 s.	185
Fig. 5. 5. Cation fractions detected by AR-XPS at 45° and 90° take-off angle for (a) Cr22-MPEA and (b) Cr14-MPEA passive films potentiostatically formed at $-0.25 V_{SCE}$ for 100 s, 1ks, 10 ks, and 86.4 ks (24 h) after initial cathodic reduction at $-1.3V_{SCE}$ for 600 s in deaerated 0.1 M NaCl + HCl at pH 4. The bulk atomic fraction for each alloying element is indicated by the horizontal dashed lines. Native air oxide XPS cation fraction is shown on the y-axis. Cation fractions of Cr22-MPEA and Ni-24Cr cathodically pretreated surface is indicated by the colored outline data points at time = 30 s.	187
Fig. 5. 6. Oxide fractions detected by AR-XPS at 45° and 90° take-off angle of (a) Cr22-MPEA, (b) Cr14-MPEA, and (c) Ni-24Cr passive films potentiostatically formed at $-0.25 V_{SCE}$ for 100 s,	

1ks, 10 ks, and 86.4 ks (24 h) after initial cathodic reduction at $-1.3V_{SCE}$ for 600 s in deaerated 0.1 M NaCl + HCl at pH 4. Native air oxide XPS oxide fraction is shown on the y-axis..... 189

Fig. 5. 7. Cr22-MPEA XPS enrichment/depletion factor (f_A) where A = Ni, Fe, Cr, Mn, and Co for both A cations within native air oxide (y-axis), the passive film ($f_{A,ox}$) and elemental "A" within the altered zone ($f_{A,az}$) (i.e., metal/oxide interface) formed during potentiostatic passivation at $-0.25 V_{SCE}$ for 100 s, 1ks, 10 ks, and 86.4 ks (24 h) after initial cathodic reduction at $-1.3V_{SCE}$ for 600 s in deaerated 0.1 M NaCl + HCl at pH 4. 193

Fig. 5. 8. Cr14-MPEA XPS enrichment/depletion factor (f_A) where A = Ni, Fe, Cr, Mn, and Co for both "A" cations within the passive film ($f_{A,ox}$) and elemental "A" within the altered zone ($f_{A,az}$) (i.e., metal/oxide interface) formed during potentiostatic passivation at $-0.25 V_{SCE}$ for 100 s, 1ks, 10 ks, and 86.4 ks (24 h) after initial cathodic reduction at $-1.3V_{SCE}$ for 600 s in deaerated 0.1 M NaCl + HCl at pH 4..... 195

Fig. 5. 9. Ni-24Cr binary alloy XPS enrichment/depletion factor (f_A) where A = Ni, Fe, Cr, Mn, and Co for both "A" cations within the passive film ($f_{A,ox}$) and elemental "A" within the altered zone ($f_{A,az}$) (i.e., metal/oxide interface) formed during potentiostatic passivation at $-0.25 V_{SCE}$ for 100 s, 1ks, 10 ks, and 86.4 ks (24 h) after initial cathodic reduction at $-1.3V_{SCE}$ for 600 s in deaerated 0.1 M NaCl + HCl at pH 4..... 197

Fig. 5. 10. Cr(III) oxide fractions detected by AR-XPS at 45° take-off angle at each bulk Cr at. % concentration versus exposure time (100 s, 1 ks, 10 ks, and 86.4 ks) of passive films potentiostatically formed at $-0.25 V_{SCE}$ after initial cathodic reduction at $-1.3V_{SCE}$ for 600 s in deaerated 0.1 M NaCl + HCl at pH 4 of Ni-24Cr, Cr22-MPEA and Cr14-MPEA. The low-frequency impedance modulus for each exposure time is indicated by data point color. The low-frequency impedance for 100 s and 1 ks was 0.1 Hz and was 1 mHz for 10 ks and 86.4 ks. Passive current densities were obtained from LSV curves shown in Fig. 5.3..... 202

Fig. 8. 1. Ranging criteria for APT mass spectrum analysis for the base alloy and oxide film for from (a) 0-40 Da and (b) from 40-100 Da for Cr22-MPEA. A bin width of 0.1 Da was used. 216

Fig. 8. 2. Theoretical oxide layer configurations (top-bottom) (a) $Fe_2O_3-Cr_2O_3-NiO$, (b) $Fe_2O_3-NiO-Cr_2O_3$, (c) $Cr_2O_3-Fe_2O_3-NiO$, (d) corundum solid solution assuming X- Cr_2O_3 , and (e) rock-salt solid solution assuming X- NiO , where X = Ni, Fe, Cr, Mn, and Co. All oxide thicknesses were 1 nm..... 220

Fig. 8. 3. APT concentration profile of Cr22-MPEA oxide formed at $300^\circ C-10$ mbar $O_{2(g)}$ for 2 minutes. Concentration profile (a) was determined using proximity histogram across a 20 at. % iso-concentration surface with a bin width of 0.3 nm. Concentration profile (b) only shows the elemental/cation fraction of principle alloying elements and was calculated from (a). Plots were from a 10 nm thick region of interest through the center of the reconstructed volume..... 221

Fig. 8. 4. (a) elemental fractions, (b) Cation fractions (c, d) oxide fractions detected by AR-XPS at 30° to 90° take-off angle of Cr22-MPEA oxide formed at $300^\circ C-10$ mbar $O_{2(g)}$ for 2 minutes. The bulk atomic fraction for each alloying element is indicated by the horizontal dotted lines in (a) and (b). Plot (c) exhibits all detect oxides by AR-XPS. Plot (d) illustrates the sum oxide fraction of XCr_2O_4 (X=Ni, Fe) oxide and Mn(II) + Co(II) oxides produced from plot (c)..... 223

Fig. 8. 5. Theoretical XPS cation fraction of various oxide layer configurations (top-bottom) (a) $Fe_2O_3-Cr_2O_3-NiO$, (b) $Fe_2O_3-NiO-Cr_2O_3$, and (c) $Cr_2O_3-Fe_2O_3-NiO$. Cation fractions were

calculated from XPS intensity expressions assuming exponential attenuation in a homogenous thin overlayer. 225

Fig. 8. 6. Theoretical XPS cation fraction of (a) Corundum solid solution assuming X-Cr₂O₃ and (b) rock-salt solid solution assuming X-NiO, where X = Ni, Fe, Cr, Mn, and Co. Cation fractions were calculated from XPS intensity expressions assuming exponential attenuation in a homogenous thin overlayer. 226

List of Abbreviations and Symbols

CRA _s	Corrosion resistant alloys
PRE/PREN	Pitting resistance equivalency number
HEAs	High entropy alloys
CCAs	Compositionally complex alloys
MPEAs	Multi-principal element alloys
ΔS_{mix}	Entropy of mixing
LSV	Linear sweep voltammetry
EIS	Electrochemical impedance spectroscopy
OCP	Open circuit potential
APT	Atom probe tomography
XPS	X-ray photoelectron spectroscopy
SF-EIS	Single frequency EIS
AESEC	Atomic emission spectroelectrochemistry
Cr ₂₂ -MPEA	Ni ₃₈ Fe ₂₀ Cr ₂₂ Mn ₁₀ Co ₁₀
Cr ₁₄ -MPEA	Ni ₃₈ Fe ₂₀ Cr ₁₄ Mn ₁₄ Co ₁₄
Cr ₁₀ -MPEA	Ni ₃₈ Fe ₂₀ Cr ₁₀ Mn ₁₆ Co ₁₆
Cr ₆ -MPEA	Ni ₃₈ Fe ₂₀ Cr ₆ Mn ₁₈ Co ₁₈
AR-XPS	Angle-resolved X-ray photoelectron spectroscopy
i_{corr}	Corrosion current densities
E_{pit}	Pitting potentials
SCE	Saturated calomel electrode
$-Z''$	Imaginary impedance component
α_{film}	Constant phase element exponent
ϵ	Oxide dielectric constant
ϵ_0	Vacuum permittivity
f	Frequency
$\rho\delta$	Boundary resistivity
I	XPS intensity
l_{ox}	Oxide thickness
f_A	Enrichment term
$X_A^{\text{Ox}/s}$	Oxide or surface XPS cation fraction
X_A^b is	Bulk alloy fraction of element
R_A ,	Enrichment factor
i_{Ref}	Passive current density of the reference element
i_A	Passive current density of alloying element A,
X_A^s	Surface concentration of a particular element
ICP-AES	Inductively couple plasma atomic emission spectrometer
λ	Characteristic wavelength
I_λ ,	Emission intensity of an element at a characteristic wavelength

C_M	Concentration
κ_λ	Sensitivity factor for a given wavelength
v_M^{exp}	Elemental dissolution rates,
f	Flow rate, (/ mL min ⁻¹),
i_M^{exp}	Equivalent elemental current density
F	Faraday constant
z	Oxidation state
X_M	Atomic fraction of element M in the bulk material
Θ_M	Moles or grams per unit area
Q_M	Total quantity of dissolved element M per unit area
σ	Standard counting error
c_i	local concentration of species i,
N_T	Total number of atoms in the concentration measurement
t	Time
Z_{mod}	Impedance modulus
$-Z_{\text{phz}}$	Phase angle
ΔG_f°	Oxide formation energies
i	Current density
i_{pass}	Passive Current density
CPE_f	Film constant phase element
R_f	Film resistance
W_f	Warburg impedance
$\text{CPE}_{f/e}$	Film/electrolyte constant phase element
$\alpha_{f/e}$	Film/electrolyte constant phase element exponential
$R_{f/e}$	Film/electrolyte resistance
R_s	Solution resistance
$q_{\text{ox}}/q_{\text{total}}$	Charge efficiency
q_{total}	Total electrochemistry charge density
q_{ox}	Oxide charge density
M	Oxide molar mass
n	Number of electrons transferred to produce the oxide from its elements
ρ	Oxide density
AZ	Altered zone (i.e., oxide/metal interface)
s	Seconds
h	Hour
EAL, λ	Electron attenuation length
RSF, I_i^∞	Relative sensitivity factor

1. Introduction

1.1 Motivation

Conventional solid solution corrosion resistant alloys (CRAs) in aqueous solutions commonly contain Cr, Mo, and Ni as in the case of alloy C-22, (Ni-Cr-Mo-W alloy). These alloys have been shown to form a protective passive film that regulate the corrosion rate [1-3]. Passive films often involve combinations of alloying elements, as in spinels or single element oxides, such as Cr_2O_3 [4-7]. Designing new CRAs can be challenging due to the complexity of the aqueous corrosion process involving thermodynamics, kinetics, and many mechanistic processes. For example, during localized corrosion there are many different surface interactions contributing to the overall corrosion process: bulk material, oxide/metal (i.e., altered zone), and oxide/environment. Localized corrosion occurs when a passive film or protective film undergoes a localized breakdown event leading to local attack such as pitting or crevice corrosion [8-11]. Designing CRAs with a focus on passivity also requires an understanding on how material composition, processing, and environment effect the passive film's chemical identity, morphology, and thickness. Environment plays a large role in aqueous corrosion due to chemical interactions between solution species and the oxide on the material. For example, in Cl^- containing solutions the Cl^- anion can adsorb onto the passive film surface and/or may migrate through the oxide at grain boundaries leading to passive film thinning and/or breakdown [11, 12]. The above phenomena has been theoretically explained through the point defect model [11, 13].

Empirical observations have been made connecting alloying elements and corrosion resistance. When considering conventional alloys, like stainless steels and Ni based alloys, studies have shown an improvement in corrosion behavior with the addition of Cr, Mo, and/or W [2, 5, 6, 14-26]. Different properties of passivation and localized corrosion are affected by the listed alloying additions. Breakdown and passive current density are a complex function of many processes. Alloying elements can mitigate pit stabilization or function in increasing the formation and protectiveness of the passive film or both. Cr improves passivity through the formation of a stable resistant Cr oxide [6]. Mo and W are argued to not effect passivity but rather the repassivation potential, which occurs after pitting [18, 27-29]. On the other hand, recent studies have shown Mo and W are also beneficial to enhancing passivity. It has been demonstrated that, when minor

additions of Mo and/or W are added to a Cr-containing alloy, the resulting passive film becomes thicker and more enriched with Cr [5, 25, 26]. It is possible the improved oxide formation is a result of a “third element effect” where elements promoting Cr_2O_3 thermodynamic stability but kinetic contributions must be considered as well. From these empirical observations, a commonly used corrosion descriptor or figure of merit was derived to predict pitting resistance as a function of alloying element concentration called the pitting resistance equivalency number (PRE/PREN) [9, 30-36]. PRE is an empirical parameter based on the correlation observed between the pitting potential and a metric that is based on the alloying elements, shown in **Fig. 1.1** [30-37]. Lorentz and Medawar first showed this relationship between pitting potential and $\text{PRE} = \% \text{Cr} + 3.3 \% \text{Mo}$ [37]. Many other variations have been derived in which additional alloying elements are included in various amounts for example: $y\text{N}$ ($y = 12.8^{[36]}$ vs. $16^{[33]}$) and $u\text{W}$ ($u = 3.3^{[33]}$ and $0.5^{[35]}$), shown in **Fig. 1.2** [30-37]. Such expressions are designed empirically by correlating corrosion properties like pitting potential (E_{pit}) with composition representations based on Cr and Mo and some “potency factor” while neglecting other elements. Derived corrosion descriptors like PRE are empirical and typically come from a trial-and-error material design approach instead of fundamental science. Since, the pitting potential arises as function of many variables and represents a parameter that related to both the passive film, its breakdown, pit stabilization and growth; it cannot discern effects in the passive film due to the alloying elements. Furthermore, it is limited to a few alloying elements, it is not possible to predict anything about passivity. An enhanced corrosion resistance system must be developed to produce MPEA CRAs with many degrees of freedom utilizing a quantitative approach to better represent the qualities of a protective passive film.

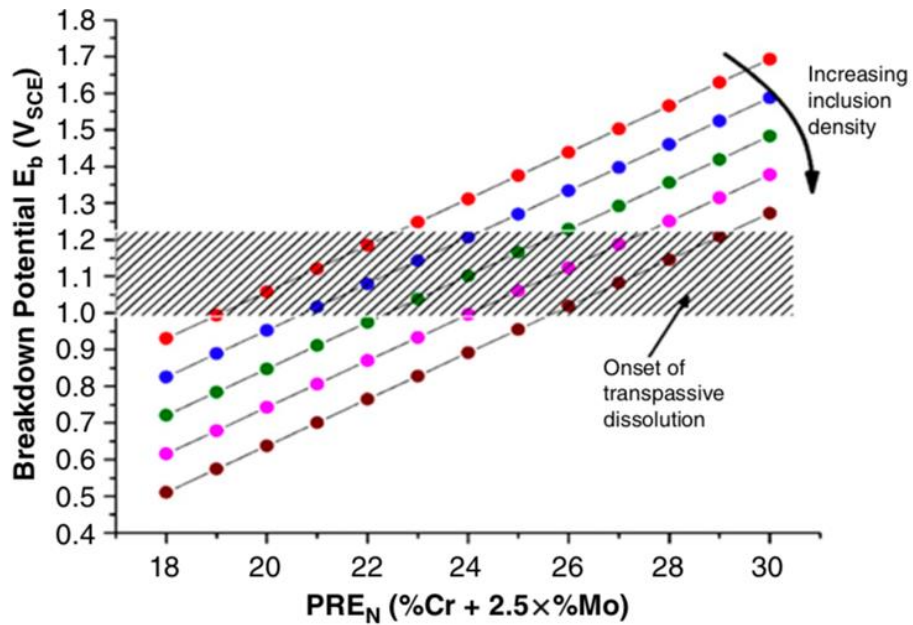


Fig 1. 1. Breakdown potential as a function of PRE_N (&Cr+2.5%Mo) for Type 444 Stainless Steels. Dowling, et. al., *CORROSION* 55 (1999): pp. 187–199

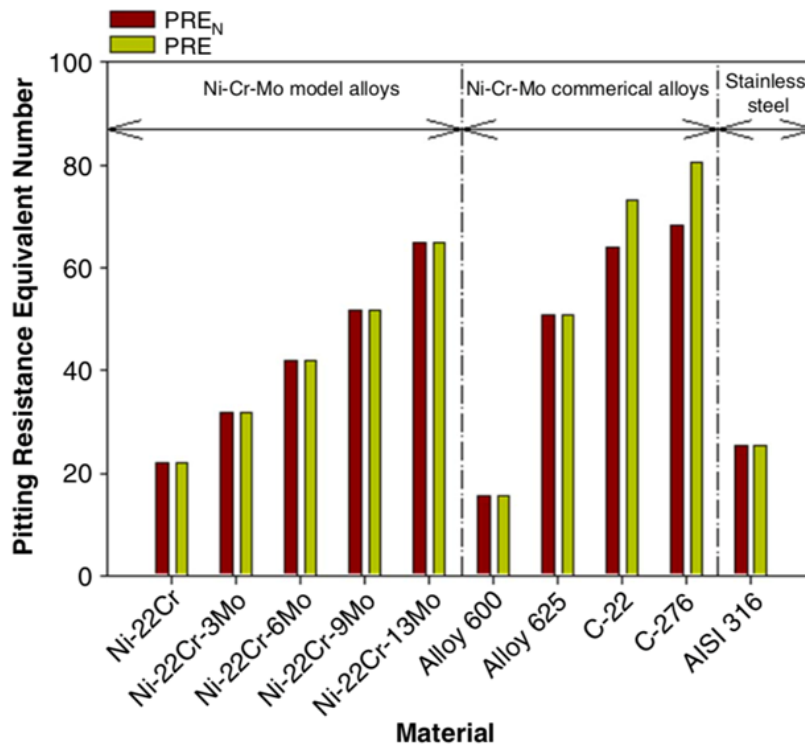


Fig 1. 2. *Pitting resistance equivalency numbers for a number of model Ni-22Cr (wt. %) alloys and the indicated commercial alloys according to the relationship indicated taking into account Cr, Mo, and W. A.Y. Gerard, et. al., CORROSION, 76 (2020) 485-499*

Alloys with five or more principal alloying elements in equiatomic proportions that result in a single phase solid solution alloy due to a high entropy of mixing was first termed high entropy alloys (HEAs) [38]. This class of materials have expanded in definition to incorporate alloys that can obtain a high entropy of mixing with just four principle alloying elements and the minor alloying of one or more elements in equiatomic concentrations called compositionally complex alloys (CCAs) [39, 40]. As more research has been conducted on these HEAs, a broader definition has been utilized allowing more freedom in alloy design, termed multi-principal element alloys (MPEAs), and is illustrated in **Fig. 1.3** [41, 42]. MPEAs can contain 3 or more principal element alloys with a non-equiatomic concentration with element concentrations as low as 5 at. % [38, 43]. Thermodynamically, the complex mixture of elements recreates a large entropy of mixing allowing the stabilization of a single homogeneous solid-solution phase ($\Delta S_{\text{mix}} \geq 1.5R$, R is ideal gas constant). With high concentrations of alloying elements, desirable properties can be developed capitalizing on the number of degrees of freedom and the known beneficial alloying elements, such as passivators, shown in **Fig. 1.4**. Also, by taking advantage of possible alloying combinations by utilizing favorable attributes such as large mutual solubilities, anomalous diffusion, and extended options in easily passivating alloying elements at higher bulk concentrations compared to conventional alloys [44-47]. This unique material design provides an opportunity to develop alloys with interesting corrosion properties based on the choice of alloying elements that contribute to corrosion resistance. However, the degrees of freedom are not without limit as other constraints exist, such as the desire to produce a single phase solid solution [1].

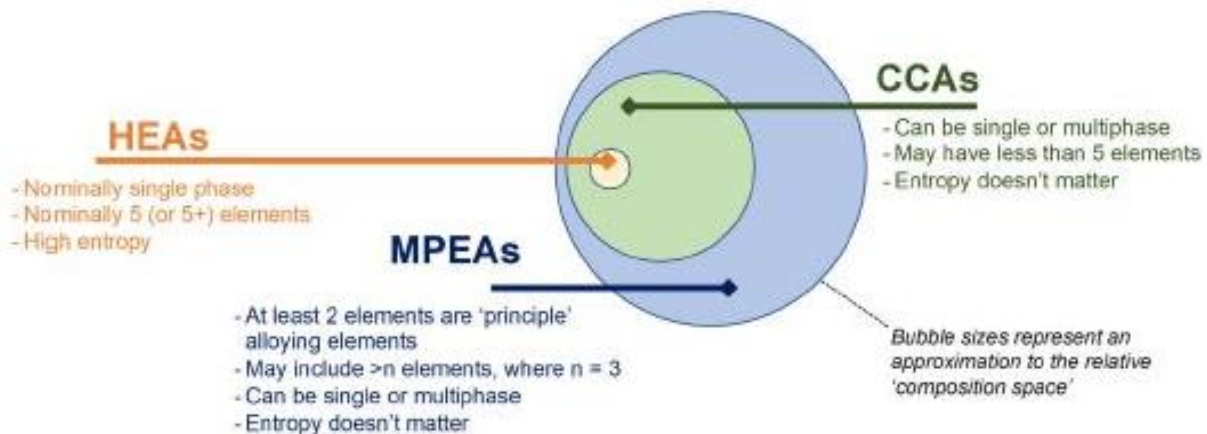


Fig 1. 3. A schematic of the broad classification for MPEAs, HEAs, and CCAs. N. Birbilis, et al., *npj Materials Degradation*, 5 (2021) 14.

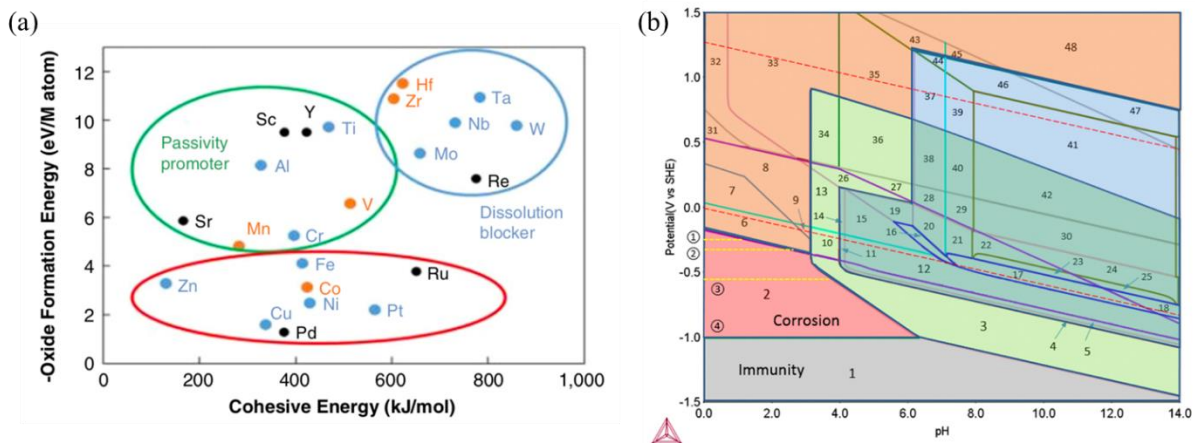


Fig 1. 4. (a) Oxide formation energy as a function of cohesive energy. Elements are listed either as passivity promotor (high negative free energy – easily passivate) or dissolution blockers (high cohesive energy). (b) E-pH stability diagram for Ni₃₈Cr₂₁Fe₂₀Ru₁₃Mo₆ in 1 kg H₂O at 25 C and 1 atm calculated by CALPHAD. Green regions are correlated to Cr₂O₃, Blue is Fe-Ni and Ni-Cr Spinels (XY₂O₄), and orange are other oxides. (a) C.D. Taylor, et al., *npj Materials Degradation*, 2 (2018) 6. (b) P. Lu, et al., *Scripta Materialia*, 153 (2018) 19-22.

Understanding the interactions of multiple elements and their effect on corrosion resistance and passivity is essential in creating new CRAs guided by understanding versus trial and error, based on the MPEA concept. Protective passive films typically demonstrate high durability and chemical resistance through forming a uniform oxide containing beneficial elements which are sometimes enriched, commonly seen with Cr-containing alloys [1]. These favorable properties are typically a result of thermodynamic and kinetic stability promoting the formation of either an ion-selective membrane, transport barrier, regulator of anodic and cathodic reactions, as well as by modifying characteristics of anion adsorption [1, 22, 48]. The most reactive element in oxygen and water could be regarded as the most likely to form, but this assumes that thermodynamic factors dominate. An opportunity does exist in the development of new CRAs through understanding the atomistic processes alloying elements influence in producing a protective passive film. This is a long-range goal. In the short term it is not clear how the oxide structure, composition, and nature will be based on the bulk composition of the MPEA. The fate of each alloying element during passivation is difficult to track and multiple tools are necessary. A more detailed review of MPEAs reveals that little is known to date about oxides formed during aqueous corrosion.

1.2 Background

MPEAs are different from conventional alloys because composition is not dominated by one element or the solvent-solute relationship typical of binary alloys. MPEAs were first synthesized in 2004 by Cantor and colleagues. They fabricated an equiatomic $\text{Fe}_{20}\text{Cr}_{20}\text{Mn}_{20}\text{Ni}_{20}\text{Co}_{20}$ ¹ alloy by induction melting, resulting in a multiphase microstructure dominated by the FCC phase [49]. Since then, these alloys have become a popular area of research especially for corrosion engineering.

Many studies exist on various equiatomic and non-equiatomic MPEAs suggesting potentially excellent aqueous corrosion and oxidation resistance in varying environments [50-80]. The origins of such corrosion resistance are not entirely understood. In fact, a wide range of corrosion current densities and pitting potentials are reported (often accepted as being regulated by the nature of the passive film). Excellent passivity in MPEAs was observed in reducing acids characterized by

¹ MPEA concentrations are reported exactly as done in literature (i.e., molar fraction versus atomic %).

broad passive regions. Tianshu and colleagues conducted a study comparing the corrosion behavior of a homogenous single FCC phase $\text{Ni}_{38}\text{Cr}_{21}\text{Fe}_{20}\text{Ru}_{13}\text{Mo}_6\text{W}_2$ (at.%) alloy vs. commercial SS316L in Cl^- [57]. The $\text{Ni}_{38}\text{Cr}_{21}\text{Fe}_{20}\text{Ru}_{13}\text{Mo}_6\text{W}_2$ demonstrated superior local corrosion resistance compared to SS316L in 0.6 M NaCl and 1 M, 6 M, 12 M HCl. Pitting corrosion was not observed on the $\text{Ni}_{38}\text{Cr}_{21}\text{Fe}_{20}\text{Ru}_{13}\text{Mo}_6\text{W}_2$ surface for any environment. Active dissolution of the MPEA was only observed after 24 hr immersion in 12 M HCl. The depassivation in 12 M HCl at room temperature suggests it is difficult to form the critical pit chemistry required for active pits. The corrosion rate was calculated for each alloy after 24 hr immersion in 12 M HCl. The $\text{Ni}_{38}\text{Cr}_{21}\text{Fe}_{20}\text{Ru}_{13}\text{Mo}_6\text{W}_2$ had a much lower rate (0.193 mm/year) compared to SS316L (1837 mm/year) [57]. Within the same study the passive behavior of $\text{Ni}_{38}\text{Cr}_{21}\text{Fe}_{20}\text{Ru}_{13}\text{Mo}_6\text{W}_2$ was compared to a Ni-based commercial alloy, C-22, by oxide growth in deaerated 6 M HCl $\text{N}_{2(\text{g})}$. This enhanced resistance was suggested to be caused by the formation of a continuous stable passive film promoted by the MPEAs homogenous single phase microstructure [57]. Other studies have also demonstrated that MPEAs show outstanding passivity and localized corrosion resistance attributed to improved passive behavior compared to conventional alloys [59, 62, 67, 68]. Lee and colleagues studied the effect of Al vs. pitting resistance for a $\text{Al}_x\text{CrFe}_{1.5}\text{MnNi}_{0.5}$ HEA where $x = 0, 0.3, \text{ and } 0.5$ in 15% H_2SO_4 . Each $\text{Al}_x\text{CrFe}_{1.5}\text{MnNi}_{0.5}$ HEA demonstrated a stable constant low current density passive region from 0.2 to 1.1 V_{SHE} (Volts versus Standard Hydrogen Electrode) suggesting the formation of a passive film [50]. These results often vary in corrosion properties and lack in detail on the passive films atomistic contributions to forming protective films.

The beneficial role of chromium in the corrosion resistance of conventional alloys has been known for many years. Commonly, alloying with Cr is linked to empirical observations, such as increasing Cr concentrations generally improves corrosion resistance, with either an abrupt or gradual decrease in i_{pass} shown in **Fig. 1.5**. This phenomenon is commonly observed in Fe- and Ni-based alloys, in which increasing Cr content causes a decrease in passive current densities [6, 15, 17, 21, 24, 81]. It has also been seen in MPEAs where Cr additions are beneficial to their corrosion protection [61, 69, 72, 82-88]. Koga et al. investigated the effects of bulk Cr concentration on the corrosion response of a series of CrCoNi MPEAs in simulated seawater [69]. Linear sweep voltammetry (LSV) showed that as bulk Cr concentration increased the corrosion current density and passive current density (i_{pass}) decreased, for example $\text{Cr}_{25}\text{Co}_{27.5}\text{Ni}_{27.5}$ $i_{\text{pass}} = 1.6 \mu\text{A cm}^{-2}$ and $\text{Cr}_{45}\text{Co}_{27.5}\text{Ni}_{27.5}$ $i_{\text{pass}} = 1.43 \mu\text{A cm}^{-2}$. Electrochemical impedance spectroscopy (EIS)

measurements were conducted to further probe the CrCoNi MPEAs corrosion properties after 1 hr immersion at the open circuit potential (OCP). Bode plots indicated an increase in bulk Cr concentration the polarization resistance increased, suggesting the formation of a more protective passive film [69]. Similar results have been observed for a FeCoNiCr_x ($x = 0, 13.22, 24.23$ wt. %) MPEA in 0.5 M H₂SO₄ and 3.5 wt. % NaCl in which the passive current density decreased from 0 wt. % Cr to higher Cr concentrations [83]. These MPEA studies focus on the effect of Cr and its general corrosion response, many unknowns remain on how Cr benefits MPEA passivity in forming protective passive films. It's important to improve the understanding of Cr in MPEA passivity, especially when Cr is typically already at or above the critical threshold known in conventional alloys like Fe-Cr, which is 12-13 at. % (**Fig. 1.5**) [17, 24].

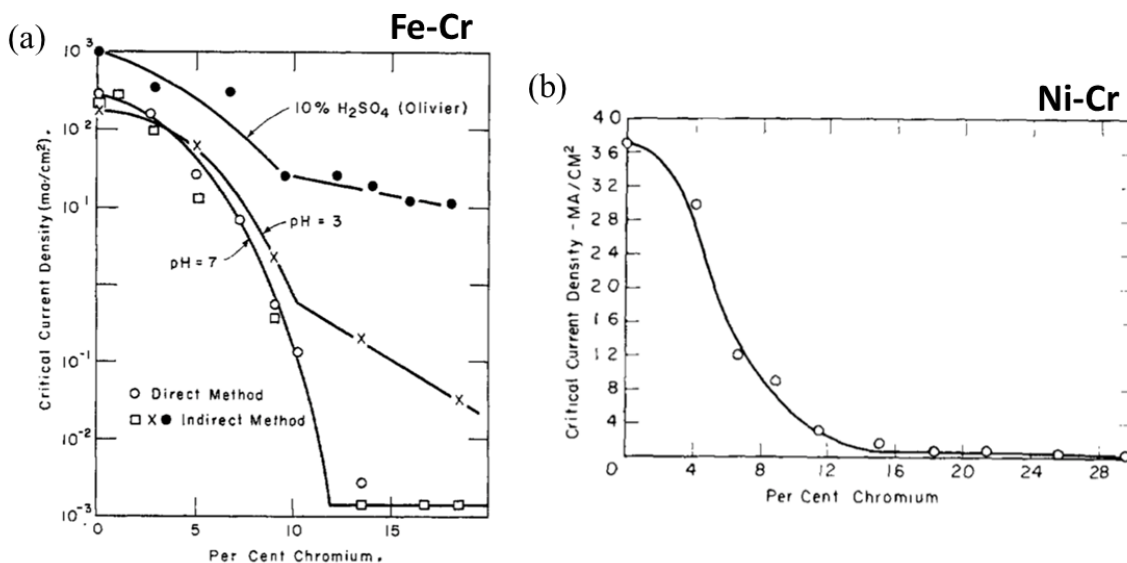


Fig 1. 5. Passive current density as a function of Bulk Cr concentration for (a) Fe-Cr binary alloys in H₂SO₄ and (b) Ni-Cr binary alloys in 1 N H₂SO₄. (a) P.F. King, et. al., *The Journal of Physical Chemistry*, 63 (1959) 2026-2032. (b) .A.P. Bond, et. al., *Journal*

Many investigations have been conducted in which researchers have electrochemically formed a passive film on a MPEA surface and characterized its atomistic properties [53, 56, 59, 84-99]. Majority of these passive film studies focus on the formation of a film under acidic conditions. Quiambao and colleagues conducted a detailed chemical and structural analysis of a potentiostatically-formed oxide on Ni₃₈Cr₂₁Fe₂₀Ru₁₃Mo₆W₂ MPEA in H₂SO₄ persulfate at pH 4 at

0.617 V_{SHE} [59]. The passive film was characterized by ex-situ atom probe tomography (APT) and X-ray photoelectron spectroscopy (XPS), which revealed a solid-solution oxide containing all oxidized alloying elements. Cr was observed to be enriched throughout the oxide. It was concluded that the passive film was a non-equilibrium, non-stoichiometric solid-solution oxide. Exceptional corrosion resistance was observed, which was attributed to the formation of a complex oxide containing Cr, Mo, and W [59]. Similarly, another study conducted by Zhou et al. saw similar results for a Hf_{0.5}Nb_{0.5}Ta_{0.5}Ti_{1.5}Zr alloy. The researchers found after potentiostatic passivation at passive potentials in 3.5 wt. % NaCl, the formed passive film was a single-phase solid solution oxide containing high concentrations of passivity promoting elements such as, Ti, Zr, Hf, Nb, and Ta, which was concluded from XPS [56]. Other investigations show similar results or suggests the formed passive films consists of stoichiometric oxides that are Cr rich or rich in other now passivating elements such as, Al [50, 53, 85, 86, 100]. To further understand MPEA passivity and their limitations, alkaline conditions should be considered especially when studies have shown differences in passive behavior between the two pH levels [5, 25, 101-107]. Consider conventional Ni- and Fe- alloys when passive films are formed under acidic conditions the resulting film is usually Cr rich [5, 25, 101, 106, 108]. When in alkaline conditions, the passive film is no longer rich with Cr species but enrichment switches to Fe or Ni depending on the alloy [104, 106], this is illustrated in **Fig. 1.6**. With a high number of principal alloying elements, it is important to characterize the electrochemical passive behavior of MPEAs when exposed to alkaline pH levels how it differs from acidic conditions. A few investigates exist in which the passive behavior of MPEAs is explored in alkaline pH levels [59, 89, 109, 110]. Choudhary et al. investigated the passive behavior of an equiatomic CoCrFeNi MPEA in 0.1 M NaCl at three different pH levels: 2, 6, and 10. XPS characterization of passive films formed after 4 hr immersion revealed that at all pH levels the passive films were enriched with Cr(III) species but the concentration of Ni(II) and Co(II) increased with pH level[89]. Similar results were obtained by Wang and colleagues for an equiatomic CoCrFeMoNi alloy in 0.34 M NaCl at four different pH levels: 1, 3, 5, and 7. From LSV a decrease in passive current density was observed with increase in pH level. XPS characterization of passive films formed for 1 hr at 0.5V_{SCE} at each pH level revealed all films were enriched with Cr but enrichment decreased with increase in pH level. Also, as pH increased the concentration of Ni(II), Co(II), Fe(II), and Fe(III) increased [109]. In both studies it was concluded the increase in non-Cr oxides was due to an increase thermodynamic stability at more

alkaline pH levels, which is demonstrated in **Fig. 1.7**. With limited research of MPEA passive films and the effect of alkaline pH levels, many knowns exist on the fate of each alloying element such as but not limited to, elemental dissolution during passivation and the elemental fraction at the oxide/metal interface.

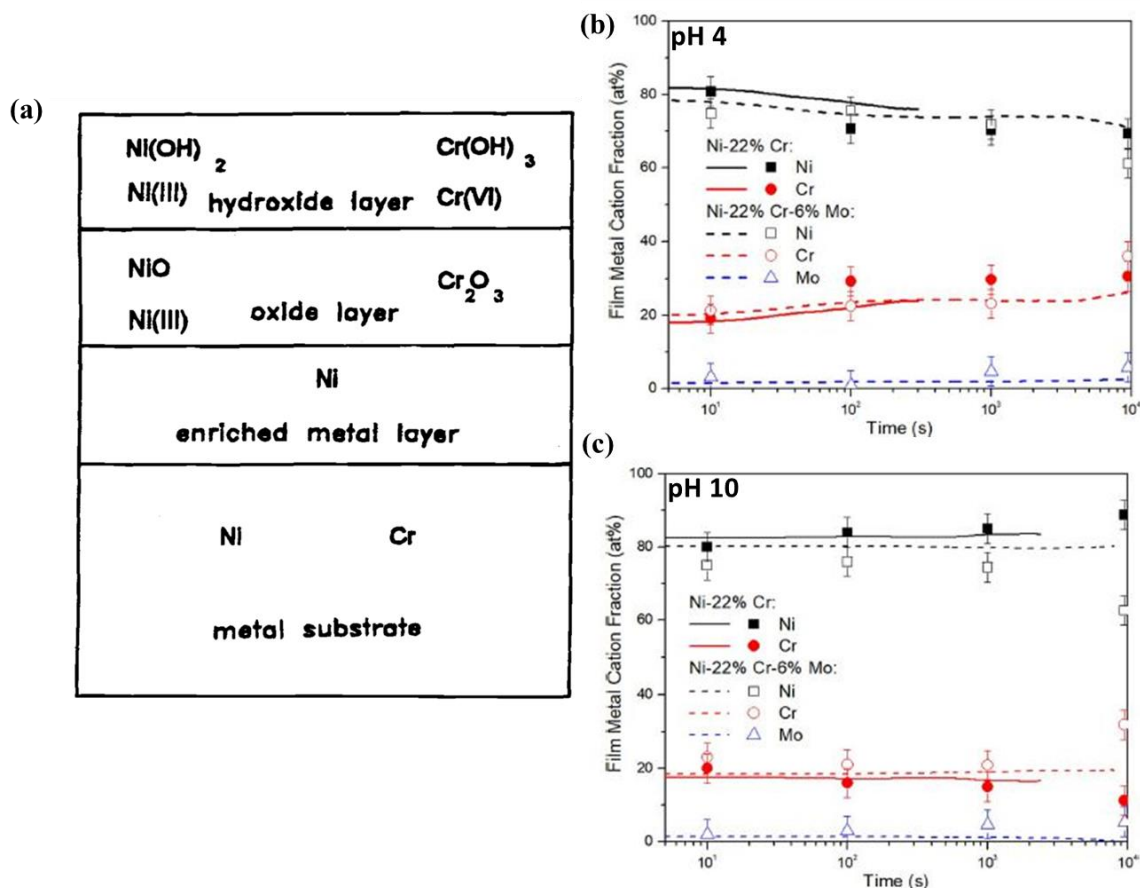


Fig 1. 6. (a) Model for passive films formed on Ni-Cr alloys. At acidic pH levels Cr-rich films form and at alkaline pH levels Ni-rich films form. Cation fraction as a function of exposure time for Potentiostatically formed passive films at $0.2V_{SCE}$ on Ni-Cr alloys in 0.1 M NaCl (b) pH 4 and (c) pH 10. (a) T. Jabs, et. al., *Journal of The Electrochemical Society*, 144 (1997) 1231-1243 and (b,c) K.L. Cwalina, et. al., *Journal of The Electrochemical Society*, 166 (2019) C3241-C3253.

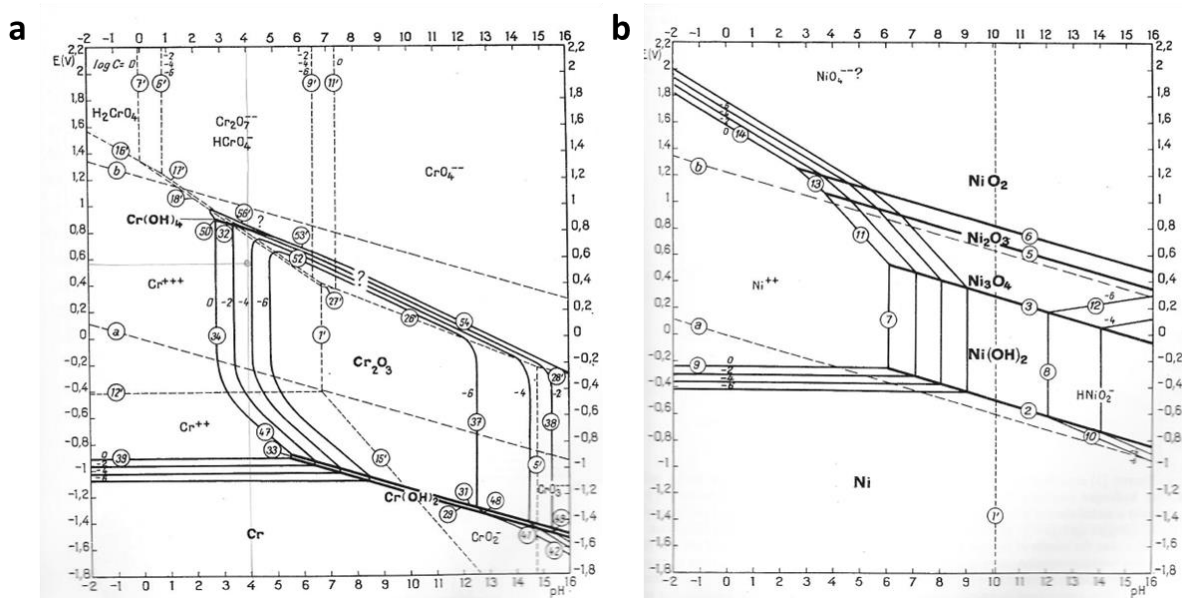


Fig 1. E-pH stability diagram in water at 25 °C for (a) Pure Cr and (b) Pure Ni. M. Pourbaix, National Association of Corrosion Engineers, Houston, TX, 1974.

During aqueous oxidation, many conventional alloys form a layered phase-separated oxide structure when formed slowly at a constant potential [5, 25, 26, 111-113]. When oxide growth is rapid, it has been suggested that a non-equilibrium solute-captured passive film can form [114]. This oxidation phenomenon was observed on an oxide film grown in solution on Ni-22Cr (wt. %) in which a large amount of Cr was observed to be “captured” within a Ni oxide when the oxide is grown relatively quickly [12]. Unlike these conventional alloys, it has been reported that, even during slow oxide growth of MPEAs, the resulting oxide has a complex nature [45, 59, 74-79, 115-122]. For example, Ni₃₈Cr₂₁Fe₂₀Ru₁₃Mo₆W₂ MPEA formed a non-equilibrium, non-stoichiometric solid-solution oxide from slow aqueous oxidation at a constant potential, conducted from XPS and APT [59]. The APT concentration profile for the solid solution oxide is shown in **Fig. 1.8** and compared to a layered APT concentration profile. Another study conducted by Wang and colleagues reported different findings for a Cr₁₅Fe₁₀Co₅Ni₆₀Mo₁₀ MPEA in which a passive film formed a layered structure after a relatively short period of time [123]. After forming a passive film for 1 h at 0 V_{MSE} in 0.05 M H₂SO₄ on the surface of a Cr₁₅Fe₁₀Co₅Ni₆₀Mo₁₀ MPEA the film consisted of an outer layer composed of Ni/Cr hydroxides and Fe and Mo oxides and an inner layer consisted mainly of Cr oxides [123]. How these solid solution and layered oxides formed were not discussed and remains unknown how these passive films develop over time.

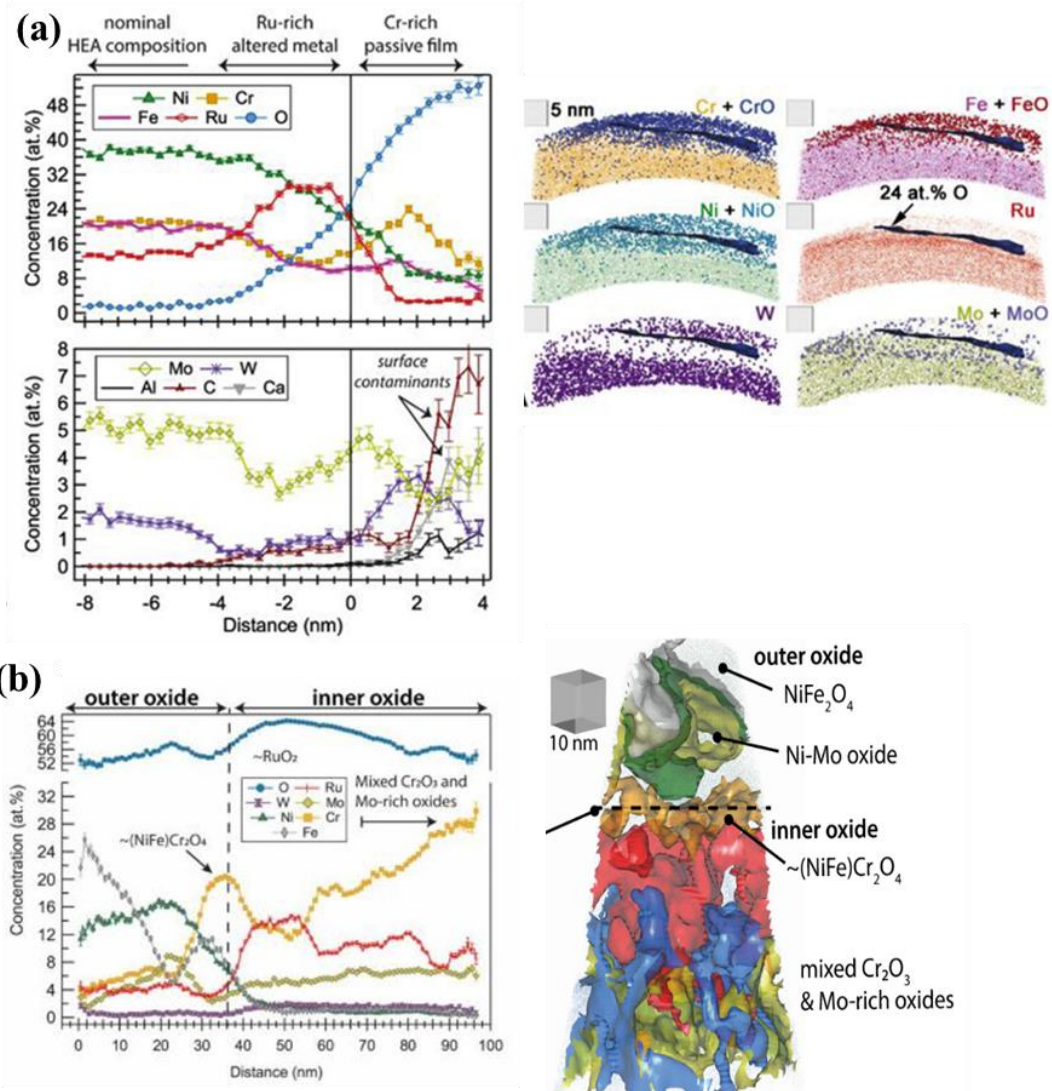


Fig 1. 8. APT concentration profiles and their corresponding 3D reconstruction of $Ni_{38}Cr_{21}Fe_{20}Ru_{13}Mo_6W_2$ MPEA (a) passive film electrochemically formed at 0.617 VSCE in H_2SO_4 persulfate pH 4 for 10 ks and (b) passive film formed by Air oxidation at 600 °C for 1080 mins.

Studies have investigated the effect of exposure time but often lack in detail about the passive film properties and focus on the general corrosion response as a function of exposure time and/or only investigate elemental dissolution utilizing techniques such as AESEC [84, 93, 95]. Choudhary et al. investigated the evolution of passivity in an equiatomic CoCrFeNi MPEA in 0.1 M NaCl solution at the open-circuit potential (OCP) at following time intervals: 1800 s, 1 h, 2 h, and 4 h and characterized by EIS [89]. Bode plots showed as exposure time increased the resulting

polarization resistance also increased. Details of the passive film atomistic properties were not explored at each exposure time. With such varying results seen in MPEA passive film structure and little information on film formation it is not well understood how these solid solution or layered oxides initially form and evolve over time.

The effect of high and low concentrations of bulk alloying elements on improved oxidation or poor oxidation is not completely understood. There is a need to close the knowledge gaps on how MPEA alloying elements promote the formation of a protective passive film. In this dissertation, close attention will be given to how these elements are incorporated into the oxide and their effect on the passive film's oxide configuration, chemistry, valence state, and electrochemical properties.

1.3 Critical Unresolved Issues

The passivation of MPEAs, both natural and electrochemically driven, is not well understood. Processes associated with passive film formation become complex when multiple alloying elements are present, compared to conventional alloys. To develop an improved understanding of elemental oxidation and dissolution during the passivation of MPEAs, each alloying element must be tracked to determine if they are: (1) oxidized and present in the passive film, (2) dissolved into solution, or (3) trapped in the oxide and retained at the oxide/metal interface. Electrochemical and passive film analyses must consist of both in situ and ex situ methods to better understand passive film formation and the fate of each principal alloying elements.

It is well known Cr is beneficial in improving the corrosion resistance of Fe- and Ni-based alloys and recently in MPEAs. Unfortunately, many unknowns remain on how Cr effects MPEA passivity and the passive films properties. Information pertaining to its role in the oxide and its relationship to a material's electrochemical response is important and the following questions should be considered: (1) is Cr reactive and is a corundum phase thermodynamically favored on MPEAs, (2) is there Cr enrichment in the oxide and (3) is there a Cr threshold for good passivation as observed in binary alloys? What limits Cr cation enrichment or that of any element?

Previous studies have focused on the electrochemical behavior of MPEA in various acidic environments. However, knowledge is limited to understanding the physical response and contains only simplistic statements on the molecular nature of detected oxides, which often are not

corroborated by a variety of methods. Commonly, little detail is given regarding the passive behavior, or this is only investigated in one particular environment. To better understand the passivation of multiple principal elements, detailed evaluation of the passive behavior and the formed passive film is needed in different pH levels, specifically at E-pH combinations where different elements might be protective.

Many investigations have demonstrated the influence of formation and/or exposure time on passive film formation during aqueous oxidation for conventional alloys. In the case of MPEAs, many passivation experiments are conducted at a set exposure time. How passive films develop on MPEA surfaces and form either layered stoichiometric oxides, non-equilibrium solute-captured oxide, layering of complex stoichiometric oxides, complex oxide mixtures, or non-stoichiometric multi-element solid solution oxide remains unclear. For an improved understanding of MPEAs aqueous oxidation, a range of exposure times must be explored in order to evaluate how these varies passive films form on MPEA surfaces.

1.4 Overall Objective

Evaluation of the role of alloying elements towards corrosion resistance and passivity has been shown to be complex in multi-element alloys, such as MPEAs. This dissertation aims to provide an in-depth evaluation of the role of various alloying elements, their fate in oxide, solution, altered layer (i.e., oxide/metal interface) and their influence on passive film formation and the resulting corrosion properties. The objectives will focus on further understanding how alloying elements effect oxide chemistry, oxidation state, cation fraction, layering versus solute-trapped oxides, and oxide identity of a passive film formed in aqueous conditions. Various in-situ and ex-situ characterization techniques will be utilized in order to provide an improved understanding of the oxide structure through elemental tracking of composition at the metal/oxide interface, across the oxide structure, and the oxide/environment interface.

1.5 Organization of Dissertation

The organization of the dissertation will consist of four chapters and an appendix:

Chapter 2 focuses on natural and electrochemically formed passive films on a $\text{Ni}_{38}\text{Fe}_{20}\text{Cr}_{22}\text{Mn}_{10}\text{Co}_{10}$ MPEA in acidic Cl^- electrolyte and compared to a binary Ni-24Cr alloy. An

in-depth analysis was conducted on electrochemically formed passive films and the fate of alloying elements both in the bulk alloy, oxide, and at the oxide/metal interface. Passive film formation will be monitored as function of time and characterization of electrochemical properties using single frequency electrochemical impedance spectroscopy (SF-EIS), electrochemical impedance spectroscopy (EIS), and LSV. Electrochemical techniques will provide information on the passive films thickness, impedance properties, and the relation to electrochemical polarization behavior. Atomistic and surface-sensitive analyses will consist of various techniques, such as: atom probe tomography (APT), X-ray photoelectron spectroscopy (XPS), and atomic emission spectroelectrochemistry (AESEC). These methods will provide an improved understanding of the oxide structure through elemental tracking of composition at the oxide/metal interface, across the oxide structure, and the oxide/environment interface.

Chapter 3 investigates the effect of Cr in $\text{Ni}_{38}\text{Fe}_{20}\text{Cr}_x\text{Mn}_{21-0.5x}\text{Co}_{21-0.5x}$ ($x = 22, 14, 10, 6$ at. % - i.e., Cr_x-MPEAs) MPEA passivity and comparisons are made with binary Fe-Cr, Ni-Cr, and Co-Cr alloys. The electrochemical passivation of each Cr alloy was explored using the same techniques discussed above for Chapter 2. A particular focus was made on the electrochemical passive properties and its correlation to bulk Cr and passive film Cr cation concentration. Cr enrichment and depletion factors were computed for the passive film and oxide/metal interface, respectively. Further Cr enrichment and depletion predications were made for a range of bulk Cr concentrations for passive films formed on the Cr-MPEA surfaces.

Chapter 4 will evaluate the electrochemical passive behavior and passive films formed on $\text{Ni}_{38}\text{Fe}_{20}\text{Cr}_x\text{Mn}_{21-0.5x}\text{Co}_{21-0.5x}$ ($x = 22, 14, 10, 6$ at. %) in alkaline Cl^- electrolyte and compared to binary Fe-Cr, Ni-Cr, and Co-Cr alloys. The same techniques discussed in Chapter 2 are used to evaluate the electrochemical behavior and comparisons were made with pH 4 work conducted in Chapter 2 and 3. Comparisons between experimental results and thermodynamic predications based from potential-pH stability diagrams for MPEAs at a pH of 10 were discussed.

Chapter 5 examines the effect of exposure time on $\text{Ni}_{38}\text{Fe}_{20}\text{Cr}_x\text{Mn}_{21-0.5x}\text{Co}_{21-0.5x}$ MPEAs ($x = 22, 14$ at. %) electrochemical passive behavior and passive film formation during aqueous oxidation in acidic Cl^- solution. The techniques used in Chapter 2 were utilized within this Chapter. Passive film chemistry, valence state, and configuration was characterized by angle-resolved X-ray photoelectron spectroscopy (AR-XPS) The electrochemical properties of the resulting passive

films were evaluated. Various comparisons as a function of exposure time were conducted such as, passive film cation fraction, oxide fraction, total Cr(III) oxide fraction, principal alloying element enrichment and depletion factors within the passive film and oxide/metal interface.

Chapter 6 summarizes the conclusions and key research points of each chapter.

Chapter 7 provides suggestions for future work based on the findings from this dissertation.

Chapter 8 is the appendix containing extra dissertational work. Investigations focus on understanding the nature of oxides formed on MPEA surfaces such as, phase separated versus solid solution oxides. The $\text{Ni}_{38}\text{Fe}_{20}\text{Cr}_{22}\text{Mn}_{10x}\text{Co}_{10}$ MPEA underwent thermal treatment forming a nm thick oxide and was characterized by ATP and AR-XPS. Various AR-XPS theoretical cation fraction predictions were computed assuming different configurations of phase separated oxides and solid solution oxides. Comparisons were made between experimental AR-XPS data and AR-XPS theoretical cation fraction predications.

1.6 References

1. Taylor, C.D., et al., *Integrated computational materials engineering of corrosion resistant alloys*. npj Materials Degradation, 2018. **2**(1): p. 6.
2. Lutton Cwalina, K., et al., *Revisiting the effects of molybdenum and tungsten alloying on corrosion behavior of nickel-chromium alloys in aqueous corrosion*. Current Opinion in Solid State and Materials Science, 2019. **23**(3): p. 129-141.
3. Rhodes, P.R., *Environment-Assisted Cracking of Corrosion-Resistant Alloys in Oil and Gas Production Environments: A Review*. CORROSION, 2001. **57**(11): p. 923-966.
4. Cwalina, K.L., et al., *In Operando Analysis of Passive Film Growth on Ni-Cr and Ni-Cr-Mo Alloys in Chloride Solutions*. Journal of The Electrochemical Society, 2019. **166**(11): p. C3241-C3253.
5. Zhang, X., D. Zagidulin, and D.W. Shoesmith, *Characterization of film properties on the NiCrMo Alloy C-2000*. Electrochimica Acta, 2013. **89**: p. 814-822.
6. Asami, K., K. Hashimoto, and S. Shimodaira, *An XPS study of the passivity of a series of iron—chromium alloys in sulphuric acid*. Corrosion Science, 1978. **18**(2): p. 151-160.
7. SUGIMOTO, K. and Y. SAWADA, *The Role of Alloyed Molybdenum in Austenitic Stainless Steels in the Inhibition of Pitting in Neutral Halide Solutions*. CORROSION, 1976. **32**(9): p. 347-352.
8. Scully, J.R., *Future Frontiers in Corrosion Science and Engineering, Part I*. CORROSION, 2018. **74**(1): p. 3-4.
9. Scully, J.R., *Future Frontiers in Corrosion Science and Engineering, Part II: Managing the Many Stages of Corrosion*. CORROSION, 2019. **75**(2): p. 123-125.
10. Scully, J.R. and P.V. Balachandran, *Future Frontiers in Corrosion Science and Engineering, Part III: The Next “Leap Ahead” in Corrosion Control May Be Enabled by Data Analytics and Artificial Intelligence*. CORROSION, 2019. **75**(12): p. 1395-1397.

11. Frankel, G.S., T. Li, and J.R. Scully, *Perspective—Localized Corrosion: Passive Film Breakdown vs Pit Growth Stability*. Journal of The Electrochemical Society, 2017. **164**(4): p. C180-C181.
12. Yu, X.-x., et al., *New Insights on the Role of Chloride During the Onset of Local Corrosion: TEM, APT, Surface Energy, and Morphological Instability*. CORROSION, 2019. **75**(6): p. 616-627.
13. McCafferty, E., *Introduction to Corrosion Science*. 2010, 233 Spring St, New York, NY 10013 USA: Springer.
14. Bocher, F., R. Huang, and J. Scully, *Prediction of Critical Crevice Potentials for Ni-Cr-Mo Alloys in Simulated Crevice Solutions as a Function of Molybdenum Content*. Corrosion, 2010. **66**.
15. Bond, A.P. and H.H. Uhlig, *Corrosion Behavior and Passivity of Nickel-Chromium and Cobalt-Chromium Alloys*. Journal of The Electrochemical Society, 1960. **107**(6): p. 488.
16. BRIGHAM, R.J., *Pitting of Molybdenum Bearing Austenitic Stainless Steel*. CORROSION, 1972. **28**(5): p. 177-179.
17. King, P.F. and H.H. Uhlig, *Passivity in the Iron-Chromium Binary Alloys*. The Journal of Physical Chemistry, 1959. **63**(12): p. 2026-2032.
18. Klapper, H. and J. Stevens, *Influence of alloying elements on the pitting corrosion resistance of CrMn-stainless steels in simulated drilling environments*. NACE - International Corrosion Conference Series, 2015. **2015**.
19. Klapper, H.S., N.S. Zadorozne, and R.B. Rebak, *Localized Corrosion Characteristics of Nickel Alloys: A Review*. Acta Metallurgica Sinica (English Letters), 2017. **30**(4): p. 296-305.
20. Marcus, P., *On some fundamental factors in the effect of alloying elements on passivation of alloys*. Corrosion Science, 1994. **36**(12): p. 2155-2158.
21. Osozawa, K. and H.J. Engell, *The anodic polarization curves of iron-nickel-chromium alloys*. Corrosion Science, 1966. **6**(8): p. 389-393.
22. Samin, A.J. and C.D. Taylor, *First-principles investigation of surface properties and adsorption of oxygen on Ni-22Cr and the role of molybdenum*. Corrosion Science, 2018. **134**: p. 103-111.
23. Sugimoto, K. and Y. Sawada, *The role of molybdenum additions to austenitic stainless steels in the inhibition of pitting in acid chloride solutions*. Corrosion Science, 1977. **17**(5): p. 425-445.
24. Uhlig, H.H. and G.E. Woodside, *Anodic Polarization of Passive and Non-passive Chromium-Iron Alloys*. The Journal of Physical Chemistry, 1953. **57**(3): p. 280-283.
25. Lloyd, A.C., et al., *Cr, Mo and W alloying additions in Ni and their effect on passivity*. Electrochimica Acta, 2004. **49**(17): p. 3015-3027.
26. Lloyd, A.C., et al., *The open-circuit ennoblement of alloy C-22 and other Ni-Cr-Mo alloys*. JOM, 2005. **57**(1): p. 31-35.
27. Gruss, K.A., et al., *Repassivation Potential for Localized Corrosion of Alloys 625 and C22 in Simulated Repository Environments*, in CORROSION 98. 1998, NACE International: San Diego, California. p. 15.
28. Mulford, S.J. and D. Tromans, *Crevice Corrosion of Nickel-Based Alloys in Neutral Chloride and Thiosulfate Solutions*. CORROSION, 1988. **44**(12): p. 891-900.

29. Kehler, B.A., G.O. Ilevbare, and J.R. Scully, *Crevice Corrosion Stabilization and Repassivation Behavior of Alloy 625 and Alloy 22*. CORROSION, 2001. **57**(12): p. 1042-1065.
30. Agarwal, D.C. and W.R. Herda, *The "C" family of Ni-Cr-Mo alloys' partnership with the chemical process industry: The last 70 years*. Materials and Corrosion, 1997. **48**(8): p. 542-548.
31. Cleland, J.H., *What does the pitting resistance equivalent really tell us?* Engineering Failure Analysis, 1996. **3**(1): p. 65-69.
32. Dowling, N.J.E., et al., *Effect of Alloying Elements and Residuals on Corrosion Resistance of Type 444 Stainless Steel*. CORROSION, 1999. **55**(2): p. 187-199.
33. Huang, R., et al., *Localized Corrosion Resistance of Fe-Cr-Mo-W-B-C Bulk Metallic Glasses Containing Mn+Si or Y in Neutral and Acidified Chloride Solutions*. CORROSION, 2010. **66**(3): p. 035003-035003-15.
34. Jargelius-Pettersson, R.F.A., *Application of the Pitting Resistance Equivalent Concept to Some Highly Alloyed Austenitic Stainless Steels*. CORROSION, 1998. **54**(2): p. 162-168.
35. Mishra, A.K. and D.W. Shoesmith, *Effect of Alloying Elements on Crevice Corrosion Inhibition of Nickel-Chromium-Molybdenum-Tungsten Alloys Under Aggressive Conditions: An Electrochemical Study*. CORROSION, 2014. **70**(7): p. 721-730.
36. Renner, M., et al., *Temperature as a pitting and crevice corrosion criterion in the FeCl₃ test*. Materials and Corrosion, 1986. **37**(4): p. 183-190.
37. Lorenz, K. and G. Medawar, *Über das Korrosionsverhalten austenitischer Chrom-Nickel-(Molybdän-) Stähle mit und ohne Stickstoffzusatz unter besonderer Berücksichtigung ihrer Beanspruchbarkeit in chloridhaltigen Lösungen* Thyssenforschung, 1969. **1**(3): p. 97-108.
38. Yeh, J.-W., et al., *Nanostructured High-Entropy Alloys with Multiple Principal Elements: Novel Alloy Design Concepts and Outcomes*. Advanced Engineering Materials, 2004. **6**(5): p. 299-303.
39. Yeh, J.-W., *Alloy Design Strategies and Future Trends in High-Entropy Alloys*. JOM, 2013. **65**(12): p. 1759-1771.
40. Gorsse, S., J.-P. Couzinié, and D.B. Miracle, *From high-entropy alloys to complex concentrated alloys*. Comptes Rendus Physique, 2018. **19**(8): p. 721-736.
41. Frankel, G.S., J. Vienna, and J. Lian, *WastePD, an innovative center on materials degradation*. npj Materials Degradation, 2017. **1**(1): p. 5.
42. Miracle, D., et al., *Exploration and Development of High Entropy Alloys for Structural Applications*. Entropy, 2014. **16**(1): p. 494-525.
43. Birbilis, N., et al., *A perspective on corrosion of multi-principal element alloys*. npj Materials Degradation, 2021. **5**(1): p. 14.
44. Laplanche, G., et al., *Phase stability and kinetics of σ -phase precipitation in CrMnFeCoNi high-entropy alloys*. Acta Materialia, 2018. **161**: p. 338-351.
45. Senkov, O.N., et al., *Oxidation behavior of a refractory NbCrMo_{0.5}Ta_{0.5}TiZr alloy*. Journal of Materials Science, 2012. **47**(18): p. 6522-6534.
46. Z. Tang, L.H., W. He, P.K. Liaw, *Alloying and Processing Effects on the Aqueous Corrosion Behavior of High-Entropy Alloys*. Entropy, 2014. **16**(2): p. 895-911.
47. Butler, T.M. and M.L. Weaver, *Oxidation behavior of arc melted AlCoCrFeNi multi-component high-entropy alloys*. Journal of Alloys and Compounds, 2016. **674**: p. 229-244.

48. Gerard, A.Y., et al., *Progress in Understanding the Origins of Excellent Corrosion Resistance in Metallic Alloys: From Binary Polycrystalline Alloys to Metallic Glasses and High Entropy Alloys*. CORROSION, 2020. **76**(5): p. 485-499.
49. Cantor, B., et al., *Microstructural development in equiatomic multicomponent alloys*. Materials Science and Engineering: A, 2004. **375-377**: p. 213-218.
50. Lee, C.P., et al., *Enhancing pitting corrosion resistance of Al_xCrFe1.5MnNi0.5 high-entropy alloys by anodic treatment in sulfuric acid*. Thin Solid Films, 2008. **517**(3): p. 1301-1305.
51. Pang, J., et al., *Oxide MnCr₂O₄ induced pitting corrosion in high entropy alloy CrMnFeCoNi*. Materialia, 2019. **6**: p. 100275.
52. Qiu, Y., et al., *Microstructural evolution, electrochemical and corrosion properties of Al_xCoCrFeNiTi_y high entropy alloys*. Materials & Design, 2019. **170**: p. 107698.
53. Raza, A., et al., *Corrosion resistance of weight reduced Al_xCrFeMoV high entropy alloys*. Applied Surface Science, 2019. **485**: p. 368-374.
54. Shang, X., et al., *The intrinsic mechanism of corrosion resistance for FCC high entropy alloys*. Science China Technological Sciences, 2018. **61**(2): p. 189-196.
55. Shang, X.-L., et al., *Effect of Mo Addition on Corrosion Behavior of High-Entropy Alloys CoCrFeNiMox in Aqueous Environments*. Acta Metallurgica Sinica (English Letters), 2019. **32**(1): p. 41-51.
56. Zhou, Q., et al., *Corrosion behavior of Hf_{0.5}Nb_{0.5}Ta_{0.5}Ti_{1.5}Zr refractory high-entropy in aqueous chloride solutions*. Electrochemistry Communications, 2019. **98**: p. 63-68.
57. Li, T., et al., *Localized corrosion behavior of a single-phase non-equimolar high entropy alloy*. Electrochimica Acta, 2019. **306**: p. 71-84.
58. Nene, S.S., et al., *Corrosion-resistant high entropy alloy with high strength and ductility*. Scripta Materialia, 2019. **166**: p. 168-172.
59. Quiambao, K.F., et al., *Passivation of a corrosion resistant high entropy alloy in non-oxidizing sulfate solutions*. Acta Materialia, 2019. **164**: p. 362-376.
60. Shi, Y., et al., *Homogenization of Al_xCoCrFeNi high-entropy alloys with improved corrosion resistance*. Corrosion Science, 2018. **133**: p. 120-131.
61. Xiao, D.H., et al., *Microstructure, mechanical and corrosion behaviors of AlCoCuFeNi-(Cr,Ti) high entropy alloys*. Materials & Design, 2017. **116**: p. 438-447.
62. Chen, Y.Y., et al., *Microstructure and electrochemical properties of high entropy alloys—a comparison with type-304 stainless steel*. Corrosion Science, 2005. **47**(9): p. 2257-2279.
63. Chou, Y.L., J.W. Yeh, and H.C. Shih, *The effect of molybdenum on the corrosion behaviour of the high-entropy alloys Co_{1.5}CrFeNi_{1.5}Ti_{0.5}Mox in aqueous environments*. Corrosion Science, 2010. **52**(8): p. 2571-2581.
64. Jayaraj, J., et al., *Corrosion behavior and surface film characterization of TaNbHfZrTi high entropy alloy in aggressive nitric acid medium*. Intermetallics, 2017. **89**: p. 123-132.
65. Kao, Y.-F., et al., *Electrochemical passive properties of Al_xCoCrFeNi (x=0, 0.25, 0.50, 1.00) alloys in sulfuric acids*. Corrosion Science, 2010. **52**(3): p. 1026-1034.
66. Lin, C.-M. and H.-L. Tsai, *Evolution of microstructure, hardness, and corrosion properties of high-entropy Al_{0.5}CoCrFeNi alloy*. Intermetallics, 2011. **19**(3): p. 288-294.
67. Qiu, Y., et al., *Corrosion characteristics of high entropy alloys*. Materials Science and Technology, 2015. **31**(10): p. 1235-1243.

68. Qiu, Y., et al., *Corrosion of high entropy alloys*. npj Materials Degradation, 2017. **1**(1): p. 15.
69. Koga, G.Y., et al., *Corrosion resistant and tough multi-principal element Cr-Co-Ni alloys*. Journal of Alloys and Compounds, 2021. **884**: p. 161107.
70. Sahu, S., et al., *Localized Corrosion Behavior of Non-Equiatomic NiFeCrMnCo Multi-Principal Element Alloys*. Electrochimica Acta, 2020. **354**: p. 136749.
71. Qiu, Y., et al., *Microstructure and corrosion properties of the low-density single-phase compositionally complex alloy AlTiVCr*. Corrosion Science, 2018. **133**: p. 386-396.
72. Rodriguez, A., J.H. Tylczak, and M. Ziomek-Moroz, *Corrosion Behavior of CoCrFeMnNi High-Entropy Alloys (HEAs) Under Aqueous Acidic Conditions*. ECS Transactions, 2017. **77**(11): p. 741-752.
73. Backman, L., et al., *Selective Oxidation in Refractory High Entropy Materials*. arXiv, 2019. **Condensed Matter, Materials Science**.
74. Butler, T.M., et al., *High temperature oxidation behaviors of equimolar NbTiZrV and NbTiZrCr refractory complex concentrated alloys (RCCAs)*. Journal of Alloys and Compounds, 2017. **729**: p. 1004-1019.
75. Chang, C.-H., M.S. Titus, and J.-W. Yeh, *Oxidation Behavior between 700 and 1300 °C of Refractory TiZrNbHfTa High-Entropy Alloys Containing Aluminum*. Advanced Engineering Materials, 2018. **20**(6): p. 1700948.
76. Daoud, H.M., et al., *Oxidation Behavior of Al₈Co₁₇Cr₁₇Cu₈Fe₁₇Ni₃₃, Al₂₃Co₁₅Cr₂₃Cu₈Fe₁₅Ni₁₅, and Al₁₇Co₁₇Cr₁₇Cu₁₇Fe₁₇Ni₁₇ Compositionally Complex Alloys (High-Entropy Alloys) at Elevated Temperatures in Air*. Advanced Engineering Materials, 2015. **17**(8): p. 1134-1141.
77. Gorr, B., et al., *Phase equilibria, microstructure, and high temperature oxidation resistance of novel refractory high-entropy alloys*. Journal of Alloys and Compounds, 2015. **624**: p. 270-278.
78. Gorr, B., et al., *High temperature oxidation behavior of an equimolar refractory metal-based alloy 20Nb20Mo20Cr20Ti20Al with and without Si addition*. Journal of Alloys and Compounds, 2016. **688**: p. 468-477.
79. Gorr, B., et al., *High-Temperature Oxidation Behavior of Refractory High-Entropy Alloys: Effect of Alloy Composition*. Oxidation of Metals, 2017. **88**(3): p. 339-349.
80. Holcomb, G.R., J. Tylczak, and C. Carney, *Oxidation of CoCrFeMnNi High Entropy Alloys*. JOM, 2015. **67**(10): p. 2326-2339.
81. Wegrelius, L., F. Falkenberg, and I. Olefjord, *Passivation of Stainless Steels in Hydrochloric Acid*. Journal of The Electrochemical Society, 1999. **146**(4): p. 1397-1406.
82. Yang, S., et al., *Effect of Cr content on corrosion behavior of AlCr_xFeNi₂Cu_{1.6} high entropy alloys*. Materials Research Express, 2019. **6**(7): p. 076501.
83. Chai, W., T. Lu, and Y. Pan, *Corrosion behaviors of FeCoNiCr_x (x = 0, 0.5, 1.0) multi-principal element alloys: Role of Cr-induced segregation*. Intermetallics, 2020. **116**: p. 106654.
84. Han, J., et al., *Potential Dependent Mn Oxidation and Its Role in Passivation of Ni₃₈Fe₂₀Cr₂₂Mn₁₀Co₁₀ Multi-Principal Element Alloy Using Multi-Element Resolved Atomic Emission Spectroelectrochemistry*. Journal of The Electrochemical Society, 2021. **168**(5): p. 051508.

85. Hsu, K.-M., S.-H. Chen, and C.-S. Lin, *Microstructure and corrosion behavior of FeCrNiCoMnx (x = 1.0, 0.6, 0.3, 0) high entropy alloys in 0.5 M H₂SO₄*. Corrosion Science, 2021. **190**: p. 109694.
86. Yang, J., et al., *Effects of Mn on the electrochemical corrosion and passivation behavior of CoFeNiMnCr high-entropy alloy system in H₂SO₄ solution*. Journal of Alloys and Compounds, 2020. **819**: p. 152943.
87. Wang, L., et al., *Study of the surface oxides and corrosion behaviour of an equiatomic CoCrFeMnNi high entropy alloy by XPS and ToF-SIMS*. Corrosion Science, 2020. **167**: p. 108507.
88. Luo, H., et al., *Corrosion behavior of an equiatomic CoCrFeMnNi high-entropy alloy compared with 304 stainless steel in sulfuric acid solution*. Corrosion Science, 2018. **134**: p. 131-139.
89. Choudhary, S., N. Birbilis, and S. Thomas, *Evolution of Passivity for the Multi-Principal Element Alloy CoCrFeNi with Potential, pH and Exposure in Chloride Solution*. Corrosion, 2021.
90. Gerard, A.Y., et al., *Aqueous passivation of multi-principal element alloy Ni₃₈Fe₂₀Cr₂₂Mn₁₀Co₁₀: Unexpected high Cr enrichment within the passive film*. Acta Materialia, 2020. **198**: p. 121-133.
91. Gerard, A.Y., et al., *The role of chromium content in aqueous passivation of a non-equiatomic Ni₃₈Fe₂₀Cr_xMn_{21-0.5x}Co_{21-0.5x} multi-principal element alloy (x = 22, 14, 10, 6 at%) in acidic chloride solution*. Acta Materialia, 2023. **245**: p. 118607.
92. Inman, S.B., et al., *Effect of Mn Content on the Passivation and Corrosion of Al_{0.3}Cr_{0.5}Fe₂Mn_xMo_{0.15}Ni_{1.5}Ti_{0.3} Compositionally Complex Face-Centered Cubic Alloys*. Corrosion, 2021. **78**(1): p. 32-48.
93. Li, X., et al., *Communication—Dissolution and Passivation of a Ni-Cr-Fe-Ru-Mo-W High Entropy Alloy by Elementally Resolved Electrochemistry*. Journal of The Electrochemical Society, 2020. **167**(6): p. 061505.
94. Panindre, A.M., et al., *Corrosion of Ni-Fe-Cr-Mo-W-X Multi-Principal Element Alloys*. Journal of The Electrochemical Society, 2021. **168**(3): p. 031513.
95. Qiu, Y., et al., *Real-time dissolution of a compositionally complex alloy using inline ICP and correlation with XPS*. npj Materials Degradation, 2020. **4**(1): p. 7.
96. Qiu, Y., et al., *A Surface Study of the Native Oxide upon a Compositionally Complex Alloy*. CORROSION, 2018. **74**(12): p. 1312-1317.
97. Wang, K., et al., *Potential-pH diagrams considering complex oxide solution phases for understanding aqueous corrosion of multi-principal element alloys*. npj Materials Degradation, 2020. **4**(1): p. 35.
98. Wang, Z., et al., *Effect of temperature on the passive film structure and corrosion performance of CoCrFeMoNi high-entropy alloy*. Corrosion Science, 2022. **208**: p. 110661.
99. Zhang, B., Y. Zhang, and S.M. Guo, *A thermodynamic study of corrosion behaviors for CoCrFeNi-based high-entropy alloys*. Journal of Materials Science, 2018. **53**(20): p. 14729-14738.
100. Qiu, X.-W. and C.-G. Liu, *Microstructure and properties of Al₂CrFeCoCuTiNi_x high-entropy alloys prepared by laser cladding*. Journal of Alloys and Compounds, 2013. **553**: p. 216-220.

101. Olefjord, I., B. Brox, and U. Jelvestam, *Surface Composition of Stainless Steels during Anodic Dissolution and Passivation Studied by ESCA*. Journal of The Electrochemical Society, 1985. **132**(12): p. 2854-2861.
102. Gray, J.J. and C.A. Orme, *Electrochemical impedance spectroscopy study of the passive films of alloy 22 in low pH nitrate and chloride environments*. Electrochimica Acta, 2007. **52**(7): p. 2370-2375.
103. LECKIE, H.P., *Effect of pH on the Stable Passivity of Stainless Steels*. CORROSION, 1968. **24**(3): p. 70-74.
104. Mishra, A.K. and D.W. Shoesmith, *The activation/depasivation of nickel–chromium–molybdenum alloys: An oxyanion or a pH effect—Part II*. Electrochimica Acta, 2013. **102**: p. 328-335.
105. Pardo, A., et al., *Influence of pH and Chloride Concentration on the Pitting and Crevice Corrosion Behavior of High-Alloy Stainless Steels*. CORROSION, 2000. **56**(4): p. 411-418.
106. Wang, Z., et al., *Effect of pH on the Electrochemical Behaviour and Passive Film Composition of 316L Stainless Steel*. Acta Metallurgica Sinica (English Letters), 2019. **32**(5): p. 585-598.
107. Gray, J.J., et al., *Influence of Solution pH, Anion Concentration, and Temperature on the Corrosion Properties of Alloy 22*. Journal of The Electrochemical Society, 2006. **153**(3): p. B61.
108. Lutton, K., et al., *Passivation of Ni-Cr and Ni-Cr-Mo Alloys in Low and High pH Sulfate Solutions*. Journal of The Electrochemical Society, 2023. **170**(2): p. 021507.
109. Wang, Z., et al., *Corrosion behavior and surface characterization of an equiatomic CoCrFeMoNi high-entropy alloy under various pH conditions*. Journal of Alloys and Compounds, 2022. **900**: p. 163432.
110. Zheng, Z.Y., et al., *Microstructure and corrosion behaviour of FeCoNiCuSn_x high entropy alloys*. Materials Science and Technology, 2015. **31**(10): p. 1148-1152.
111. Mishra, A.K., et al., *The activation/depasivation of nickel–chromium–molybdenum alloys in bicarbonate solution: Part I*. Electrochimica Acta, 2013. **100**: p. 118-124.
112. Hayes, J.R., et al., *Influence of Chromium and Molybdenum on the Corrosion of Nickel-Based Alloys*. CORROSION, 2006. **62**(6): p. 491-500.
113. Zagidulin, D., et al., *Characterization of surface composition on Alloy 22 in neutral chloride solutions*. Surface and Interface Analysis, 2013. **45**(6): p. 1014-1019.
114. Yu, X.-x., et al., *Nonequilibrium Solute Capture in Passivating Oxide Films*. Physical Review Letters, 2018. **121**(14): p. 145701.
115. Jayaraj, J., et al., *Microstructure, mechanical and thermal oxidation behavior of AlNbTiZr high entropy alloy*. Intermetallics, 2018. **100**: p. 9-19.
116. Liu, C.M., et al., *Microstructure and oxidation behavior of new refractory high entropy alloys*. Journal of Alloys and Compounds, 2014. **583**: p. 162-169.
117. Otto, F., et al., *Decomposition of the single-phase high-entropy alloy CrMnFeCoNi after prolonged anneals at intermediate temperatures*. Acta Materialia, 2016. **112**.
118. Senkov, O.N., et al., *Development and exploration of refractory high entropy alloys—A review*. Journal of Materials Research, 2018. **33**(19): p. 3092-3128.
119. Waseem, O.A., et al., *A combinatorial approach for the synthesis and analysis of Al_xCr_yMo_zNbTiZr high-entropy alloys: Oxidation behavior*. Journal of Materials Research, 2018. **33**(19): p. 3226-3234.

120. Waseem, O.A., et al., *The effect of Ti on the sintering and mechanical properties of refractory high-entropy alloy $Ti_xWTaVCr$ fabricated via spark plasma sintering for fusion plasma-facing materials*. *Materials Chemistry and Physics*, 2018. **210**: p. 87-94.
121. Yang, Y., J.H. Perepezko, and C. Zhang, *Oxidation synthesis of $Hf_6Ta_2O_{17}$ superstructures*. *Materials Chemistry and Physics*, 2017. **197**: p. 154-162.
122. Zheng, J., et al., *Isothermal oxidation mechanism of a newly developed Nb–Ti–V–Cr–Al–W–Mo–Hf alloy at 800–1200°C*. *International Journal of Refractory Metals and Hard Materials*, 2016. **54**: p. 322-329.
123. Wang, X., et al., *Origin of enhanced passivity of Cr–Fe–Co–Ni–Mo multi-principal element alloy surfaces*. *npj Materials Degradation*, 2023. **7**(1): p. 13.

2 Aqueous Passivation of Multi-Principal Element Alloy Ni₃₈Fe₂₀Cr₂₂Mn₁₀Co₁₀: Unexpected High Cr Enrichment within the Passive Film

A manuscript summarizing this chapter has been published:

A.Y. Gerard, J. Han, S.J. McDonnell, K. Ogle, E.J. Kautz, D.K. Schreiber, P. Lu, J.E. Saal, G.S. Frankel, J.R. Scully, Aqueous passivation of multi-principal element alloy Ni₃₈Fe₂₀Cr₂₂Mn₁₀Co₁₀: Unexpected high Cr enrichment within the passive film, *Acta Materialia*, 198 (2020) 121-133.

2.1 Abstract

The aqueous passivation of a non-equiatomic Ni₃₈Fe₂₀Cr₂₂Mn₁₀Co₁₀ - at. % (Ni₄₀Fe₂₀Cr₂₀Mn₁₀Co₁₀ - wt. %) multi-principal element alloy (MPEA) was investigated in 0.1 M NaCl at pH 4 and compared to a conventional binary Ni₇₆Cr₂₄ - at. % (Ni₇₈Cr₂₂ - wt. %) alloy. The electrochemical behavior and oxide film characteristics were explored utilizing in-situ electrochemical and ex-situ surface-sensitive techniques. The passive film composition, thickness, and elemental valence states, and fate of each element were studied by in-situ atomic emission spectro-electrochemistry, ex-situ X-ray photoelectron spectroscopy, and atom probe tomography. The Ni₃₈Fe₂₀Cr₂₂Mn₁₀Co₁₀ MPEA demonstrated slightly better corrosion resistance compared to the binary Ni₇₆Cr₂₄ alloy. Passive films on the MPEA contained primarily Cr, and small amounts of Ni, Fe and Mn, while dissolution of Ni, Fe, Co was observed. Ni⁰ was enriched at the oxide/metal interface while Cr was depleted. Enrichment of Cr in the passive film occurred to a greater extent in the MPEA than for the Ni-Cr binary alloy. Enrichment factors were determined and the origins of enrichment are discussed.

2.2 Introduction

Multi-principal element alloys (MPEAs), a subset of which include high entropy alloys (HEAs), contain 5 or more principal elements, typically in the range of 5 to 35 at. % [1-5]. The term “high entropy” is derived from their high configurational entropy, typically greater than 1.5

R, where R is the ideal gas constant. More broadly, the high number of principal elements for MPEAs increases the degrees of freedom in alloy composition, especially when non-equiatomic concentrations are considered [6, 7]. The alloys also have the ability to form a homogenous solid solution, due in part to their high configurational entropy of mixing and near-zero enthalpy of mixing, particularly when the principal elements share similar atomic sizes [8-11]. MPEAs often have desirable properties derived from their unique attributes, such as large mutual solid solubilities, anomalous diffusion behavior, and the presence of multiple readily oxidized alloying elements present at significant bulk concentrations compared to most conventional alloys [12-15]. Concerning the design of corrosion resistant alloys (CRAs) based on MPEAs without consideration of high strength, the desired alloy properties include a homogenous solid solution phase, compositional stability, as well as a minimization of structural and chemical non-uniformities [3, 16]. Such alloys may form passive films with protective qualities towards corrosion depending on either the presence of strong passivating elements and/or the formation of a unique oxide based on unusual combinations of alloying elements.

Only a few studies of HEAs or MPEAs correlate protective film properties with aqueous corrosion or thermal oxidation behavior [8, 13, 17-33]. Corrosion current densities (i_{corr}) vary from 10^{-8} to 10^{-1} A/cm², indicating passive as well as active corrosion, and pitting potentials (E_{pit}) from -800 to +900 mV_{SCE} (mV versus saturated calomel electrode) depending on the alloy and environment [1, 3, 4, 6, 8-10, 32-45]. However, it is not clear what factors contribute to these large differences in corrosion behavior. The homogenization of Al_xCoCrFeNi with varying Al content ($x = 0.3, 0.5, 0.7$) was investigated in 3.5 wt. % NaCl [36]. Homogenized samples demonstrated a higher E_{pit} and lower passive current densities (i_{pass}) than otherwise seen. E_{pit} for as-cast Al_{0.3}CoCrFeNi was 522 mV_{SCE}, and increased to 808 mV_{SCE} after alloy homogenization [36]. The effects of Cr and Ti additions on the passive behavior of AlCoCuFeNi alloy were also examined in 0.5 M H₂SO₄ [35]. AlCoCuFeNi, AlCoCuFeNi+Cr, AlCoCuFeNi+CrTi, and AlCoCuFeNi+Ti all demonstrated broad passive regions during potentiodynamic polarization in 0.5 M H₂SO₄ at room temperature. Increased corrosion resistance upon Cr and Cr-Ti alloying was attributed to a protective Cr passive film [35]. Li et al. studied the localized corrosion of single-phase non-equiatomic Ni₃₈Cr₂₁Fe₂₀Ru₁₃Mo₆W₂ exposed to various HCl concentrations (1, 6, and 12 M)[32]. Superior corrosion resistance was seen in 1 M and 6 M HCl compared to a commercial Ni-Cr-Mo-W alloy (C-22). The MPEA experienced spontaneous passivation and had a broad passive region

in 1 and 6 M HCl. The only form of corrosion observed was transpassive dissolution of Cr and Ru at high potentials. In 12 M HCl, this alloy experienced active corrosion but at a relatively low rate. No pits were observed at room temperature in all three chloride environments. The high pitting resistance of the $\text{Ni}_{38}\text{Cr}_{21}\text{Fe}_{20}\text{Ru}_{13}\text{Mo}_6\text{W}_2$ was attributed to both resistance to pit initiation due to formation of a stable continuous passive film, as well as the inability to form an acidified Cl^- rich solution at a critical depassivating composition to enable fast dissolution of active pits at room temperature [32]. Although the Cr-Mo-W content in this alloy was similar to alloy C-22 (Ni-Cr-Mo-W), the alloy demonstrated better passivity [32]. The question is whether protective films on HEAs and MPEAs possess unique attributes that differ from those on conventional alloys. The nature of the passive film on $\text{Ni}_{38}\text{Cr}_{21}\text{Fe}_{20}\text{Ru}_{13}\text{Mo}_6\text{W}_2$ alloy formed during potentiostatic polarization at 0.54 V_{SHE} (V versus standard hydrogen electrode) in pH 4, 0.1 M $\text{Na}_2\text{SO}_4 + \text{H}_2\text{SO}_4$ consisted of an oxide film rich in Cr (present as both $\text{Cr}(\text{OH})_3$ and Cr_2O_3) and Ru (present as RuO_2) containing small amounts of oxidized Ni, Fe, Mo, and W within a highly disordered corundum structure [8]. It was concluded from X-ray photoelectron spectroscopy (XPS) spectra deconvolution and atom probe tomography (APT) that all alloying elements were oxidized and present within the passive film but some were preferentially enriched while others were depleted.

While protective passivating elements like Ti, Al, and Cr improve the corrosion resistance over a range of different material classes including stainless steels, Ni-based alloys, MPEAs, the key beneficial attributes of passive films on the latter remain unknown [46]. If passivity was solely attributable to Cr oxides, it is unclear why MPEAs with Cr contents similar to conventional commercial Ni-based alloys and stainless steels would have better, worse or similar corrosion resistance.

Selected passive film forming elements are often enriched while others are depleted in the oxide and at the oxide/metal interface during aqueous passivation of an alloy, but in the case of MPEAs the connection with corrosion resistance is often very tentative. The passive behavior of an equiatomic CoCrFeMnNi in 0.05 M H_2SO_4 solution was investigated at 0.2, 0.4, and 0.6 V_{SCE} using XPS and Time-of-Flight Secondary Ions Mass Spectrometry (ToF-SIMS) but was not compared to any other alloy [33]. At all three potentials, the passive film behavior was similar with slight changes observed in cation and metallic near-surface concentrations just below the oxide. The passive film was consistently enriched in Cr^{3+} substantially above the at. % present in

the alloy. Cr^{3+} was interpreted from XPS as mainly $\text{Cr}(\text{OH})_3$ with some Cr_2O_3 in the outer and inner layers of the film. However, no explicit structural data were provided. At each potential, Fe and Co oxides were primarily located in the outer oxide layer while Mn was found mainly in the inner oxide region. No oxidized Ni was detected in the passive film at any potential but elemental Ni enrichment was observed at the oxide/metal interface, which was depleted in elemental Cr, Fe, and Mn [33]. The passive film formed on a CoCrFeMnNi HEA in 0.1 M H_2SO_4 at $\sim 0.16 \text{ V}_{\text{SCE}}$ for 2 hours was also investigated using XPS and compared to SS304L [44]. All alloying elements were oxidized and Mn and Co were present in various valence states. The oxide was slightly enriched in Fe and depleted in oxidized Ni and Cr. This stands in marked contrast with the findings of others where Cr cations were enriched in the passive film to levels of three fold their bulk concentration [33, 44]. SS304L (Fe-18Cr-8Ni; wt. %), possessing a passive film that is typically enriched in oxidized Cr and Fe with limited Ni, had superior corrosion resistance compared to the CoCrFeMnNi with a low Cr cation fraction in its passive film [44]. Rodriguez et al. did not analyze the oxide film composition but found that a series of equiatomic and non-equiatomic CoCrFeMnNi HEAs exhibited variable corrosion behavior [45]. For instance, corrosion resistance was inferior to SS316 (Fe-18Cr-10Ni-3Mo; wt. %), equal to SS316 and, in one case, almost as good as C276 (57Ni-16Cr-16Mo-7[Fe+Co]-4W-1Mn; wt. %) depending on the exact CoCrFeMnNi alloy composition when tested in 0.6 M NaCl at 40 °C [45]. Together these reports highlight potential differences in MPEA corrosion behavior and suffer from a lack of definitive passive film characterization or contain contradictory findings regarding the passive film. Therefore, the key beneficial attributes of protective passive films formed on MPEAs that regulate corrosion remain unclear.

Understanding the attributes contributing to the formation of protective films on MPEAs is critical to understanding the corrosion performance of this class of materials. This requires a comprehensive investigation of chemical composition, valence state, morphology, layering, and structure of the passive film. All elements must be tracked to ascertain their fate with corroborating methods [47]. It also requires careful comparison to a model binary alloy with similar Cr content. The most comprehensive studies of passive films on MPEAs utilized ToF-SIMS combined with XPS [33] or performed XPS along with 3D APT [8], but no study to date has combined the complementary aspects of these various methods in a comparison to a binary alloys with the same

Cr content. Insights into the origins of and theories embodying elemental enrichment and depletion need to be developed as well.

In this study, a non-equimolar, single phase, solid solution $\text{Ni}_{38}\text{Fe}_{20}\text{Cr}_{22}\text{Mn}_{10}\text{Co}_{10}$ (at. %) alloy was compared to a single phase, solid solution $\text{Ni}_{76}\text{Cr}_{24}$ (at. %) binary alloy with the goals of (a) making a more definitive connection between the fate of alloying elements and the cation fractions of the alloying elements in the oxide and (b) connecting the composition and other attributes of the oxide with corrosion properties. Attention was given to the fate of all the elements during passivation using XPS, AESEC, and APT. The pitting behavior of this alloy and similar alloys with lower Cr content was recently presented [48]; this work focuses on the nature of the passive film and its connection to passive dissolution and passive film breakdown.

2.3 Experimental

The $\text{Ni}_{38}\text{Fe}_{20}\text{Cr}_{22}\text{Mn}_{10}\text{Co}_{10}$ - at. % MPEA was arc-melted, cast, and homogenized at 1100 °C [7]. Within this region, a single FCC phase solid solution is stable [7]. A solid solution $\text{Ni}_{76}\text{Cr}_{24}$ - at. % alloy was used for comparison. The $\text{Ni}_{76}\text{Cr}_{24}$ binary alloy was arc-melted, cast, rolled, solutionized at 1100 °C, and recrystallized, resulting in a homogenous single-phase alloy. All tested materials and corresponding compositions are listed in **Table 2.1**. For electrochemical testing, sample surfaces were mechanically ground to 1200 grit using SiC and then polished with a 0.25 μm diamond suspension. Samples were degreased with isopropanol, rinsed with deionized water, and dried with nitrogen gas.

Table 2.1. Model Multi-Principal Element Alloy and Binary Alloy Compositions

Alloy	Chemical Composition (at. %)	Chemical Composition (wt. %)
NiFeCrMnCo	38Ni-20Fe-22Cr-10Mn-10Co	40Ni-20Fe-20Cr-10Mn-10Co
Ni-24Cr	76Ni-24Cr	78Ni-22Cr

Electrochemical tests were conducted in $\text{N}_{2(\text{g})}$ -deaerated 0.1 M NaCl, with a final pH adjusted to 4 using 10^{-4} M HCl. Experiments were performed with a Gamry Instrument Reference 600+™ potentiostat. A standard three-electrode flat cell was utilized with a Pt mesh counter electrode, a saturated calomel reference electrode, and a MPEA or $\text{Ni}_{76}\text{Cr}_{24}$ sample as the working electrode. The samples were pressed against a Teflon® O-ring to expose an area of 0.1 cm^2 . All potentials

are reported against SCE. Potentiodynamic polarization experiments were conducted over a range of applied potentials (-1.3 V_{SCE} to +0.8 V_{SCE}) with a scan rate of 0.5 mV/s. Two procedures were utilized. In the first, an initial potentiostatic hold of -1.3 V_{SCE} was conducted for 600 s to cathodically reduce the air-formed oxide. This was followed by an upward potential scan at 0.5 mV/s starting from the reduction potential. Using Gamry Instruments impedance software, the imaginary impedance component (-Z'') was monitored during the potential sweep utilizing an applied AC voltage of 20 mV_{rms} at 1 Hz. In the other procedure utilized, natural air-formed oxides were tested. The air-formed oxide was developed in lab air at 22 °C with a relative humidity of 50 % for no longer than 1 hour before testing. The natural, air-formed oxide was then exposed to the test solution for 30 min at the open circuit potential (OCP). Following this, an electrochemical impedance spectroscopy (EIS) spectrum from 100 kHz to 1 mHz was acquired at the OCP with an AC potential magnitude of 20 mV_{RMS}. Upward polarization scans were performed at a scan rate of 0.5 mV/s starting at an initial potential of -0.1 V vs. OCP to +0.8 V_{SCE}. Long-term electrochemical passivation was explored in the passive region, determined from the polarization curves for each alloy. Potential step passivation was conducted using the following procedure: (1) cathodic reduction of air-formed oxide at -1.3 V_{SCE} for 600 s, (2) a step potential hold at either -0.25 or 0 V_{SCE} within the passive region for 10 ks, and (3) a full spectrum EIS test while remaining at -0.25 or 0 V_{SCE}. Passive film growth as a function of time was also monitored in-situ using a single-frequency EIS (SF-EIS) method [8, 49] and subsequently analyzed with an equivalent circuit model established for alloy C-22 and adapted for MPEAs [8, 32, 50]. Oxide thickness (*l_{ox}*) as a function of time was calculated based on the relationship between the equivalent circuit model and constant phase element exponent (α_{film}), shown in **Eq. 2.1** [32, 49-52].

$$l_{ox}(t) = \frac{(2\pi\epsilon\epsilon_0 f)^\alpha \cdot |Z_{img}(t)|}{\rho_\delta^{1-\alpha} \cdot \sin\left(\frac{\alpha\pi}{2}\right) \cdot [2.88(1-\alpha)^{2.375}]} \quad (2.1)$$

where ϵ is the oxide dielectric constant, ϵ_0 is vacuum permittivity, f is frequency, and ρ_δ is the boundary resistivity assumed to be 450 $\Omega\cdot\text{cm}$ [8, 51]. The Ni₃₈Fe₂₀Cr₂₂Mn₁₀Co₁₀ MPEA and Ni₇₆Cr₂₄ oxide dielectric constant was calculated using a weighted average of various oxide percentages obtained from XPS analysis. Passive films were consistent with 42% Cr(OH)₃, 36% FeCr₂O₄, 12% NiCr₂O₄, and 10% NiO for the MPEA and 56 % Cr(OH)₃, 31% NiO, 10% Ni(OH)₂, and 3% Cr₂O₃ for Ni₇₆Cr₂₄. The dielectric constant used for each passive film grown on the MPEA

and Ni₇₆Cr₂₄ was based on a weighted average of the values for the different detected oxides. The following dielectric constants were considered: $\epsilon_{\text{Cr}_2\text{O}_3} = 30$ [53], $\epsilon_{\text{Cr Spinel}} = 4$ [54, 55], $\epsilon_{\text{NiO}} = 11.9$ [56] and $\epsilon_{\text{Ni(OH)}_2} = 2.7$ [57] as utilized previously for Ni₃₈Fe₂₀Cr₂₁Ru₁₃Mo₆W₂ MPEA [8]. The full details of oxide thickness determination has been previous discussed in detail elsewhere [8].

XPS spectra were acquired using Al K α X-rays (1468.7 eV) at a pass energy of 26 eV and take off angle of 45° in a PHI VersaProbe IIITM system. Estimates of cation fractions in the passive film and elements just below the oxide/metal interface (relative to all cations or elements detected) were determined by spectral deconvolution of individual core-level spectra using KOLXPDTM analysis software implemented with Voigt functions for oxides, asymmetric Doniach Sunjic-like features for metals [58] and a Shirley background subtraction [59]. The core 2p feature for each alloying element was deconvoluted using the known multiplet splitting from reference stoichiometric compounds previously reported by Biesinger et al. [60]. The O 1s core feature was deconvoluted considering the hydroxide, oxide, and organic oxygen features. The methodology used in this work for confining the fitting parameters is detailed in our prior work [8] and explained here.

The multiplet metallic and oxidized features for a given compound were confined to fixed relative separations, intensities, and full width half maximums. This ensures that the fit is not unrealistic and is free of constraints. It allows the entire complex feature associated with a given compound to vary in unison, without changing shape. Analysis utilizing oxide solutions in a fixed crystal structure was not attempted, given the limited data available.

The Ni 2p_{3/2} spectrum was deconvoluted and intensity overlaps of the Mn Auger features were ignored. Given the low intensity of the Mn 2p core-level spectra we can infer the maximum intensity of the Auger lines and see that they have no impact on the deconvolution of the Ni 2p_{3/2} spectra. To deconvolute the Ni2p spectra (**Figure 2.11a**), we assume that the underlying Ni feature, including the shake-up at 859 eV maintain their shape and relative intensities. This assumption is similar to the approach used in prior reports [61, 62]. The intensity of the NiCr₂O₄ feature in the Ni2p spectra was found to be 37.5 which was consistent with the corresponding NiCr₂O₄ feature in the Cr2p core-level spectra. To obtain an accurate fit to the raw data the, inclusion of a NiO 2p core feature is required.

In the Cr 2p_{3/2} spectra (**Figure 2.12a**) we observe features assigned to mostly Cr hydroxide, and some FeCr₂O₄, and NiCr₂O₄. The hydroxide signal has the greatest intensity and suggests that hydroxide accounts for 42% of the total Cr(III) present in the oxide.

The Fe 2p_{1/2} peak feature is examined because the intensity Fe 2p_{3/2} overlaps with Ni Auger features. Given the high level of noise in the data a detailed deconvolution is not possible. However, we can use this data to check for consistency with our Cr 2p deconvolution. Since FeCr₂O₄ is detected in the Cr 2p spectra, it must also be observable in the Fe 2p_{1/2} spectra. After accounting for differences in the relative sensitivity factors, we can also account for the Fe 2p_{1/2} level being half the intensity of a 2p_{3/2} and also that FeCr₂O₄ has half the number of Fe atoms compared to Cr. The intensity of the corresponding FeCr₂O₄ feature ($I_{\text{FeCr}_2\text{O}_4} = 39.4$) in the Fe 2p_{1/2} spectra is observable under the noise. Therefore, the Fe 2p feature is consistent with the Cr 2p deconvolution but was not detectable above the Fe 2p noise level.

The Mn 2p_{1/2} and Co 2p_{1/2} were analyzed due to intensity overlaps between Co- and Mn- 2p_{3/2} with Ni Auger features. In the Mn and Co core-level spectra, similar signal-to-noise issues were encountered as seen in the case of Fe 2p. This is exacerbated by the fact that the Mn and Co were present at lower concentration in the alloy. Therefore, deconvolution of the Mn and Co 2p_{1/2} spectra, a peak intensity limit of less than the intensity of noise ($I_{\text{Noise}}^{2p} \geq I_{\text{Fit}}^{2p}$) was considered to determine an upper threshold of the signal that could exist within that level of noise. We find that the expected Mn and Co oxide concentration given $I_{\text{Mn}} = 29.1$ and $I_{\text{Co}} = 25.6$ falls below the noise and therefore would not be detectable above the noise in this data.

A surface enrichment approach developed by Castle and Asami [63] was utilized to obtain an enrichment term, f_A , which is calculated from cation fractions determined by experimental XPS analysis as shown in **Eq. 2.2** [63];

$$f_A = \frac{\frac{X_A^{Ox/s}}{(X_A^{Ox/s} + \sum_j X_j^{Ox/s})}}{\frac{X_A^b}{(X_A^b + \sum_j X_j^b)}} \quad (2.2)$$

where $X_A^{Ox/s}$ is the oxide or surface XPS cation fraction for element A, $\sum_j X_j^{Ox/s}$ is the sum of the oxide or surface XPS cation fraction for all other elements excluding A, X_A^b is the bulk alloy

fraction of element A, and $\sum_j X_j^b$ is the sum of the bulk alloy fraction for all other alloying elements excluding A. The surface cation fraction of elements at the oxide-metal interface was calculated utilizing metallic core 2p features, assuming the different element core 2p features do not interact and major oxide element secondary interactions are neglected [63-65]. Calculated surface element zero valence state fractions for each element were taken to be the oxide-metal interface elemental fraction. The value of f_A can be less than one (i.e., depletion) or greater than one (i.e., enrichment). A depletion term was calculated for this near surface alloy composition relative to the bulk composition of the alloy using a similar approach

A relative enrichment factor for any elements, such as A, as a function of X_A^b , R_A , can also be determined from the enrichment or depletion factor of the individual elements as shown in **Eq. 2.3** [63];

$$R_A = \frac{f_A (1 - X_A^b)}{(1 - f_A \cdot X_A^b)} \quad (2.3)$$

R_A reflects any physical phenomenon such as a undefined rate process that could account for enrichment or depletion. In addition to R_A , another approach to obtain an alternative enrichment-depletion factor was considered that utilizes a relationship between the passive current densities of each pure metal element and the alloy passive oxide enrichment factor [64, 65]. Kirchhiem [64], as well as Marcus and Grimal [65], both considered that enrichment and depletion factors were related to the ratio of experimental dissolution rates of selected individual elements (R'_A). Dissolution rates were assumed to equal to the observed current density of each element at the passive growth potential studied (i.e. -0.25 V_{SCE}) [64, 65], shown in **Eq. 2.4**;

$$R'_A = \frac{i_{Ref}}{i_A} \quad (2.4)$$

here i_{Ref} is the passive current density of the reference element (in the case of binary alloys this would be the solvent element at -0.25 V_{SCE}), and i_A is the passive current density of alloying element A, excluding the reference element. For the Ni₃₈Fe₂₀Cr₂₂Mn₁₀Co₁₀ MPEA which is non-equiatomic, the reference element was assumed to be Ni due to its greater elemental bulk material concentration (38 at. %) and thermodynamic instability of its oxides. Using **Eqs. 2.1** and **2.2** the

surface concentration of a particular element (X_A^s) can be estimated using the bulk alloy fraction for that element and R_A , given in **Eq. 2.5** [63];

$$X_A^s = \frac{R_A \cdot X_A^b}{1 - X_A^b (1 - R_A)} \quad (2.5)$$

where R_A can be either Castle R_A [63] or Kirchhiem-Marcus R'_A [64, 65]. This approach was applied to analyze the passive film and modified metallic concentration just below the metal/oxide interface (**Eq. 2.5**).

AESEC was used to measure elemental dissolution of Fe, Cr, Ni, Co, and Mn simultaneously along with the total electrochemical current. The Cr enrichments in the passive potential domain of Fe-Cr, Ni-Cr, and stainless steel alloys in various solutions were previously determined via mass-balance using this technique [66-68]. AESEC has been described in detail elsewhere [69, 70]. The specimen of interest was placed vertically with the three-electrode electrochemical flow cell. The dissolved elements from the working electrode were transported to an Ultima 2C Horiba Jobin Yvon inductively couple plasma atomic emission spectrometer (ICP-AES). The time resolved concentration of Ni, Fe, Cr, Mn and Co were determined from the emission intensity of the plasma monitored at 231.60 nm, 259.94 nm, 267.72 nm, 257.61 nm and 228.62 nm wavelength, respectively, with a Paschen-Runge polychromator (focal distance 0.5 m). Ni was measured with a monochromator (focal distance 1.0 m) purged O_2 to avoid the absorption, by a N_2 generator (Air Liquide). The emission intensity of an element at a characteristic wavelength (λ), I_λ , has a proportional relationship with its concentration C_M ($\mu\text{g mL}^{-1}$) at the exit of the flow cell which enters to the plasma as, **Eq. 2.6**;

$$C_M = (I_M - I_M^\circ) / \kappa_\lambda \quad (2.6)$$

where I_M° is the background intensity signal and κ_λ is the sensitivity factor for a given wavelength [71, 72]. The C_M may be converted to the elemental dissolution rates, v_M^{exp} ($\mu\text{g s}^{-1} \text{cm}^{-2}$), with a flow rate, f (mL min^{-1}), and the exposed surface area A (cm^2) as, **Eq. 2.7**:

$$v_M^{\text{exp}} = f C_M / A \quad (2.7)$$

An equivalent elemental current density (i_M^{exp}) may be calculated by Faraday constant F as, **Eq. 2.8**;

$$i_M^{\text{exp}} = z F v_M^{\text{exp}} \quad (2.8)$$

where z is the valence electron removed or oxidation state of the dissolving ions from $M \rightarrow M^{z+} + z e^-$. In this work, z for each element was used according to their applicable oxidation states at the test conditions used: Ni(II), Fe(II), Cr(III), Mn(II) and Co(II). Congruent dissolution measured by AESEC was determined by comparing the normalized individual elemental dissolution rate (i_M') with $i_{\text{Ni}}^{\text{exp}}$, assuming that Ni completely dissolves to the electrolyte, **Eq. 2.9**;

$$i_M' = i_M^{\text{exp}} (z_{\text{Ni}} X_{\text{Ni}}) / (z_M X_M) \quad (2.9)$$

where X_M is the atomic fraction of element M in the bulk material. If one element dissolves congruently, $i_M' = i_{\text{Ni}}$. When $i_M' > i_{\text{Ni}}$, it may indicate that the element M is selectively dissolved with respect to the bulk composition. $i_M' < i_{\text{Ni}}$ means the element M dissolves less than the bulk composition, in other words, the excess M is collecting at the surface instead of in the electrolyte. The quantification of this enriched M expressed as a coulombs, moles or grams per unit area, defined as Θ_M , relative to Ni may be determined through a mass-balance as, **Eq. 2.10**;

$$\Theta_M = [(X_M / X_{\text{Ni}}) Q_{\text{Ni}}] - Q_M \quad (2.10)$$

where Q_M is the total quantity of dissolved element M per unit area. $Q_M(t)$ may be calculated by integrating the v_M as, **Eq. 2.11**:

$$Q_M(t) = \int_0^t v_M^{\text{exp}}(t) dt \quad (2.11)$$

APT was also utilized to track elements and provide spatial location. The oxidized surface of the $\text{Ni}_{38}\text{Fe}_{20}\text{Cr}_{22}\text{Mn}_{10}\text{Co}_{10}$ alloy prepared in the same manner as the single step passivation procedure described above was coated with ~50 nm Ti using an ion beam sputtering system prior to APT sample preparation, similar to the approach detailed previously [8, 73]. Titanium was selected as the coating material because it is not present in the base alloy composition. The Ti layer also acted as a fiducial marker for the oxide/metal interface to assist in capturing this interface in the final APT needle apex. APT sample preparation was performed using a FEI Helios dual-beam

focused ion beam-scanning electron microscope (FIB-SEM). FIB annular milling produced the ~100 nm diameter, needle-shaped APT specimens with ~20-50 nm Ti capping remaining at the apex. Details regarding FIB-based APT needle preparation are detailed in prior work [74]. The composition across the oxide/metal interface was normalized to consider only the base alloy cation species (Ni, Cr, Fe, Mn and Co), which emphasizes their redistribution relative to the bulk alloy. Additional details on data collection, mass spectrum, peak identification, and concentration profiles are given below.

A CAMECA local electrode atom probe (LEAP) 4000X HR system equipped with a 355 nm wavelength UV laser was used for APT data collection with the following user-selected parameters: 60 pJ/pulse laser energy, 125 kHz pulse repetition rate, 45 K specimen base temperature, and 0.003 detected ions/pulse detection rate. The analysis chamber was kept at a less than 2×10^{-11} Torr. The detector efficiency of the LEAP used in this work is approximately 36 %. Data were reconstructed and analyzed using the Interactive Visualization and Analysis Software (IVAS), version 3.8.4 by CAMECA. An isoconcentration surface of 6 at% oxygen (O) was generated in 3D to delineate the boundary between the thin oxide layer and the base alloy. The proximity histogram method [75] was used to quantify a concentration profile across the oxide/metal interface relative to this isoconcentration surface in 3D. The corresponding concentration profile is provided in **Figure 2.1**. Peak identification within the APT mass spectra are provided in **Figure 2.2**, where prominent peaks are labeled. Hydrogen peaks at 1 and 2 Da, primarily from UHV background, were excluded in these analyses. Error reported in the concentration profiles represent 1σ from standard counting error, defined as: $\sigma = \sqrt{c_i(100 - c_i)/N_T}$, where c_i is local concentration of species i , and N_T is the total number of atoms in the concentration measurement.

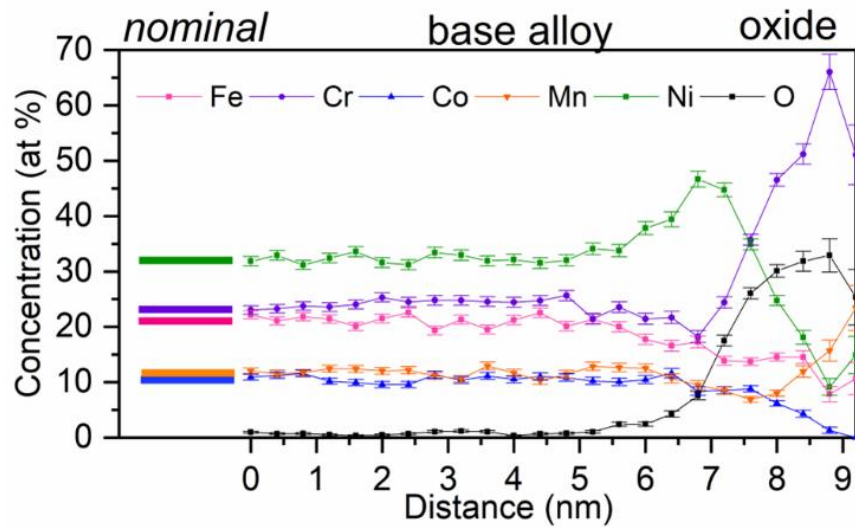


Fig. 2. 1. APT characterization of the passive film formed on a MPEA after 10,000 seconds exposure at -0.25 VSCE in an aqueous solution of 0.1 molar NaCl (pH 4), and the adjacent base alloy. The concentration profile above gives concentration of all elements across a 6 at% O iso-composition surface, where uncertainties shown as error bars represent 1σ . Bin width for proximity histogram analysis is 0.4 nm. Nominal concentration determined via APT is given by horizontal lines.

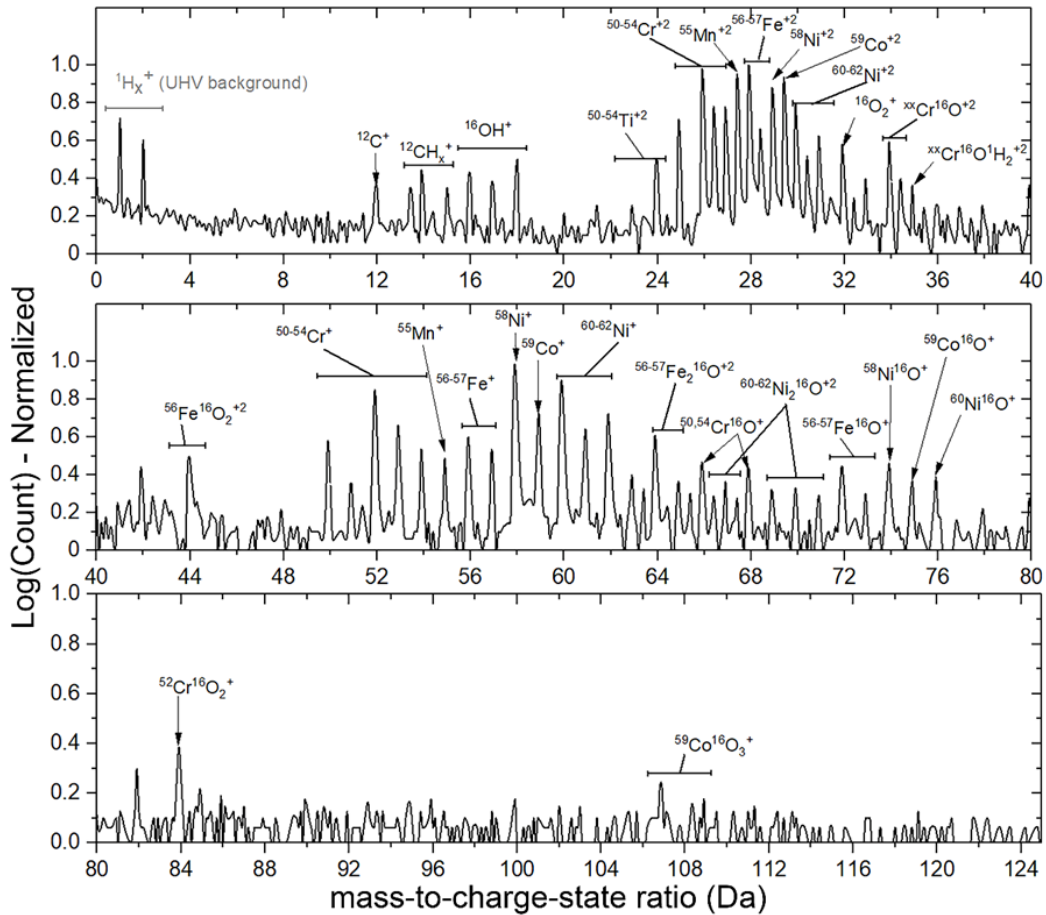


Fig. 2.2. Ranging criteria for atom probe tomography mass spectrum analysis for the base alloy and corrosion film. The mass spectrum is normalized to the peak with the maximum count ($^{56}\text{Fe}^{+2}$).

2.4 Results

2.4.1 Electrochemical Passivation

Anodic polarization curves of $\text{Ni}_{38}\text{Fe}_{20}\text{Cr}_{22}\text{Mn}_{10}\text{Co}_{10}$ and $\text{Ni}_{76}\text{Cr}_{24}$ in deaerated 0.1 M NaCl + HCl pH 4 under different initial conditions are shown in **Figures 2.3a and 2.3b**, respectively. The $\text{Ni}_{38}\text{Fe}_{20}\text{Cr}_{22}\text{Mn}_{10}\text{Co}_{10}$ alloy with an air-formed oxide (initial OCP hold in the figure) exhibited a more positive corrosion potential (E_{corr}) compared to the reduced case. Each condition demonstrated a passive region with low ($\sim \mu\text{A}/\text{cm}^2$) passive current densities (i_{pass}) followed by

film breakdown in the form of crevice corrosion under the O-ring above +0.3 V_{SCE}. It is evident that the air-formed film exposure affords protection and spontaneous passivation in solution. When the air-formed oxide is cathodically reduced, an active-passive transition is observed, perhaps with some oxidation of hydrogen generated in the cathodic region [47]. Similar behavior was observed for Ni₇₆Cr₂₄, shown in **Figure 2.3b**, including active-passive behavior for the cathodically reduced sample, although it exhibited 3 zero current potentials. The zero current potentials are a result of similarities between i_{pass} and the limiting current for oxygen reduction, likely caused by residual O₂ even after deaeration. The similarity on each material leads to this condition and no specific fundamental material properties can be concluded from this. Low i_{pass} values were observed in both conditions followed by breakdown in the form of crevice corrosion at high potentials. The breakdown potential differed between the two conditions for both materials (**Figure 2.3a**). The air-formed and OCP exposed Ni₇₆Cr₂₄ exhibited a breakdown potential of +0.6 V_{SCE}, while the cathodically treated sample showed a lower breakdown potential of +0.2 V_{SCE} (**Figure 2.3b**). The i_{corr} at OCP was calculated in both cases for the MPEA and Ni-Cr binary alloy utilizing the Stern-Geary approach using the polarization resistance (R_p) determined from EIS measurements [76-78]. The R_p for the MPEA was estimated to be $2.8 \times 10^5 \Omega \cdot \text{cm}^2$ while for Ni₇₆Cr₂₄ it was $3.1 \times 10^5 \Omega \cdot \text{cm}^2$. The i_{corr} for the MPEA and Ni₇₆Cr₂₄ were $4.7 \times 10^{-7} \text{ A/cm}^2$ and $4.3 \times 10^{-7} \text{ A/cm}^2$, respectively, using anodic and cathodic Tafel slopes of $\beta_a = \infty$ and $\beta_c = 0.31 \text{ V/decade}$, respectively, the latter being representative for the hydrogen evolution reaction on Ni [79].

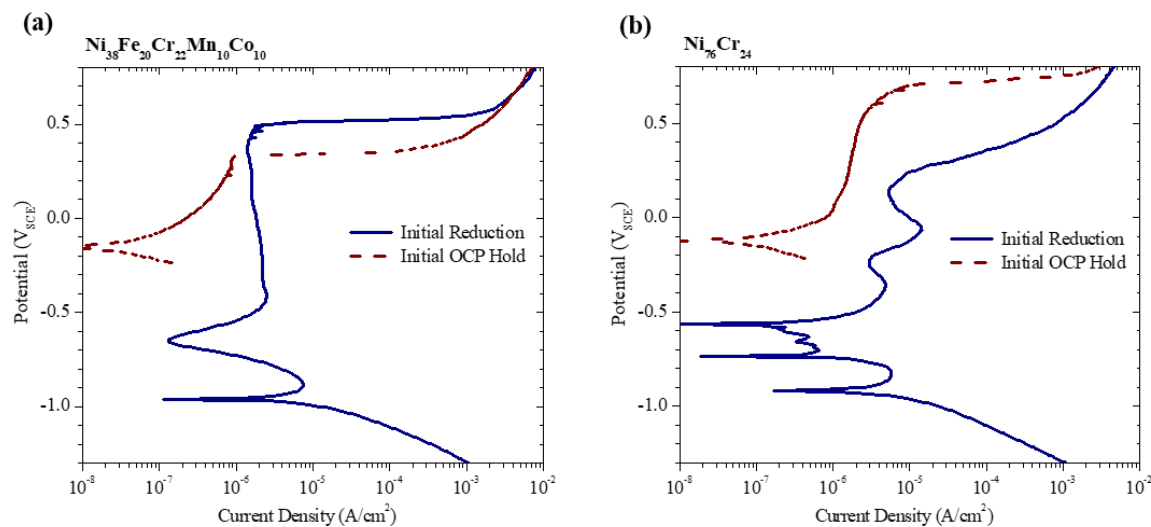


Fig. 2.3. Anodic polarization behavior in deaerated 0.1 M NaCl + HCl at pH 4 with different surface pretreatments: (1) after initial cathodic reduction at -1.3 V_{SCE} for 10 mins and (2) after initial open circuit hold for 30 mins for (a) Ni₃₈Fe₂₀Cr₂₂Mn₁₀Co₁₀ MPEA and (b) Ni₇₆Cr₂₄ binary alloy

The polarization curves for the cathodically pretreated Ni₃₈Fe₂₀Cr₂₂Mn₁₀Co₁₀ and Ni₇₆Cr₂₄ are overlaid in **Figure 2.4a**. The Ni₃₈Fe₂₀Cr₂₂Mn₁₀Co₁₀ exhibits a larger passive region with lower i_{pass} (2×10^{-6} A/cm²). The passivity of each alloy can also be related to the potential dependence of the intermediate-frequency imaginary impedance component (Z''), shown in **Figure 2.4b**. The Z'' component at these frequencies is inversely related to the capacitance of the passive film and provides a relative indication of the oxide thickness, **Eq. 2.1** [32, 49-52]. For the MPEA, **Figure 2.4b** shows an increase in Z'' as the potential moves into the passive region followed by a gradual decrease at potentials $0 < E < +0.3$ V_{SCE}. Z'' is observed to be much larger for the MPEA compared to the Ni₇₆Cr₂₄ alloy. At potentials above +0.5 V_{SCE} for the MPEA and +0.2 V_{SCE} for Ni-Cr, a sudden drop in Z'' and increase in current density is observed, corresponding to film breakdown by crevice corrosion. Passivation at two static potentials, -0.25 V_{SCE} and 0 V_{SCE}, were examined within the passive region of both alloys. These passive potentials are indicated in **Figure 2.4** by broken lines.

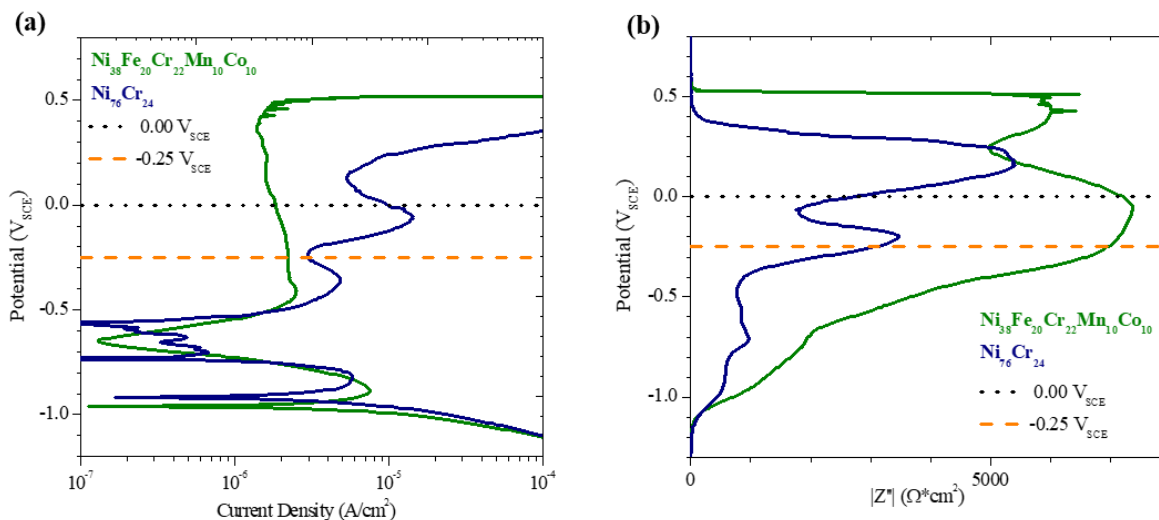


Fig. 2. 4. Comparison of anodic potentiodynamic polarization data comparing $Ni_{38}Fe_{20}Cr_{22}Mn_{10}Co_{10}$ and $Ni_{76}Cr_{24}$ in deaerated 0.1 M NaCl + HCl at pH 4. (a) Upward polarization with dotted lines at $-0.25 V_{SCE}$ and $0 V_{SCE}$ indicating passive potentials and current densities used for 10 ks oxide growth. (b) Potential vs. high frequency Imaginary component of impedance ($-Z''$) during upward polarization displaying regions of active-to-passive transitions, passivity, and breakdown.

2.4.2 Oxide Growth and Breakdown at Applied Potentials of $-0.25 V_{SCE}$ and $0.0 V_{SCE}$

The current decays observed during single step potentiostatic holds at $-0.25 V_{SCE}$ and $0 V_{SCE}$ are shown in **Figures 2.5a** and **2.5b**, respectively. At $-0.25 V_{SCE}$, both alloys demonstrate a current density that decreases from $\sim 10^{-4} A/cm^2$ to $10^{-8} A/cm^2$ from early to later times in the experiment. The $Ni_{38}Fe_{20}Cr_{22}Mn_{10}Co_{10}$ had slightly lower current density compared to the binary $Ni_{76}Cr_{24}$ alloy in the early stages. At approximately 400 s and 750 s, the current densities of the $Ni_{76}Cr_{24}$ alloy and $Ni_{38}Fe_{20}Cr_{22}Mn_{10}Co_{10}$, respectively, decreased faster and then became negative (not shown), indicating that the cathodic reaction rates exceeded the anodic rates at $t > 800$ s and $t > 1400$ s, respectively. **Figure 2.5b** shows the current density vs. time behavior at $0 V_{SCE}$ for the MPEA and the $Ni_{76}Cr_{24}$ alloy. The current density of the MPEA decayed continuously with time but multiple instantaneous metastable breakdown events were evident. For the $Ni_{76}Cr_{24}$, the current density decreased for the first 50 s but then increased with time until stabilizing at a higher current density after 1100 s. This gradual increase in current density indicates passive film breakdown, confirmed by the observation of crevice corrosion after the test, which was not observed for the MPEA.

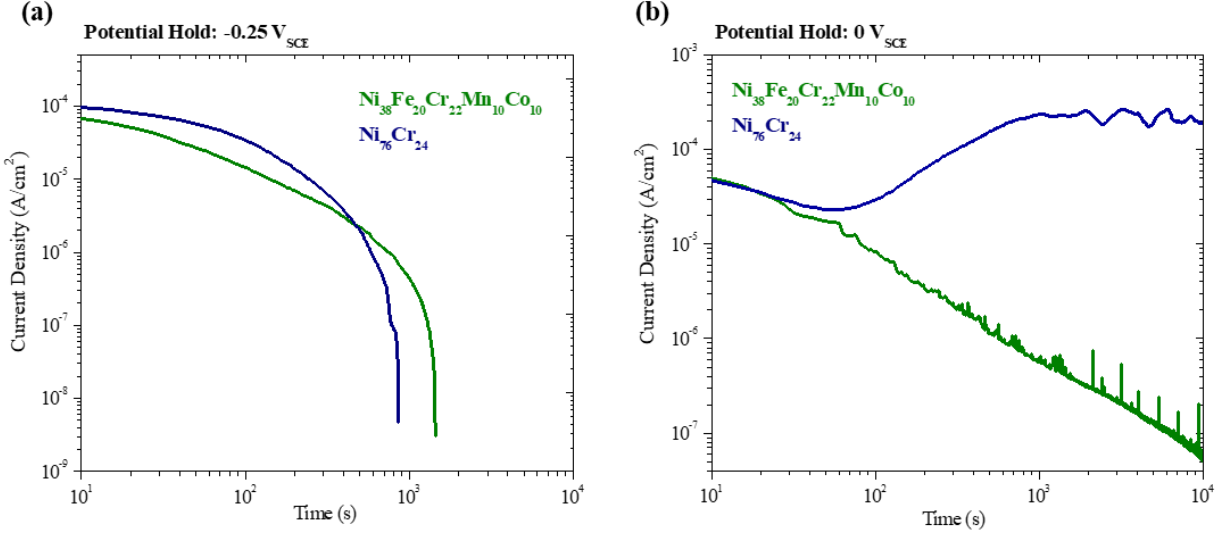


Fig. 2. 5. Measured electrochemical passive current density during potentiostatic oxide growth for 10 ks of $\text{Ni}_{38}\text{Fe}_{20}\text{Cr}_{22}\text{Mn}_{10}\text{Co}_{10}$ and $\text{Ni}_{76}\text{Cr}_{24}$ in Deaerated 0.1 M NaCl + HCl at pH 4 at (a) -0.25 V_{SCE} and (b) 0 V_{SCE}

Figures 2.6a and **2.6b** show the Bode plots for the $\text{Ni}_{38}\text{Fe}_{20}\text{Cr}_{22}\text{Mn}_{10}\text{Co}_{10}$ and binary $\text{Ni}_{76}\text{Cr}_{24}$ alloy, respectively, after a period of 10 ks at the fixed potential of -0.25 V_{SCE} . The low frequency impedance magnitude of both alloys was high ($3 \times 10^5 \Omega \cdot \text{cm}^2$ and $1 \times 10^5 \Omega \cdot \text{cm}^2$ for the MPEA and Ni-Cr, respectively) suggesting the formation of a protective oxide film. Utilizing an equivalent circuit model shown elsewhere [32, 50], the exponent α_{film} of the constant phase element (CPE) associated with the film was determined to be 0.90 for both alloys. The lines in **Figures 2.6a** and **2.6b** represent the fits to the electrical equivalent circuit model describing the oxide interface utilizing the fitted parameters obtained. Using **Eq. 2.1**, the oxide thickness estimated during the 10 ks potential hold at -0.25 V_{SCE} is given in **Figure 2.7** for both materials. The oxide thicknesses and their compositions were estimated through XPS and AESEC analyses as discussed below (see **Tables 2** and **3**). The passive film on the MPEA grew faster and to a greater thickness. At approximately 3000 s, the EIS oxide thickness on both alloys approached a stationary value with the MPEA having a final thickness of around 3 nm compared to ~2 nm on the $\text{Ni}_{76}\text{Cr}_{24}$. The passive film thicknesses determined from the impedance data on the MPEA is in general agreement with AESEC (3.7 nm) and XPS (≤ 2 nm) thickness estimations.

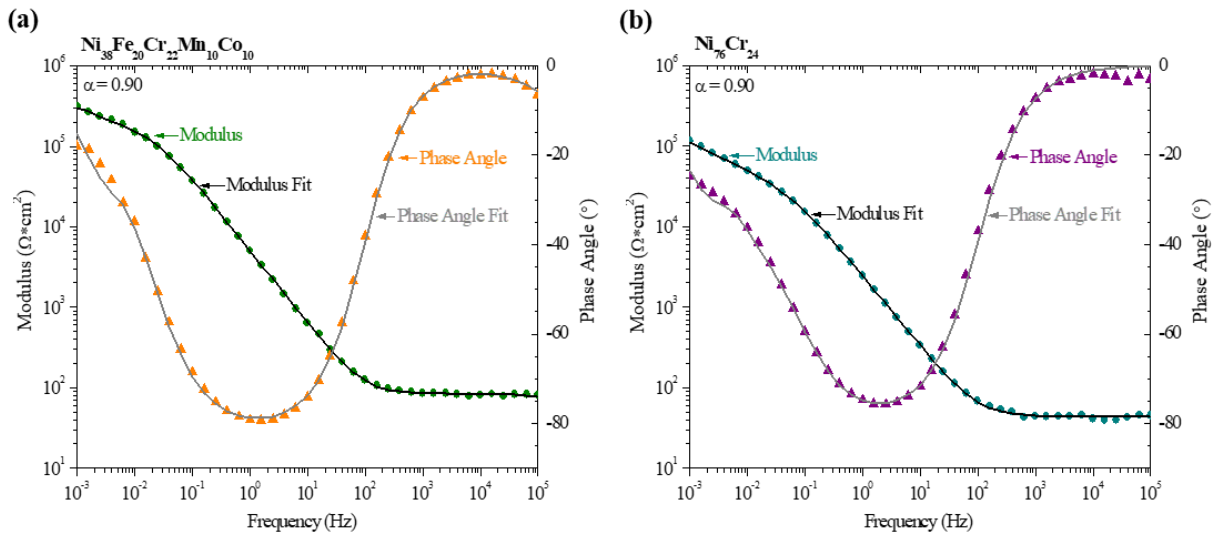


Fig. 2. 6. Bode plot of (a) $Ni_{38}Fe_{20}Cr_{22}Mn_{10}Co_{10}$ MPEA (b) $Ni_{76}Cr_{24}$ in deaerated 0.1 M NaCl + HCl pH 4 after 10 ks oxide growth at $-0.25 V_{SCE}$. Experimental Z_{mod} and Z_{phz} were fit to an equivalent circuit yielding a film constant phase element exponential of 0.90 for both alloys. HEA Fitting Parameters: $CPE_f = 3.8 \times 10^{-5} S \cdot sec^\alpha \cdot cm^{-2}$, $\alpha_{film} = 0.90$, $R_f = 1.7 \times 10^5 \Omega \cdot cm^2$, $W_f = 8.9 \times 10^{-6} S \cdot sec^{1/2}$, $CPE_{fje} = 2.2 \times 10^{-7} S \cdot sec^\alpha \cdot cm^{-2}$, $\alpha_{fje} = 0.79$, $R_{fje} = 36.2 \Omega \cdot cm^2$, and $R_s = 46.8 \Omega \cdot cm^2$. $Ni_{76}Cr_{24}$ Fitting Parameters: $CPE_f = 1.9 \times 10^{-4} S \cdot sec^\alpha \cdot cm^{-2}$, $\alpha_{film} = 0.90$, $R_f = 4.8 \times 10^4 \Omega \cdot cm^2$, $W_f = 1.1 \times 10^{-5} S \cdot sec^{1/2}$, $CPE_{fje} = 1.4 \times 10^{-4} S \cdot sec^\alpha \cdot cm^{-2}$, $\alpha_{fje} = 0.87$, $R_{fje} = 1.6 \times 10^4 \Omega \cdot cm^2$, and $R_s = 43.1 \Omega \cdot cm^2$ - utilizing circuit model shown by [Tianshu doi.org/10.1016/j.electacta.2019.03.104].

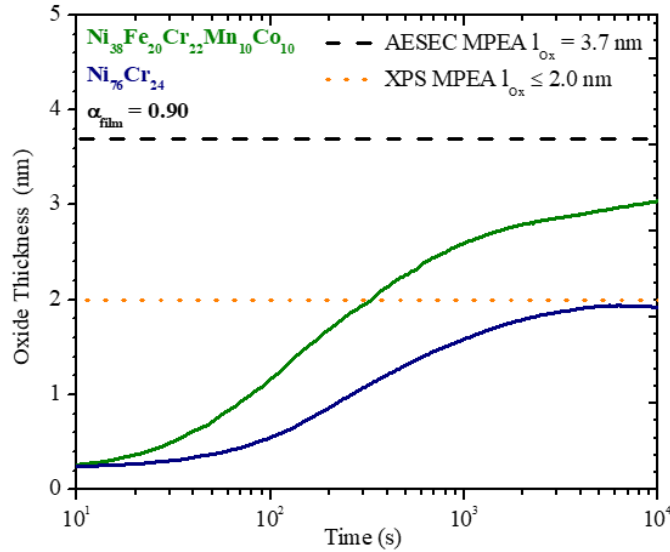


Fig. 2. 7. In situ measurement of oxide thickness (l_{ox}) as a function of time for $Ni_{38}Fe_{20}Cr_{22}Mn_{10}Co_{10}$ MPEA and $Ni_{76}Cr_{24}$ during 10 ks oxide growth at $-0.25 V_{SCE}$ in deaerated $0.1 M NaCl + HCl$ pH 4. Utilizing 1 Hz CPE component of impedance data, the MPEA's final oxide thickness was ~ 3 nm. AESEC estimations showed l_{ox} is 3.7 nm and XPS oxide thickness analysis indicated a slightly thinner oxide of ≤ 2 nm.

2.4.3 Real-time Solution Analyses for all Cations during a Fixed Potential Hold

The elemental dissolution rates of the $Ni_{38}Fe_{20}Cr_{22}Mn_{10}Co_{10}$ during a potentiostatic hold at $-0.25 V_{SCE}$ were recorded by AESEC in a deaerated $0.1 M NaCl + HCl$, pH 4.0 solution. **Figure 2.8** shows the specific elemental current densities normalized (i_M' , calculated by **Eqs. 2.8** and **2.9**) to the Ni dissolution rate signal (i_{Ni}^{exp}) during the potentiostatic hold for 10 ks. The i_M' curves are plotted with offsets to better distinguish them. The top curve is the sum of elemental dissolution rates, $i_{\Sigma} = i_{Ni}^{exp} + i_{Fe}^{exp} + i_{Cr}^{exp} + i_{Mn}^{exp} + i_{Co}^{exp}$ and the electrical current density (i_e). At the initiation of the potential hold, i_M' and i_e increased immediately to a maximum value then decayed during passivation as also shown in **Figure 2.5a**. i_M' dropped below the detection limit and i_e decreased to 0 for $t > 3000$ s. The black dashed line on each curve indicates i_{Ni}^{exp} . If $i_M' < i_{Ni}^{exp}$, the dissolution of element M was non-congruent and collected elsewhere with a leading possibility that it joins the passive film on the surface. $i_M' = i_{Ni}^{exp}$ implies that the dissolution of M was congruent, assuming all Ni dissolves in this electrolyte, a reasonable assumption at pH 4. The initial Cr and

Mn dissolution rates were lower than $i_{\text{Ni}}^{\text{exp}}$, while Co and Fe dissolved congruently as $i_{\text{Co}}' \approx i_{\text{Fe}}' = i_{\text{Ni}}^{\text{exp}}$. The non-congruent dissolution of Cr and Mn is further demonstrated in **Figure 2.9** in $\log |i_{\text{M}}|$ vs. \log time plots. For Cr, the integral of the difference between $i_{\text{Ni}}^{\text{exp}}$ and i_{Cr}' (yellow highlighted area) yields $12.8 \text{ nmol cm}^{-2}$ of Cr^{3+} added to the surface in that it was oxidized at the rates shown but not found in the solution. This atomic density per unit area, hypothetically, is equivalent to a $3.7 \text{ nm Cr}_2\text{O}_3$ layer, assuming a uniform Cr_2O_3 layer with 5.2 g cm^{-3} density and 152.0 g mol^{-1} molar mass. Similarly, the enrichment of oxidized Mn was equivalent to 2.1 nmol cm^{-2} of Mn located on the surface and not in the electrolyte.

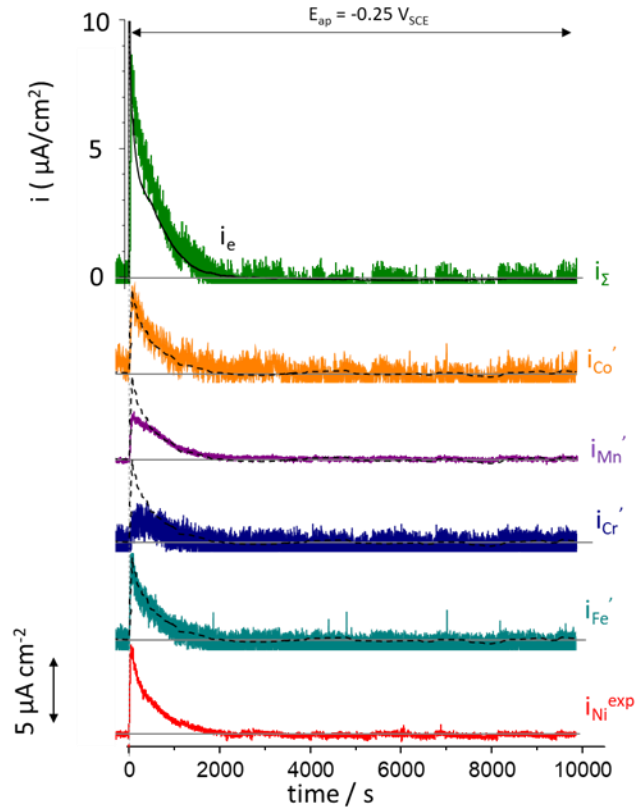


Fig. 2. 8. AESEC elemental dissolution rate vs. time behavior for $\text{Ni}_{38}\text{Fe}_{20}\text{Cr}_{22}\text{Mn}_{10}\text{Co}_{10}$ MPEA exposed at $-0.25 \text{ V}_{\text{SCE}}$ in $0.1 \text{ M NaCl} + \text{HCl pH } 4$, deaerated electrolyte. The horizontal lines are the detection limit of each alloy element. The elemental dissolution rates are shown as equivalent elemental current densities, i_{M} . The i_{M} is normalized (i_{M}') based on the bulk composition utilizing Eq. 2.9. Dashed lines indicate $i_{\text{Ni}}^{\text{exp}}$ to determine congruent dissolution of each element.

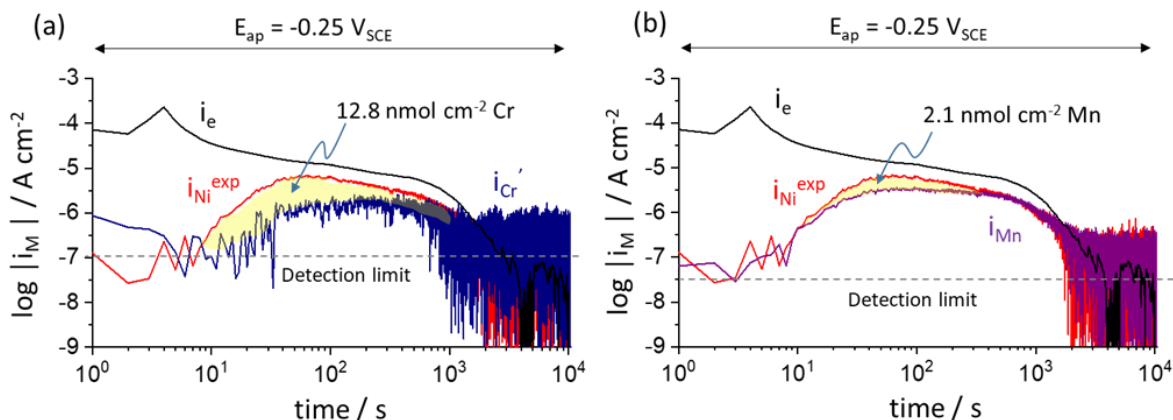


Fig. 2. 9. Comparison between i_{Ni}^{exp} and; (a) i_{Cr}' and (b) i_{Mn}' at $E_{app} = -0.25 V_{SCE}$ based on data from Fig. 6. The highlighted light-yellow area indicates the surface enriched amount of oxidized Cr (a) or Mn(b), calculated from Eqs. 2.10 and 2.11.

The total quantity of accumulated elements at the surface during the potentiostatic hold at $-0.25 V_{SCE}$ is shown in **Figure 2.10**. The area density of enriched oxidized element M given as Θ_M , from **Figure 2.8** and calculated by **Eq. 2.10** are shown in **Figure 2.10a**, and the ratios of the integral of Θ_M as a function of time are presented as lines in **Figure 2.10b**. Also shown in **Figure 2.10b** as symbols are the surface cation fractions determined from XPS and described below. Both the AESEC and XPS data indicate that Cr surface enrichment occurred from the initial stage of the potentiostatic hold. The cation fraction of Cr at the surface and not found dissolved in solution was maintained at a fraction of 0.7 - 0.85 of all cations during the entire potential. The Ni cation fraction collected at the surface was determined from the XPS data to be less than 0.1, but the exact fraction could not be determined by AESEC as 100 % Ni dissolution was assumed for the calculation of the enriched elements. The AESEC data indicates that the excess Mn increased to 0.4 of the cation fraction then decreased to its bulk level (0.1) after 600 s (**Figure 2.10b**). No Mn signal was identified in the XPS spectrum, although given the large amount of noise in the data coupled with the overlapping Ni Auger line, a cation fraction of up to 0.06 would not rise above the noise, consistent with the AESEC data.

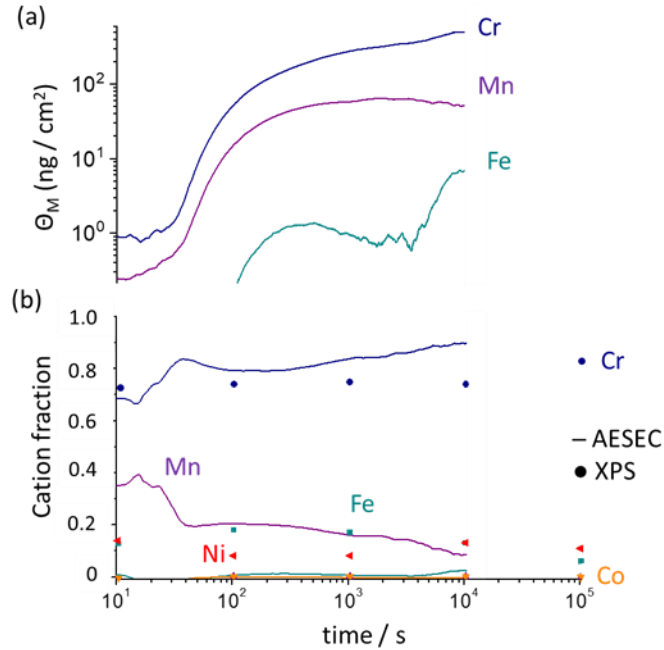


Fig. 2. 10. Surface cation fractions for $Ni_{38}Fe_{20}Cr_{22}Mn_{10}Co_{10}$ MPEA based on (a) The mass density per unit area of an alloying element collected on surface (Θ_M), (b) Cation fractions derived from the density per unit area of an element (line) and from XPS calculation (symbol) during at $-0.25 V_{SCE}$ potentiostatic hold in $0.1 M NaCl + HCl$ pH 4.0, N_2 deaerated electrolyte

2.4.4 Oxide Valence State and Local Environment Identified by XPS

The chemical states and compositions of the electrochemically grown passive films on $Ni_{38}Fe_{20}Cr_{22}Mn_{10}Co_{10}$ and $Ni_{76}Cr_{24}$ binary alloy surfaces determined by XPS are summarized in **Tables 2.2** and **2.3**, respectively. Overall, the oxide film consisted of small concentrations of Ni and Fe and a large enrichment of Cr. No signal was evident in the Mn and Co 2p spectra, suggesting, as mentioned above, that the oxide contained a cation fraction of 0.06 or less Co and Mn species. The binding energies were consistent with oxidation states of Cr^{3+} , Ni^{2+} , and Fe^{2+} as expected at the applied potential investigated. The binding energies in **Table 2.4** were utilized for fitting. The cation fractions (**Table 2.2**) were calculated both by assuming that Co and Mn were not present in the oxide, and alternatively that they were present at the maximum possible concentration not exceeding the XPS signal noise at the appropriate binding energy. The Cr cation

fraction was 0.73 or 0.64 compared to 0.22 in the alloy (**Table 2.2**), indicating a large enrichment. XPS analysis of the passive film grown on Ni₇₆Cr₂₄ binary alloy is summarized in **Table 2.3**. The Ni₇₆Cr₂₄ also showed high enrichment of Cr within the oxide, with a cation fraction of 0.59, compared to the bulk Cr atomic fraction of 0.24. The level of Cr enrichment in the passive film of the MPEA was greater than for Ni₇₆Cr₂₄, even when Mn and Co were considered to be present. **Figure 2.10** suggests general agreement between indirect AESEC derived cation fractions in passive films compared to XPS determined fractions.

Table 2. 2. Elemental Fractions in Ni₃₈Fe₂₀Cr₂₂Mn₁₀Co₁₀ Bulk Material and Electrochemical Passive Film after 10 ks at -0.25 V_{SCE}

Element	XPS Cation		XPS Elemental Fractions	Ni ₃₈ Fe ₂₀ Cr ₂₂ Mn ₁₀ Co ₁₀ Bulk Composition	
	^y Oxide	^u Oxide	Oxide / Metal Interface	Elemental Fraction	Atomic %
Ni	0.15	0.13	0.67	0.38	38
Fe	0.12	0.11	0.05	0.20	20
Cr	0.73	0.64	0.25	0.22	22
Mn	0	0.06	0.03	0.10	10
Co	0	0.06	0.01	0.10	10

^yAssuming Mn and Co are not present in oxide

^uAssuming max allowed Mn and Co fractions in oxide consistent with XPS 2p signal

Table 2. 3. Elemental Fractions in Ni₇₆Cr₂₄ Bulk Material and Electrochemical Passive Film after 10 ks at -0.25 V_{SCE}

Element	XPS Cation	XPS Elemental Fractions	Ni ₇₆ Cr ₂₄ Bulk Composition	
	Oxide	Oxide / Metal Interface	Elemental Fraction	Atomic %
Ni	0.41	0.79	0.76	76
Cr	0.59	0.21	0.24	24

Table 2. 4. Binding energy (eV) of XPS Spectra used for passive film analysis

Species	Oxidation	Multiplet 1	Multiplet 2	Multiplet 3	Multiplet 4	Multiplet 5
Ni 2p _{3/2}						
Ni ⁰	0	852.6	856.3	858.7	--	--
NiO	2	853.7	855.4	860.9	864	--
Ni(OH) ₂	2	854.9	855.7	857.7	860.5	861.5
NiCr ₂ O ₄	2	853.8	855.8	856.5	861	861.3
Cr 2p _{3/2}						
Cr ⁰	0	574.2	--	--	--	--
Cr ₂ O ₃	3	575.7	576.7	577.5	578.5	578.9
Cr(OH) ₃	3	577.3	--	--	--	--
FeCr ₂ O ₄	3	575.9	577.9	578.9	--	--
NiCr ₂ O ₄	3	575.2	576.2	577	578.1	579.2
Fe 2p _{3/2}						
Fe ⁰	0	706.6	--	--	--	--
FeO	2	708.4	709.7	710.9	712.1	715.4
α-Fe ₂ O ₃	2	709.8	710.7	711.4	713.3	714.3
FeCr ₂ O ₄	2	709	710.3	711.2	713	713.8

Biesinger doi: 10.1016/j.apsusc.2010.10.051

Enrichment and depletion factors were calculated from **Eqs. 2.2, 2.3, and 2.4** using experimental cation fractions reported in **Tables 2.2 and 2.3**. These are shown in **Tables 2.5 and 2.6**. The passive film is mostly Cr(OH)₃ with a very small amount of Ni(OH)₂ and Fe oxides as confirmed from XPS deconvolution of Ni 2p_{3/2}, Cr 2p_{3/2}, and O 1s core features, (**Figures 2.11, 12, and 13**). The O 1s spectrum showed a large intensity for the hydroxide feature compared to O²⁻ and organic O, supporting the notion that the passive film is dominated by hydroxide species (**Figure 13**). The oxide thickness was estimation from XPS by considering the ratio of the O 1s feature (representing the entire oxide) to the intensity of the metallic chromium feature, which represents the substrate. The estimated XPS oxide thickness for the MPEA was ≤ 2 nm. At the oxide/metal interface, elemental Ni was enriched while most other elements are slightly depleted.

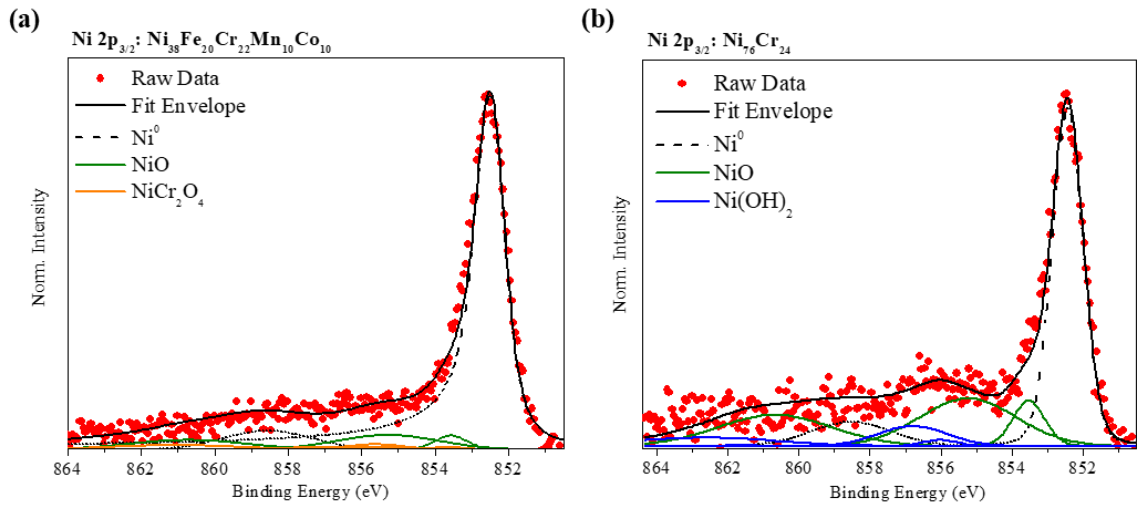


Fig. 2. 11. XPS spectral analysis and deconvolution of the Ni $2p_{3/2}$ core level of (a) $Ni_{38}Fe_{20}Cr_{22}Mn_{10}Co_{10}$ and (b) $Ni_{76}Cr_{24}$ passive film grown at $-0.25 V_{SCE}$ for 10 ks in deaerated $0.1 M NaCl + HCl$ pH 4.

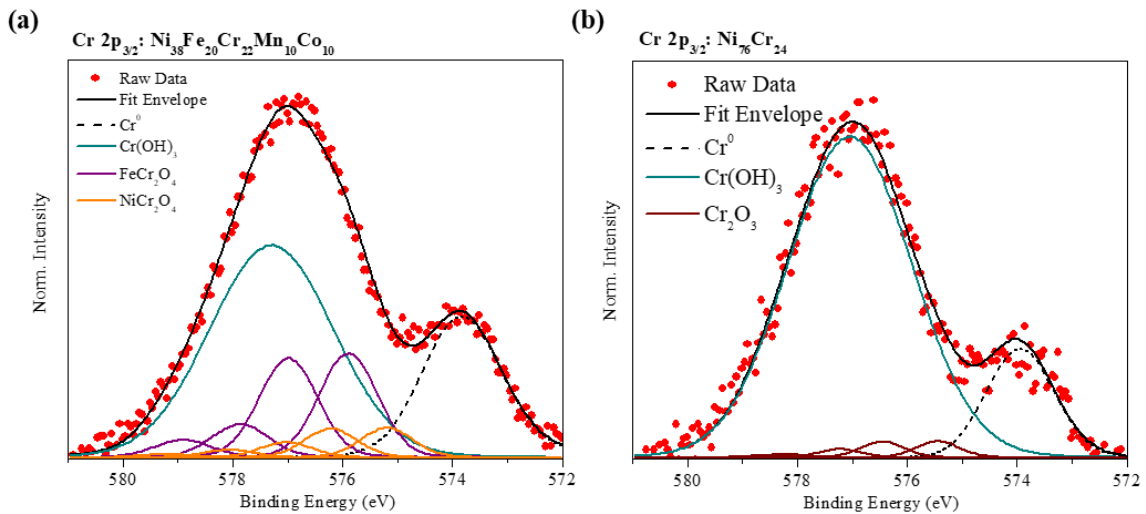


Fig. 2. 12. XPS spectral analysis and deconvolution of the Cr $2p_{3/2}$ core level of (a) $Ni_{38}Fe_{20}Cr_{22}Mn_{10}Co_{10}$ and (b) $Ni_{76}Cr_{24}$ passive film grown at $-0.25 V_{SCE}$ for 10 ks in deaerated $0.1 M NaCl + HCl$ pH 4.

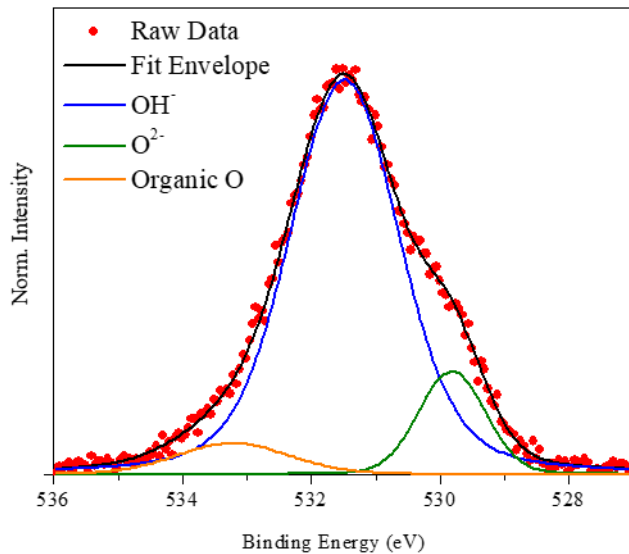


Fig. 2. 13. XPS spectral analysis and deconvolution of the O1s core level of Ni₃₈Fe₂₀Cr₂₂Mn₁₀Co₁₀ passive film grown at -0.25 V_{SCE} for 10 ks in deaerated 0.1 M NaCl + HCl pH 4.

2.4.5 Surface Oxide and Interface Compositions from Atom Probe Tomography

APT was performed on the MPEA after 10 ks exposure to pH 4 0.1 M NaCl solution at -0.25 V_{SCE} SCE (same conditions as XPS and EIS) to further understand elemental partitioning and segregation between the base alloy and the newly formed passive film. The APT atom maps and concentration profiles are presented in **Figure 2.14**. The outer part of the oxide consistently delaminated from the tip during field evaporation, so only the inner oxide is shown in the reconstructed data. These data clearly show a Cr-rich inner oxide with an upward trend of Mn towards the outer oxide that partially delaminated. Beneath the oxide is a clear enrichment of Ni, accompanied by slight Cr and Fe depletion. Importantly, there is no evidence for Mn enrichment at the oxide/metal interface. In fact, slight depletion might be proposed. This observation, in tandem with the lack of Mn in the solution analysis, indicates that Mn is present the outer film, but at a concentration below the XPS detectability limit.

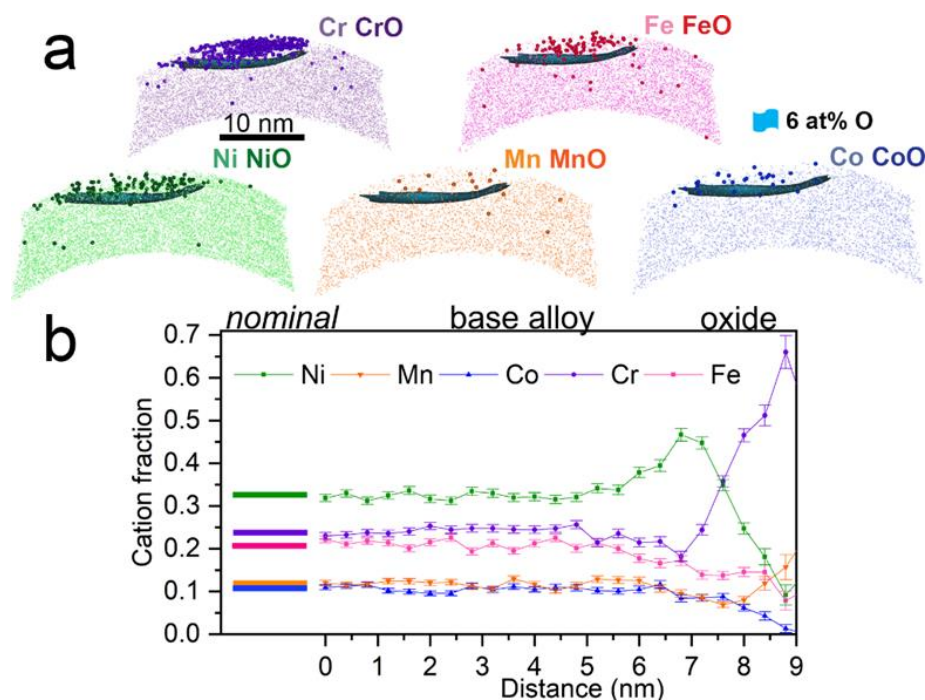


Fig. 2. 14. APT characterization of the corrosion film formed on a MPEA after 10,000 seconds exposure in an aqueous solution of 0.1 M NaCl (pH 4), and the adjacent base alloy. (a) Three dimensional ion maps for all alloying elements and oxide molecular peaks, and (b) concentration of cations across the 6 at% O iso-concentration surface given in (a). Uncertainties shown as error bars represent 1σ from standard counting error. The nominal base alloy composition as determined by APT is given by horizontal lines to the left of the concentration profile.

2.4.6 Surface Enrichment and Depletion Factors for Alloying Elements

Enrichment and depletion factors for each alloying element in the $\text{Ni}_{38}\text{Fe}_{20}\text{Cr}_{22}\text{Mn}_{10}\text{Co}_{10}$ and $\text{Ni}_{76}\text{Cr}_{24}$ were computed using the Castle [63], Marcus [65], and Kirchhiem [64] approaches, as summarized in **Tables 2.5** and **2.6**. The passive film enrichment factor for Cr in the passive film on the MPEA is very high ($R_A = 9.59$). In contrast, the factors for Ni and Fe ($R_A = 0.29$ and 0.55 , respectively) indicate depletion. The $\text{Ni}_{76}\text{Cr}_{24}$ demonstrated some enrichment of Cr in the passive film, but not as great as the MPEA (enrichment factor, $R_A = 4.56$). All models predict a high Cr enrichment within the oxide for both alloys and agree with XPS and APT observations (**Table 2.5** and **Figure 12**). This may reflect the exposure to NaCl where Ni, Fe, and Co will be more prone to dissolve as metal chlorides. Enrichment of elemental Ni at the oxide/metal interface was also

indicated by both APT (**Figure 12**) and XPS (**Table 2.5**). It is important to note the difference in Cr oxide enrichment and metal/interface Cr depletion between the two different alloys. With only 0.22 at. fraction Cr (22 at %) in the MPEA, an enrichment to 0.73 cation fraction was observed compared to the Cr cation fraction enrichment of 0.59 for Ni₇₆Cr₂₄ with 24 at. % Cr. Cr depletion at the oxide/metal interface was observed for passivated Ni₇₆Cr₂₄. A slight depletion was seen in the MPEA by 3D APT. The origins of Cr enrichment of the passive film formed on the Ni₃₈Fe₂₀Cr₂₂Mn₁₀Co₁₀ in NaCl are further examined below.

Table 2. 5. Surface Enrichment Model Parameters for Ni₃₈Fe₂₀Cr₂₂Mn₁₀Co₁₀

Element	Oxide Enrichment						Metal Enrichment			Marcus Oxide Enrichment R'A	
	γf_A	μf_A	γR_A	μR_A	γX_{Ox}	μX_{Ox}	f_A	R_A	X_S	R'_A	γX_{Ox}
Ni	0.4	0.34	0.29	0.24	0.15	0.13	1.75	3.22	0.67	1	0.38
Fe	0.6	0.55	0.55	0.49	0.12	0.11	0.25	0.21	0.05	0.01	0
Cr	3.32	2.91	9.59	6.3	0.73	0.64	1.13	1.17	0.25	11.23	0.76
Mn	0	0.6	0	0.57	0	0.06	0.3	0.28	0.03	0.01	0
Co	0	0.6	0	0.57	0	0.06	0.1	0.09	0.01	0.22	0.02

XPS Enrichment Term (f_A)

Enrichment or Depletion Factor/rate (Castle- R_A and Marcus = R'_A)

X_{Ox}/S = Oxide or Surface Fraction (Concentration)

γ Assuming Mn and Co are not present in oxide

μ Assuming max allowed Mn and Co fractions in oxide: Mn2p and *Co2p Spectra Deconvolution
Limit: $I_{Noise2p} \geq I_{Fit2p}$

Table 2. 6. Surface Enrichment Model Parameters for Ni₇₆Cr₂₄

Element	Oxide Enrichment			Metal Enrichment		
	f_A	R_A	Surface Conc.	f_A	R_A	Surface Conc.
Ni	0.54	0.22	0.41	1.04	1.19	0.79
Cr	2.46	4.56	0.59	0.88	0.84	0.21

XPS Enrichment Term (f_A)

Enrichment or Depletion Factor/rate (Castle- R_A)

2.5 Discussion

2.5.1 Passive Film Chemical Identity and Composition

In conventional alloys, it is commonplace to propose possible passivating oxides using thermodynamic principles such as oxide formation energies or Pourbaix diagrams. For MPEAs, this approach is fraught with uncertainties associated with preferential dissolution changing surface chemistry and kinetic effects. Moreover, second or third element effects on formation energies [80] and M-O binding energy [81], as well as interfacial energy effects based on epitaxy [82] and film thickness effects also affect oxide stability. Nevertheless, single element E-pH stability diagrams at a potential hold of $-0.25V_{SCE}$ ($0 V_{SHE}$) and pH 4 predict soluble Fe^{2+} , Ni^{2+} , Mn^{2+} , and Co^{2+} , and to a lesser extent Cr^{3+} , which is in excellent agreement with the AESEC results (**Figure 2.14**). Only Cr_2O_3 and $Cr(OH)_3$ are predicted to be stable at pH 4 when considering the electrochemical stability of the individual elements comprising the MPEA [83]. Considering formation of only stoichiometric oxide formation energies², Cr oxides and hydroxides, spinels with Fe-Cr as well as Co-Cr, and Mn oxides are suggested to form. Based on these, the passive film may be expected to consist of various stoichiometric compounds such as $Cr(OH)_3$, Cr_2O_3 , $FeCr_2O_4$, $NiCr_2O_4$, and Mn_3O_4 . However, these predictions are unlikely to prevail. Recent E-pH stability diagrams for a NiFeCrMnCo single phase MPEA alloy suggest the thermodynamically favored formation of $CoCr_2O_4$ and $FeCr_2O_4$ spinels at the tested potential and pH [80]. Unfortunately, it may be difficult to discern these spinels or various other oxide solid solution compositions uniquely using the XPS 2p signals. Peak broadening due to the dominance of hydroxides, the presence of amorphous films, and photoelectron features such as multiplet splitting limit detailed isolation of these compounds. Cr_2O_3 and $NiCr_2O_4$ have five final state features in the $2p_{3/2}$ spectra and $FeCr_2O_4$ has four such features [60, 85] so XPS peak fitting must resort to deconvolution of the experimental data into multiple multi-component features of low peak intensities that all overlap in binding energy. As noted in the experimental section, it is vital that such multi-component features be rigorously constrained to prevent unrealistic fitting. XPS spectral deconvolution (**Figures 2.11a** and **2.12a**) suggests the formation of a passive film consistent with

² Oxide formation energies (kJ/mol): $Cr_2O_3 \Delta G_f^\circ = -1058$, $Cr(OH)_3 \Delta G_f^\circ = -1064$, $FeCr_2O_4 \Delta G_f^\circ = -1344$, $NiCr_2O_4 \Delta G_f^\circ = -1257$, $NiO \Delta G_f^\circ = -212$, $Fe_2O_3 \Delta G_f^\circ = -742$, $CoO \Delta G_f^\circ = -214$, $Co_3O_4 \Delta G_f^\circ = -774$, $MnO \Delta G_f^\circ = -363$, and $Mn_3O_4 \Delta G_f^\circ = -1283.2$ 84. Speight, J.G., and Lange, N.A., *Lange's Handbook of Chemistry* ed. 17. 2017, New York: McGraw-Hill Education.

a local atomic binding environment similar to those seen for Cr_2O_3 , $\text{Cr}(\text{OH})_3$, FeCr_2O_4 , NiCr_2O_4 , and NiO . However, this does not independently confirm the presence of these oxide phases since structural confirmation was not obtained in this study. While Mn and Co were not observed in the XPS spectra, based on APT, we considered them to be within the (0.06) 6% noise limit in the XPS detection for these features.

APT indicates that Mn and Co are present in the oxide film at levels < 0.1 near the oxide/metal interface, which is consistent with the XPS threshold estimates (**Figure 2.14**). APT indicates the presence of small concentration of Ni, Co, Fe, and Mn within the passive film (**Figure 2.14**). If the total concentrations of Ni^{2+} , Co^{2+} Fe^{2+} are considered, it is not possible to account for the entire observed Cr^{3+} spectral features by assigning them to spinels only. These results are instead consistent with a significant presence of $\text{Cr}(\text{OH})_3$, which is a major component of protective passive films on many conventional binary and ternary alloys [53, 62, 86-88]. This is also in agreement with recent results on the Cantor alloy where both Cr^{3+} species (Cr_2O_3 and $\text{Cr}(\text{OH})_3$) are seen in passive films [33]. Other characterization techniques will be needed to determine the precise film structure, valence state, and composition. Careful studies of protective films should be undertaken with this in mind and compared to corrosion resistance.

2.5.2 Fate of the Alloying Elements during Aqueous Passivation

Enrichment and depletion of certain elements within a passive film as well as at the oxide/metal interface in Fe-Cr and Ni-Cr based alloys is often observed [49, 86, 87, 89-97]. Consideration of the oxide enrichment/depletion factors for the MPEA alloying elements, derived from XPS data (**Table 2.4**), suggests that low concentrations of Ni, Fe, Mn, and Co, and a larger enrichment of Cr will be seen in the passive film compared to a conventional Ni-Cr alloy. Such behavior helps explain enrichment of Cr in films on an equiatomic CrCoFeMnNi alloy in H_2SO_4 tested at similar applied potentials assuming the same phenomena in different alloys and solutions [33]. Enrichment of Ni^0 was seen at the oxide/metal interface for both the MPEA as well as the Ni-Cr alloy, as described elsewhere [33, 64, 90, 91]. This is expected. The lack of oxide enrichment of Cr reported by Luo et al. is not explained herein, but may account for its poor corrosion resistance [44].

2.5.3 Factors Contributing to High Cr Enrichment

Cr^{3+} oxides and hydroxides both contribute to the observed Cr passive film enrichment as expected given the high affinity between Cr and O as seen in experiments (**Figures 2.8, 2.9, and 2.10**). Enrichment of some MPEA elements in an oxide and a depletion of others after 10 ks passivation is likely due to a combination of both thermodynamic and kinetic factors. In this study, all elements were oxidized at applied potentials far above their respective oxidation potentials [80]. The thermodynamically favored dissolution of Fe, Ni, Co, and Mn at the oxide/electrolyte interface may occur at rates that are non congruent as seen in **Figure 2.8 and 2.9**. However, selective dissolution may not fully explain the observed Cr enrichment. During oxidation, vacancies created by metal removal at the oxide/metal interface during metal removal to form metal cations create a vacancy flux that is directionally inward from that interface [98]. Kirkendall vacancy production also occurs due to the differential transport rates of alloying elements to the interface [99]. A Kirkendall flux is directed from the oxide/metal interface inward toward the bulk when selective oxidation of fast diffusing elements (Cr and Mn here) occurs (**Figure 2.10 and Table 2.2**) [99]. The Kirkendall flux will add to the surface injection vacancy flux, and Cr and Mn are thus depleted at the oxide/metal interface for the $\text{Ni}_{38}\text{Fe}_{20}\text{Cr}_{22}\text{Mn}_{10}\text{Co}_{10}$ MPEA (**Tables 2.4 and 2.5**) while Ni is enriched [99]. This unusual combination of multiple vacancy sources arises from different rates of vacancy-mediated transport, differences in interfacial or surface reaction rates, and selective oxidation or dissolution rates for the MPEA elements, which could all factor into the observed Cr enrichment [12, 64, 65]. Mn enrichment might also be explained by the same phenomenon. Inter-diffusion of Ni, Fe, Cr, Co, and Mn was studied in the temperature range 1173 to 1373 K in solid solution CoCrFeMnNi alloy [100]. In rank order, the diffusion rates were $\text{Mn} > \text{Cr} > \text{Fe} > \text{Co} > \text{Ni}$ although sluggish diffusion is often suggested in HEAs [100]. In an $\text{Al}_{1.5}\text{CrFeMnTi}$ alloy, Cr, Mn, and Fe diffusion were faster than the other elements at high temperature [101]. Moreover, modeling has shown that Cr and Mn diffusion in nickel occurs on surfaces and grain boundaries with a 10x lower activation barrier than the bulk [102]. Phase transformations in CrMnFeCoNi MPEAs also demonstrate faster intergranular or interfacial diffusion rates compared to the bulk [12]. This trend is likely to be seen for other MPEAs containing Ni, Cr and Mn.

One must also recognize that the observed Cr depletion cannot be explained by extrapolation of Cr diffusion rates in Ni and Ni-Cr alloys alone from high to room temperature, which yields insufficient rates at 25°C [103]. If all these factors affecting relative Cr oxidation and accumulation rates are operative, and preferential dissolution of the other alloying elements is favored as well, then enrichment of Cr in the passive film could be understood on that basis. Further work is required to elucidate the origins of this interesting effect in a variety of MPEAs.

2.6 Conclusion

The passive behavior of a Ni₃₈Fe₂₀Cr₂₂Mn₁₀Co₁₀ MPEA was investigated in 0.1 M NaCl + HCl at pH 4 deaerated and compared to a solid solution Ni₇₆Cr₂₄ binary alloy.

- The electrochemical corrosion behavior for the MPEA was similar to Ni₇₆Cr₂₄ as both exhibited a broad passive region with low passive current densities. Passive film breakdown associated with localized corrosion in the form of crevice corrosion was observed at anodic potentials in both cases.
- The passivity of the MPEA was slightly improved over the Ni₇₆Cr₂₄. Cr was enriched in the protective films of both alloys. Slightly better corrosion properties of the MPEA compared to Ni₇₆Cr₂₄ was consistent with greater Cr enrichment in the passive oxide film even though Ni₇₆Cr₂₄ contained a slightly greater concentration of alloyed Cr.
- The passive oxide film was consistent with either Cr(OH)₃, corundum, or spinel containing small amounts of Mn, Fe, Ni and Co. There was not enough Fe, Ni, Mn, or Co within oxides relative to Cr to support assignment of the entire protective film layer exclusively to spinels.
- Cr enrichment in the passive film is likely attributed to a combination of thermodynamic and kinetic factors as well as depletion of Fe, Ni, Co, and Mn governed by chemical dissolution kinetics exacerbated by the NaCl environment.

2.7 References

1. Miracle, D.B. and O.N. Senkov, *A critical review of high entropy alloys and related concepts*. Acta Materialia, 2017. **122**: p. 448-511.

2. Chen, J., et al., *A review on fundamental of high entropy alloys with promising high-temperature properties*. Journal of Alloys and Compounds, 2018. **760**: p. 15-30.
3. Qiu, Y., et al., *Corrosion of high entropy alloys*. npj Materials Degradation, 2017. **1**(1): p. 15.
4. Wang, H.L., et al., *Microstructure, thermal properties, and corrosion behaviors of FeSiBALNi alloy fabricated by mechanical alloying and spark plasma sintering*. International Journal of Minerals Metallurgy and Materials, 2016. **23**(1): p. 77-82.
5. Miracle, D.B., et al., *Exploration and Development of High Entropy Alloys for Structural Applications*. Entropy, 2014. **16**(1): p. 494-525.
6. Lu, P., et al., *Computational materials design of a corrosion resistant high entropy alloy for harsh environments*. Scripta Materialia, 2018. **153**: p. 19-22.
7. Lu, P., et al., *Computational design and initial corrosion assessment of a series of non-equimolar high entropy alloys*. Scripta Materialia, 2019. **172**: p. 12-16.
8. Quiambao, K.F., et al., *Passivation of a corrosion resistant high entropy alloy in non-oxidizing sulfate solutions*. Acta Materialia, 2019. **164**: p. 362-376.
9. Qiu, Y., et al., *Corrosion characteristics of high entropy alloys*. Materials Science and Technology, 2015. **31**(10): p. 1235-1243.
10. Chou, Y.L., J.W. Yeh, and H.C. Shih, *The effect of molybdenum on the corrosion behaviour of the high-entropy alloys Co_{1.5}CrFeNi_{1.5}Ti_{0.5}Mo_x in aqueous environments*. Corrosion Science, 2010. **52**(8): p. 2571-2581.
11. Feng, R., et al., *Design of Light-Weight High-Entropy Alloys*. Entropy, 2016. **18**(9).
12. Laplanche, G., et al., *Phase stability and kinetics of σ -phase precipitation in CrMnFeCoNi high-entropy alloys*. Acta Materialia, 2018. **161**: p. 338-351.
13. Senkov, O., et al., *Oxidation behavior of a refractory NbCrMo_{0.5}Ta_{0.5}TiZr alloy*. Journal of Materials Science, 2012. **47**: p. 6522-6534.
14. Z. Tang, L.H., W. He, P.K. Liaw, *Alloying and Processing Effects on the Aqueous Corrosion Behavior of High-Entropy Alloys*. Entropy, 2014. **16**(2): p. 895-911.
15. Butler, T.M. and M.L. Weaver, *Oxidation behavior of arc melted AlCoCrFeNi multi-component high-entropy alloys*. Journal of Alloys and Compounds, 2016. **674**: p. 229-244.
16. Taylor, C.D., et al., *Integrated computational materials engineering of corrosion resistant alloys*. npj Materials Degradation, 2018. **2**(1): p. 6.
17. Senkov, O.N., et al., *Development and exploration of refractory high entropy alloys—A review*. Journal of Materials Research, 2018. **33**(19): p. 3092-3128.
18. Zhou, Q., et al., *Corrosion behavior of Hf_{0.5}Nb_{0.5}Ta_{0.5}Ti_{1.5}Zr refractory high-entropy in aqueous chloride solutions*. Electrochemistry Communications, 2019. **98**: p. 63-68.
19. Shang, X.-L., et al., *Effect of Mo Addition on Corrosion Behavior of High-Entropy Alloys CoCrFeNiMo_x in Aqueous Environments*. Acta Metallurgica Sinica (English Letters), 2019. **32**(1): p. 41-51.
20. Raza, A., et al., *Corrosion resistance of weight reduced Al_xCrFeMoV high entropy alloys*. Applied Surface Science, 2019. **485**: p. 368-374.
21. Qiu, Y., et al., *A Surface Study of the Native Oxide upon a Compositionally Complex Alloy*. CORROSION, 2018. **74**(12): p. 1312-1317.
22. Waseem, O.A., et al., *The effect of Ti on the sintering and mechanical properties of refractory high-entropy alloy Ti_xWTaVCr fabricated via spark plasma sintering for fusion plasma-facing materials*. Materials Chemistry and Physics, 2018. **210**: p. 87-94.

23. Chang, C.-H., M.S. Titus, and J.-W. Yeh, *Oxidation Behavior between 700 and 1300 °C of Refractory TiZrNbHfTa High-Entropy Alloys Containing Aluminum*. Advanced Engineering Materials, 2018. **20**(6): p. 1700948.
24. Gorr, B., et al., *High-Temperature Oxidation Behavior of Refractory High-Entropy Alloys: Effect of Alloy Composition*. Oxidation of Metals, 2017. **88**(3): p. 339-349.
25. Butler, T.M., et al., *High temperature oxidation behaviors of equimolar NbTiZrV and NbTiZrCr refractory complex concentrated alloys (RCCAs)*. Journal of Alloys and Compounds, 2017. **729**: p. 1004-1019.
26. Zheng, J., et al., *Isothermal oxidation mechanism of a newly developed Nb–Ti–V–Cr–Al–W–Mo–Hf alloy at 800–1200°C*. International Journal of Refractory Metals and Hard Materials, 2016. **54**: p. 322-329.
27. Gorr, B., et al., *High temperature oxidation behavior of an equimolar refractory metal-based alloy 20Nb20Mo20Cr20Ti20Al with and without Si addition*. Journal of Alloys and Compounds, 2016. **688**: p. 468-477.
28. Gorr, B., et al., *Phase equilibria, microstructure, and high temperature oxidation resistance of novel refractory high-entropy alloys*. Journal of Alloys and Compounds, 2015. **624**: p. 270-278.
29. Liu, C.M., et al., *Microstructure and oxidation behavior of new refractory high entropy alloys*. Journal of Alloys and Compounds, 2014. **583**: p. 162-169.
30. Lee, C.P., et al., *Enhancing pitting corrosion resistance of Al_xCrFe1.5MnNi0.5 high-entropy alloys by anodic treatment in sulfuric acid*. Thin Solid Films, 2008. **517**(3): p. 1301-1305.
31. Qiu, Y., et al., *Microstructural evolution, electrochemical and corrosion properties of Al_xCoCrFeNiTi_y high entropy alloys*. Materials & Design, 2019. **170**: p. 107698.
32. Li, T., et al., *Localized corrosion behavior of a single-phase non-equimolar high entropy alloy*. Electrochimica Acta, 2019. **306**: p. 71-84.
33. Wang, L., et al., *Study of the surface oxides and corrosion behaviour of an equiatomic CoCrFeMnNi high entropy alloy by XPS and ToF-SIMS*. Corrosion Science, 2020. **167**: p. 108507.
34. Shang, X., et al., *The intrinsic mechanism of corrosion resistance for FCC high entropy alloys*. Science China Technological Sciences, 2018. **61**(2): p. 189-196.
35. Xiao, D.H., et al., *Microstructure, mechanical and corrosion behaviors of AlCoCuFeNi-(Cr,Ti) high entropy alloys*. Materials & Design, 2017. **116**: p. 438-447.
36. Shi, Y., et al., *Homogenization of Al_xCoCrFeNi high-entropy alloys with improved corrosion resistance*. Corrosion Science, 2018. **133**: p. 120-131.
37. Lee, C.P., et al., *The Effect of Boron on the Corrosion Resistance of the High Entropy Alloys Al_[sub 0.5]CoCrCuFeNiB_[sub x]*. Journal of The Electrochemical Society, 2007. **154**(8): p. C424.
38. Kao, Y.F., et al., *Electrochemical passive properties of Al_xCoCrFeNi (x=0, 0.25, 0.50, 1.00) alloys in sulfuric acids*. Corrosion Science, 2010. **52**(3): p. 1026-1034.
39. Lee, C.P., et al., *Effect of the aluminium content of Al_xCrFe1.5MnNi0.5 high-entropy alloys on the corrosion behaviour in aqueous environments*. Corrosion Science, 2008. **50**(7): p. 2053-2060.
40. Chen, Y.Y., et al., *Microstructure and electrochemical properties of high entropy alloys—a comparison with type-304 stainless steel*. Corrosion Science, 2005. **47**(9): p. 2257-2279.

41. Lin, C.-M. and H.-L. Tsai, *Evolution of microstructure, hardness, and corrosion properties of high-entropy Al_{0.5}CoCrFeNi alloy*. Intermetallics, 2011. **19**(3): p. 288-294.
42. Hsu, Y.-J., W.-C. Chiang, and J.-K. Wu, *Corrosion behavior of FeCoNiCrCux high-entropy alloys in 3.5% sodium chloride solution*. Materials Chemistry and Physics, 2005. **92**(1): p. 112-117.
43. Wang, H.-l., et al., *Microstructure, thermal properties, and corrosion behaviors of FeSiBAlNi alloy fabricated by mechanical alloying and spark plasma sintering*. International Journal of Minerals, Metallurgy, and Materials, 2016. **23**(1): p. 77-82.
44. Luo, H., et al., *Corrosion behavior of an equiatomic CoCrFeMnNi high-entropy alloy compared with 304 stainless steel in sulfuric acid solution*. Corrosion Science, 2018. **134**: p. 131-139.
45. Rodriguez, A., J.H. Tylczak, and M. Ziomek-Moroz, *Corrosion Behavior of CoCrFeMnNi High-Entropy Alloys (HEAs) Under Aqueous Acidic Conditions*. ECS Transactions, 2017. **77**(11): p. 741-752.
46. Gerard, A. Y., et al., *Progress in Understanding the Origins of Excellent Corrosion Resistance in Metallic Alloys: From Binary Polycrystalline Alloys to Metallic Glasses and High Entropy Alloys*. CORROSION. **0**(0): p. null.
47. Li, X., et al., *Communication—Dissolution and Passivation of a Ni-Cr-Fe-Ru-Mo-W High Entropy Alloy by Elementally Resolved Electrochemistry*. Journal of The Electrochemical Society, 2020. **167**(6): p. 061505.
48. Sarita, S., Swanson, O. J., Li, T., Gerard, A. Y., Scully, J. R., Frankel, G. S. , *Localized Corrosion Behavior of Non-Equiatomic NiFeCrMnCo High Entropy Alloys*. Electrochimica Acta-Submitted, 2020.
49. Lutton, K., et al., *Understanding multi-element alloy passivation in acidic solutions using operando methods*. Electrochemistry Communications, 2017. **80**: p. 44-47.
50. Jakupi, P., et al., *The impedance properties of the oxide film on the Ni–Cr–Mo Alloy-22 in neutral concentrated sodium chloride solution*. Electrochimica Acta, 2011. **56**(17): p. 6251-6259.
51. Chen, Y.-M., et al., *Application of Impedance Spectroscopy and Surface Analysis to Obtain Oxide Film Thickness*. Journal of The Electrochemical Society, 2017. **164**(9): p. C563-C573.
52. Hirschorn, B., et al., *Determination of effective capacitance and film thickness from constant-phase-element parameters*. Electrochimica Acta, 2010. **55**(21): p. 6218-6227.
53. Zagidulin, D., et al., *Characterization of surface composition on Alloy 22 in neutral chloride solutions*. Surface and Interface Analysis, 2013. **45**(6): p. 1014-1019.
54. Bush, A.A., et al., *Preparation and X-ray diffraction, dielectric, and Mössbauer characterization of Co_{1-x}Ni_xCr₂O₄ solid solutions*. Inorganic Materials, 2013. **49**(3): p. 296-302.
55. Kamran, M., et al., *Structural, magnetic, and dielectric properties of multiferroic Co_{1-x}Mg_xCr₂O₄ nanoparticles*. Journal of Magnetism and Magnetic Materials, 2017. **433**: p. 178-186.
56. Rao, K.V. and A. Smakula, *Dielectric Properties of Cobalt Oxide, Nickel Oxide, and Their Mixed Crystals*. Journal of Applied Physics, 1965. **36**(6): p. 2031-2038.
57. Motori, A., F. Sandrolini, and G. Davolio, *Electrical properties of nickel hydroxide for alkaline cell systems*. Journal of Power Sources, 1994. **48**(3): p. 361-370.

58. Doniach, S. and M. Sunjic, *Many-electron singularity in X-ray photoemission and X-ray line spectra from metals*. Journal of Physics C: Solid State Physics, 1970. **3**(2): p. 285-291.
59. KOLXPD, <http://kolxpd.kolibrik.net>.
60. Biesinger, M.C., et al., *Resolving surface chemical states in XPS analysis of first row transition metals, oxides and hydroxides: Cr, Mn, Fe, Co and Ni*. Applied Surface Science, 2011. **257**(7): p. 2717-2730.
61. Tyuliev, G.T. and K.L. Kostov, *XPS/HREELS study of NiO films grown on Ni(111)*. Physical Review B, 1999. **60**(4): p. 2900-2907.
62. Cwalina, K.L., et al., *In Operando Analysis of Passive Film Growth on Ni-Cr and Ni-Cr-Mo Alloys in Chloride Solutions*. Journal of The Electrochemical Society, 2019. **166**(11): p. C3241-C3253.
63. Castle, J.E. and K. Asami, *A more general method for ranking the enrichment of alloying elements in passivation films*. Surface and Interface Analysis, 2004. **36**(3): p. 220-224.
64. Kirchheim, R., et al., *The passivity of iron-chromium alloys*. Corrosion Science, 1989. **29**(7): p. 899-917.
65. Marcus, P. and J.M. Grimal, *The anodic dissolution and passivation of NiCrFe alloys studied by ESCA*. Corrosion Science, 1992. **33**(5): p. 805-814.
66. Hamm, D., et al., *Passivation of Fe-Cr alloys studied with ICP-AES and EQCM*. Corrosion Science, 2002. **44**(7): p. 1443-1456.
67. Li, X. and K. Ogle, *The Passivation of Ni-Cr-Mo Alloys: Time Resolved Enrichment and Dissolution of Cr and Mo during Passive-Active Cycles*. Journal of The Electrochemical Society, 2019. **166**(11): p. C3179-C3185.
68. Ogle, K., M. Mokaddem, and P. Volovitch, *Atomic emission spectroelectrochemistry applied to dealloying phenomena II. Selective dissolution of iron and chromium during active-passive cycles of an austenitic stainless steel*. Electrochimica Acta, 2010. **55**(3): p. 913-921.
69. Ogle, K. and S. Weber, *Anodic Dissolution of 304 Stainless Steel Using Atomic Emission Spectroelectrochemistry*. Journal of The Electrochemical Society, 2000. **147**(5): p. 1770-1780.
70. Ogle, K., *Atomic Emission Spectroelectrochemistry: Real-Time Rate Measurements of Dissolution, Corrosion, and Passivation*. CORROSION, 2019. **75**(12): p. 1398-1419.
71. Betova, I., et al., *Contact electric impedance and resistance studies of the conduction mechanism in passive films on ferrous alloys*. Electrochimica Acta, 2001. **46**(24): p. 3627-3640.
72. Bojinov, M., P. Kinnunen, and G. Sundholm, *Electrochemical Behavior of Nickel-Chromium Alloys in a High-Temperature Aqueous Electrolyte*. CORROSION, 2003. **59**(2): p. 91-103.
73. Taylor, S.D., et al., *Resolving Iron(II) Sorption and Oxidative Growth on Hematite (001) Using Atom Probe Tomography*. J. Phys. Chem. C, 2018. **122**(7): p. 3903-3914.
74. Thompson, K., et al., *In situ site-specific specimen preparation for atom probe tomography*. Ultramicroscopy, 2007. **107**(2): p. 131-139.
75. Hellman, O.C., et al., *Analysis of three-dimensional atom-probe data by the proximity histogram*. Microscopy and Microanalysis, 2000. **6**(5): p. 437-444.
76. Stern, M., *The Mechanism of Passivating-Type Inhibitors*. Journal of The Electrochemical Society, 1958. **105**(11): p. 638.

77. Stern, M. and A.L. Geaby, *Electrochemical Polarization*. Journal of The Electrochemical Society, 1957. **104**(1): p. 56.
78. Stern, M. and R.M. Roth, *Anodic Behavior of Iron in Acid Solutions*. Journal of The Electrochemical Society, 1957. **104**(6): p. 390.
79. Lange, E., *B. E. Conway: Electrochemical Data. XX und 374 Seiten, 23 × 16 cm. Elsevier Publishing Company Amsterdam Houston London New York 1952. Preis: 55s.* Zeitschrift für Elektrochemie, Berichte der Bunsengesellschaft für physikalische Chemie, 1953. **57**(5): p. 388B-389.
80. Wang, K., Gerard, A.Y., Han, J., Bi-Cheng, Z., Scully, J.R., *Potential-pH diagram with oxide solution phases for aqueous corrosion of multi-principal element alloys*. In Progress, 2020.
81. Oberdorfer, C. and W. Windl, *Bond-order bond energy model for alloys*. Acta Materialia, 2019. **179**: p. 406-413.
82. Huang, L.-F., et al., *Understanding Electrochemical Stabilities of Ni-Based Nanofilms from a Comparative Theory–Experiment Approach*. The Journal of Physical Chemistry C, 2019. **123**(47): p. 28925-28940.
83. Pourbaix, M., *Atlas of Electrochemical Equilibria in Aqueous Solutions* 1974, Houston, TX: National Association of Corrosion Engineers.
84. Speight, J.G., and Lange, N.A., *Lange's Handbook of Chemistry* ed. 17. 2017, New York: McGraw-Hill Education.
85. Biesinger, M.C., et al., *X-ray photoelectron spectroscopy studies of chromium compounds*. Surface and Interface Analysis, 2004. **36**(12): p. 1550-1563.
86. Seo, M. and N. Sato, *Surface Characterization of Stainless Steels Prepared with Various Surface Treatments*. Transactions of the Japan Institute of Metals, 1980. **21**(12): p. 805-810.
87. Wegrelius, L., F. Falkenberg, and I. Olefjord, *Passivation of Stainless Steels in Hydrochloric Acid*. Journal of The Electrochemical Society, 1999. **146**(4): p. 1397-1406.
88. Macdonald, D.D., et al., *An electrochemical impedance study of Alloy-22 in NaCl brine at elevated temperature: II. Reaction mechanism analysis*. Journal of Electroanalytical Chemistry, 2004. **572**(2): p. 421-431.
89. Gusieva, K., et al., *Repassivation Behavior of Individual Grain Facets on Dilute Ni–Cr and Ni–Cr–Mo Alloys in Acidified Chloride Solution*. The Journal of Physical Chemistry C, 2018. **122**(34): p. 19499-19513.
90. Jabs, T., P. Borthen, and H.H. Strehblow, *X-Ray Photoelectron Spectroscopic Examinations of Electrochemically Formed Passive Layers on Ni-Cr Alloys*. Journal of The Electrochemical Society, 1997. **144**(4): p. 1231-1243.
91. Jeng, S.-P., P.H. Holloway, and C.D. Batich, *Surface passivation of Ni/Cr alloy at room temperature*. Surface Science, 1990. **227**(3): p. 278-290.
92. Leygraf, C., et al., *Selective dissolution and surface enrichment of alloy components of passivated Fe18Cr and Fe18Cr3Mo single crystals*. Corrosion Science, 1979. **19**(5): p. 343-357.
93. Olefjord, I., *The passive state of stainless steels*. Materials Science and Engineering, 1980. **42**: p. 161-171.
94. Olefjord, I., B. Brox, and U. Jelvestam, *Surface Composition of Stainless Steels during Anodic Dissolution and Passivation Studied by ESCA*. Journal of The Electrochemical Society, 1985. **132**(12): p. 2854-2861.

95. Olefjord, I. and C.R. Clayton, *Surface Composition of Stainless Steel during Active Dissolution and Passivation*. ISIJ International, 1991. **31**(2): p. 134-141.
96. Olefjord, I. and B.-O. Elfstrom, *The Composition of the Surface during Passivation of Stainless Steels*. CORROSION, 1982. **38**(1): p. 46-52.
97. Zhang, X., et al., *Effect of Oxide Film Properties on the Kinetics of O₂ Reduction on Alloy C-22*. Journal of The Electrochemical Society, 2017. **164**(13): p. C911-C917.
98. Evans, H.E., *Cavity formation and metallurgical changes induced by growth of oxide scale*. Materials Science and Technology, 1988. **4**(12): p. 1089-1098.
99. Desgranges, C., et al., *Depletion and Voids Formation in the Substrate During High Temperature Oxidation of Ni–Cr Alloys*. Oxidation of Metals, 2013. **79**(1): p. 93-105.
100. Tsai, K.Y., M.H. Tsai, and J.W. Yeh, *Sluggish diffusion in Co–Cr–Fe–Mn–Ni high-entropy alloys*. Acta Materialia, 2013. **61**(13): p. 4887-4897.
101. Feng, R., et al., *Phase stability and transformation in a light-weight high-entropy alloy*. Acta Materialia, 2018. **146**: p. 280-293.
102. Alexandrov, V., et al., *Ab Initio Modeling of Bulk and Intragranular Diffusion in Ni Alloys*. The Journal of Physical Chemistry Letters, 2015. **6**(9): p. 1618-1623.
103. Gheno, T., et al., *Tracer diffusion of Cr in Ni and Ni-22Cr studied by SIMS*. Materialia, 2018. **3**: p. 145-152.

3. The Role of Chromium Content on Aqueous Passivation of Non-Equiatomic $\text{Ni}_{38}\text{Fe}_{20}\text{Cr}_x\text{Mn}_{21-0.5x}\text{Co}_{21-0.5x}$ Multi-Principal Element Alloy ($x = 22, 14, 10, 6$ at. %) in Acidic Chloride Solution

A manuscript summarizing this chapter has been published:

A.Y. Gerard, E.J. Kautz, D.K. Schreiber, J. Han, S. McDonnell, K. Ogle, P. Lu, J.E. Saal, G.S. Frankel, J.R. Scully, The role of chromium content in aqueous passivation of a non-equiatomic $\text{Ni}_{38}\text{Fe}_{20}\text{Cr}_x\text{Mn}_{21-0.5x}\text{Co}_{21-0.5x}$ multi-principal element alloy ($x = 22, 14, 10, 6$ at%) in acidic chloride solution, *Acta Materialia*, 245 (2023) 118607.

3.1 Abstract

The effect of the Cr content on the corrosion behavior in a series of single-phase non-equiatomic $\text{Ni}_{38}\text{Fe}_{20}\text{Cr}_x\text{Mn}_{21-0.5x}\text{Co}_{21-0.5x}$ ($6 < x < 22$ at. %) multi-principal element alloys (MPEAs) were investigated in acidified NaCl solutions. Comparisons were made with binary solid solution Co-Cr, Ni-Cr, and Fe-Cr alloys over a similar range of Cr contents. The corrosion behavior was evaluated using in-situ AC and DC electrochemical methods and ex-situ surface sensitive characterization techniques. Passivity and various levels of local corrosion resistance was obtained in the MPEA with 10 at. % Cr and above. The binary Ni-Cr alloys with 12 – 30 at. % Cr behaved similarly. The MPEA with 6 at. % Cr and binary alloys with 5, 6, or 10 at. % Cr were marginally passive or active and underwent localized corrosion during both linear sweep voltammetry and potentiostatic hold experiments. Passive films formed during potentiostatic hold experiments were characterized with X-ray photoelectron spectroscopy and atom probe tomography. Cr cation enrichment in the passive films was observed for all alloys and similar enrichment term were obtained as a function of Cr content regardless of whether MPEA or binary alloy except for the Fe-Cr alloy. Moreover, passive current density was correlated with the Cr cation fraction in the passive film. The degree of Cr enrichment was attributed to a combination of thermodynamic and kinetic factors, such as selective chemical dissolution of alloying elements as well as limitation due to solute depletion at the metal oxide interface in alloys with a bulk Cr content ≤ 10 at. %.

3.2 Introduction

It is well known that Cr plays a critical role in corrosion resistant alloys toward corrosion resistance in a number of aqueous environments. For example, the effect of Cr on the passivity of a system has been extensively studied in binary (i.e., Fe-Cr, Ni-Cr, Co-Cr)[1-11] and ternary (i.e., Ni-Cr-Mo, Fe-Ni-Cr) [2, 11-19] alloy systems. In complex alloys, such as stainless steels, the alloy becomes more likely to passivate and exhibit a significant decrease in passive current density (i_{pass}) with increasing bulk Cr concentration.

Improved passivity with increasing Cr content has at times been described via a critical Cr concentration above which the alloy becomes effectively “fully passive” to a given environment. By extension, at bulk Cr concentrations above the critical Cr concentration, the alloy is expected to form a passive film at similarly low levels of critical potential and current density [5-10, 14, 18-20]. Conversely, below the critical Cr concentration, passive films formed on Fe-Cr or Ni-Cr alloys are generally described as more “Fe-like” or “Ni-like” with inferior corrosion resistances [5, 21]. For example, Asami et al. investigated the passive films formed on a series of Fe-xCr binary alloys ($10 < x < 80$ at. %) in deaerated 1 M Na₂SO₄ solution at a passivating potential of 500 mV versus saturated calomel electrode (SCE). The passive films were characterized by X-ray photoelectron spectroscopy (XPS) and showed a change in Cr passive film composition at bulk Cr concentrations greater than 12.5 at. %. It was concluded that at a low Cr concentration (i.e., 10 at. %) the passive film consisted mainly of Fe hydroxide species while at bulk Cr concentrations ≥ 12.5 at. %, the film consisted of Cr hydroxide species [5]. Different critical Cr concentrations, depending on the alloying elements, have been reported [6, 7, 22]. For Fe-Cr alloys, a critical Cr content of 13 at. % has been reported [7, 10, 23], and for Co-Cr alloys 9 at. % Cr critical content was documented [6]. Theoretical models have been proposed to account for the origin of the critical Cr content such as graph [8, 9, 18, 22-25] and percolation theory [21, 26-28]. Commonly, these investigations report critical values in aqueous solutions that do not contain Cl⁻, which has shown to influence an alloys passive behavior [29-31].

Fe-Mn and Ni-Mn binary alloys are reported to form relatively unprotective passive films in aqueous Cl⁻ solutions [11, 32-39]. Improved corrosion resistance of such systems could be achieved by adding Cr but these are inferior to alloys without Mn [40]. Zhu et al. investigated a

series of Fe-Mn-xCr alloys ($1 < x < 7$ wt. %) [11]. These alloys showed lower corrosion current densities and increased corrosion potentials with increasing alloy Cr concentration in a 1 M Na₂SO₄ solution. The alloys also exhibited a less pronounced active-to-passive current density transition and broader passive potential regions with increasing Cr content during potentiodynamic polarization experiments [11]. They observed that the 7 wt. % Cr alloy exhibited lowest passive current density of 1×10^{-5} A cm⁻². In chloride-containing solution (3.5 wt. % NaCl), the Fe-Mn-xCr alloys did not show a clear passive potential domain, although the corrosion current densities decreased and corrosion potentials increased with bulk Cr content [11]. In the case of Ni-Cr-Mo alloy systems, lower passive current densities were observed for Ni-Cr-Mo alloys with bulk Cr \geq 20 at. % compared to 16 at. % in NaCl + H₂SO₄ solution [14]. Vigorous testing has been conducted on binary and ternary alloy systems but information is lacking on the effects of Cr content on alloys containing five or more alloying elements.

Multi-principal element alloys (MPEAs) have unusual attributes in which provide the opportunity for unique combinations of properties that may make them interesting candidates for corrosion resistant alloys[41]. However, relatively little is known about the dependencies on the corrosion mechanism of MPEA passivity on Cr content compared to the binary and ternary alloys. In particular, it has yet to be established how the MPEA alloy complexity may affect Cr enrichment in passive films and resulting passivity as a function of Cr content. Systematic studies of Cr content and details on the electrochemical passive response as a function of bulk and film Cr concentrations are lacking, although numerous reports on MPEAs show that Cr is beneficial to the corrosion resistance of the passive film [32, 42-50]. Chai et al. investigated the role of Cr-induced segregation on the corrosion behavior of an FeCoNiCr_x (Cr_x = 0, 13.22, 24.23 wt. %) MPEA [46]. Potentiodynamic polarization and electrochemical impedance spectroscopy (EIS) were utilized to evaluate the corrosion properties and passivation mechanism in 0.5 M H₂SO₄ and 3.5 wt. % NaCl solutions at 25 °C. FeCoNiCr_{13.22} MPEA showed enhanced corrosion resistance compared to the Cr₀ and Cr_{24.23} MPEAs, as indicated by a more positive passivity breakdown potential, lower corrosion current density, and lower passive current density (i_{pass}), in each testing solution. The EIS characterization revealed that the Cr_{13.22} addition stabilized the passive film because of higher oxide resistance compared to that of the Cr₀ MPEA. In the case of Cr_{24.23} MPEA, the Cr addition resulted in a lower oxide resistance, indicating a less stable passive film formation. It was concluded that the high Cr concentration in the Cr_{24.23} MPEA led to the development of new phases

and a dendritic morphology with a heterogeneous Cr distribution. Cr partitioning in the Cr_{24.23} MPEA resulted in a noncontinuous passive layer susceptible to localized corrosion [46].

Recent reports post detrimental corrosion behavior in MPEAs that contain more than 15% Mn in spite of a high Cr content. Yang et al. investigated the passivation behavior of CoFeNiMnCr MPEAs in H₂SO₄ solution [48]. Two sets of MPEAs were explored containing Mn where the Cr concentration was set to 20 and 25 at. %, CoFeNiMnCr and (CoFeNiMn)₇₅Cr₂₅, respectively. These were compared to MPEAs containing no Mn, (CoFeNi)₈₀Cr₂₀ and CoFeNiCr₂₅. For both sets of MPEAs, a broad passive potential region was observed during potentiodynamic polarization experiments. The Cr-MPEAs with no Mn showed better corrosion resistance indicated by potentiodynamic polarization curves and EIS polarization resistance. The (CoFeNi)₈₀Cr₂₀ and CoFeNiCr₂₅ MPEAs showed slightly lower i_{pass} and significantly lower current densities in the region where an active to passive potential transition occurred than the Mn-containing alloys, i.e. $\sim 10^{-4}$ A cm⁻² for CoFeNiMnCr, vs. 10^{-5} A cm⁻² for (CoFeNi)₈₀Cr₂₀ and 10^{-5} A cm⁻² for CoFeNiMn)₇₅Cr₂₅ vs. 10^{-6} A cm⁻² for CoFeNiCr₂₅ [48]. EIS analysis after a 1 hr stable open-circuit potential measurement showed that the polarization resistances of the (CoFeNi)₈₀Cr₂₀ MPEA and CoFeNiCr₂₅ MPEA were much higher than the Mn-containing MPEAs, suggesting the formation of a more protective passive film in the case of the Mn-free MPEAs. It was concluded that the addition of Mn decreased the general corrosion resistance of the MPEAs by forming a relatively unstable passive film compared to the Mn-free MPEAs [48]. Another Cr-containing MPEA study showed similar results but also lacked a detailed analysis regarding current densities as a function of Cr concentration in the bulk and passive film [51].

Understanding the beneficial role and limitations of Cr content in MPEA passivity, and potential synergistic or detrimental interactions with the diversity of other alloying elements requires a detailed analysis of passive films formed during aqueous oxidation on Cr-containing MPEAs. At the same time, comparisons with simpler systems such as binary alloys with similar bulk Cr concentrations are critical to identify more complex interactions. To explore these effects further, the corrosion protectiveness of the formed passive films must be studied for varying alloy Cr content. This requires a complex set of analytical datasets, including valence states present in the passive film, elemental composition, and cation distribution in conjunction with its electrochemical corrosion behavior. Complementary techniques, including XPS and atom probe

tomography (APT), are ideal in this context to provide quantitative analyses of nanoscale elemental segregation and partitioning, localized enrichment/depletion, and chemical states.

In this study, a series of non-equimolar, single phase, solid solution $\text{Ni}_{38}\text{Fe}_{20}\text{Cr}_x\text{Mn}_{21-0.5x}\text{Co}_{21-0.5x}$ MPEAs previously reported [32, 35, 52-55], where $x = 6 - 22$ at. %, were compared to a series of high-purity Ni-Cr, Fe-Cr, and Co-Cr binary alloys. The goal of this investigation was to enhance the understanding of the role of Cr in the corrosion properties of transition metal MPEAs for the condition when the sum of the other elements in the MPEA is equivalent to the solvent concentration in binary alloys and bulk Ni and Fe content are kept constant in the MPEAs. Explored herein are (a) the enrichment and/or depletion of Cr throughout the passive film; (b) comparison of Cr-containing MPEAs to similar Cr-containing binary alloys at low, intermediate, and high Cr contents; (c) possible explanations for Cr enrichment or depletion expressed as cation fraction in the oxide/hydroxide film as well as the possible governing factors.

3.3 Experimental

The $\text{Ni}_{38}\text{Fe}_{20}\text{Cr}_x\text{Mn}_{21-0.5x}\text{Co}_{21-0.5x}$ – at. % MPEAs were arc-melted, cast, and homogenized at 1100 °C for 96 hours using methods described previously [52]. Within this region, a single FCC phase solid solution is stable over a range of Cr concentrations, where $x = 22, 14, 10, 6$ at. %, compensated by variable Mn and Co concentrations. For simplicity, these MPEAs will be referred to as Cr22-, Cr14-, Cr10-, and Cr6-MPEA, respectively. Fe-xCr ($x = 30, 20, 10, 5$ at. %) binary alloys were produced from pure elemental Fe and Cr (> 99 % purity). The Fe was placed on the bottom of the crucible and the Cr was placed on top because of its higher melting point. The precursor materials were vacuum arc-melted in a water-cooled copper crucible under an Ar atmosphere of 0.5 atm pressure. The buttons were flipped and re-melted under similar conditions for a minimum of five times to ensure homogeneity. The ~10 g buttons were cut by electrical discharge machining into 2 mm slices. The sliced Fe-30Cr and Fe-20Cr samples were further homogenized at 1100 °C for 2 hr to obtain a BCC solid solution phase. Similarly, the Fe-10Cr and Fe-5Cr samples were homogenized at 700 °C for 24 hr to obtain a BCC solid solution phase. The Co-xCr alloys ($x = 30, 20, 10, 5$ at. %) were fabricated from pure elemental Co and Cr (> 99 % trace metal basis) with a multistep vacuum arc-melting process similar to the Fe-Cr alloys. The Co-xCr alloy slices were homogenized at 1100 °C for 24 hr to obtain an FCC solid solution phase.

A series of Ni-xCr binary alloys (x = 30, 20, 10, 5 at. % Cr) were cast from ultra-high purity Ni base material and ultra-high purity Cr. Samples were hot forged at 900 °C followed by a solution anneal at 950 °C for 1 hr and water quenched [56]. For passive film characterization, separate Ni-Cr alloys were used. These alloys were solid solution Ni-24Cr and Ni-12Cr (at. %) binary alloys that were arc-melted, cast, rolled, solutionized at 1100 °C, and recrystallized, resulting in a homogenous single-phase FCC alloy [57, 58]. All tested materials and corresponding compositions are listed in **Table 3.1**.

Table 3. 1. Multiple-Principal Element Alloys and Binary Alloys Composition

Alloy	Nominal Chemical Composition (at. %)
Cr22-MPEA*	38Ni-20Fe-22Cr-10Mn-10Co
Cr14-MPEA*	38Ni-20Fe-14Cr-14Mn-14Co
Cr10-MPEA*	38Ni-20Fe-10Cr-16Mn-16Co
Cr6-MPEA**	38Ni-20Fe-6Cr-18Mn-18Co
Fe-30Cr	70Fe-30Cr (72.4Fe-27.6Cr)
Fe-20Cr*	80Fe-20Cr (80.8Fe-19.2Cr)
Fe-10Cr	90Fe-10Cr (87.2Fe-12.8Cr)
Fe-5Cr	95Fe-5Cr (95.1Fe-4.9Cr)
Co-30Cr*	70Co-30Cr (70.0Co-30.0Cr)
Co-20Cr*	80Co-20Cr (78.9Co-21.1Cr)
Co-10Cr**	90Co-10Cr (91.2Co-8.8Cr)
Co-5Cr	95Co-5Cr (95.6Co-4.4Cr)
Ni-30Cr	70Ni-30Cr
Ni-20Cr	80Ni-20Cr
Ni-10Cr	90Ni-10Cr
Ni-5Cr	95Ni-5Cr
Ni-24Cr*	76Ni-24Cr
Ni-12Cr*	88Ni-12Cr

(*) alloys passivated at 0 V_{SCE} and resulting film characterized
(**) alloys initially passive but broke down during 10ks oxide growth at 0 V_{SCE}
(Elemental Composition determined by Energy Dispersive X-ray Spectroscopy)

For electrochemical testing, samples were mechanically ground to 1200 grit using SiC, degreased with acetone, rinsed with deionized water, and dried with $N_{2(g)}$. For potentiostatic passivation and characterization experiments, samples were mechanically ground to 1200 grit using SiC, polished with 0.25 μm diamond suspension, and then polished with colloidal silica with a final finish of 0.06 μm . Samples were degreased after polishing by sonicating in acetone, 1:1 acetone and isopropanol, isopropanol, and deionized water, each for 1 min, and dried with $N_{2(g)}$.

Electrochemical tests were conducted in $N_{2(g)}$ – deaerated 0.1 M and 1 mM NaCl, with the final pH adjusted to 4 using 0.1 M HCl. The 1 mM NaCl electrolyte was utilized for electrochemical passivation experiments, in order to evaluate the passivation of low Cr-alloys for comparison to high Cr-alloys within a slightly acidified Cl^- environment. Experiments were performed with a Gamry Instruments Reference 600+TM potentiostat. A standard three-electrode cell was utilized with a Pt mesh counter electrode, a saturated calomel reference electrode (SCE) reference electrode and an MPEA or binary alloy sample as the working electrode. Samples were pressed against a rubber O-ring to expose an area of 0.1 cm^2 . All potentials are reported against SCE.

Linear sweep voltammetry (LSV) experiments (potentiodynamic) were conducted over a range of applied potentials (-1.3 V_{SCE} to 0.8 V_{SCE}) with a scan rate of 0.5 mV s^{-1} . Prior to polarization, samples underwent an initial potentiostatic hold of -1.3 V_{SCE} for 600 s to minimize the effect of the air-formed oxide after polishing procedure. During LSV, the imaginary impedance component ($-Z''$) was monitored at an applied AC voltage of 20 mV_{RMS} at $f=1$ Hz. LSV experiments were also conducted on Pure Ni, Fe, Cr, Mn, and Co with the same surface preparation stated above. Pure element LSV experiments were conducted over a range of applied potentials (-1.3 V_{SCE} to 0.8 V_{SCE} for Pure Ni, Fe, Cr, and Co and -1.5 V_{SCE} to 0.8 V_{SCE} for Pure Mn) with a scan rate of 0.5 mV s^{-1} .

Electrochemical passivation was investigated within the passive potential region by potentiostatic passivation, where the passive potential was determined from LSV. Potentiostatic passivation was conducted using the following procedure: (1) cathodic treatment to minimize the effect of the air-formed oxide at -1.3 V_{SCE} for 600 s, (2) step potential hold at 0.0 V_{SCE} within the passive potential region for 10 ks, followed by (3) an EIS measurement from 100 kHz to 1 mHz at the same potential as (2). During the potentiostatic hold experiment, passive film growth was monitored as a function of time using a single-frequency EIS method (SF-EIS) at 1 Hz and an AC

potential magnitude of 20 mV_{rms} [54, 57, 59]. All EIS data were analyzed with an equivalent circuit model initially established for alloy C-22 and adapted for MPEAs [13, 54, 59, 60]. Approximate oxide thickness (ℓ_{ox}) as a function of time was calculated based on the relationship between the equivalent circuit model, constant phase element exponential, and $-Z''$, equation and methodology shown elsewhere and explained in Chapter 2 [54, 57, 59]. The following fitting parameters obtained from EIS: film constant phase element (CPE_f), film resistance (R_f), Warburg impedance (W_f), film/electrolyte constant phase element ($CPE_{f/e}$), film/electrolyte constant phase element exponential ($\alpha_{f/e}$), film/electrolyte resistance ($R_{f/e}$), and solution resistance (R_s) for all alloys and the assumed oxide dielectric constants are summarized in **Tables 3.2 and 3.3**, respectively.

Table 3. 2. Fitted EIS parameters obtained from model circuit fit for Cr22-, Cr14-, Cr10-MPEA, Fe-20Cr, Co-30Cr, Co-20Cr, Ni-24Cr, and Ni-12Cr

Alloy	CPE_f (S sec ^{α} cm ⁻²)	α_f	R_f (Ohm cm ²)	W_f (S sec ^{1/2})	$CPE_{f/e}$ (S sec ^{α} cm ⁻²)	$\alpha_{f/e}$	$R_{f/e}$ (Ohm cm ²)	R_s (Ohm cm ²)
Cr22-MPEA	3.2×10^{-5}	0.91	3.8×10^5	2.2×10^{-6}	4.0×10^{-9}	0.72	4.5×10^3	280.5
Cr14-MPEA	3.1×10^{-5}	0.90	3.8×10^5	2.6×10^{-6}	1.3×10^{-8}	0.64	4.6×10^3	0.38
Cr10-MPEA	3.6×10^{-5}	0.90	2.3×10^5	4.4×10^{-6}	1.2×10^{-8}	0.66	4.0×10^3	626.1
Fe-20Cr	5.1×10^{-5}	0.90	3.2×10^5	2.0×10^{-6}	8.8×10^{-9}	0.64	5.4×10^3	1.9
Co-30Cr	2.3×10^{-5}	0.93	4.5×10^5	1.7×10^{-6}	2.9×10^{-9}	0.74	4.5×10^3	32.7
Co-20Cr	2.6×10^{-5}	0.90	2.8×10^5	2.9×10^{-6}	2.4×10^{-9}	0.73	5.3×10^3	5.3×10^{-4}
Ni-24Cr	2.1×10^{-5}	0.90	3.9×10^5	1.9×10^{-6}	1.8×10^{-8}	0.62	4.6×10^3	972.8
Ni-12Cr	2.8×10^{-5}	0.90	2.3×10^5	3.4×10^{-6}	5.9×10^{-9}	0.70	4.0×10^3	942.8

Model circuit shown by [Li et al. doi.org/10.1016/j.electacta.2019.03.104]

Table 3. 3. Oxides detected by XPS and their molar mass, density, electrons, and dielectric constant.

Oxide	Molar Mass (g mol ⁻¹)	Density (g cm ⁻³)	Electrons ^[61]	Dielectric Constant
NiO	74.69	6.79	2	11.9 [62]
Ni(OH) ₂	92.71	4.10	2	2.7 [63]
NiCr ₂ O ₄	240.56	5.24	8	4.0 [64, 65]
FeCr ₂ O ₄	223.84	5.06	8	4.0 [64, 65]
FeO	71.84	5.74	2	22.6 [66]
Fe ₂ O ₃	159.69	5.24	6	14.2 [67]
Cr ₂ O ₃	151.99	5.21	6	30.0 [68]
Cr(OH) ₃	103.00	1.36	3	30.0 [68]
MnO	70.94	5.37	2	18.8 [69]
CoO	74.93	6.44	2	12.9 [62]

The charge efficiency (q_{ox}/q_{total}) of each passive film formed at 0.0 V_{SCE} was calculated from the total electrochemistry charge (q_{total}) and oxide charge (q_{ox}) densities over 10 ks or until a steady state passive current density was obtained. Oxide charge densities for the exact same conditions was calculated utilizing the relationship shown in **Eq. 3.1**;

$$q_{ox} = \frac{\ell_{ox} n F \rho}{M} \quad (3.1)$$

Where ℓ_{ox} is the EIS derived oxide thickness, , M is the oxide molar mass, n is the number of electrons transferred to produce the oxide from its elements, ρ is the oxide density of assumed oxides, and F is the Faraday constant (96485 C mol⁻¹). Hydroxides were considered as well as oxides. For charge calculations, weighted averages for M, ρ , and n were used for each alloy and oxides based on XPS cation fractions, as shown in **Tables 3.3 and 3.4**.

Table 3. 4. Deconvoluted oxides from XPS and their corresponding fractions.

Alloy	Oxide									
	NiO	Ni(OH) ₂	NiCr ₂ O ₄	FeCr ₂ O ₄	Cr ₂ O ₃	Cr(OH) ₃	MnO	CoO	FeO	Fe ₂ O ₃
Cr22-MPEA	--	0.03	0.120	0.19	0.11	0.49	0.02*	0.04*	--	--
Cr14-MPEA	0.02	0.09	0.09	0.19	0.03	0.50	0.02*	0.06*	--	--
Cr10-MPEA	0.01	0.13	--	0.18	--	0.59	0.01*	0.08*	--	--
Fe-20Cr	--	--	--	--	0.09	0.68	--	--	0.15	0.08
Co-30Cr	--	--	--	--	0.23	0.7	--	0.07	--	--
Co-20Cr	--	--	--	--	0.06	0.83	--	0.11	--	--
Ni-24Cr	0.09	0.18	--	--	0.07	0.66	--	--	--	--
Ni-12Cr	0.05	0.26	--	--	0.03	0.66	--	--	--	--

*Assuming max allowed Mn and Co fractions consistent with XPS 2p_{1/2} signal.

The elemental dissolution profile of the Co-20 at.% Cr was investigated by the atomic emission spectroelectrochemistry (AESEC) technique. The detailed analytical method and principle of the AESEC technique is available elsewhere [70, 71]. The sample was positioned vertically to an electrochemical flow cell. The electrolyte flow rate was controlled by a peristaltic pump. When the electrolyte was in contact with the specimen of interest, the released ions dissolved in the electrolyte were transferred to an Ultima 2CTM Horiba Jobin-Yvon inductively coupled plasma atomic emission spectrometer (ICP-AES). The atomic intensities of Co (231.6 nm) and Cr (267.7 nm) were monitored by a polychromator (0.5 m focal distance) and a monochromator (1.0 m focal distance), respectively. The use of monochromator is to obtain a better resolution of Cr signal, the minor element of this alloy. The equivalent elemental current densities of an element M, i_M , were calculated as, **Eq. 3.2**:

$$i_M = z_M F v_M / M_M \quad (3.2)$$

where z_M is the oxidation state of M (*e.g.*, $M \rightarrow M^{z+} + z_M e^-$), F is the Faraday constant (96485 C mol⁻¹), M_M is the atomic weight of M. The elemental dissolution rates (v_M) were calculated from the atomic emission intensities, again described in [70]. The z_M in this work was determined to be Co(II) and Cr(III) from thermodynamic simulations in our previous work [35].

XPS spectra were acquired using Al K α X-rays (binding energy: 1468.7 eV) with a take-off angle of 45° at a pass energy of 26 eV with a spot size of 100 μ m and an analysis depth of < 10

nm in a PHI VersaProbe IIITM system. Cation fraction within the passive film and elemental composition just below the metal/film interface (relative to all cations or elements detected) were determined by spectral deconvolution of individual core-level spectra with KOLXPDTM analysis software. Spectral deconvolution was implemented with Voigt functions for oxides, asymmetric Doniach Sunjic-like features for metals, and a Shirley background subtraction [72, 73]. For each alloying element, the 2p core feature was deconvoluted utilizing reported parameters for multiplet splitting of reference stoichiometric compounds [74]. Due to Ni Auger overlap with Mn 2p_{3/2}, Co 2p_{3/2}, and Fe 2p_{2/3} spectra, the 2p_{1/2} feature was utilized for XPS spectral deconvolution. A peak intensity limit of less than or equal to the intensity of noise was considered for Co and Mn 2p_{1/2} spectra, in order to establish an upper limit to the Mn(II) and Co(II) fractions present within the passive film. A more detailed description of XPS spectral deconvolution has been provided previously in Chapter 2 [32, 54, 59].

APT was utilized to track elements and their distribution throughout the passive films and across the metal/film interface after the above electrochemical passivation procedure for the Cr22-, Cr10-MPEA, Fe-20Cr, and Co-20Cr in order to explore similar Cr levels and one low Cr level. Passive films formed at 0.0 V_{SCE} were coated with \approx 20 nm Cr and \approx 50 nm Ni using an ion beam sputtering system prior to APT sample preparation. This Ni/Cr bilayer was used as a marker for targeting the coating/passive film/alloy interfaces in the final APT needle apex. APT sample preparation was performed using an FEI HeliosTM dual beam focused ion beam-scanning electron microscope (FIB-SEM) [75]. APT needles were prepared by depositing a Pt protective layer and extracting a cantilever from the sample with the base alloy/passive film and Ni/Cr coating. Samples were prepared so that the Ni/Cr capping layer/passive film/base alloy interfaces were perpendicular to the analysis direction.

A CAMECA local electrode atom probe (LEAP) 4000X HR APT system equipped with a 355 nm wavelength UV laser was used for APT data collection with the following user-selected parameters: 60 pJ/pulse laser energy, 125 kHz pulse repetition rate, 40 K specimen base temperature, and 0.003 detected ions/pulse detection rate. Data were reconstructed and analyzed using the Interactive Visualization and Analysis Software (IVAS), version 3.8.8 by CAMECA. Mass spectrum peak ranging is defined in **Figures 3.1 to 3.3**, with prominent peaks labeled. Each mass spectra contains signal from the base alloy, passive film, and Cr capping layer. Peak

deconvolution based on natural isotopic abundances were done for overlaps at 27 Da ($^{56}\text{Fe}^{2+}/^{56}\text{Cr}^{2+}$) and 56 Da ($^{56}\text{Fe}^+ / ^{56}\text{Cr}^+$) for MPEAs and the Fe-20Cr alloy.

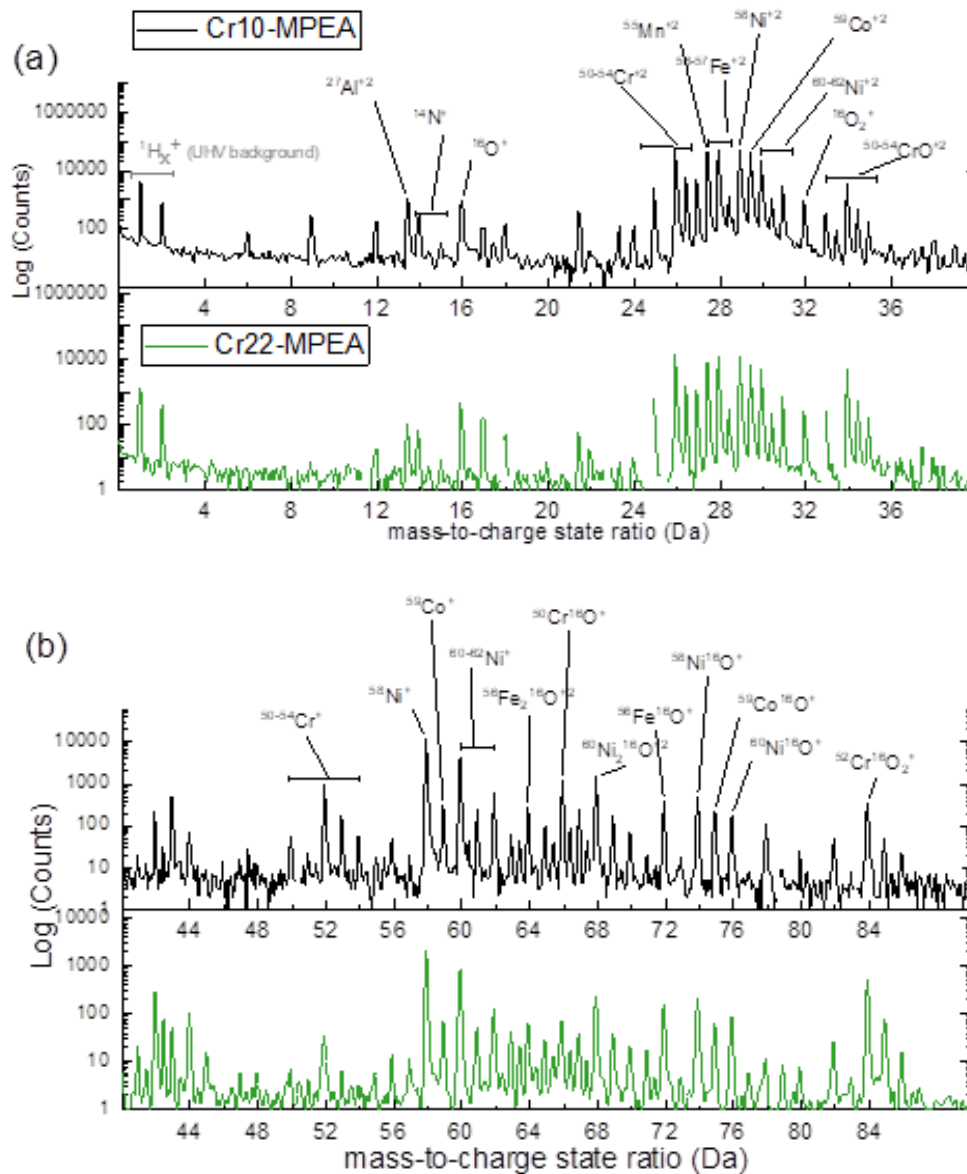


Fig. 3. 1. Ranging criteria for APT mass spectrum analysis for the base alloy, passive film, and Cr capping layer for Cr-10 and Cr22 MPEAs.

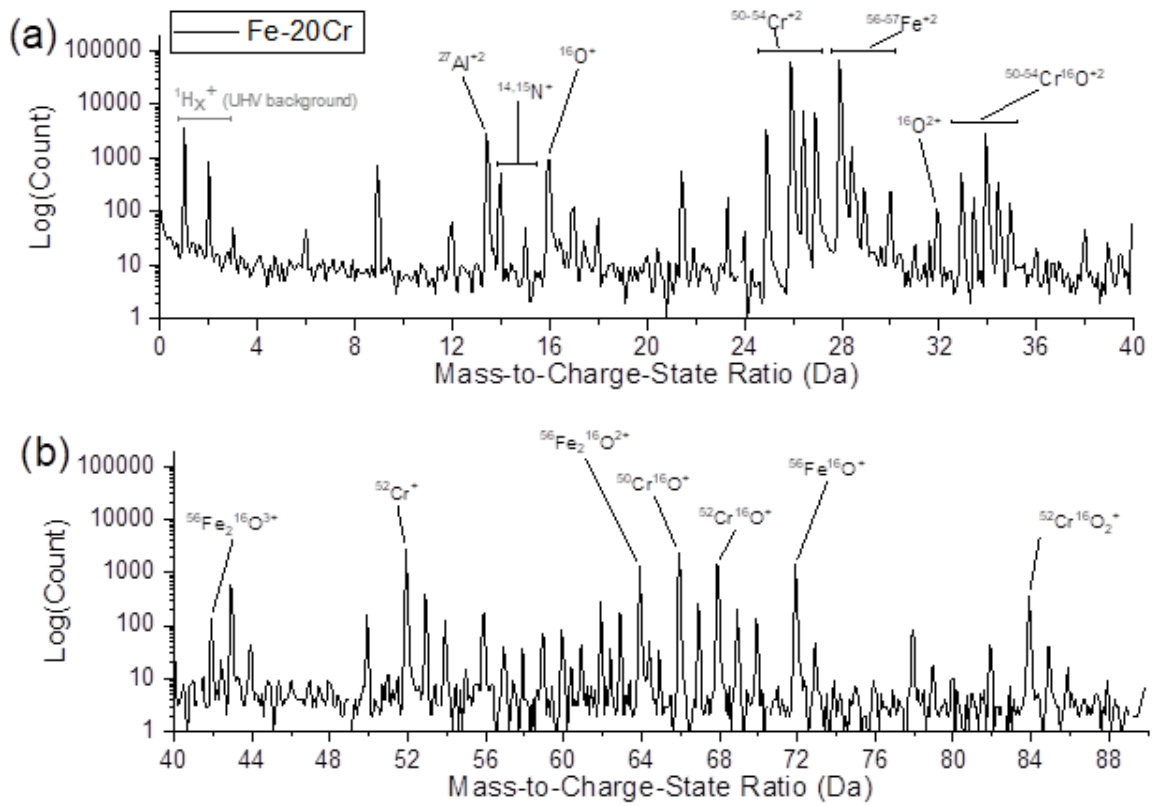


Fig. 3. 2. Ranging criteria for APT mass spectrum analysis for the base alloy, passive film, and Cr capping layer for the Fe-20Cr alloy.

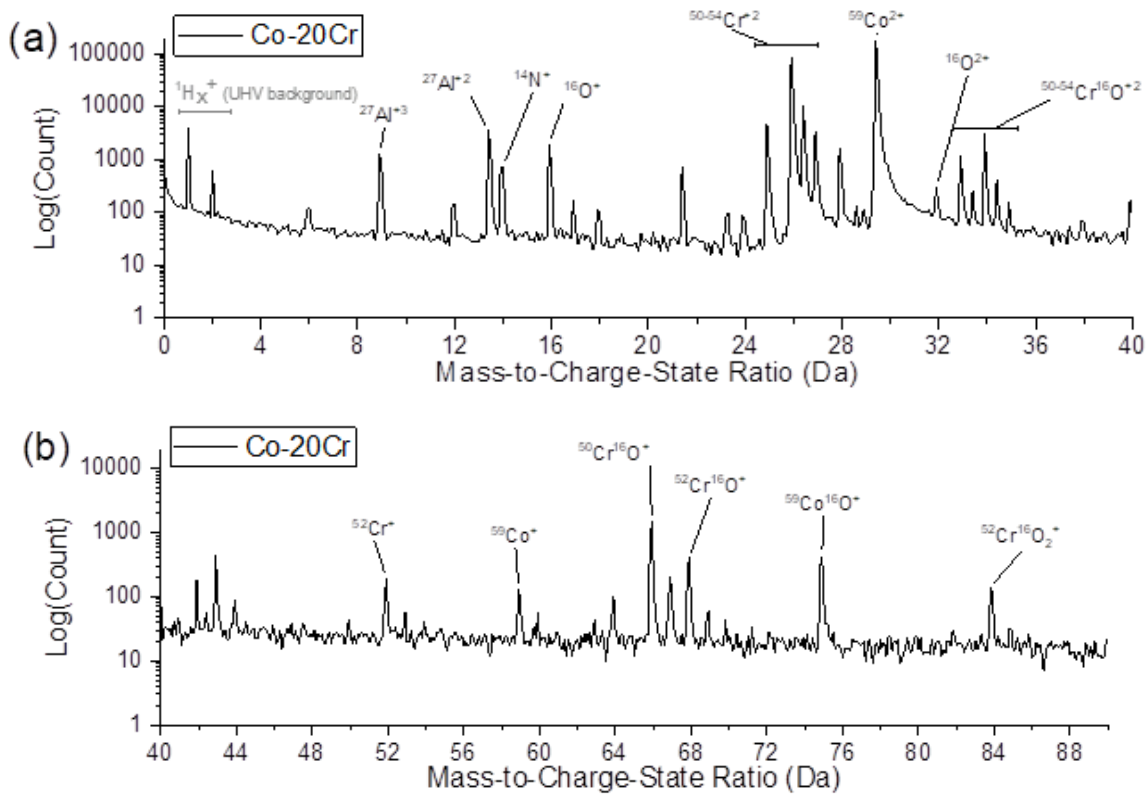


Fig. 3.3. Ranging criteria for APT mass spectrum analysis for the base alloy, passive film, and Cr capping layer for the Co-20Cr (at. %) alloy.

Elemental composition profiles were determined using the proximity histogram method across O isoconcentration surfaces (located at the approximate base alloy/passive film interface, which varied in at. % for each alloy), with a bin width of 0.2 nm. An oxygen isoconcentration surface (i.e., isosurface) indicates a surface in 3D where the oxygen concentration is a constant value. Oxygen isosurface concentrations were selected for each base alloy to approximate the substrate/passive film interface. The O isosurface selected in each case was continuous across the reconstructed volume. Definitions of base alloy (metal)/passive film, and passive film/Cr cap interfaces are summarized in **Table 3.5**. Concentration profiles are reported here including all elements, and for fractions of principal alloying elements only in **Figures 3.4-3.7**. Error reported in the concentration profiles represent 1σ from standard counting error, defined as: $\sigma = \sqrt{c_i(100 - c_i)/N_T}$, where c_i is local concentration of species i , and N_T is the total number of atoms in the concentration measurement. In addition to concentration profiles, 3D element distribution

maps are given in **Figures 3.4-3.7** to visually show the distribution of elemental and molecular peaks across the passive film/substrate interface. The extracted concentration profiles were normalized to consider only alloy principal elements (i.e., excluding O or other trace species) to enable more direct interrogation of enrichment or depletion relative to the base alloy composition. Some differences in the Cr capping layer composition can be observed in **Figures 3.4-3.7(a)-(b)**. These differences can be attributed to some variability in sample preparation conditions. The Cr10- and Cr22-MPEAs were prepared separately using the same ion beam sputtering (IBS) system for Ni/Cr capping layer deposition, and Fe-Cr and Co-Cr alloys were coated simultaneously. The IBS system is very sensitive to vacuum level, which also impacts capping layer composition. In the case of the Cr22-MPEA, the vacuum levels were erratic during the coating process, which led to a coating layer that was Cr oxide as opposed to a metallic Cr layer. Hence, in **Figure 3.5**, the Cr capping layer is labeled as ‘Cr (oxide) cap’. Capping layer composition contained less oxygen for the 10 at. % Cr MPEA and binaries because the vacuum seal was cleaned between coating procedures.

Table 3. 5. Definitions used for defining the isoconcentration surfaces and interfaces in the APT reconstructions.

Alloy	Oxygen isoconcentration value for proximity histogram	Base alloy/passive film	Passive film/Cr Cap
Cr22-MPEA	20 at. % O	≈ 0.4 nm from the peak in Ni profile (‘pile-up in base alloy’)	Plateau in Cr profile
Cr10-MPEA	20 at. % O	≈ 0.4 nm from the peak in Ni profile (‘pile-up in base alloy’), agrees well with inflection point in Mn profile	Inflection point in Mn profile
Fe-20Cr	13 at. % O	Inflection point in oxygen profile	Inflection point in the Fe profile
Co-20Cr	20 at. % O	Inflection point in oxygen profile	Inflection point in Al concentration profile

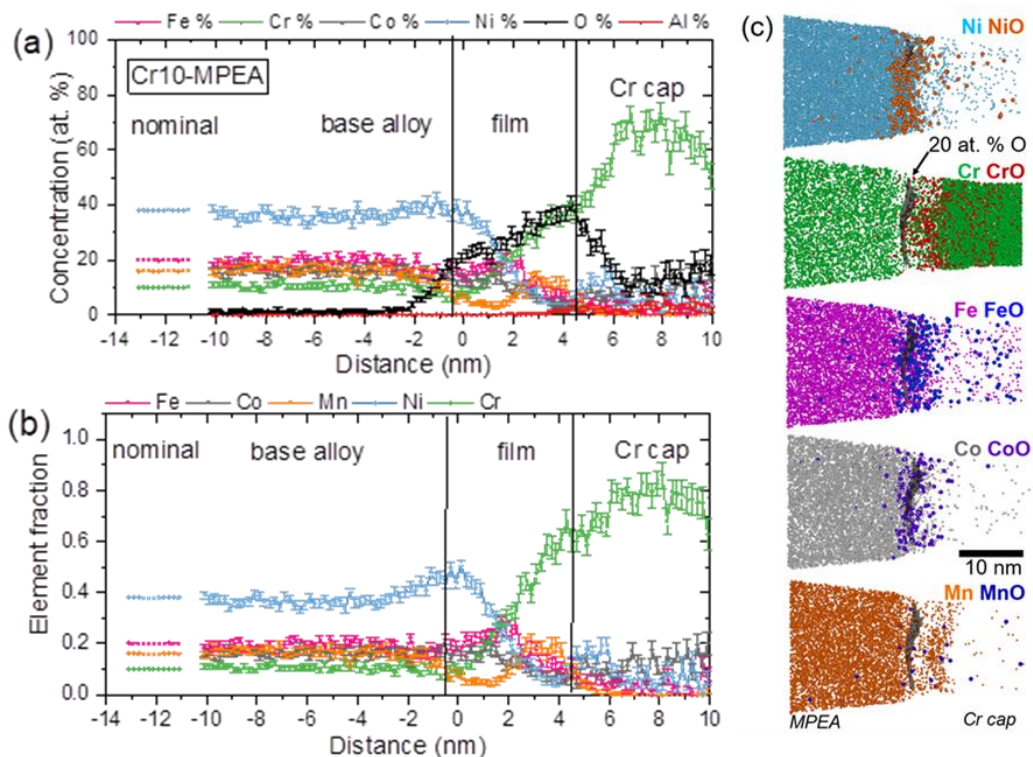


Fig. 3. 4. (a,b) APT concentration profiles and (c) element distribution maps of the Cr10-MPEA. The passive film was formed electrochemically during step-potentiostatic oxide growth at 0.0 V_{SCE} for 10 ks in deaerated 1 mM NaCl + HCl pH 4. The concentration profile in (a) was determined using a proximity histogram across a 20 at. % O isoconcentration surface with a bin width of 0.2 nm. The concentration profile in (b) shows only element fraction of principal alloying elements, and was calculated from (a). The 3D element distribution maps given in (c) show elemental and corresponding molecular species present in the film and base alloy. All maps are for a 10 nm thick region of interest through the center of the reconstructed volume.

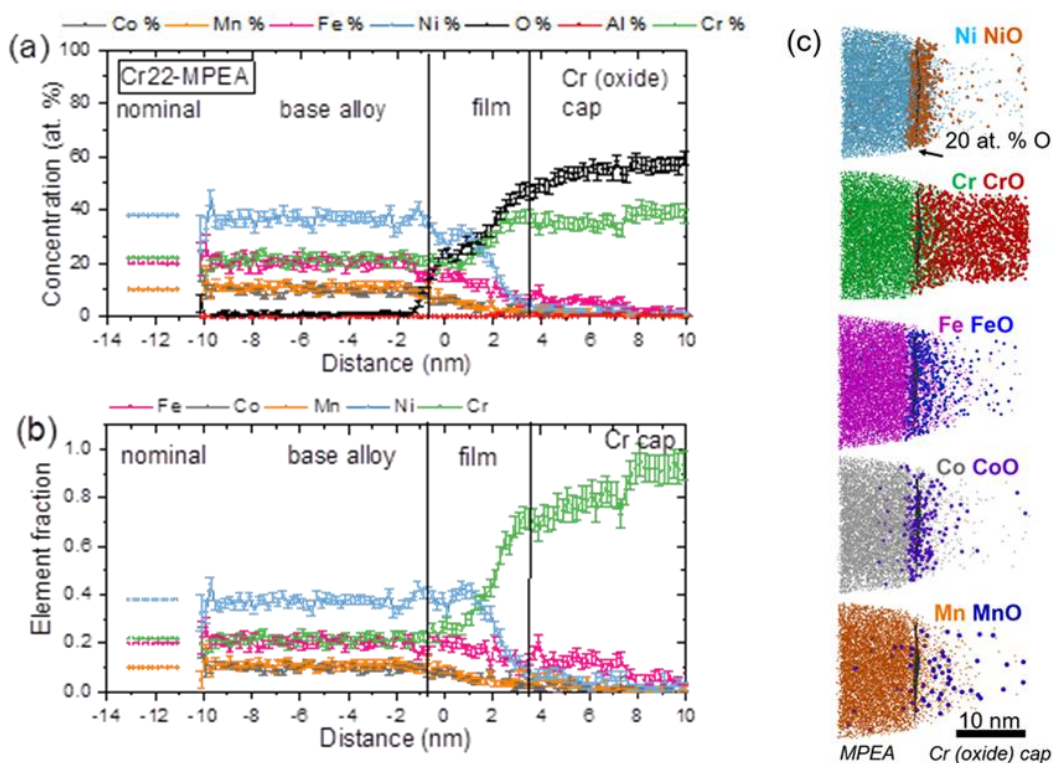


Fig. 3. 5. (a,b) APT concentration profiles and (c) element distribution maps of the Cr22-MPEA. The passive film was formed electrochemically during step-potentiostatic oxide growth at 0.0 V_{SCE} for 10 ks in deaerated 1 mM NaCl + HCl pH 4. The concentration profile in (a) was determined using a proximity histogram across a 20 at. % O isoconcentration surface with a bin width of 0.2 nm. The concentration profile in (b) shows only element fraction of principal alloying elements, and was calculated from (a). The 3D element distribution maps given in (c) show elemental and corresponding molecular species present in the film and base alloy. All maps are for a 10 nm thick region of interest through the center of the reconstructed volume.

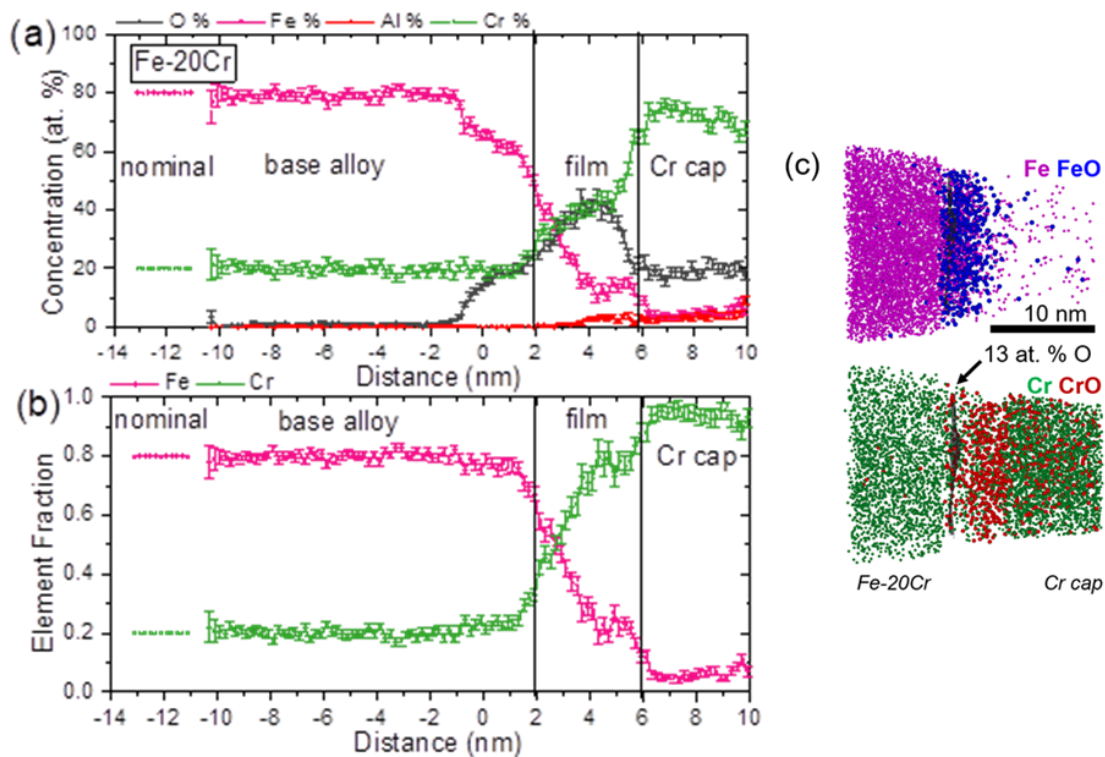


Fig. 3. 6. (a,b) APT concentration profiles and (c) element distribution maps of the Fe-20Cr alloy. The passive film was formed electrochemically during step-potentiostatic oxide growth at 0.0 V_{SCE} for 10 ks in deaerated 1 mM NaCl + HCl pH 4. The concentration profile in (a) was determined using a proximity histogram across a 13 at. % O isoconcentration surface with a bin width of 0.2 nm. The concentration profile in (b) shows only element fraction of principal alloying elements, and was calculated from (a). (c) The 3D element distribution maps given in (c) show elemental and corresponding molecular species present in the film and base alloy. All maps are for a 10 nm thick region of interest through the center of the reconstructed volume.

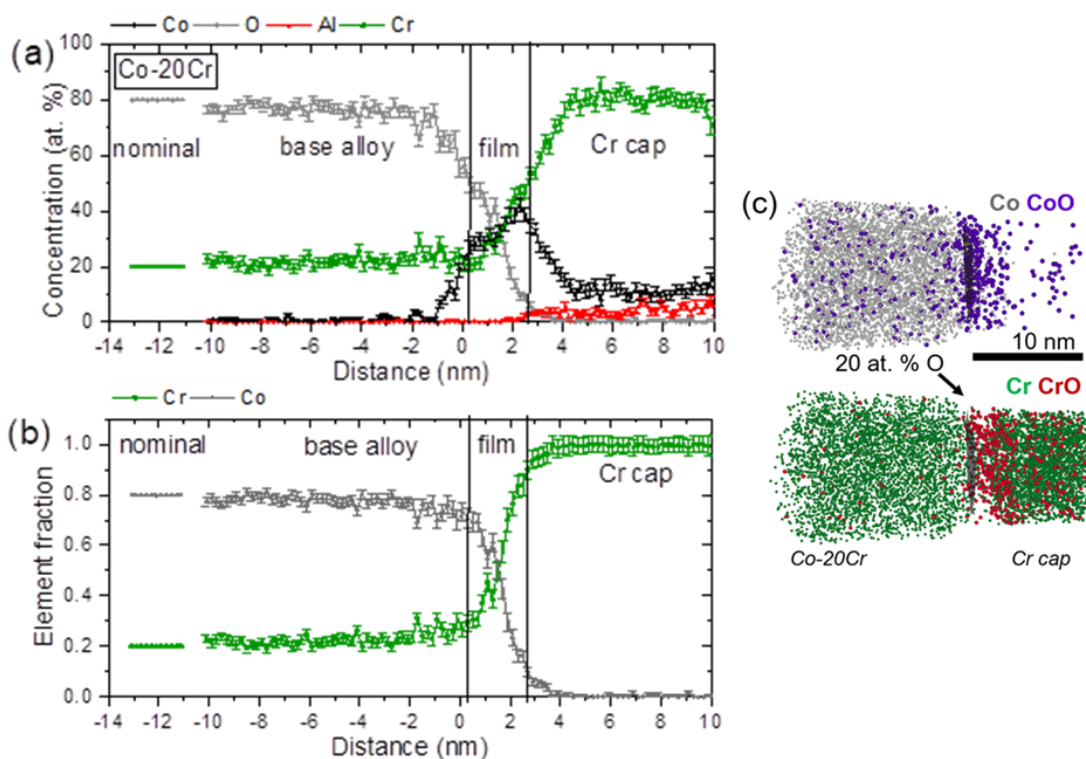


Fig. 3. 7. (a,b) APT concentration profiles and (c) element distribution maps of the Co-20Cr alloy. The passive film was formed electrochemically during step-potentiostatic oxide growth at 0.0 V_{SCE} for 10 ks in deaerated 1 mM NaCl + HCl pH 4. The concentration profile in (a) was determined using a proximity histogram across a 20 at. % O isoconcentration surface with a bin width of 0.2 nm. The concentration profile in (b) shows only element fraction of principal alloying elements, and was calculated from (a). (c) The 3D element distribution maps given in (c) show elemental and corresponding molecular species present in the film and base alloy. All maps are for a 10 nm thick region of interest through the center of the reconstructed volume.

A surface enrichment-depletion calculation approach, developed by Castle and Asami [76], was utilized to calculate a cation/elemental enrichment or depletion term for chromium, f_{Cr} , within passive films formed during electrochemical passivation at 0.0 V_{SCE}. Cr Enrichment and depletion terms were determined from all cation fractions within the passive film ($f_{Cr,ox}$) from XPS as well as separately for the metallic concentration at the metal/film interface, hereafter referred to as the altered zone ($f_{Cr,az}$), determined from XPS and APT. The altered zone region within APT concentration profile was determined based on Ni and Cr concentrations just below the metal/film interface correlated with the oxygen isoconcentration surface (defined in supplemental information) and in conjugation with XPS elemental Ni and Cr concentrations (i.e. enriched metallic Ni and depleted metallic Cr). APT cation fractions for the altered zone and passive film were determined from taking the average atom concentration of each element within each region. By utilizing the relationship between passive film and altered zone f_{Cr} and bulk alloy concentration, the expected Cr concentration within the passive film and altered zone were predicted over a range of relevant bulk Cr concentrations [54, 76]. This was performed within the range of Cr solid solution contents indicated by CALPHAD for the Cr-MPEA alloy [52]. A key initial assumption was that the enrichment term is independent of bulk alloy Cr content. A more detailed enrichment methodology has been previously provided with equations in our prior work and in Chapter 2 [54].

A hypothetical Cr depletion zone depth or size was calculated for a range of hypothetical charge efficiencies utilizing mass balance between bulk Cr concentration in the alloy necessary to supply the XPS-based Cr cation fraction reported for the passive film given its Cr content. An efficiency less than 100% means that a fraction of the Cr oxidized as Cr(III) was lost to the solution and does not contribute to the passive film thickness nor its composition. The following assumptions are considered: (a) the sum of Cr(III) in the oxide and dissolve must equal the mass balance removed from the metal altered zone, (b) the Cr concentration is zero (depleted at the oxide/metal interface) and depleted some alloy depth or “zone” required to achieve mass balance, (c) the oxide metal interface does not move or that vacancies injected as a result of metal dissolution are annihilated [77] and (d) Cr solid state diffusion through the altered zone is assumed to be equivalent in all alloys for the sake of this initial calculation.

3.4 Results

3.4.1 Electrochemical Passivation Behavior of Cr-MPEAs

LSV curves of the Cr-MPEAs and Cr binary alloys in deaerated 1 mM NaCl + HCl electrolyte and 0.1 M NaCl + HCl electrolyte at pH 4 solutions are shown in **Figs. 3.8** and **3.9**, respectively. The focus here is the electrochemical passivation and any active-passive transition observed during the upward potential scan. In each testing solution, the passive behavior (i.e., broader passive potential region, lower passive current densities, and higher breakdown potentials) was improved with increasing bulk Cr concentration for all materials.

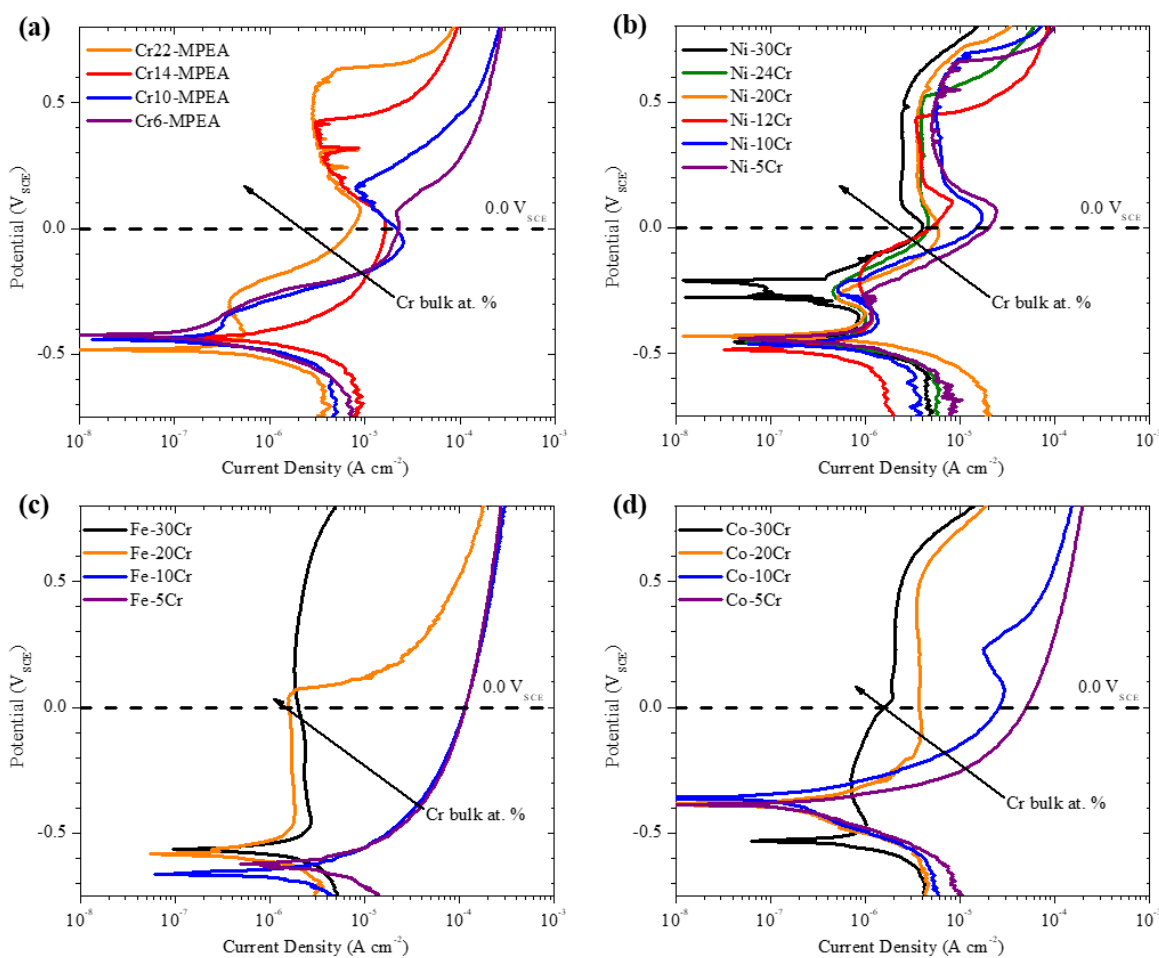


Fig. 3. 8. Linear sweep voltammetry in $N_{2(g)}$ deaerated 1 mM NaCl + HCl electrolyte at pH 4 after initial cathodic reduction at $-1.3 V_{SCE}$ for 600 s for (a) Cr-MPEAs, (b) Ni-xCr binary alloys ($x = 30, 20, 24, 12, 10, 5$ Cr atomic %), (c) Fe-xCr binary alloys and (d) Co-xCr binary alloys. Where $x = 30, 20, 10, 5$ Cr at. %.

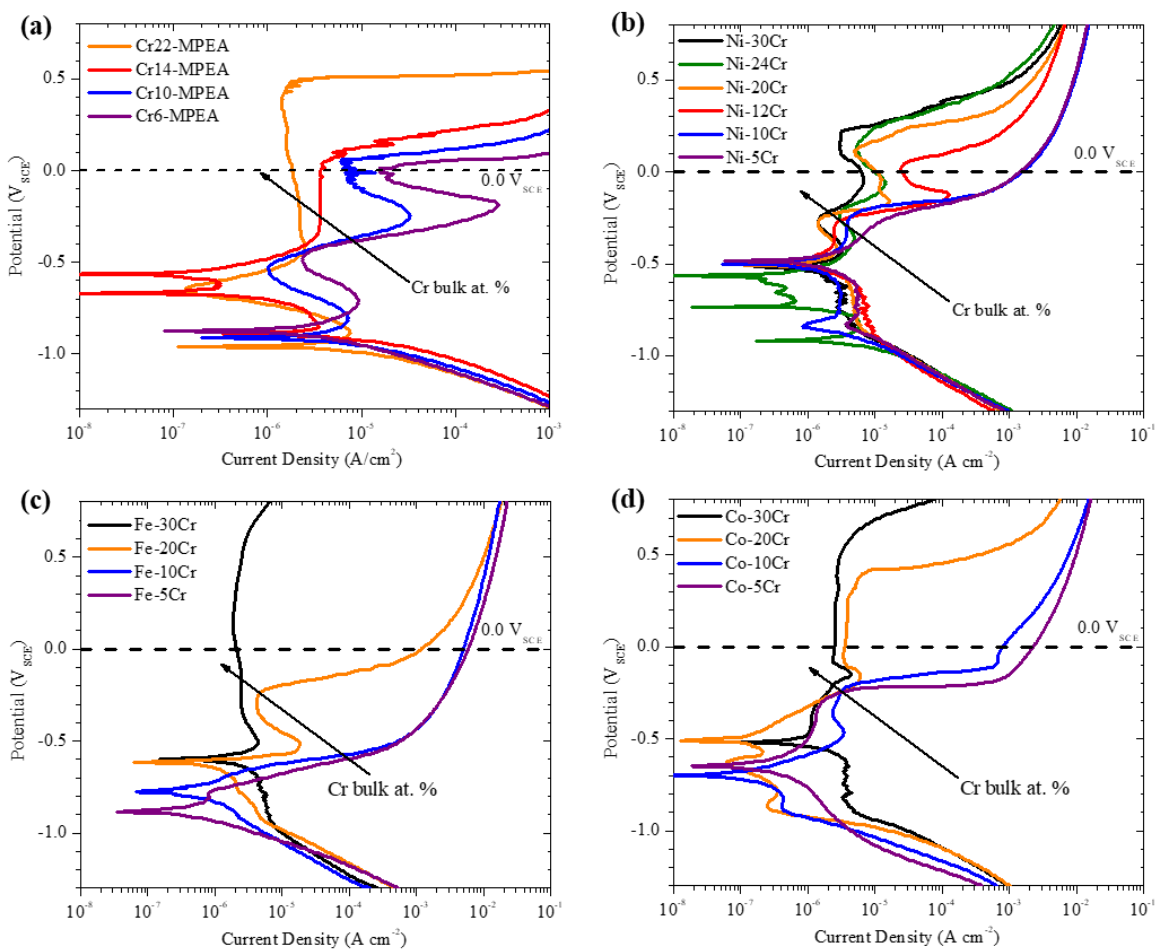


Fig. 3. 9. Linear sweep voltammetry in $N_2(g)$ deaerated $0.1\text{ M NaCl} + \text{HCl}$ at pH 4 after initial cathodic reduction at -1.3 V_{SCE} for 600 s for (a) Cr-MPEAs, (b) Ni- x Cr binary alloys ($x = 30, 20, 24, 12, 10, 5$ Cr atomic %), (c) Fe- x Cr binary alloys and (d) Co- x Cr binary alloys. Where $x = 30, 20, 10, 5$ Cr at. %.

The Cr-MPEAs showed passive potential regions at all Cr concentrations as indicated by a potential range greater than approximately 100 mV and current density below 10^{-4} A cm^{-2} in each solution (**Figs. 3.8** and **3.9**). In the case of the Fe-10Cr and Fe-5Cr binary alloys, active corrosion was exhibited with no evidence of passivity in each solution (**Figs. 3.8c** and **3.9c**) as indicated by large increases in anodic current density with applied potential, according to the criteria above. It should be noted, the Co-10Cr and -5Cr showed a small potential-passive region width of $\sim 200\text{ mV}$ in 0.1 M NaCl prior to crevice corrosion (**Fig. 3.9d**). Ni-10Cr and Ni-5Cr also showed active corrosion in 0.1 M NaCl as shown in **Fig. 3.9b**, but they showed clearly defined passive potential domain in 1 mM NaCl solution as shown in **Fig. 3.8b**. In 1 mM NaCl solution, the Cr-MPEAs

exhibited current spikes throughout their passive potential region, suggesting metastable pitting events (**Fig. 3.8a**). Zero current potentials were observed for Ni-30Cr in 1 mM NaCl and for Cr14-MPEA and Ni-24Cr in 0.1 M NaCl. The zero current potentials are an outcome from similarities between the passive current density and the limiting current for oxygen reduction caused by the presence of residual $O_{2(g)}$. It should be noted that pitting has been evaluated elsewhere on these MPEAs in Cl^- containing solutions and is not the focus of this work [53].

The Cr-MPEAs and Ni-Cr binary alloys showed passive current densities ranging from 10^{-6} to 10^{-5} $A\ cm^{-2}$ during upward LSV in 1 mM NaCl solution, shown in **Fig. 3.8a**. In the case of the Fe-Cr binary alloys (**Fig. 3.8c**), Fe-30Cr and Fe-20Cr showed lower passive current densities ($\sim 1 \times 10^{-6}$ $A\ cm^{-2}$) compared to the Cr-MPEAs. The Co-30Cr binary alloy (**Fig. 3.8d**) had a lower i_{pass} ($\sim 2 \times 10^{-6}$ $A\ cm^{-2}$) compared to the Cr14, Cr10, Cr6-MPEAs and other low Cr content Co-Cr binary alloys. The binary Co-20Cr (**Fig. 3.8d**) alloy exhibited a low i_{pass} at more negative passive potentials, but at higher potentials its i_{pass} was slightly higher than that of the Cr22-MPEA. In 0.1 M NaCl solution, Cr22-MPEA exhibited a slightly lower i_{pass} compared to Ni-30Cr (**Figs. 3.9a and 3.9b**) and similar i_{pass} magnitudes ($\sim 10^{-6}$ $A\ cm^{-2}$) as Fe-30Cr and Co-30Cr (**Figs. 3.9c and 3.9d**). The Cr14 and Cr10-MPEAs exhibited i_{pass} values similar to those of the Ni-20Cr, Fe-20Cr, and Co-20Cr binary alloys (**Fig. 3.9**).

The potential dependence of the imaginary impedance component ($-Z''$) at $f = 1$ Hz for Cr22-MPEA versus Ni-24Cr, and Cr6-MPEA versus Ni-5Cr is shown in **Figs. 3.10a and 3.10b**, respectively. At $f = 1$ Hz, $-Z''$ scales linearly with oxide thickness given a fixed constant phase element exponential (α_f), shown in **Table 3.2** [2]. The negative of the imaginary component of impedance, $-Z''$, is small but increasing below and near the corrosion potential signaling passive film formation. Increases continue for all high Cr content alloys during upward linear voltage sweeps within the passive region ($0.0\ V_{SCE} < E < 0.4\ V_{SCE}$), The Cr22-MPEA indicated the highest $-Z''$ values (**Fig. 3.10a**) in this potential region. In the case of the low Cr content alloys, the Cr6-MPEA and Ni-5Cr (**Fig. 3.10b**) also displayed an increase in $-Z''$ at potentials from $-1.0\ V_{SCE}$ to $-0.2\ V_{SCE}$. The Ni-5Cr binary alloy had a larger magnitude of $-Z''$ compared to the 6Cr-MPEA at potentials greater than $0.0\ V_{SCE}$. At potentials above 0.31 and $0.37\ V_{SCE}$, $-Z''$ begins to decrease for the Ni-24Cr and Cr22-MPEA (**Fig. 3.10a**), respectively, correlating with passive film breakdown. At potentials above $0.13\ V_{SCE}$ for the Cr6-MPEA and $0.40\ V_{SCE}$ for Ni-5Cr, $-Z''$ also

displayed a sudden decrease (**Fig. 3.10b**). The peaks in $-Z''$ are suggestive of formation of specific oxides given the specific oxide formation potentials shown in **Fig. 3.11**. However, there is not a direct correlation owing to kinetic factors such as the need for overpotentials.

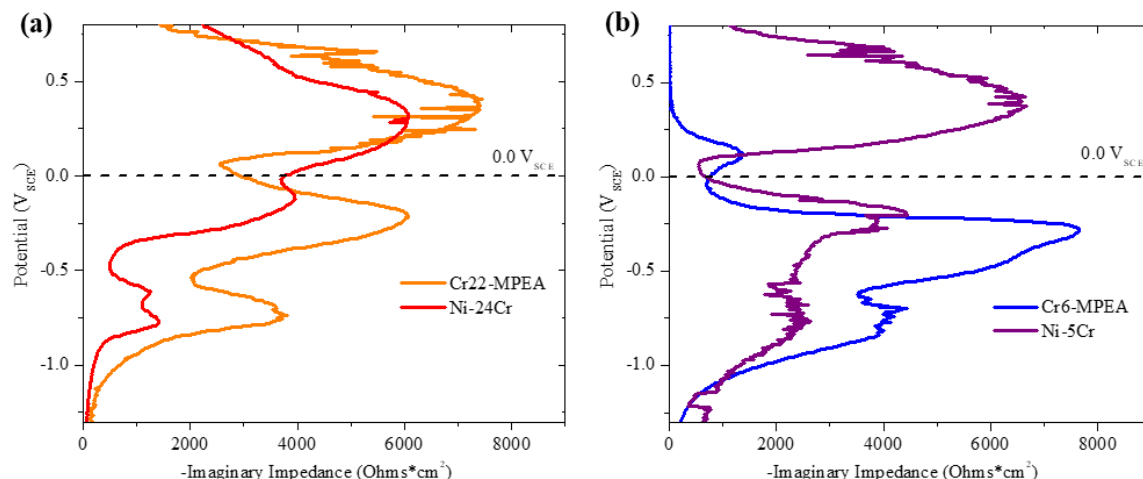


Fig. 3. 10. Potential vs. imaginary component of impedance ($-Z''$) at $f = \text{Hz}$ during LSV with 0.5 mV s^{-1} scan rate in $\text{N}_{2(g)}$ deaerated $1 \text{ mM NaCl} + \text{HCl}$ at $\text{pH } 4$ after initial cathodic reduction at $-1.3V_{\text{SCE}}$ for 600 s for (a) Cr22-MPEA versus Ni-24Cr, and (b) Cr6-MPEA versus Ni-5Cr.

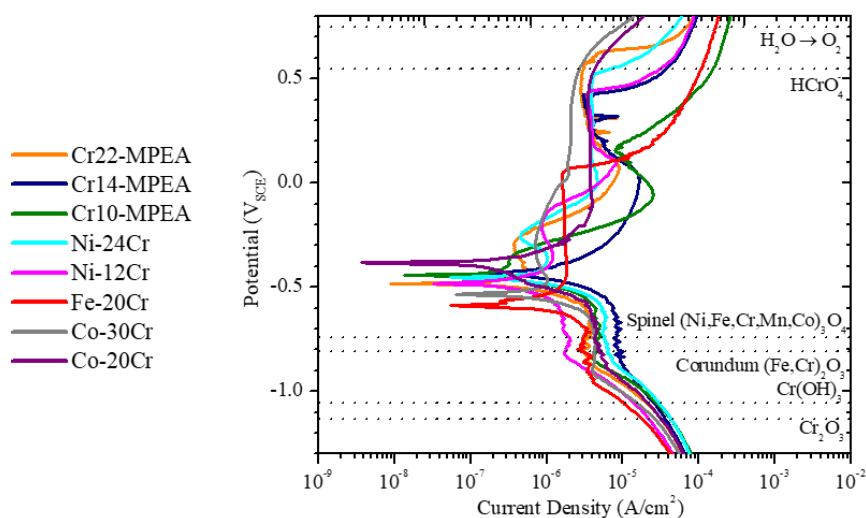


Fig. 3. 11. Linear sweep voltammetry in $\text{N}_{2(g)}$ deaerated $1 \text{ mM NaCl} + \text{HCl}$ at $\text{pH } 4$ after initial cathodic reduction at $-1.3 V_{\text{SCE}}$ for 10 mins for Cr22-MPEA, Cr14-MPEA, Cr10-MPEA, Ni-24Cr, Ni-12Cr, Fe-20Cr, Co-30Cr, and Co-20Cr. Horizontal dotted lines indicate potentials in which various oxides are predicted to be stable at $\text{pH } 4$. Oxide formation potentials were obtained from potential-pH stability diagrams retrieved from Wang et al. doi: 10.1038/s41529-020-00141-6.

The current densities in the passive potential domain at 0.0 V_{SCE} collected from LSV experiments for each alloy are summarized in **Fig. 3.12**. For each alloy class, the current density decreases with increasing Cr content in each testing solution. There is a large decrease in current density in 0.1 M NaCl between 10 and 20 % Cr for all alloys except Fe-Cr but exact threshold values cannot be determined. In 1 mM NaCl, all of the Cr-MPEAs and some binary alloys (Ni-Cr alloys at 10 and 5 at. % Cr, and all Co-Cr alloys) display similar current density ($\sim 10^{-4}$ A cm⁻²), as shown in **Fig. 3.12a**. The Fe-Cr binary alloys at 10 and 5 at. % Cr exhibited high current density values at 0.0 V_{SCE} (10^{-4} and 10^{-3} A cm⁻²) compared to all alloys in both 1 mM and 0.1 M NaCl, respectively. In 0.1 M NaCl the Cr22, Cr14, Cr10, and Cr6-MPEAs had lower current densities at 0.0 V_{SCE} than all the binary alloys, as shown in **Fig. 3.12b**. A noteworthy observation is that the Cr10-MPEA exhibited much lower current density (10^{-4} A cm⁻²) than any of 10Cr binary alloys, suggestive of superior protection.

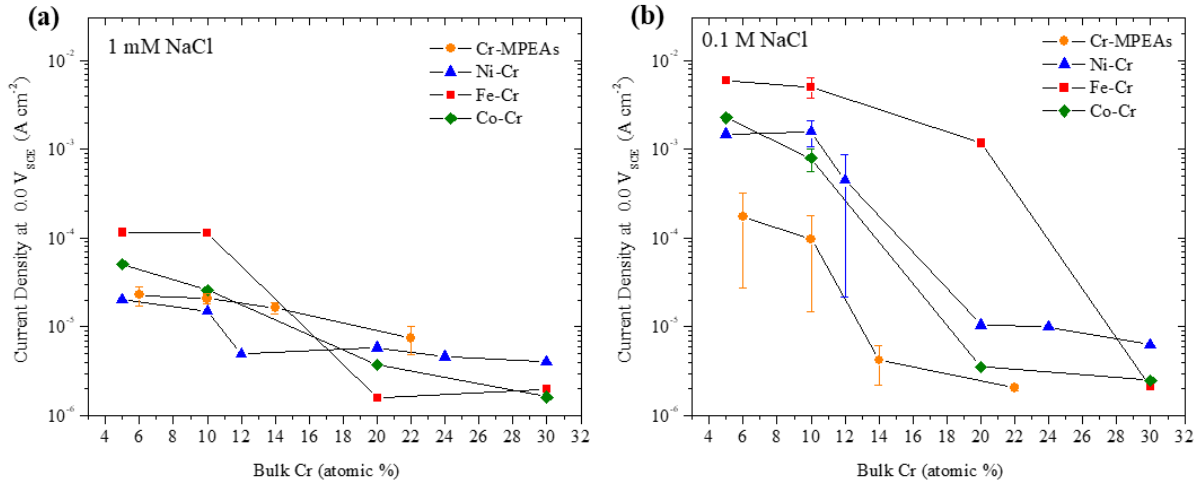


Fig. 3. 12. Comparison of current density versus bulk alloy Cr concentration at 0.0 V_{SCE} acquired from linear sweep voltammetry for Cr-MPEAs, Ni-Cr, Fe-Cr, and Co-Cr alloys in (a) N_{2(g)} deaerated 1 mM NaCl + HCl at pH 4 and (b) N_{2(g)} deaerated 0.1 M NaCl + HCl at pH 4. Standard errors bars were computed from repeated experiments.

3.4.2 Aqueous Oxidation at an Applied Passive Potential of 0.0 V_{SCE}

Passive current density decays during a potentiostatic hold at 0.0 V_{SCE} were utilized to characterize electrochemical passivation behavior. Current decays in 1 mM NaCl at 0.0 V_{SCE} for select alloys are shown in **Figs. 3.13** and **3.14**. Large decreases in the passive current density were observed for Cr22-, Cr14, Cr10-MPEAs, as well as Ni-24Cr, Ni-12Cr, Ni-10Cr, Fe-20Cr, Co-30Cr, and Co-20Cr during 10 ks potentiostatic hold (**Fig. 3.13**). The current density-time behavior was characterized by an initial plateau for $\sim 10^2$ seconds followed by a t^{-n} time dependency with n near 1. Metastable breakdown events were observed for most alloys as indicated by transient current density signal spikes, and more frequently for the Cr-MPEAs (**Fig. 3.13**). Similar current density profiles were observed initially for Cr6-MPEA and Co-10Cr binary alloy at 0.0 V_{SCE} in **Fig. 3.14**. The current densities of the Cr6-MPEA and Co-10Cr binary alloy initially decrease indicating passivation, then sharply increase at longer times, $t > 700$ s and 2800 s, respectively. This increase in current density at 0.0 V_{SCE} signals passive film breakdown leading to localized corrosion, which was confirmed by the observation of crevice corrosion after the 10 ks of potential hold. Similar inferior passivation results are observed for Fe-Cr and Co-Cr binary alloys containing 5 and 10 at. % Cr, which indicates relatively inferior breakdown protection attributed to passive films formed on these alloys. In contrast, the Cr10-MPEA and Ni-10Cr alloy showed clear evidence of sustained passivation indicated a continually decaying passive current density when held at the passive potential of 0.0 V_{SCE} as observed in **Fig. 3.13**.

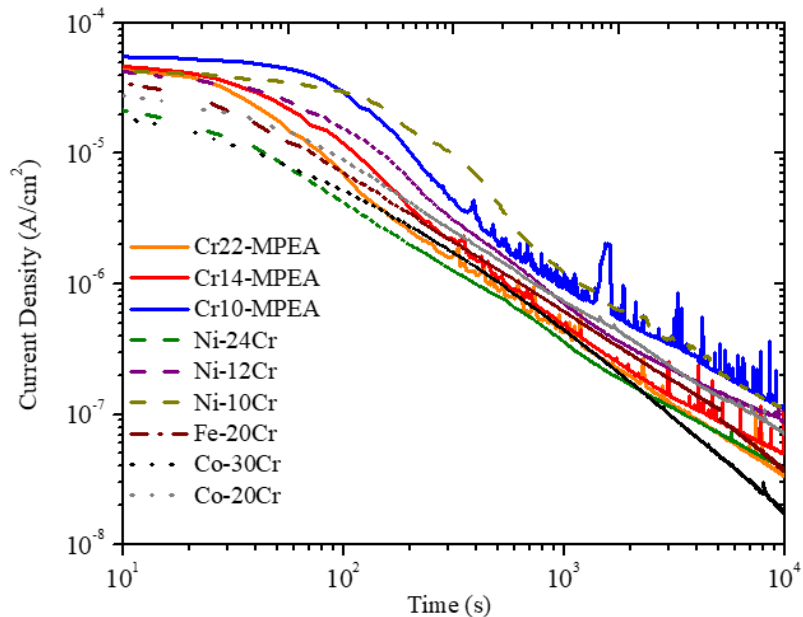


Fig. 3. 13. Measured electrochemical current density during potentiostatic hold at $0.0 V_{SCE}$ for 10 ks 4 after initial cathodic reduction at $-1.3V_{SCE}$ for 600 s in deaerated 1 mM NaCl + HCl at pH 4 of Cr22-MPEA, Cr14-MPEA, Cr10-MPEA, Ni-24Cr, Ni-12Cr, Ni-10Cr, Fe-20Cr, Co-30Cr, and Co-20Cr.

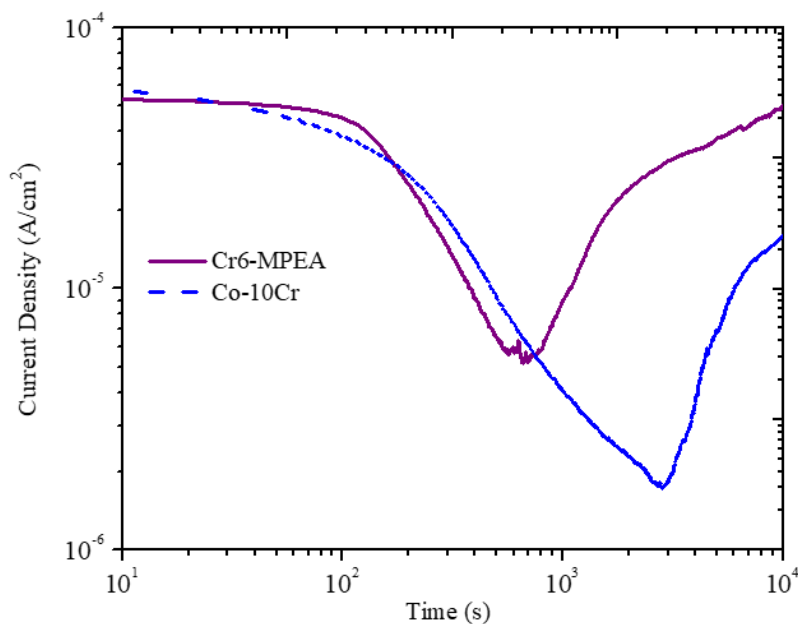


Fig. 3. 14. Measured electrochemical current density during potentiostatic hold at $0.0 V_{SCE}$ for 10 ks 4 after initial cathodic reduction at $-1.3V_{SCE}$ for 600 s in deaerated 1 mM NaCl + HCl at pH 4 of Cr6-MPEA and Co-10Cr.

Potentiostatic EIS was conducted at the end of the 10 ks hold at 0.0 V_{SCE} to monitor the impedance behavior of the film as well as to obtain the impedance properties of the corroding interface. The fitted EIS parameters are shown in **Table 3.2**. Bode plots for the selected alloys passivated at 0.0 V_{SCE} in 1 mM NaCl electrolyte are shown in **Fig. 3.15**. The Co-30Cr exhibited the highest low-frequency impedance magnitude of $10^6 \Omega \text{ cm}^2$ while the other alloys displayed magnitudes greater than $3 \times 10^5 \Omega \text{ cm}^2$. The high low-frequency impedance magnitudes for each alloy suggest the formation of a relatively protective passive film.

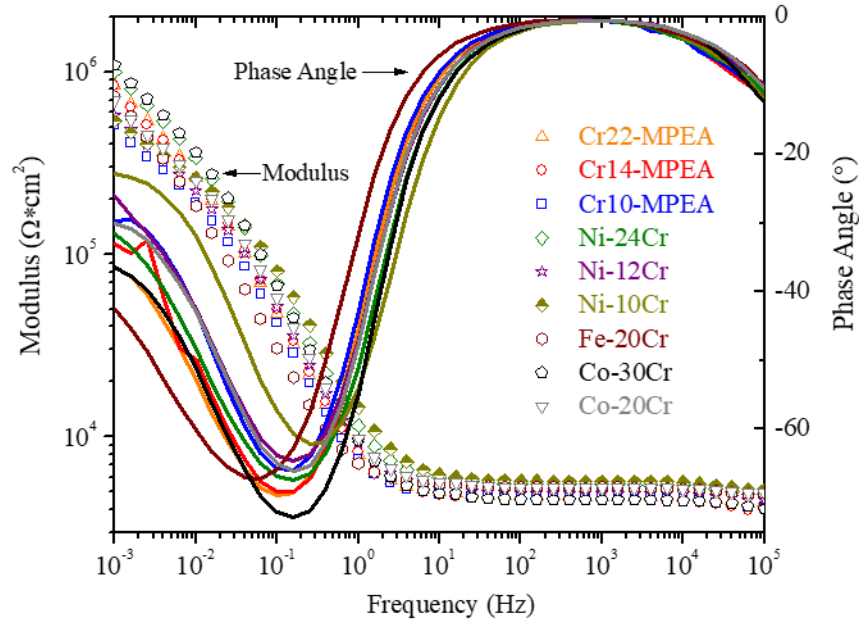


Fig. 3. 15. Bode plot of Cr22-MPEA, Cr14-MPEA, Cr10-MPEA, Ni-24Cr, Ni-12Cr, Ni-10Cr, Fe-20Cr, Co-30Cr, and Co-20Cr in deaerated 1 mM NaCl + HCl at pH 4 after potentiostatic hold at 0.0 V_{SCE} for 10 ks.

The calculated oxide thickness as a function of time for each passive film is plotted in **Fig. 3.16**. The passive film on the Cr22- and Cr10-MPEA grew towards a steady state thickness of approximately 4 nm after 10ks. The Cr22-MPEAs passive film formed at a faster rate than the low Cr-MPEAs as indicated by a thicker layer at earlier passivation times with Cr10-MPEA exhibiting the slowest growth rate. All Cr-MPEAs oxide thicknesses approached a steady state value after approximately 6000 s. Compared to the binary alloys, Fe-20Cr was estimated to have similar passive film thickness as Cr22- and Cr10-MPEA (~ 4 nm). All other binary alloys showed a slightly thicker calculated passive film than the Cr-MPEAs.

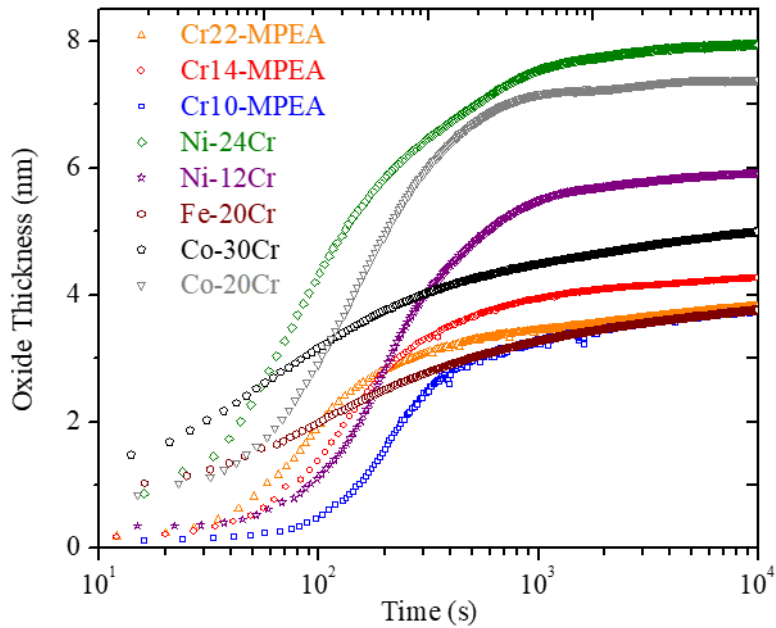


Fig. 3. 16. *In-situ estimation of oxide thickness for Cr22-MPEA, Cr14-MPEA, Cr10-MPEA, Ni-24Cr, Ni-12Cr, Fe-20Cr, Co-30Cr, and Co-20Cr during potentiostatic hold at 0.0 V_{SCE} for 10 ks in deaerated 1 mM NaCl + HCl at pH 4*

The total electrochemical charge, ion ejection charge ($q_{\text{total}} - q_{\text{ox}}$), and charge efficiency associated with passivation as a function of bulk Cr content for each passive film formed during 10 ks potential hold are shown in **Fig. 3.17**. The total electrochemical charge and ion ejection charge decreased as Cr content increased in all tested alloys (**Figs. 3.17a** and **3.17b**). The charge efficiency for passivation, computed from q_{total} and q_{ox} given by Eq. 1, increased with bulk Cr concentrations (**Fig. 3.17c**) and nearly approached 1 for 30% Cr alloys. The Cr-MPEAs and binary alloys follow the same trend with no distinction between MPEAs and binary alloys. Cr22-MPEA exhibited a lowered ion ejection charge and better efficiency than all other tested low Cr-alloys, as did the Ni-24Cr and Co-30Cr binary alloys. The Cr10-MPEA exhibited the highest ion ejection charge and lowest efficiency compared to all the other alloys, suggesting the greatest rate of ion dissolution to solution in contrast with joining the passive film among these alloys (**Fig. 3.17**). Ni-12Cr was the next highest in total electrochemical charge and ion ejection charge, and correspondingly the next lowest in efficiency. However, other low Cr alloys did not passivate and are therefore not included in this plot. It can be suspected that the trend for low efficiencies typical

of 5, 6 and 10 at. % Cr alloys produce conditions where passivation cannot be achieved on these alloys in this electrolyte.

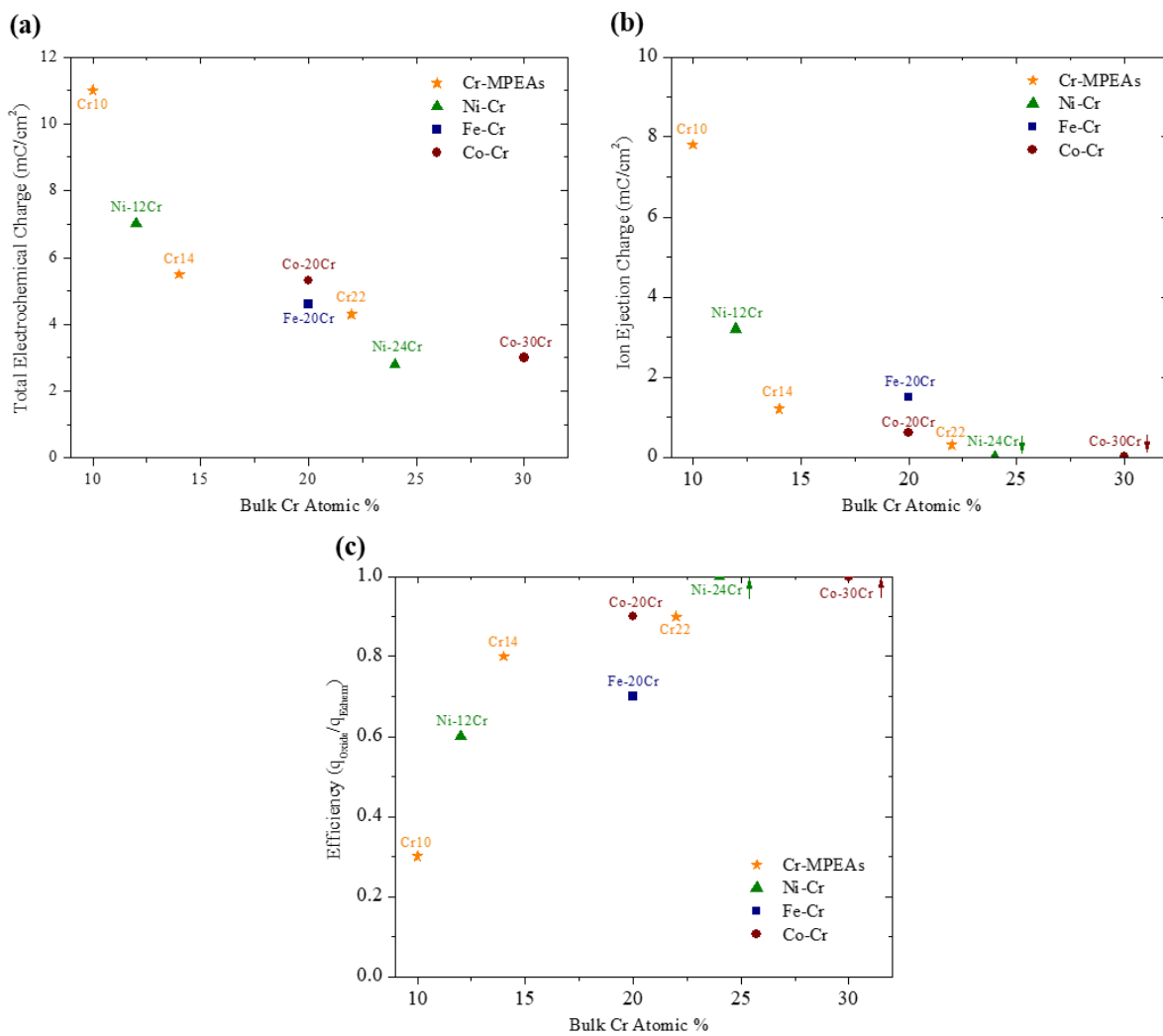


Fig. 3. 17. (a) Total electrochemical charge, (b) ion ejection charge, and (c) efficiency of passive films formed on Cr22-MPEA, Cr14-MPEA, Cr10-MPEA, Ni-24Cr, Ni-12Cr, Fe-20Cr, Co-30Cr, and Co-20Cr during potentiostatic hold at 0.0 V_{SCE} for 10 ks in deaerated 1 mM NaCl + HCl at pH 4. Values were estimated from measured current density and oxide thickness as a function of time.

3.4.3 AESEC during 10 ks Potentiostatic Hold at 0.0 VSCE for Co-20Cr

Fig. 3.18 shows the elemental dissolution profiles of in equivalent current densities of Co and Cr during passivation at 0.0 V vs. SCE following to a cathodic pulse at -1.3 V vs. SCE for 600 s in a 0.1 M NaCl, pH 4 deaerated solution. The non-dissolved species formation is indicated as $i_e \gg i_{Cr} + i_{Co}$, assuming that cathodic contribution is negligible at this potential. The Cr dissolution was under the detection limit whereas Co showed an initial dissolution transient. This result is in agreement with the thermodynamic simulation at this potential at pH 4 [35] where no soluble Cr(III) or Cr(II) and soluble Co(II) were predicted. It may indicate that the non-dissolved Cr contributed to form Cr-based oxides/hydroxides, confirmed by the XPS result discussed below.

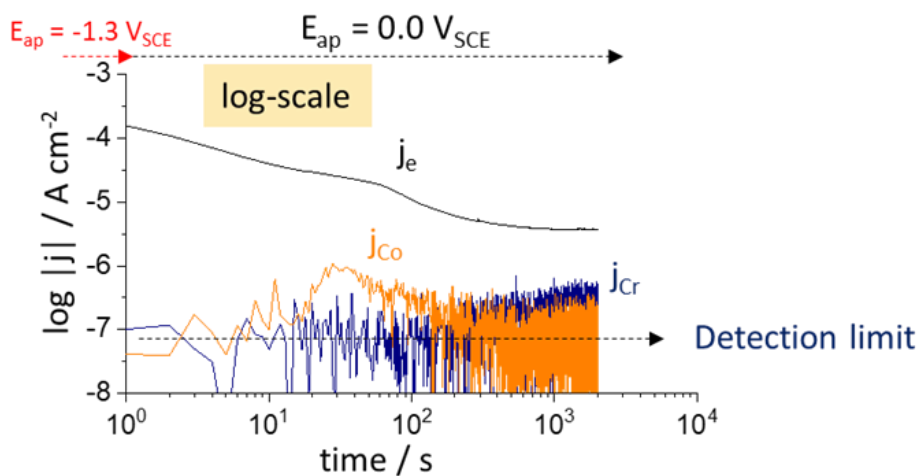


Fig. 3. 18. Atomic emission spectroelectrochemistry of Co-20Cr during potentiostatic hold at 0.0 V_{SCE} for 10 ks in deaerated 1 mM NaCl + HCl at pH 4 after initial cathodic reduction at -1.3 V_{SCE} for 600 s.

3.4.4 Oxide Valence State and Cation Fractions Identified by XPS

The chemical states and composition of the electrochemically formed passive films on the Cr-MPEAs and binary alloys were determined by XPS and are summarized in **Table 3.6**. Overall, all passive films contain a large amount of Cr(III), present as both oxide and hydroxide. The Cr-MPEAs passive films consisted mainly of Cr(III) and small amounts of Ni(II) and Fe(II) species. . Mn(II), Mn(III), and Co(II) $2p_{1/2}$ signals were not evident above the detection limit, suggesting that the Mn and Co species are either present in the oxides at very low levels or are not oxidized. This upper limit for Mn, ≤ 0.06 cation fraction, remains similar throughout the Cr-MPEA series even though the bulk Mn concentration increases with decreasing bulk Cr (**Table 3.6**). Conversely, the Co upper limit increases with decreasing bulk Cr concentrations. The Fe cation fraction remained constant for each Cr-MPEA. The Ni cation fraction of 0.07 was lowest in the Cr22-MPEA and increases to 0.14 for Cr14- and Cr10-MPEA. Cr22-MPEA exhibited a higher Cr concentration in the oxide/hydroxide passive layer compared to the binaries Fe-20Cr, Ni-24Cr, and Ni-12Cr. The Co-30Cr and Co-20Cr had the highest Cr cation fraction of 0.93 and 0.89, respectively. This result agrees with the elemental *in-situ* elemental dissolution profile of Co-20Cr, investigated by atomic emission spectroelectrochemistry (AESEC) technique. During passivation at 0.0 V_{SCE} for 10 ks, Cr dissolution was below the detection limit whereas Co showed an initial dissolution transient (these results are shown in the **Fig. 3.18**). These AESEC observations are in agreement with XPS findings in which passive films formed on Co-Cr binary alloys were primarily Cr(III) species (**Table 3.6**).

The elemental fractions within the altered metal zone beneath the passivating film were also determined by XPS, as shown in **Table 3.6**. The Cr-MPEAs and Ni-Cr binary alloys exhibited an enrichment of Ni with respect to bulk Ni concentrations. The Cr elemental fraction in the altered zone was similar to the bulk concentration for the Cr22- and Cr14-MPEAs, with elemental fractions of 0.25 and 0.16, respectively. In the case of the Cr10-MPEA, a clear depletion of Cr was observed with an elemental fraction of 0.04. Depletion of Fe, Mn, and Co was also observed in the altered zone for each Cr-MPEA (**Table 3.6**). The simpler binary alloys had Cr concentrations similar to their bulk Cr concentrations within the altered zone (**Table 3.6**).

Table 3. 6. All cation and elemental fractions detected by XPS for passive films formed at 0.0 V_{SCE} for 10 ks in 1 mM NaCl + HCl pH 4 N_{2(g)} deaerated solution and within the altered zone.

Alloy	Passive Film Cation Fraction					Altered Zone Elemental Fraction				
	Ni(II)	Fe(II)	Cr(III)	Mn(II)	Co(II)	Ni	Fe	Cr	Mn	Co
Cr22-MPEA	0.07	0.07	0.8	0.02*	0.04*	0.57	0.12	0.25	0.03*	0.03*
Cr14-MPEA	0.14	0.07	0.71	0.02*	0.06*	0.64	0.13	0.16	0.03*	0.04*
Cr10-MPEA	0.14	0.07	0.70	0.01*	0.08*	0.77	0.06	0.04	0.06*	0.07*
Fe-20Cr	--	0.23	0.77	--	--	--	0.82	0.18	--	--
Co-30Cr	--	--	0.93	--	0.07	--	--	0.28	--	0.72
Co-20Cr	--	--	0.89	--	0.11	--	--	0.20	--	0.80
Ni-24Cr	0.27	--	0.73	--	--	0.74	--	0.26	--	--
Ni-12Cr	0.31	--	0.69	--	--	0.89	--	0.11	--	--

*Assuming max allowed Mn and Co fractions consistent with XPS 2p_{1/2} signal.

Deconvolution of the XPS spectra was performed and the resulting fits are shown in **Fig. 3.19**. The observed binding energies were consistent with the oxidation states Ni(II), Cr(III), and Fe(II) for all Cr-MPEAs. The passive films for all of the alloys consisted of primarily of hydrated Cr(III) rather than anhydrous Cr(III) (i.e., Cr(OH)₃ versus Cr₂O₃, respectively) as shown in **Table 3.4**. This is in agreement with O 1s spectra for each alloy, in which a large intensity for the hydroxide feature was observed (**Fig. 3.19**). The hydroxide species was observed as the majority of the Cr(III) and Ni(II) cations. The Co-30Cr contained the largest fraction of anhydrous Cr(III) (0.24) with all other alloys having fractions ≤ 0.11 (**Table 3.4**). The Cr-MPEAs also contained a small fraction of Cr(III) whose best fit was associated with Cr-spinels such as (NiCr₂O₄ and/or FeCr₂O₄), unlike the passive films of the binary alloys (**Fig. 3.19 and Table 3.4**).

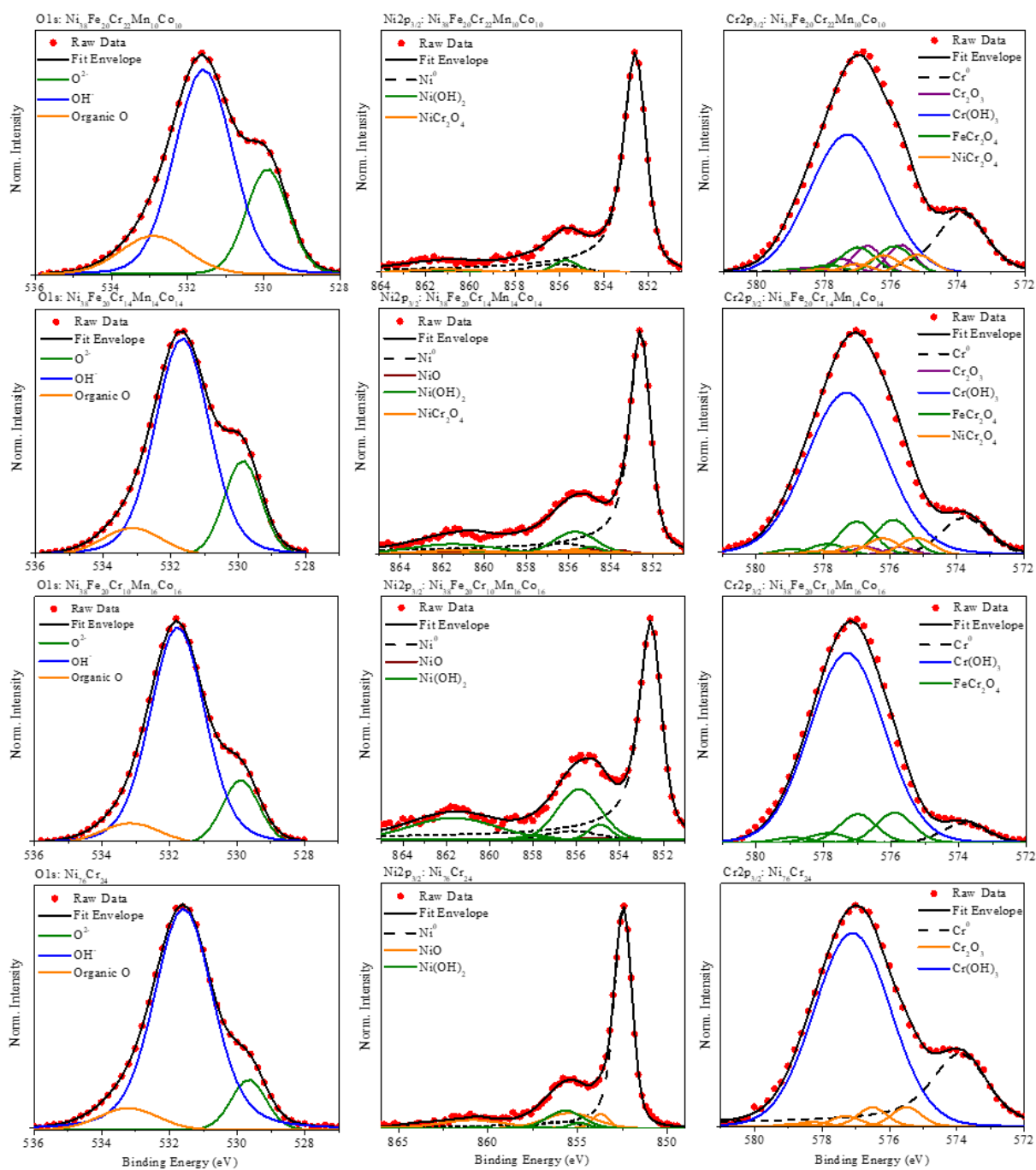


Fig. 3. 19. XPS spectral deconvolution of O 1s, Ni 2p_{3/2}, and Cr 2p_{3/2} core level for the passive films formed during step-potentiostatic oxide growth at 0.0 V_{SCE} for 10 ks in deaerated 1 mM NaCl + HCl at pH 4 on Cr22-, Cr14-, Cr10-MPEA, Ni-24Cr, Ni-12Cr, Fe-20Cr, Co-30Cr, and Co-20Cr.

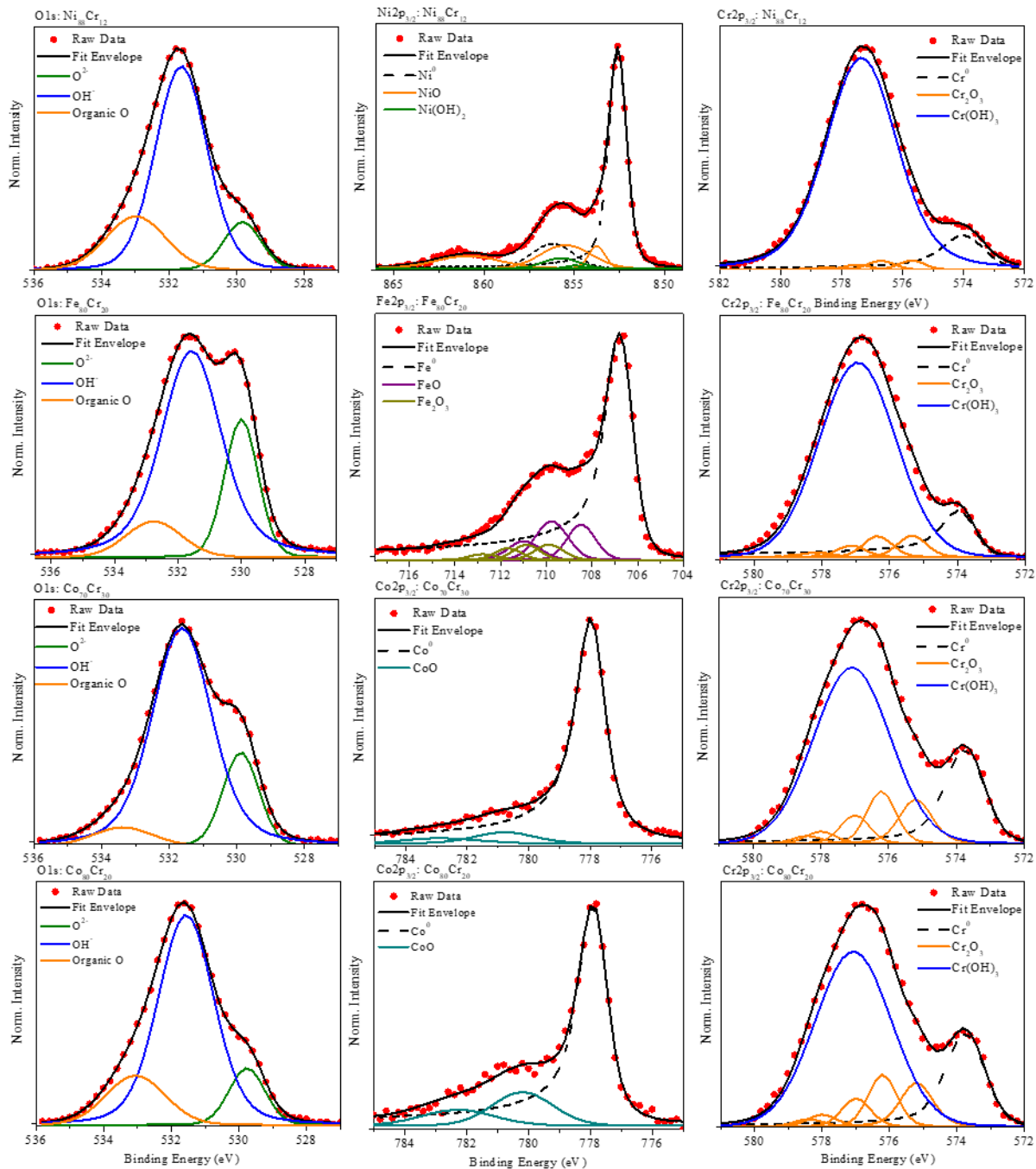


Figure 3.19 continued. XPS spectral deconvolution of O 1s, Ni 2p_{3/2}, and Cr 2p_{3/2} core level for the passive films formed during step-potentiostatic oxide growth at 0.0 V_{SCE} for 10 ks in deaerated 1 mM NaCl + HCl at pH 4 on Cr22-, Cr14-, Cr10-MPEA, Ni-24Cr, Ni-12Cr, Fe-20Cr, Co-30Cr, and Co-20Cr.

3.4.5 Passive Film and Interface Compositions from APT

To better understand the elemental distribution within the electrochemically formed passive film and within the altered zone (i.e., metal/film interface), APT was performed on Cr10-MPEA, Cr22-MPEA, Co-20Cr and Fe-20Cr after potentiostatic passivation in deaerated 1 mM NaCl + HCl at pH 4. Results on the latter three alloys are reported as experimental information (**Fig. 3.1-3.3 and 3.4-3.7**). Concerning the Cr10-MPEA, good agreement between XPS and APT is seen. A large enrichment of Cr ($0.68 \leq \text{Cr fraction}$) is observed in the outer layer (i.e., from 1.10 to 4.50 nm) of the passive film shown in **Fig. 3.20**, similar to the XPS results (**Table 3.6**). A depletion of Mn ($0.04 \leq \text{Mn fraction}$) is observed within the inner oxide and altered metal zone (-1.90 to 1.10 nm). In the outer oxide, the Mn elemental fraction increases up to 0.21 initially but then decreases to 0.08. Overall, this is consistent with XPS results (**Table 3.6**). Enrichment of Ni is observed within the altered zone and inner oxide ($0.50 \leq \text{Ni fraction}$). The elemental fraction of Ni begins to decrease throughout the inner and outer oxide, also consistent with XPS (**Table 3.6**). Slight depletion of Cr ($0.09 \leq \text{Cr fraction}$) and Mn ($0.06 \leq \text{Mn fraction}$) is indicated within the altered zone as their fractions were lower than the nominal alloy values.

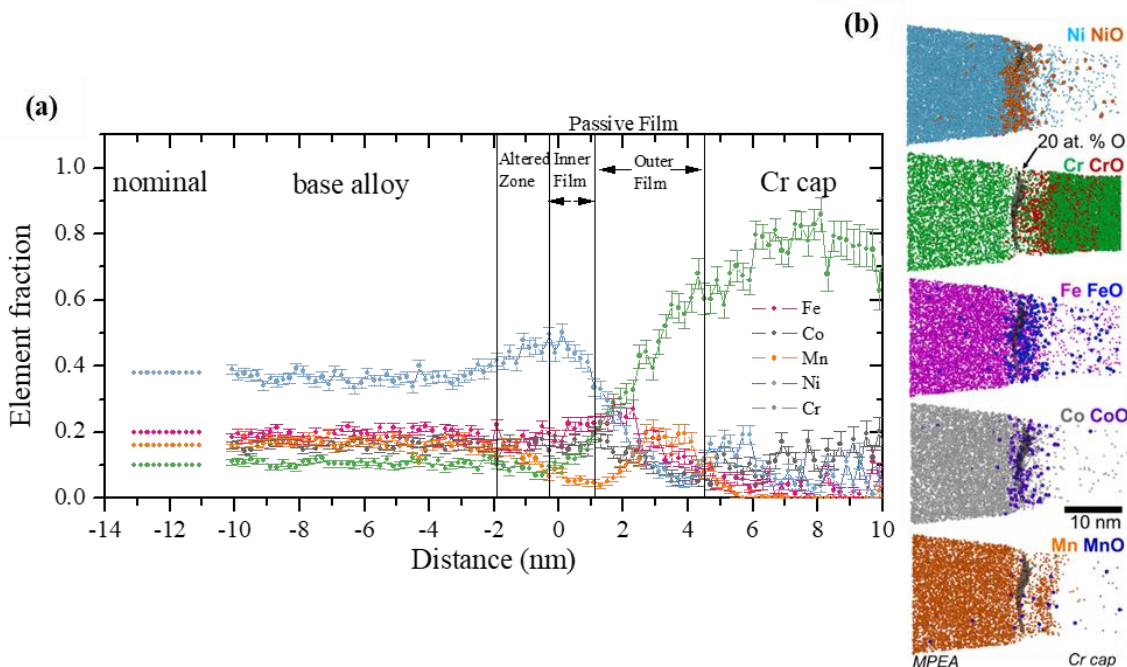


Fig. 3. 20. (a) APT concentration profile and (b) element distribution maps of the Cr10-MPEA electrochemically formed passive film during potentiostatic hold at 0.0 V_{SCE} for 10 ks in deaerated 1 mM NaCl + HCl pH 4. The concentration profile in (a) was determined using a proximity histogram across a 20 at.% O isoconcentration surface with a bin width of 0.2 nm. The 3D element distribution maps given in (b) show elemental and corresponding molecular species (e.g., Ni, NiO) present in the film and base alloy. All maps are for a 10 nm thick region of interest through the center of the reconstructed volume.

3.4.6 Passive Film and Altered Zone Alloying Element Enrichment and Depletion Factors

Cr enrichment and depletion terms within the electrochemically formed passive film ($f_{Cr,ox}$) and altered zone ($f_{Cr,az}$) for each MPEA and binary alloy is summarized in **Fig. 3.21**. **Figure 3.21** shows f_{Cr} for both the altered zone (red symbols) and passive film (black symbols) as a function of the bulk Cr alloying content. The passive film $f_{Cr,ox}$ values indicated similar Cr enrichment for all alloys at high bulk Cr content except for the case of the Fe-20Cr binary. The $f_{Cr,ox}$ ranged from 3.6 to 7.0 under the conditions described above. The enrichment term, $f_{Cr,ox}$ is larger in the low-Cr containing alloys but this is also observed for both the MPEA and the binary alloys with the same or similar trend. Notably, Cr10-MPEA exhibited the highest Cr enrichment term ($f_{Cr,ox} = 7.0$). The binary alloys follow the same trend as the MPEAs but do not exceed an $f_{Cr,ox}$ of 5.7. For example,

Ni-12Cr has a higher bulk Cr content than Cr10-MPEA but shows a lower passive film $f_{Cr,ox}$ value of 5.7 compared to 7.0. The elemental $f_{Cr,az}$ within the altered zone did not change in any perceptible manner which can be discerned, with the exception of Cr10-MPEA. The Cr10-MPEA had the largest depletion of Cr with an $f_{Cr,az}$ of 0.4 within the altered zone.

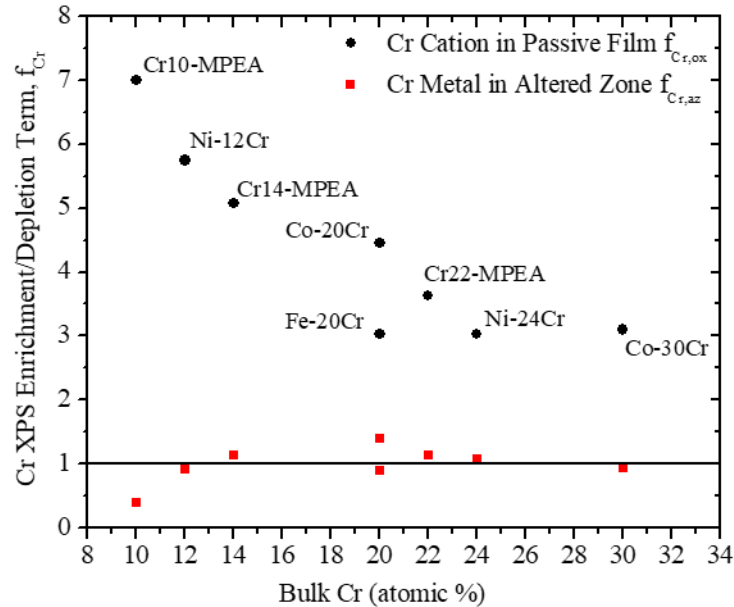


Fig. 3. 21. XPS Cr enrichment/depletion factor (f_{Cr}) for both Cr cations within the passive film ($f_{Cr,ox}$) and elemental Cr within the altered zone ($f_{Cr,az}$) (i.e., metal/oxide interface).

From enrichment and depletion terms, the expected Cr concentration within the passive film and altered zone as a function of various bulk Cr concentrations are shown in **Fig. 3.22**. The enrichment or depletion of Cr is indicated by lines above or below the dashed line. The dashed line corresponds to the condition when the Cr concentration within the passive film (X^{ox}) is equal to the bulk Cr content (X^S). Both XPS and APT enrichment curves predict Cr enrichment in the passive film and slight depletion in the altered zone. XPS enrichment curves predict a higher Cr concentration than APT (**Fig. 3.22**), which could be due to the low Cr concentration observed within the inner oxide (**Fig. 3.20**). Experimental cation fractions for binary alloys (**Table 3.6**) were plotted and compared to the computed MPEA enrichment and depletion curves. The Co-Cr binary alloys were above the enrichment curve while the Ni-Cr and Fe-Cr alloys were slightly below. Further work would be needed to clarify the behavior of Cr10-MPEA.

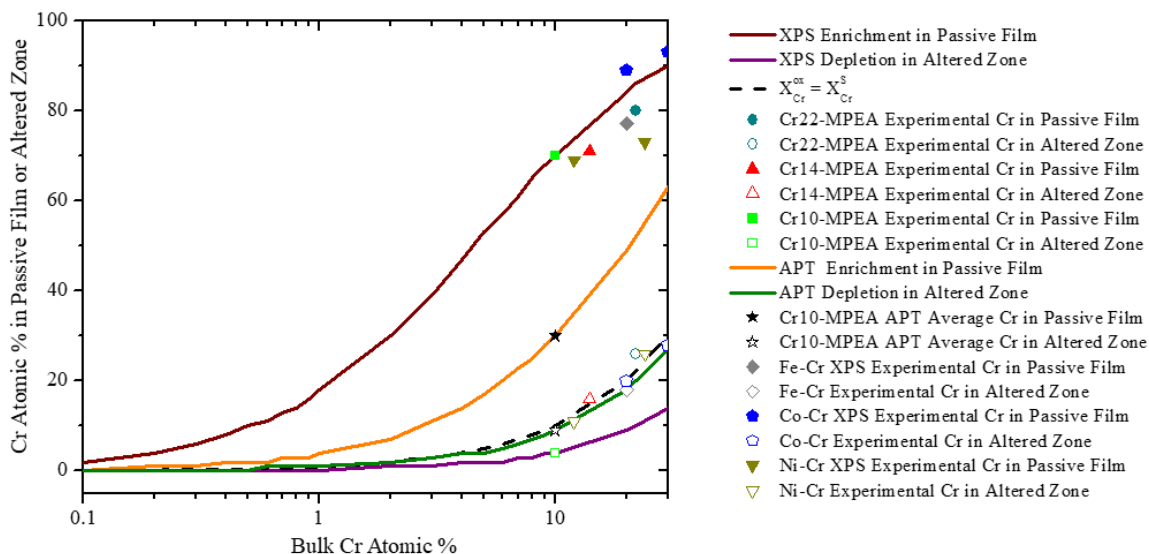


Fig. 3. 22. Enrichment and depletion predictions for Cr in the altered zone and passive films formed on $Ni_{38}Fe_{20}Cr_xMn_{21-0.5x}Co_{21-0.5x}$, where $x = 22, 14,$ and 10 . The black dotted line is the ideal condition in which the Cr oxide concentrations is equal to the bulk Cr concentration ($X^{ox} = X^S$). Above this dotted line Cr is to be enriched and below Cr is depleted. Hypothetical enrichment and depletion curves were based from experimental XPS and APT Cr enrichment terms obtained using Castle's method

A hypothetical mass transport controlled Cr depletion zone depth for the Cr22-MPEA, Cr10-MPEA, Ni-24Cr, Fe-20Cr, and Co-20Cr binary alloys is shown in **Fig. 3.23**. Alloys are particularly shown to exhibit a larger depletion zone when the charge efficiency is less than 100%. At high charge efficiencies, a depletion zone of below a single atomic layer might be expected. This phenomenon is represented in **Fig. 3.24**, where charge efficiency (ion dissolution) is represented as pink arrows and correlate to a certain Cr depletion zone depth in pink, called the altered zone. However, at efficiency values of 1.0 to 0.4, a depletion zone on the order of 0.3-2.5 nm is evident. The Cr22- and Cr10-MPEA showed a similar hypothetical depletion profile as the 20 at. % Fe-Cr and Co-Cr binary alloys (**Fig. 3.23**). The Ni-24Cr alloy is predicted to have the largest depletion zone at equivalent oxide efficiencies compared to the other alloys. This is likely due to the thicker Ni-24Cr passive film (~8 nm at the end of the experiment in **Fig. 3.16**) compared to the other alloys and relatively high Cr content. Thus, no special difference in the depletion zone in MPEAs versus binary allows is suggested from this analysis, nor seen in APT nor XPS analysis and thus no difference in Cr oxide enrichment as a result of an altered zone can be claimed. It is noted that

more sluggish diffusion would render enrichment more difficult and would favor a depletion profile while faster diffusion would replenish depletion profiles and aid Cr enrichment.

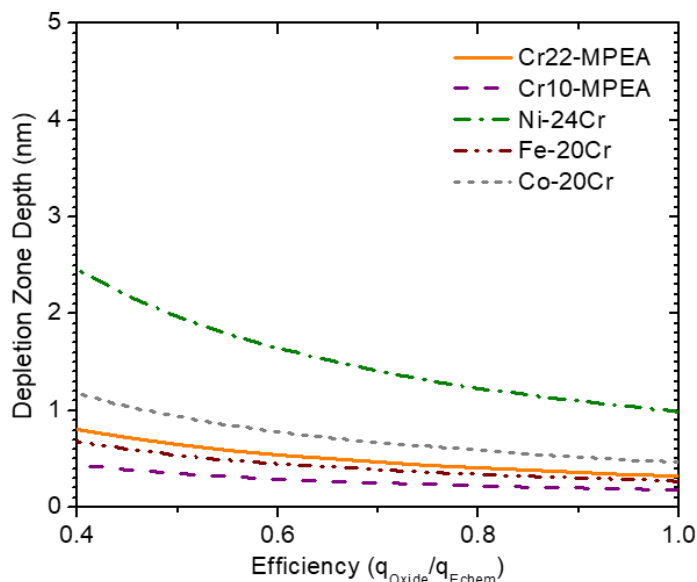


Fig. 3. 23. Hypothetical depletion zone considering conservation of mass using experimental XPS data and bulk elemental concentrations.

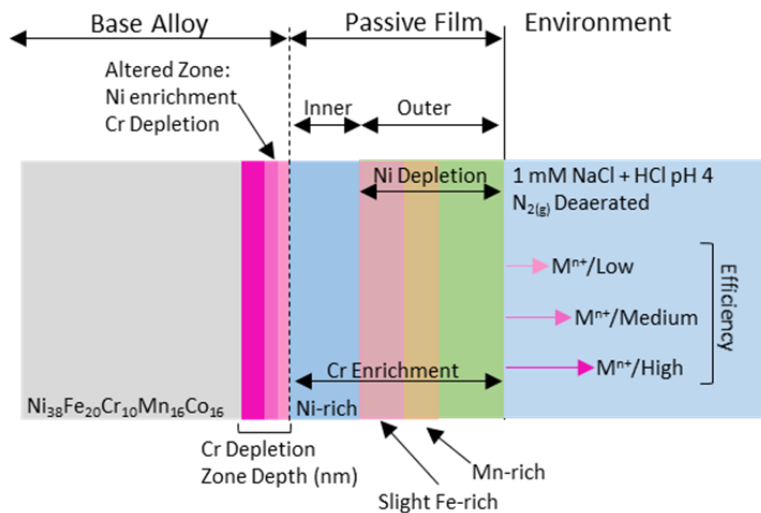


Fig. 3. 24. Schematic of passive film and altered zone at or below the metal/film interface as a function of charge efficiency for Cr10-MPEA. Passive film enrichment and depletion within the inner and outer regions were correlated to the APT concentration profile for the Cr10-MPEA electrochemically formed passive film during potentiostatic hold at 0.0 V_{SCE} for 10 ks in deaerated 1 mM NaCl + HCl pH 4.

3.5 Discussion

3.5.1 Thermodynamics and Kinetics of Aqueous Passivation of Cr-MPEAs and Binary Alloys

In transition metals or “d-block” (i.e., Cr, Mn, Fe, Co, Ni) MPEAs and binary alloys containing Cr and subjected to moderately oxidizing conditions, all alloying elements can be assumed to exist in an oxidized but metastable state when exposed to moderate potentials such as $0.0 V_{SCE}$, when the environment is slightly acidic [35, 61]. In this study, alloys above 10 at. % Cr showed clear passivation behavior and binary alloys at 5, 6, and 10 at. % Cr did not by the criterion of passivation over 10 ks at $0.0 V_{SCE}$ (**Fig. 3.8, 3.13 and 3.14**). 10Cr-MPEA was an exception that remained passive after 10ks potentiostatic hold at $0.0 V_{SCE}$ experiment while the 10 at. % Cr binary Fe-Cr and Co-Cr alloys were not passive (**Fig. 3.8 and 3.14**). The oxide on the 10Cr-MPEA is quite complex (**Fig. 3.20 and Figs. 3.1 and 3.4**) with possible phase separated layers and/or solid solutions. However, despite this, the Cr(III) enrichment is similar to that of binary alloys. In this study, both d-block non-equiatomic MPEA and all binary alloys with Cr solute exhibited Cr enrichment with Cr(III) enrichment term (f_{Cr}) ranging from 3 to 7 (**Fig. 3.21**), and the resulting Cr cation fraction within the oxide exceeded 0.6 in all alloys (**Table 3.6**). No special effect was indicated in Cr-MPEAs relative to binaries except the finding that Fe-Cr was less enriched. Moreover, other elements were not present in the oxide film or were sparingly present in the inner layer or outer layer (**Table 3.6**).

Predicting which species will reside in the passive film and which will dissolve into solution during aqueous passivation using thermodynamics and kinetic indicators is difficult when multiple elements are considered. Thermodynamic predictions can be made by utilizing oxide formation energies and potential-pH stability diagrams [35, 61]. Without direct consideration of potential and pH and other factors, limited insights can be gained from formation energies. Thermodynamic oxide/hydroxide/spinel formation energies suggest multiple oxides could exist, such as $NiCr_2O_4$ (-1269.1 kJ/mol [78]), Cr_2O_3 (-1058 kJ/mol), $Cr(OH)_3$ (-1064 kJ/mol), NiO (-211.7 kJ/mol), $Ni(OH)_2$ (-447.3 kJ/mol), Fe_2O_3 (-742.2 kJ/mol), CoO (-214 kJ/mol), MnO (-362.9 kJ/mol), and $FeCr_2O_4$ (-1343.8 kJ/mol) [79]. Because of their more negative free energies of formation, it can be expected that Cr-based oxides are more thermodynamically favored than stoichiometric Ni, Fe,

Co and Mn oxides. They also would have a high driving force to form when considering the potential that might be established by a passivating cathodic reaction [80]. This is supported by the XPS studies of MPEA passive films, where Cr-hydroxides and Cr-spinel features are more pronounced compared than Ni-oxides and Ni-hydroxides (**Fig. 3.19**). Unfortunately, these predications are limited because third element effects, formation of solid solution oxides on a host lattice, kinetic limitations, and preferential and/or selective dissolution are not factored into the analysis [14, 17, 81-84].

Utilizing potential-pH stability diagrams considering a solid solution, further predications can be made in which solid solution oxides and dissolution of alloying elements should be considered. Wang et al. constructed potential-pH stability diagram of both stoichiometric and non-stoichiometric oxides for the $\text{Ni}_{38}\text{Fe}_{20}\text{Cr}_{22}\text{Mn}_{10}\text{Co}_{10}$ MPEA [35]. At 0.0 V_{SCE} in 0.6 m NaCl pH 4 environment, the following are predicted to be stable: stoichiometric Fe_2O_3 , Cr_2O_3 and a non-stoichiometric spinel and corundum solid solution oxide containing Fe and Cr (**Fig. 3.11**). Under the same conditions, all alloying elements are also predicated to be present as aqueous species in the electrolyte as Ni(II), Fe(II), Cr(III), Mn(II), and Co(II) ions [35]. In this work, XPS deconvolution indicates the following oxides have formed: Cr_2O_3 , $\text{Cr}(\text{OH})_3$, FeCr_2O_4 , and NiCr_2O_4 (**Fig. 3.19**). Thermodynamics cannot forecast the results observed; although the potential-pH [35] approach offers the best hope. More factors must be considered to deal with the complexity of the system.

Solid solution oxides or complex oxides containing two or more elements are hard to detect experimentally via XPS because of uncertainty in the binding energies of core level electrons after a photoelectron is formed. These phases cannot be independently confirmed by XPS without structural information. Previous investigations of Cr22-MPEA have shown similar results at a more negative potential (-0.25 V_{SCE}) in 0.1 M NaCl pH 4 [54]. In that work, AESEC investigations on Cr22-MPEA showed congruent dissolution of Ni, Fe and Co and non-congruent dissolution of Cr and Mn at a passive potential of -0.25 V_{SCE} [54]. In the present work, low oxide concentrations of Ni, Fe, Co, and Mn compared to Cr were characterized by XPS (**Fig. 3.19**) and APT (**Fig. 3.20**) after a potentiostatic hold experiment at 0.0 V_{SCE} in 1 mM NaCl pH 4 electrolyte. This result suggests that these elements have dissolved into the solution, which is consistent with the above thermodynamic predictions and previous Cr22-MPEA investigations [32, 54].

This behavior is expected. Consider pure metals and their passive behavior when polarized in a slightly acidic Cl^- aqueous environment. When polarized to positive potentials, Cr and Ni commonly show a passive potential region approximately between -0.5 to 0.5 V_{SCE} whereas Fe, Mn, and Co undergo active corrosion (i.e., no passive region), shown in **Fig. 3.25**. If the passive behavior of an MPEA is similar to the pure metal tendencies, then it would be predictable that the passive species (Cr, Ni) are enriched within a MPEA passive film. With this assumption, a correlation could be made between the stationary current density at the passive electrode potential of pure metals. Enrichment or depletion within oxide film can be estimated by **Eq. 3.2**;

$$f_{\text{Cr}} = \frac{i_{\text{ss},Y}}{i_{\text{ss},\text{Cr}}} \quad (3.2)$$

where $i_{\text{ss},Y}$ is the stationary current density at 0.0 V_{SCE} for the solvent element (considered to be pure Ni for the Cr-MPEAs) and $i_{\text{ss},\text{Cr}}$ is the stationary current density of pure Cr at 0.0 V_{SCE} [82]. If the stationary current density of pure Cr is low and it is significantly higher in the other alloying elements, then enrichment occurs by the dissolution of the other alloying elements. This phenomenon could contribute to the low amounts of Fe, Mn, and Co within the passive films formed on the MPEAs at 0.0 V_{SCE} (**Table 3.6**). When polarized in deaerated 1 mM NaCl pH 4, pure Cr and Ni show passive potential regions with Cr possessing the lower passive current density at 0.0 V_{SCE} ($\sim 2 \times 10^{-6}$ and 1×10^{-5} A cm^{-2} , respectively), (**Fig. 3.25**). In the case of pure Fe, Mn, and Co, no clear passive potential region is observed and current densities are much higher ($\sim 5 \times 10^{-5}$ to 10^{-4} A cm^{-2}) than Cr and Ni. These stationary current densities all suggest Cr should be enriched within the passive film, and Fe, Mn, and Co are expected to dissolve into solution. This is indeed observed when considering the Cr22- and Cr14-MPEA passive film cation fractions (**Table 3.6**).

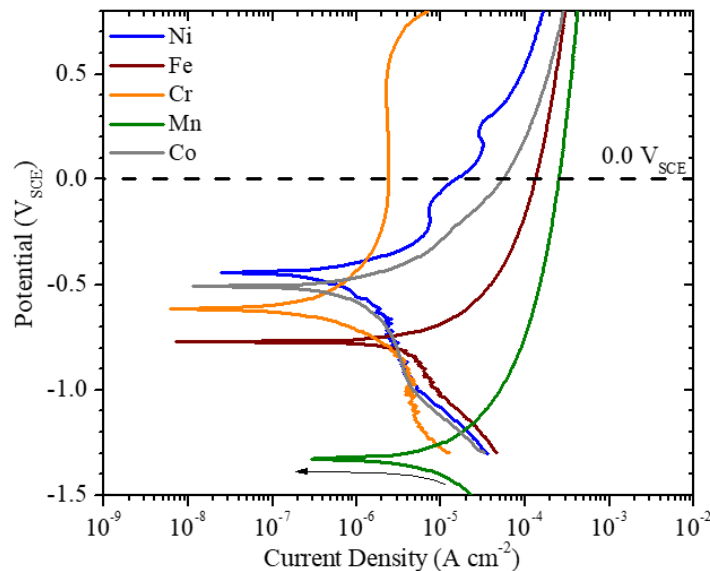


Fig. 3. 25. Linear sweep voltammetry in $N_{2(g)}$ deaerated 1 mM NaCl + HCl electrolyte at pH 4 after initial cathodic reduction at $-1.3 V_{SCE}$ for 600 s for Pure Ni, Fe, Cr, Mn, and Co

3.5.2 Other Factors Controlling Cr Enrichment and Depletion

An important question to address is what other factors limit Cr enrichment within the passive film? Kinetics are important because all alloying elements have a thermodynamic tendency for oxidation when these alloys are exposed in an oxidizing solution and this is not a discriminating factor. Meanwhile, non-congruent oxidation and chemical dissolution are likely and Cr enrichment may be enhanced by this process without theoretical limit. Moreover, the process of enriching from less than 10 at. % Cr in the alloy towards more than 60 cation % in a nm thick passive film also supports an unproven notion of fast transport in the solid solution. Cr must be supplied through the altered zone. Cr buildup in the passive film will also be influenced by inefficient Cr oxide formation (**Fig. 3.17** and **3.23**), considering that any Cr that dissolves into solution cannot contribute to oxide enrichment (**Fig. 3.24**). This effect can be observed in **Fig. 13.23**, which shows the effect of low charge efficiency on the formation of a depletion zone or altered zone below the passive film. Of the selected alloys passivated at $0.0 V_{SCE}$, the Cr10-MPEA showed high Cr enrichment within the passive film, as well as depletion of Cr within the altered zone calculated

from XPS and APT (**Fig. 3.19** and **3.20**), and low efficiency. These factors can limit Cr enrichment.

From XPS Cr enrichment and depletion factors ($f_{Cr,ox}$ and $f_{Cr,az}$), a comparison of enrichment or depletion within the altered zone can be made amongst both the binary alloys and MPEAs after electrochemical passivation (**Fig. 3.21**). The Cr10-MPEA showed a depletion of Cr within the altered zone, whereas Cr depletion could not be detected via XPS in other alloys (**Fig. 3.21** and **Table 3.6**). Besides the depletion argument which is not informed by enough data to conclude that it limits Cr enrichment in the passive film, the best argument for enrichment is that it is enabled by selective dissolution of other alloying elements during potentiostatic passivation at 0.0 V_{SCE} [21, 27, 28, 32, 51].

From the kinetic viewpoint, Fe, Co, and Mn are likely selectively depleted in the tested condition [54]. If these alloying elements are selectively dissolved, then Cr is left behind eventually creating “clusters” of Cr, available to be oxidized and inter-connected. The availability of these Cr clusters to form will depend on the bulk alloy Cr concentration, solid state diffusion, surface diffusion, ordered, random or clustered Cr and how likely other alloying elements will dissolve into solution [21, 28]. For random solid solutions at Cr bulk concentrations ≥ 14 at. % and Mn and Co bulk content of ≤ 14 at. %, there is an increase in the probability of Cr atoms surrounding each other rather than being surrounded by Mn or Co atoms. At bulk Cr concentrations ≤ 10 at. %, and Mn and Co bulk content ≥ 16 at. %, the reverse happens and Cr is more likely to be nearest neighbors with nearby Mn and Co rather than a Cr atom. Due to this situation, more bulk material would need to dissolve to supply enough Cr to form a uniform nm thick passive film. Once the oxide covers the surface, Cr is predicted to enrich.

Even with an altered zone, high Cr enrichment within the passive film is suggested for the Cr10-MPEA and this phenomenon might also be correlated to various atomistic properties such as cohesive energy and diffusion rates [85]. The diffusion process of an equiatomic FeNiCrCoCu FCC alloy was investigated by modeling of various atomic properties and then comparison to pure metals [85]. Correlations were observed with cohesive and vacancy formation energies. Diffusion rates were faster for elements with lower cohesive and vacancy formation energies (e.g., pure Cr and Fe with a cohesive energy of 4.2 eV and 4.4 eV, respectively) [85]. Cr was observed to have a faster diffusion rate both in pure Cr and the FeNiCrCoCu alloy compared to Fe. This could be

correlated to the lower cohesive energy of Cr. Moreover, if Cr diffuses faster than other alloying elements, it could readily provide a supply of Cr to the altered zone for continued Cr oxidation. It remains to be determined whether MPEAs can enable faster Cr diffusion in the altered zone than binary alloys. However, the MPEA with 10 at. % Cr investigated in this work exhibited passivation, with strong Cr enrichment in the passive film and a small amount of Cr depletion within the altered zone. Other factors could contribute to the observed enrichment and depletion of Cr in the altered zone, such as grain boundary diffusion or altered vacancy mediated diffusion [85-87]. These factors should be considered in future work.

3.6 Conclusions

Electrochemical passivation of Cr-MPEAs containing Fe, Mn, Co and Ni was investigated over a range of Cr concentrations from 6.0 to 22 at. % and compared to binary Ni-Cr, Fe-Cr, and Co-Cr alloys with similar bulk Cr concentrations. The following conclusions can be drawn:

- LSV experiments revealed well-defined passive potential regions for the MPEAs alloys with bulk Cr concentration ≥ 10 at. % and for Ni-Cr $\geq 12\%$ Cr. The Cr6-MPEA, Fe-xCr, Ni-xCr, and Co-xCr ($x \leq 10$ at. %) had limited passivity and underwent localized crevice corrosion. Notably, the MPEA alloy with 10% Cr was shown to have lower sustained passive current densities compared to binary alloys with 10% Cr.
- Alloys that showed significant passivation behavior during 10 ks potentiostatic hold experiment at 0.0 VSCE in 1 mM NaCl pH 4 formed a passive film enriched with Cr(III) species at cation fractions well above the bulk Cr content in the alloy. The Cr10-MPEA showed the highest passive film Cr enrichment term ($f_{Cr,ox}$) of 7.0 compared to all other alloys investigated in this work but passivation efficiency and enrichment term was consistent with the trends observed for binary alloys except for Fe-Cr.
- The passive film for all alloys consisted mainly of hydrous Cr(III) with small amounts of anhydrous Cr(III). The passive films of the Cr-MPEAs were also suggested to have small amounts of Cr-spinels with Ni or Fe, while these species were not detected in the passive films formed on the binary alloys.
- Cr depletion within the altered zone at the metal/oxide interface and the solid state diffusion rates of Cr should be considered as potential limiting factors in Cr oxide enrichment and not be

neglected in aqueous passivation models. Cr supply to oxides could be enabled by an alloy composition enabling enhanced vacancy assisted solid state diffusion of Cr which has been observed on similar alloys.

- The reported Cr enrichment within the electrochemically formed passive films was attributed mainly to the selective dissolution of Ni, Fe, Mn, and Co. Moreover, the enrichment term for Cr(III) could not be uniquely associated with and special alloying “third element effects” based on Ni, Co, Mn or Fe alloying elements.

3.7 References

1. Asami, K., et al., *ESCA study of the passive film on an extremely corrosion-resistant amorphous iron alloy*. Corrosion Science, 1976. **16**(12): p. 909-914.
2. Cwalina, K.L., et al., *In Operando Analysis of Passive Film Growth on Ni-Cr and Ni-Cr-Mo Alloys in Chloride Solutions*. Journal of The Electrochemical Society, 2019. **166**(11): p. C3241-C3253.
3. Jeng, S.-P., P.H. Holloway, and C.D. Batich, *Surface passivation of Ni/Cr alloy at room temperature*. Surface Science, 1990. **227**(3): p. 278-290.
4. Olefjord, I. and H. Fischmeister, *ESCA studies of the composition profile of low temperature oxide formed on chromium steels—II. Corrosion in oxygenated water*. Corrosion Science, 1975. **15**(6): p. 697-707.
5. Asami, K., K. Hashimoto, and S. Shimodaira, *An XPS study of the passivity of a series of iron—chromium alloys in sulphuric acid*. Corrosion Science, 1978. **18**(2): p. 151-160.
6. Bond, A.P. and H.H. Uhlig, *Corrosion Behavior and Passivity of Nickel-Chromium and Cobalt-Chromium Alloys*. Journal of The Electrochemical Society, 1960. **107**(6): p. 488.
7. King, P.F. and H.H. Uhlig, *Passivity in the Iron-Chromium Binary Alloys*. The Journal of Physical Chemistry, 1959. **63**(12): p. 2026-2032.
8. McCafferty, E., *Graph theory and the passivity of binary alloys*. Corrosion Science, 2000. **42**(11): p. 1993-2011.
9. McCafferty, E., *Relationship Between Graph Theory and Percolation Approaches in the Passivity of Fe–Cr Binary Alloys*. Journal of The Electrochemical Society, 2008. **155**(10): p. C501-C505.
10. Uhlig, H.H. and G.E. Woodside, *Anodic Polarization of Passive and Non-passive Chromium–Iron Alloys*. The Journal of Physical Chemistry, 1953. **57**(3): p. 280-283.
11. Zhu, X.M. and Y.S. Zhang, *Investigation of the Electrochemical Corrosion Behavior and Passive Film for Fe-Mn, Fe-Mn-Al, and Fe-Mn-Al-Cr Alloys in Aqueous Solutions*. CORROSION, 1998. **54**(1): p. 3-12.
12. Clayton, C.R., *A Bipolar Model of the Passivity of Stainless Steel: The Role of Mo Addition*. Journal of The Electrochemical Society, 1986. **133**(12): p. 2465.
13. Jakupi, P., et al., *The impedance properties of the oxide film on the Ni–Cr–Mo Alloy-22 in neutral concentrated sodium chloride solution*. Electrochimica Acta, 2011. **56**(17): p. 6251-6259.
14. Lloyd, A.C., et al., *Cr, Mo and W alloying additions in Ni and their effect on passivity*. Electrochimica Acta, 2004. **49**(17): p. 3015-3027.

15. Lloyd, A.C., et al., *The open-circuit ennoblement of alloy C-22 and other Ni-Cr-Mo alloys*. JOM, 2005. **57**(1): p. 31-35.
16. SUGIMOTO, K. and Y. SAWADA, *The Role of Alloyed Molybdenum in Austenitic Stainless Steels in the Inhibition of Pitting in Neutral Halide Solutions*. CORROSION, 1976. **32**(9): p. 347-352.
17. Zhang, X., D. Zagidulin, and D.W. Shoesmith, *Characterization of film properties on the NiCrMo Alloy C-2000*. Electrochimica Acta, 2013. **89**: p. 814-822.
18. McCafferty, E., *Oxide networks, graph theory, and the passivity of Ni–Cr–Mo ternary alloys*. Corrosion Science, 2008. **50**(12): p. 3622-3628.
19. Osozawa, K. and H.J. Engell, *The anodic polarization curves of iron-nickel-chromium alloys*. Corrosion Science, 1966. **6**(8): p. 389-393.
20. McCafferty, E., *Introduction to Corrosion Science*. 2010, 233 Spring St, New York, NY 10013 USA: Springer.
21. Qian, S., et al., *Validation of a Percolation Model for Passivation of Fe-Cr Alloys: Two-Dimensional Computer Simulations*. Journal of The Electrochemical Society, 1990. **137**(2): p. 435-439.
22. McCafferty, E., *Oxide networks, graph theory, and the passivity of binary alloys*. Corrosion Science, 2002. **44**(7): p. 1393-1409.
23. McCafferty, E., *Graph Theory and the Passivity of Iron-Chromium Binary Alloys*. Electrochemical and Solid-State Letters, 2000. **3**(1): p. 28.
24. McCafferty, E., *General Relations Regarding Graph Theory and the Passivity of Binary Alloys*. Journal of The Electrochemical Society, 2003. **150**(5): p. B238.
25. McCafferty, E., *Graph theory and binary alloys passivated by nickel*. Corrosion Science, 2005. **47**(7): p. 1765-1777.
26. Searson, P.C., R. Li, and K. Sieradzki, *Surface Diffusion in the Solid-on-Solid Model*. Physical Review Letters, 1995. **74**(8): p. 1395-1398.
27. Sieradzki, K. and R.C. Newman, *A Percolation Model for Passivation in Stainless Steels*. Journal of The Electrochemical Society, 1986. **133**(9): p. 1979-1980.
28. Xie, Y., et al., *A percolation theory for designing corrosion-resistant alloys*. Nature Materials, 2021. **20**(6): p. 789-793.
29. Elfström, B.O., *The effect of chloride ions on passive layers on stainless steels*. Materials Science and Engineering, 1980. **42**: p. 173-180.
30. Gray, J.J., et al., *Influence of Solution pH, Anion Concentration, and Temperature on the Corrosion Properties of Alloy 22*. Journal of The Electrochemical Society, 2006. **153**(3): p. B61.
31. Gray, J.J. and C.A. Orme, *Electrochemical impedance spectroscopy study of the passive films of alloy 22 in low pH nitrate and chloride environments*. Electrochimica Acta, 2007. **52**(7): p. 2370-2375.
32. Han, J., et al., *Potential Dependent Mn Oxidation and Its Role in Passivation of Ni₃₈Fe₂₀Cr₂₂Mn₁₀Co₁₀ Multi-Principal Element Alloy Using Multi-Element Resolved Atomic Emission Spectroelectrochemistry*. Journal of The Electrochemical Society, 2021. **168**(5): p. 051508.
33. Wu, X.Q., et al., *Uniform corrosion and intergranular corrosion behavior of nickel-free and manganese alloyed high nitrogen stainless steels*. Materials and Corrosion, 2008. **59**(8): p. 676-684.

34. Park, K. and H. Kwon, *Effects of Mn on the localized corrosion behavior of Fe–18Cr alloys*. *Electrochimica Acta*, 2010. **55**(9): p. 3421-3427.
35. Wang, K., et al., *Potential-pH diagrams considering complex oxide solution phases for understanding aqueous corrosion of multi-principal element alloys*. *npj Materials Degradation*, 2020. **4**(1): p. 35.
36. Wranglen, G., *Pitting and sulphide inclusions in steel*. *Corrosion Science*, 1974. **14**(5): p. 331-349.
37. Webb, E.G., T. Suter, and R.C. Alkire, *Microelectrochemical Measurements of the Dissolution of Single MnS Inclusions, and the Prediction of the Critical Conditions for Pit Initiation on Stainless Steel*. *Journal of The Electrochemical Society*, 2001. **148**(5): p. B186.
38. Fajardo, S., et al., *Effect of Mn additions on the corrosion behaviour of TWIP Fe-Mn-Al-Si austenitic steel in chloride solution*. *Corrosion Science*, 2019. **154**: p. 246-253.
39. Nguyen, T.D., J. Zhang, and D. Young, *Effect of Mn on oxide formation by Fe-Cr and Fe-Cr-Ni alloys in dry and wet CO₂ gases at 650°C*. *Corrosion Science*, 2016. **112**: p. 110-127.
40. Pardo, A., et al., *Influence of pH and Chloride Concentration on the Pitting and Crevice Corrosion Behavior of High-Alloy Stainless Steels*. *CORROSION*, 2000. **56**(4): p. 411-418.
41. Miracle, D.B. and O.N. Senkov, *A critical review of high entropy alloys and related concepts*. *Acta Materialia*, 2017. **122**: p. 448-511.
42. Rodriguez, A., J.H. Tylczak, and M. Ziomek-Moroz, *Corrosion Behavior of CoCrFeMnNi High-Entropy Alloys (HEAs) Under Aqueous Acidic Conditions*. *ECS Transactions*, 2017. **77**(11): p. 741-752.
43. Xiao, D.H., et al., *Microstructure, mechanical and corrosion behaviors of AlCoCuFeNi-(Cr,Ti) high entropy alloys*. *Materials & Design*, 2017. **116**: p. 438-447.
44. Yang, S., et al., *Effect of Cr content on corrosion behavior of AlCr_xFeNi₂Cu_{1.6} high entropy alloys*. *Materials Research Express*, 2019. **6**(7): p. 076501.
45. Koga, G.Y., et al., *Corrosion resistant and tough multi-principal element Cr-Co-Ni alloys*. *Journal of Alloys and Compounds*, 2021. **884**: p. 161107.
46. Chai, W., T. Lu, and Y. Pan, *Corrosion behaviors of FeCoNiCr_x (x = 0, 0.5, 1.0) multi-principal element alloys: Role of Cr-induced segregation*. *Intermetallics*, 2020. **116**: p. 106654.
47. Hsu, K.-M., S.-H. Chen, and C.-S. Lin, *Microstructure and corrosion behavior of FeCrNiCoMn_x (x = 1.0, 0.6, 0.3, 0) high entropy alloys in 0.5 M H₂SO₄*. *Corrosion Science*, 2021. **190**: p. 109694.
48. Yang, J., et al., *Effects of Mn on the electrochemical corrosion and passivation behavior of CoFeNiMnCr high-entropy alloy system in H₂SO₄ solution*. *Journal of Alloys and Compounds*, 2020. **819**: p. 152943.
49. Wang, L., et al., *Study of the surface oxides and corrosion behaviour of an equiatomic CoCrFeMnNi high entropy alloy by XPS and ToF-SIMS*. *Corrosion Science*, 2020. **167**: p. 108507.
50. Luo, H., et al., *Corrosion behavior of an equiatomic CoCrFeMnNi high-entropy alloy compared with 304 stainless steel in sulfuric acid solution*. *Corrosion Science*, 2018. **134**: p. 131-139.

51. Inman, S.B., et al., *Effect of Mn Content on the Passivation and Corrosion of Al_{0.3}Cr_{0.5}Fe₂MnxMo_{0.15}Ni_{1.5}Ti_{0.3} Compositionally Complex Face-Centered Cubic Alloys*. Corrosion, 2021. **78**(1): p. 32-48.
52. Lu, P., et al., *Computational design and initial corrosion assessment of a series of non-equimolar high entropy alloys*. Scripta Materialia, 2019. **172**: p. 12-16.
53. Sahu, S., et al., *Localized Corrosion Behavior of Non-Equiatomic NiFeCrMnCo Multi-Principal Element Alloys*. Electrochimica Acta, 2020. **354**: p. 136749.
54. Gerard, A.Y., et al., *Aqueous passivation of multi-principal element alloy Ni₃₈Fe₂₀Cr₂₂Mn₁₀Co₁₀: Unexpected high Cr enrichment within the passive film*. Acta Materialia, 2020. **198**: p. 121-133.
55. Kautz, E.J., et al., *Element redistributions during early stages of oxidation in a Ni₃₈Cr₂₂Fe₂₀Mn₁₀Co₁₀ multi-principal element alloy*. Scripta Materialia, 2021. **194**: p. 113609.
56. Bruemmer, S.M., et al., *Grain boundary selective oxidation and intergranular stress corrosion crack growth of high-purity nickel binary alloys in high-temperature hydrogenated water*. Corrosion Science, 2018. **131**: p. 310-323.
57. Lutton, K., et al., *Understanding multi-element alloy passivation in acidic solutions using operando methods*. Electrochemistry Communications, 2017. **80**: p. 44-47.
58. Gusieva, K., et al., *Repassivation Behavior of Individual Grain Facets on Dilute Ni–Cr and Ni–Cr–Mo Alloys in Acidified Chloride Solution*. The Journal of Physical Chemistry C, 2018. **122**(34): p. 19499-19513.
59. Quiambao, K.F., et al., *Passivation of a corrosion resistant high entropy alloy in non-oxidizing sulfate solutions*. Acta Materialia, 2019. **164**: p. 362-376.
60. Li, T., et al., *Localized corrosion behavior of a single-phase non-equimolar high entropy alloy*. Electrochimica Acta, 2019. **306**: p. 71-84.
61. Pourbaix, M., *Atlas of Electrochemical Equilibria in Aqueous Solutions* 1974, Houston, TX: National Association of Corrosion Engineers.
62. Rao, K.V. and A. Smakula, *Dielectric Properties of Cobalt Oxide, Nickel Oxide, and Their Mixed Crystals*. Journal of Applied Physics, 1965. **36**(6): p. 2031-2038.
63. Motori, A., F. Sandrolini, and G. Davolio, *Electrical properties of nickel hydroxide for alkaline cell systems*. Journal of Power Sources, 1994. **48**(3): p. 361-370.
64. Bush, A.A., et al., *Preparation and X-ray diffraction, dielectric, and Mössbauer characterization of Co_{1-x}NixCr₂O₄ solid solutions*. Inorganic Materials, 2013. **49**(3): p. 296-302.
65. Kamran, M., et al., *Structural, magnetic, and dielectric properties of multiferroic Co_{1-x}MgxCr₂O₄ nanoparticles*. Journal of Magnetism and Magnetic Materials, 2017. **433**: p. 178-186.
66. Schrettle, F., et al., *Wüstite: electric, thermodynamic and optical properties of FeO*. The European Physical Journal B, 2012. **85**(5): p. 164.
67. Kulkarni, S.S. and C.D. Lokhande, *Structural, optical, electrical and dielectrical properties of electrosynthesized nanocrystalline iron oxide thin films*. Materials Chemistry and Physics, 2003. **82**(1): p. 151-156.
68. Zagidulin, D., et al., *Characterization of surface composition on Alloy 22 in neutral chloride solutions*. Surface and Interface Analysis, 2013. **45**(6): p. 1014-1019.
69. Sehra, M.S. and R.E. Helmick, *Dielectric anomaly in MnO near the magnetic phase transition*. Physical Review B, 1981. **24**(9): p. 5098-5102.

70. Ogle, K., *Atomic Emission Spectroelectrochemistry: Real-Time Rate Measurements of Dissolution, Corrosion, and Passivation*. CORROSION, 2019. **75**(12): p. 1398-1419.
71. Ogle, K. and S. Weber, *Anodic Dissolution of 304 Stainless Steel Using Atomic Emission Spectroelectrochemistry*. Journal of The Electrochemical Society, 2000. **147**(5): p. 1770-1780.
72. Doniach, S. and M. Sunjic, *Many-electron singularity in X-ray photoemission and X-ray line spectra from metals*. Journal of Physics C: Solid State Physics, 1970. **3**(2): p. 285-291.
73. KOLXPD, <http://kolxpd.kolibrik.net>.
74. Biesinger, M.C., et al., *Resolving surface chemical states in XPS analysis of first row transition metals, oxides and hydroxides: Cr, Mn, Fe, Co and Ni*. Applied Surface Science, 2011. **257**(7): p. 2717-2730.
75. Thompson, K., et al., *In situ site-specific specimen preparation for atom probe tomography*. Ultramicroscopy, 2007. **107**(2): p. 131-139.
76. Castle, J.E. and K. Asami, *A more general method for ranking the enrichment of alloying elements in passivation films*. Surface and Interface Analysis, 2004. **36**(3): p. 220-224.
77. Evans, H.E., *Cavity formation and metallurgical changes induced by growth of oxide scale*. Materials Science and Technology, 1988. **4**(12): p. 1089-1098.
78. Jiao, Y., S. Zhang, and Y. Tan, *Thermodynamic Analysis and Crystallographic Properties of MFe₂O₄, MCr₂O₄ and MA₂O₄ (M = Fe, Ni, Zn) Formed on Structural Materials in Pressurized Water Reactor Primary Circuit under Zinc and Zinc-aluminum Water Chemistry*. Entropy, 2022. **24**(2): p. 245.
79. Lange, J.G.S.a.N.A., *Lange's Handbook of Chemistry* ed. 17. 2017, New York: McGraw-Hill Education.
80. Walters, L.N., E.L. Wang, and J.M. Rondinelli, *Thermodynamic Descriptors to Predict Oxide Formation in Aqueous Solutions*. The Journal of Physical Chemistry Letters, 2022. **13**(26): p. 6236-6243.
81. Marcus, P. and J.M. Grimal, *The anodic dissolution and passivation of NiCrFe alloys studied by ESCA*. Corrosion Science, 1992. **33**(5): p. 805-814.
82. Kirchheim, R., et al., *The passivity of iron-chromium alloys*. Corrosion Science, 1989. **29**(7): p. 899-917.
83. Giggins, C.S. and F.S. Pettit, *Oxidation of Ni-Cr-Al Alloys Between 1000° and 1200°C*. Journal of The Electrochemical Society, 1971. **118**(11): p. 1782.
84. Nowak, W.J., B. Wierzba, and J. Sieniawski, *Effect of Ti and Ta on Oxidation Kinetic of Chromia Forming Ni-Base Superalloys in Ar-O₂-Based Atmosphere*. High Temperature Materials and Processes, 2018. **37**(9-10): p. 801-806.
85. Seoane, A., D. Farkas, and X.-M. Bai, *Influence of compositional complexity on species diffusion behavior in high-entropy solid-solution alloys*. Journal of Materials Research, 2022. **37**(7): p. 1403-1415.
86. Alexandrov, V., et al., *Ab Initio Modeling of Bulk and Intragranular Diffusion in Ni Alloys*. The Journal of Physical Chemistry Letters, 2015. **6**(9): p. 1618-1623.
87. Laplanche, G., et al., *Phase stability and kinetics of σ -phase precipitation in CrMnFeCoNi high-entropy alloys*. Acta Materialia, 2018. **161**: p. 338-351.

4. Aqueous Passivation of Non-Equiatomic Ni₃₈Fe₂₀Cr_xMn_{21-0.5x}Co_{21-0.5x} Multi-Principal Element Alloy (x = 22, 14, 10, 6 at. %) in an Alkaline Chloride Solution

4.1 Abstract

The corrosion and aqueous passivation behavior of a series of Ni₃₈Fe₂₀Cr_xMn_{21-0.5x}Co_{21-0.5x} multi-principal element alloys (MPEAs) (where x = 22, 14, 10, 6 – at. %) in pH 4 and pH 10 electrolyte were investigated in deaerated NaCl solution. Comparisons were made with solid solution binary alloys Ni-yCr, Fe-uCr, and Co-uCr, where y = 24, 12, 5 – at. % and u = 20, 10, 5 – at. %. Linear sweep voltammetry and electrochemical impedance spectroscopy were used to evaluate the passivation performance. In pH 10 electrolyte, the LSV for all Cr-MPEAs and Cr binary alloys exhibited a more stable passive region and an increased passive potential range compared to polarization in pH 4 electrolyte. Potentiostatic holds in the passive potential domain were utilized to form passive films which were then characterized with X-ray photoelectron spectroscopy. Passive films formed on Cr-MPEAs in pH 10 electrolyte were enriched in Ni(II) and Cr(III) species and contained low concentrations of Fe (II), Mn(II), and Co(II). The passive films formed on the Ni-Cr and Fe-Cr binary alloys were also enriched in Cr(III) but such behavior was not seen in the Co-Cr binary alloys. Comparisons between Cr(III) vs bulk Cr content were made in passive films formed at pH 4 versus pH 10 electrolyte. Regardless of bulk Cr content, passive films formed in pH 4 electrolyte had a higher concentration of Cr(III) than compared to passivation in pH 10 electrolyte. In pH 10 electrolyte an increase in concentration of Ni and Fe oxides and/or hydroxides was observed. Differences in the corrosion behavior and passive film characteristics were attributed to differences in thermodynamic and kinetic factors between pH 4 and pH 10 electrolyte.

4.2 Introduction

Passive film features not only depend on material composition and structure [1-3] but what environment it is exposed to (i.e., solution pH). Given a particular pH and potential, various traceable to stable and metastable compounds could form [4, 5]. Depending on the properties of the solution, many different interactions can arise between the electrolyte/oxide and oxide/metal

interfaces. Several passivity investigations have explored this phenomenon, especially in the case of Cl^- ions and various solution pH levels, for many conventional alloys [1, 6-14]. A wide variability in behavior is observed depending on the testing solution conditions.

Many Fe- and Ni- alloy studies have shown pH can influence the material's corrosion resistance and passive film's composition, morphology, and structure [9, 15-22]. Consider Cr-containing alloys and passive films spontaneously formed in near neutral pH solutions. These passive films typically form a layered structure consisting of an outer hydroxide and inner oxide layer usually dominate in Cr species [14-17, 21]. Such Cr-enriched passive films show correlation with thermodynamic predictions based on potential-pH stability diagrams of pure metals. Consider pure Ni, Fe, and Cr, at near neutral pH. Ni and Fe are most stable as dissolved Ni(II) and Fe(II) ions and Cr is stable as an oxide and/or hydroxide (Cr_2O_3 and $\text{Cr}(\text{OH})_3$)[4]. At more alkaline pH levels, these alloys passive films typically are not dominated by Cr oxides or hydroxides but by some other oxide species. In the case of Fe-based alloys, the passive film will consist more of Fe(II) and Fe(III) oxides/hydroxides compared to Cr(III) hydroxide [21]. Similarly for Ni-based alloys, passive films are dominated by Ni oxide and hydroxide species [20]. These results demonstrate the variability seen in conventional solid solution alloys' passive behavior but little is known on regarding the environment influences on multi-principal element alloys' (MPEAs) passivity.

An alloy's passive behavior not only depends on the solution pH but also on the presence of Cl^- in solution. Chloride anions have been shown to cause instabilities within the passive film that contribute to local breakdown and potentially leading to pitting corrosion [6-8, 11, 12, 22]. Localized corrosion in Cl^- environments is typically linked to Cl^- adsorption and/or absorption of the passive film. It is generally agreed that the first step to local breakdown is the adsorption of Cl^- on the oxide surface at the solution/film interface [11]. Many corrosion resistant alloys (CRAs) have been shown to mediate this step by forming protective passive films resistant to Cl^- adsorption [23, 24]. Typically, these alloys contain beneficial elements in which contribute to these protective qualities. These atomic attributes may consist of the following: altered Cl^- adsorption due to favored O^{2-} and OH^- adsorption, strong M-M bonds increasing resistance to dissolution, and/or strong M-O bonds preventing the replacement of O with Cl^- [1, 10, 13, 24]. Such beneficial

attributes demonstrate the importance of the relationship between alloying elements and forming protective passive films in Cl^- .

Many studies have investigated the nature of MPEA passivity in various environments, but typically focus on the corrosion properties under acidic or near neutral Cl^- environments [25-42]. Few studies have explored the effect of alkaline pH on MPEA passivity [43-46]. Choudhary et al. investigated the passive behavior of an equiatomic CoCrFeNi MPEA in 0.1 M NaCl at three different pH levels: 2, 6, and 10, adjusted with either HCl or NaOH [43]. Potentiodynamic polarization of the MPEA showed that at all pH levels, a passive region with low passive current densities ($\sim 10^{-6} \text{ A cm}^{-2}$) was observed but metastable pitting was only seen at pH 2 and 6. X-ray photoelectron spectroscopy (XPS) was utilized to characterize passive films formed on the CoCrFeNi MPEA after 4 h immersion at each pH level. At all pH levels, the MPEA's passive film was enriched with Cr(III) cations. As the pH increased, an increase in Ni(II) and Co(II) cations was observed within the passive films. It was concluded the above results suggest at more acidic pH levels the passive film contains low levels of other alloying elements beside Cr but at more basic pH levels the thermodynamic stability of Ni(II) and Co(II) oxides species increases [43]. Wang et al. showed similar results for an equiatomic CoCrFeMoNi alloy in 0.34 M NaCl at four different pH levels: 1, 3, 5, and 7, adjusted with HCl [44]. Potentiodynamic polarization of the CoCrFeMoNi alloy exhibited an increase in passive current density with decrease in pH level. At pH 7 the passive current density was $\sim 10^{-6} \text{ A cm}^{-2}$ but increased to $\sim 10^{-5} \text{ A cm}^{-2}$ at a pH level of 1. CoCrFeMoNi alloy's passivity was further explored by potentiostatic polarization at 0.5 V_{SCE} for 1 hr at each pH level and the resulting passive films were characterized by XPS. At each pH level, the measured current density decreased during the potential hold eventually reaching a steady state value. At a pH level of 7 the lowest current density values were measured. XPS characterization showed that at each pH level, passive films were enriched with Cr(III) species but the degree of enrichment decreased with increasing pH. The decrease in Cr enrichment was correlated to an increase in oxidized Co(II), Fe(II), Fe(III), and Ni(II) species within the passive films as the pH level increased. The researchers concluded the improved passive behavior observed with increasing pH level was a result of improved stability of non-Cr oxidized species contributing to passive film formation [44]. Other passivity studies exist in which alkaline pH levels are explored but often only discuss the electrochemical parameters and lack in passive film and/or solution characterization [46, 47].

In this study, the effect of alkaline pH on the passive behavior of a series of non-equimolar, single phase, solid solution $\text{Ni}_{38}\text{Fe}_{20}\text{Cr}_x\text{Mn}_{21-0.5x}\text{Co}_{21-0.5x}$ MPEAs previously reported [5, 30, 32, 48-50], where $x = 6 - 22$ at. %, was investigated and compared to a series of high-purity Ni-Cr, Fe-Cr, and Co-Cr binary alloys. Electrochemical passivation was explored using linear sweep voltammetry (LSV), electrochemical impedance spectroscopy (EIS), and single-frequency EIS (SF-EIS). The fate of the alloying elements was tracked both within potentiostatically formed passive films and testing electrolyte by XPS and atomic emission spectroelectrochemistry (AESEC) technique, respectively.

4.3 Experimental

The $\text{Ni}_{38}\text{Fe}_{20}\text{Cr}_x\text{Mn}_{21-0.5x}\text{Co}_{21-0.5x}$ – at. % MPEAs were arc-melted, cast, and homogenized at 1100 °C for 96 h using methods described previously [48]. The MPEA forms a single-phase FCC solid solution over a range of Cr concentrations, where $x = 22, 14, 10, 6$ at. %. For simplicity, these MPEAs will be referred to as Cr22-, Cr14-, Cr10-, and Cr6-MPEA, respectively. Fe- x Cr ($x = 20, 10, 5$ at. %) binary alloys were arc-melted, cast, homogenized using methods described previously (Chapter 2 and 3 [30, 51]). Resulting Fe-Cr alloys contained a BCC solid solution phase. The Co- x Cr alloys ($x = 20, 10, 5$ at. %) were arc-melted, cast, homogenized using methods described previously (Chapter 3 [51]). Resulting Co-Cr alloys contained an FCC solid solution phase. Ni-5Cr binary alloy was cast from ultra-high purity Ni base material and ultra-high purity Cr. Samples were hot forged at 900 °C followed by a solution anneal at 950 °C for 1 hr and water quenched [52]. Solid solution Ni-24Cr and Ni-12Cr (at. %) binary alloys were arc-melted, cast, rolled, solutionized at 1100 °C, and recrystallized, resulting in a homogenous single-phase FCC alloy. All tested materials and corresponding compositions are listed in **Table 4.1**.

**Table 4. 1. Multiple-Principal Element Alloys and Binary Alloys
Nominal Composition**

Alloy	Chemical Composition (at. %)
Cr22-MPEA	38Ni-20Fe-22Cr-10Mn-10Co
Cr14-MPEA	38Ni-20Fe-14Cr-14Mn-14Co
Cr10-MPEA	38Ni-20Fe-10Cr-16Mn-16Co
Cr6-MPEA	38Ni-20Fe-6Cr-18Mn-18Co
Fe-20Cr	80Fe-20Cr
Fe-10Cr	90Fe-10Cr
Fe-5Cr	95Fe-5Cr
Co-20Cr	80Co-20Cr
Co-10Cr	90Co-10Cr
Co-5Cr	95Co-5Cr
Ni-24Cr	76Ni-24Cr
Ni-12Cr	88Ni-12Cr
Ni-5Cr	95Ni-5Cr

For electrochemical testing samples were mechanically ground to 1200 grit using SiC paper. Samples were degreased after mechanical grinding by sonicating in acetone, 1:1 acetone and isopropanol, isopropanol, and deionized water, each for 1 min, and dried with N_{2(g)}.

Electrochemical tests were conducted in N_{2(g)} – deaerated 0.1 M NaCl, with the final pH adjusted to 4 or 10 using 0.1 M HCl or NaOH, respectively. Experiments were performed with a Gamry Instruments Reference 600+™ potentiostat. A standard three-electrode cell was utilized with a Pt mesh counter electrode, a saturated calomel reference electrode (SCE) and an MPEA or binary alloy sample as the working electrode. Samples were pressed against a rubber O-ring to expose an area of 0.1 cm². All potentials are reported against SCE.

LSV experiments were conducted over a range of applied potentials (-1.3 V_{SCE} to 0.8 V_{SCE}) with a scan rate of 0.5 mV s⁻¹. An initial potentiostatic hold, prior to polarization, of -1.3 V_{SCE} for 600 s was conducted to minimize the effect of the air-formed oxide after polishing. During LSV, the imaginary impedance component (-Z'') was monitored in situ at an applied AC voltage of 20 mV_{rms} at $f=1$ Hz.

Electrochemical passivation was investigated within the passive potential region, determined by LSV. Potentiostatic passivation was conducted using the following procedure: (1) cathodic

treatment at $-1.3 \text{ V}_{\text{SCE}}$ for 600 s, (2) step potential hold at $-0.25 \text{ V}_{\text{SCE}}$ for 10 ks, (3) an EIS measurement from 100 kHz to 1 mHz at the same potential as (2). During potentiostatic hold at $-0.25 \text{ V}_{\text{SCE}}$, the passive film growth was monitored as a function of time using SF-EIS at $f = 1 \text{ Hz}$ and an AC potential magnitude of $20 \text{ mV}_{\text{rms}}$ [30, 45, 53]. All EIS data was analyzed with an equivalent circuit model initially established for alloy C-22 and adapted for Cr-MPEAs [30, 31, 45, 54]. To monitor passive film growth, the approximate oxide thickness (ℓ_{ox}) as a function of time was calculated based on the relationship between the equivalent circuit model, constant phase element exponential, and $-Z''$, equation and methodology shown in Chapter 2 [30, 45, 53].

The total electrochemical charge (q_{total}), oxide charge (q_{ox}), and ion ejection charge ($q_{\text{total}} - q_{\text{ox}}$) were calculated for each passive film formed during potentiostatic hold at $-0.25 \text{ V}_{\text{SCE}}$ for 10 ks. The oxide charge was calculated by using the relationship in **Eq. 4.1**;

$$q_{\text{ox}} = \frac{\ell_{\text{ox}} n F \rho}{M} \quad (4.1)$$

where ℓ_{ox} is the EIS derived oxide thickness, M is the oxide molar mass of the assumed oxide, n is the number of electrons transferred to produce the oxide from its elements, ρ is the density of assumed oxides, and F is the Faraday constant (96485 C mol^{-1}). Hydroxides were considered as well as oxides. For charge calculations, weighted averages for M , ρ , and n were used for each alloy and oxides based on XPS spectral deconvolution. The charge efficiency ($q_{\text{ox}}/q_{\text{total}}$) of each passive film formed at $-0.25 \text{ V}_{\text{SCE}}$ was also calculated, a detailed description is provided in Chapter 3.

XPS spectra were acquired using Al $K\alpha$ X-rays (binding energy: 1468.7 eV) with a take-off angle of 45° at a pass energy of 26 eV in a PHI VersaProbe IIITM system. Cation fraction within the passive film and elemental composition just below the metal/film interface (relative to all cations or elements detected) were determined by spectral deconvolution of individual core-level spectra with KOLXPDTM analysis software. Spectral deconvolution was implemented with Voigt functions for oxides, asymmetric Doniach Sunjic-like features for metals, and a Shirley background subtraction [55, 56]. For each alloying element, the 2p core feature was deconvoluted utilizing reported parameters for multiplet splitting of reference stoichiometric compounds [57]. Due to Ni Auger overlap with Mn 2p_{3/2}, Co 2p_{3/2}, and Fe 2p_{2/3} spectra, the 2p_{1/2} feature was utilized for XPS spectral deconvolution. A more detailed description of XPS spectral deconvolution has been provided previously in Chapter 2 [30, 45, 50].

AESEC was utilized to investigate the elemental dissolution profile of the Cr22-MPEA in N_{2(g)} – deaerated 0.1 M NaCl + NaOH pH 10. The detailed analytical method and principle of the AESEC technique is available elsewhere [58, 59]. The sample was positioned vertically to an electrochemical flow cell. The electrolyte flow rate was controlled by a peristaltic pump to 2.8 mL min⁻¹. When the electrolyte was in contact with the specimen of interest, the dissolved ions in the electrolyte were transferred to an Ultima 2CTM Horiba Jobin-Yvon inductively coupled plasma atomic emission spectrometer (ICP-AES). The atomic intensities of Ni (231.6 nm), Fe (259.9 nm), Cr (267.7 nm), Co (231.6 nm) and Mn (257.6 nm) were monitored by a polychromator (0.5 m focal distance) or a monochromator (1.0 m focal distance). The use of monochromator is to obtain a better resolution of Cr signal, the minor element of this alloy. The equivalent elemental current densities of an element M, i_M , were calculated as, **Eq. 4.2**:

$$i_M = z_M F v_M / M_M \quad (\text{Eq. 4.2})$$

where z_M is the oxidation state of M (*e.g.*, $M \rightarrow M^{z+} + z_M e^-$), F is the Faraday constant (96485 C mol⁻¹), M_M is the atomic weight of M. The elemental dissolution rates (v_M) were calculated from the atomic emission intensities, again described in [58]. The z_M in this work was determined to be Ni(II), Fe(III), Cr(III), Mn(II), and Co(II) based from thermodynamic predictions [5]. A cathodic reduction step at -1.3 V_{SCE} was applied prior to the passivation experiment for 600 s to reduce the effect of oxide formed after mechanical polishing procedure.

4.4 Results

4.4.1 Electrochemical Passivation Behavior

LSV curves of the Cr-MPEAs and Cr binary alloys in deaerated 0.1 M NaCl + HCl electrolyte at pH 4 and 0.1 M NaCl + NaOH electrolyte at pH 10 are shown in **Figs. 4.1 and 4.2**, respectively. In pH 4 electrolyte, the 22Cr-MPEA and 14Cr-MPEA showed broad passive regions with widths of ~1130 mV and 600 mV, respectively (**Fig. 4.1a**). The Cr10- and Cr6-MPEAs exhibited an unstable passive region containing a small passive window with numerous current spikes indicative of metastable pitting events. The passive region for each Cr-MPEA, exhibited a low passive current density ranging from 10⁻⁶ A cm⁻² to 10⁻⁵ A cm⁻² from high to low bulk Cr content (**Fig. 4.1a**). Similar to the 22Cr-MPEA, Ni-24Cr exhibited a broad passive region compared to Ni-12Cr and Ni-5Cr in **Fig. 4.1b**. In the case of Ni-12Cr, a small passive window was observed at

negative potentials with a width of ~ 210 mV before the current density began to increase and then decrease into another passive region prior to breakdown. The Ni-5Cr binary alloy did not show a clear passive region compared to Ni-24Cr and Ni-12Cr binary alloys. For the Fe-Cr binary alloys, Fe-20Cr exhibited a small passive-potential domain but Fe-10Cr and Fe-5Cr showed active corrosion (**Fig. 4.1c**). The Co-20Cr binary alloy exhibited a clear passive-potential domain with a width of ~ 920 mV, while Co-10Cr and Co-5Cr have much smaller passive region (**Fig. 4.1d**). It should be noted the 22Cr-MPEA and 14Cr-MPEA also exhibited a more stable passive-potential domain compared to all other testing materials in pH 4 electrolyte.

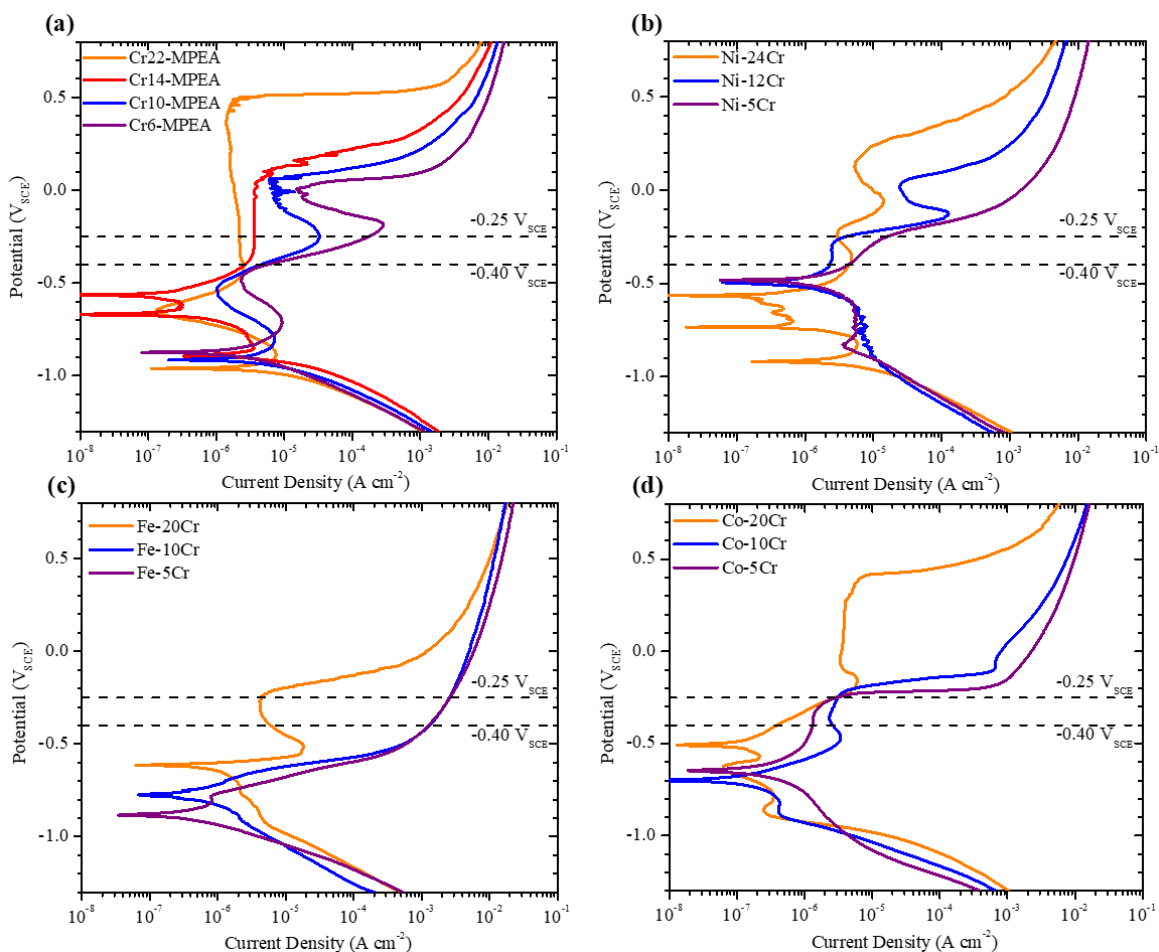


Fig. 4. 1.. Linear sweep voltammetry in $N_{2(g)}$ deaerated 0.1 M NaCl + HCl electrolyte at pH 4 after an initial cathodic reduction at $-1.3 V_{SCE}$ for 600 s for (a) x Cr-MPEAs, (b) Ni- y Cr, (c) Fe- u Cr, and (d) Co- u Cr. Where $x = 22, 14, 10, 6$ at. %, $y = 24, 12, 5$ at. %, and $u = 20, 10, 5$ at.%. alloys ($x = 30, 20, 24, 12, 10, 5$ Cr atomic %), (c) Fe- x Cr binary alloys and (d) Co- x Cr binary alloys. Where $x = 30, 20, 10, 5$ Cr at. %.

It is of interest to compare pH 4 to 10. In the case of pH 10 testing electrolyte, all Cr-MPEAs and Cr binary alloys demonstrated a more stable passive-potential domain compared to pH 4, shown in **Fig. 4.2**. A decrease in the active-to-passive transition was observed for the Cr-MPEAs compared to the transitions observed at pH 4 (**Fig. 4.2a**). Unlike the pH 4 electrolyte, each Cr-MPEA exhibited a broad passive-potential domain (~930 - 660 mV) that all had the same passive current density of $\sim 10^{-6}$ A cm⁻² when polarized in pH 10 electrolyte, suggesting the passive current density at high pH levels is independent of bulk Cr content in the Cr-MPEAs. Similar to the Cr-MPEAs, all Ni-Cr binary alloys exhibited a broad passive-potential domain with low passive current densities (**Fig. 4.2b**). In pH 10 electrolyte, the Fe-20Cr binary alloy shows a broader passive region of ~1100 mV (**Fig. 4.1c**). Also, Fe-10Cr shows a slight passive-potential domain in pH 10 electrolyte compared to active corrosion in pH 4 electrolyte. The Co-Cr binary alloys exhibit a more stable passive-potential domain with no active-to-passive transition in pH 10 electrolyte compared to pH 4.

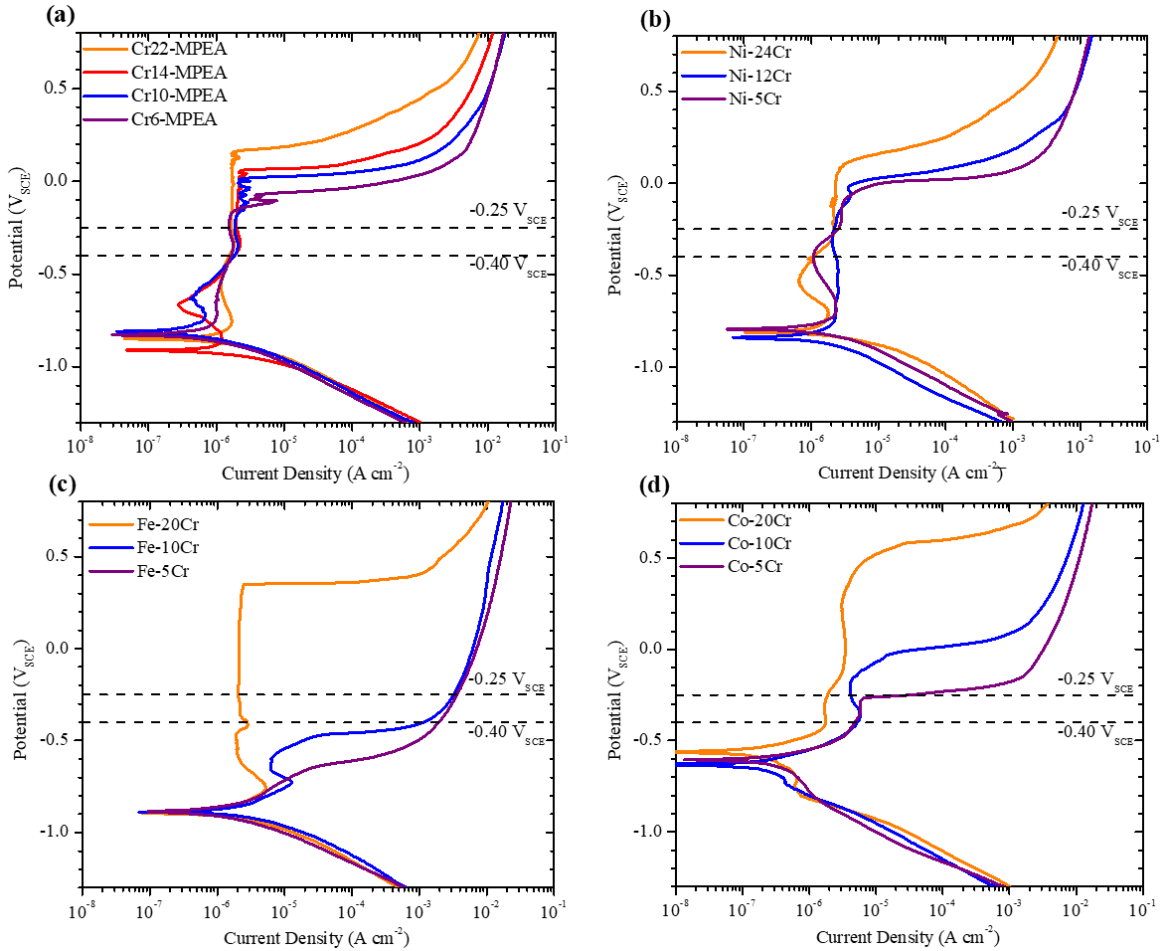


Fig. 4. 2. Linear sweep voltammetry in $N_2(g)$ deaerated $0.1 M NaCl + NaOH$ electrolyte at pH 10 after an initial cathodic reduction at $-1.3 V_{SCE}$ for 600 s for (a) xCr -MPEAs, (b) Ni_yCr , (c) Fe_uCr , and (d) Co_uCr . Where $x = 22, 14, 10, 6$ at. %, $y = 24, 12, 5$ at. %, and $u = 20, 10, 5$ at. %.

The current densities within the passive-potential domains from LSV at $-0.25 V_{SCE}$ and $-0.40 V_{SCE}$ in pH 4 and 10 testing electrolyte are summarized in **Figs. 4.3 and 4.4**, respectively. At $-0.25 V_{SCE}$, the Cr-MPEAs, Ni-Cr, and Fe-Cr binary alloys exhibited a decrease in current density with increasing bulk Cr content in pH 4 electrolyte, shown in **Fig. 4.3a**. The Co-Cr alloys had a low current density independent of bulk Cr in pH 4 solution. In pH 10 electrolyte, only the Co-Cr and Fe-Cr binary alloys showed a decrease in current density with bulk Cr content (**Fig. 4.3b**). The Cr-MPEAs and the Ni-Cr binary alloys all showed similar current densities of $10^{-6} A cm^{-2}$ at $-0.25 V_{SCE}$ in pH 10 electrolyte, regardless of bulk Cr concentration (**Fig. 4.3b**). Hence, there was a change in susceptibility with Ni-Cr and the Cr-MPEAs improved at pH 10 whilst Co-Cr was worse

at pH 10 from the passivity perspective. At $-0.40 V_{SCE}$ in both pH 4 and pH 10 electrolyte, the Cr-MPEAs and Ni-Cr binary alloys current densities were fairly similar at all bulk Cr concentrations (Fig. 4.4), which was previously seen at a potential of $-0.25 V_{SCE}$. In the case of the Fe-Cr binary alloys, a clear dependence in bulk Cr concentration was observed on current densities at both potentials, regardless of pH level (Fig. 4.3 and 4.4).

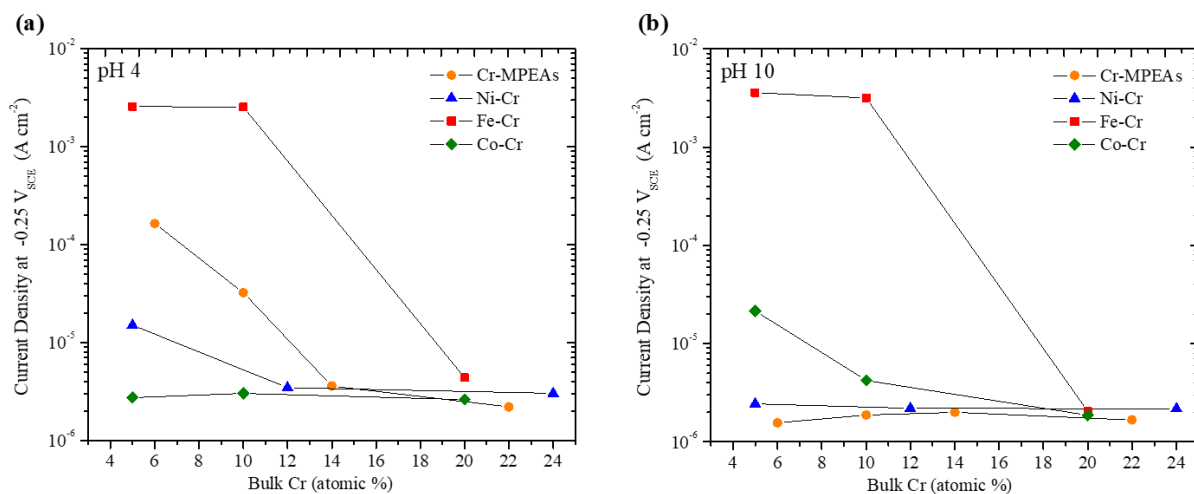


Fig. 4. 3. Comparison of current density versus bulk alloy Cr concentration from linear sweep voltammetry at $-0.25 V_{SCE}$ in $N_{2(g)}$ deaerated $0.1 M NaCl + HCl$ or $NaOH$ electrolyte at (a) pH 4 and (b) pH 10 for xCr -MPEAs, Ni - yCr , Fe - uCr , and Co - uCr . Where $x = 22, 14, 10, 6$ at. %, $y = 24, 12, 5$ at. %, and $u = 20, 10, 5$ at. %.

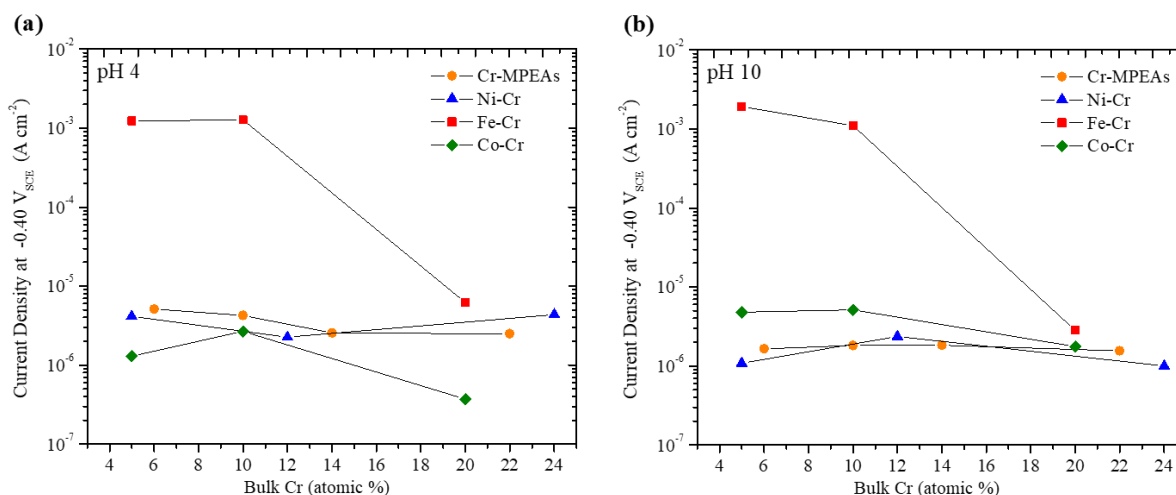


Fig. 4. 4. Comparison of current density versus bulk alloy Cr concentration from linear sweep voltammetry at $-0.40 V_{SCE}$ in $N_{2(g)}$ deaerated $0.1 M NaCl + HCl$ or $NaOH$ electrolyte at (a) pH 4 and (b) pH 10 for xCr -MPEAs, Ni - yCr , Fe - uCr , and Co - uCr . Where $x = 22, 14, 10, 6$ at. %, $y = 24, 12, 5$ at. %, and $u = 20, 10, 5$ at. %.

4.4.2 Aqueous Passivation at an Applied Passive Potential of $-0.25 V_{SCE}$

The electrochemical passive current decays during potentiostatic holds at $-0.25 V_{SCE}$ in $0.1 M NaCl + NaOH$ electrolyte at pH 10 are shown in **Fig. 4.5**. The passive current density decreased with time for the Cr22-, Cr14-, Cr-10 MPEAs, Ni-24Cr, Ni-12Cr, Fe-20Cr, Co-20Cr, and Co-10Cr binary alloys. Each alloy with a reducing current density-time behavior exhibited low passive current densities that decreased from $\sim 5 \times 10^{-5}$ to near $10^{-8} A cm^{-2}$ (**Fig. 4.5**). Transient current density spikes were observed for the Cr-MPEAs and Fe-20Cr binary alloy and are indicative of metastable breakdown events. Unlike the high Cr alloys (i.e., Cr22-MPEA), no reduction in current density was observed during potentiostatic hold for the Cr6-MPEA and Fe-10Cr binary alloy (**Fig. 4.5**). The Cr6-MPEA's current density stayed relatively constant and was higher ($\sim 4 \times 10^{-4} A cm^{-2}$) compared to the passivating Cr alloys. The Fe-10Cr binary alloy had the highest measured current density, $10^{-3} A cm^{-2}$, during potentiostatic hold. This current density-time behavior observed for the Cr6-MPEA and Fe-10Cr binary alloy is characteristic of localized corrosion which was confirmed by the presence of crevice corrosion.

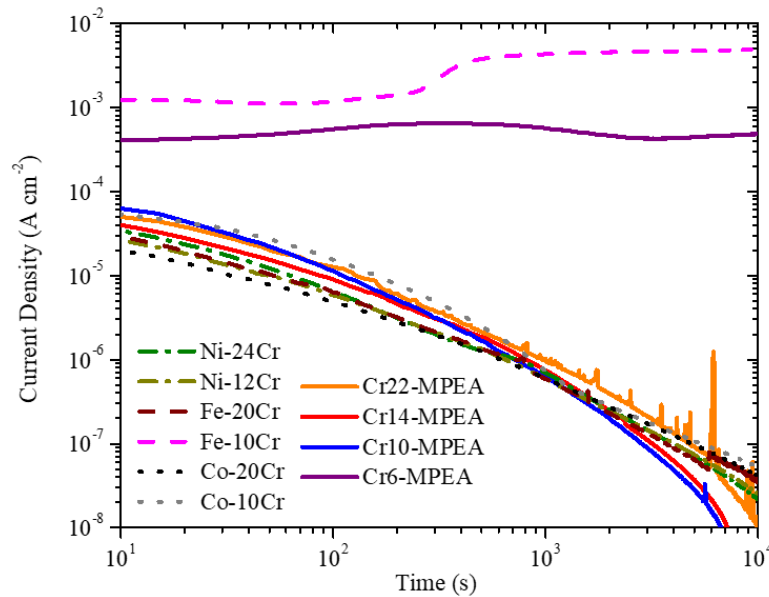


Fig. 4. 5. Measured electrochemical current density during potentiostatic hold at $-0.25 V_{SCE}$ for 10 ks after initial cathodic reduction at $-1.3V_{SCE}$ for 600 s in deaerated $0.1 M NaCl + NaOH$ at pH 10 of xCr -MPEAs, Ni - yCr , Fe - uCr , Co - uCr . Where $x = 22, 14, 10, 6$ at. %, $y = 24, 12, 5$ at. %, and $u = 20, 10, 5$ at.%.

The impedance behavior and corresponding bode plots of alloys and their passive films formed on the passivating Cr alloys during potentiostatic hold at $-0.25 V_{SCE}$ in pH 10 electrolyte are shown in **Fig. 4.6**. After 10 ks, each Cr alloy exhibited a high low-frequency magnitude of $\geq 10^6 \Omega \text{ cm}^2$, suggesting the presence of passive films affording some protection against uniform corrosion. Compared to passive films formed in deaerated 0.1 M or 1 mM NaCl + HCl pH 4 at a passive potential of $-0.25 V_{SCE}$ and $0 V_{SCE}$, respectively, the low-frequency modulus magnitude was slightly lower at $10^5 \Omega \text{ cm}^2$ (previously shown in Ch 2 and 3).

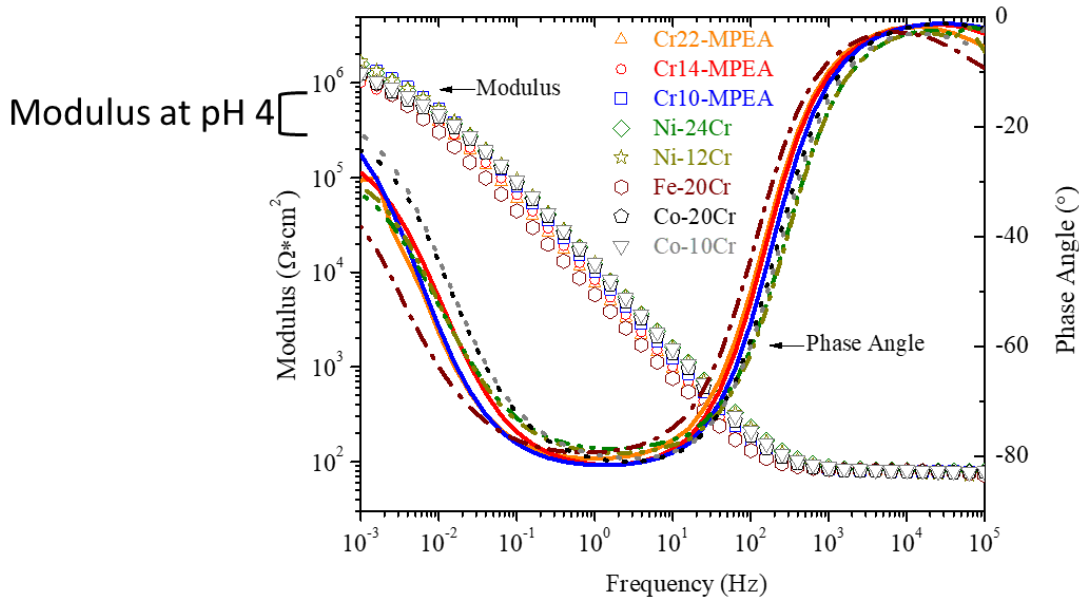


Fig. 4. 6. Bode plot of $x\text{Cr-MPEAs}$, $\text{Ni-}y\text{Cr}$, $\text{Fe-}20\text{Cr}$, $\text{Co-}u\text{Cr}$. in deaerated 0.1 M NaCl + NaOH at pH 10 after potentiostatic hold at $-0.25 V_{SCE}$ for 10 ks. Where $x = 22, 14, 10$ at. %, $y = 24, 12$ at. %, and $u = 20, 10$ at. %.

Passive film growth as a function of time during potentiostatic hold at $-0.25 V_{SCE}$ in deaerated 0.1 M NaCl at a pH of 10 for each passive alloy is plotted in **Fig. 4.7**. The Cr-MPEAs each formed a passive film relatively quickly with Cr22-MPEA being the fastest at earlier growth times, ~ 10 to 500 s. At ~ 100 s and 500 s, the Cr10-MPEAs passive film forms faster than the Cr22- and Cr14-MPEAs passive films. The Cr14-MPEAs passive film formed the slowest compared to passive films formed on the Cr22- and Cr10-MPEA. Unlike pH 10, at pH 4 the 22Cr- and 10Cr-MPEA formed thinner passive films, while Cr14-MPEA had a similar thickness regardless of pH level (**Fig. 4.7**). Compared to binary alloys, the Fe-20Cr passive film formed the slowest, while Co-

20Cr, Ni-24Cr, and Ni-12Cr passive films formed the fastest compared to all other alloys in pH 10 electrolyte.

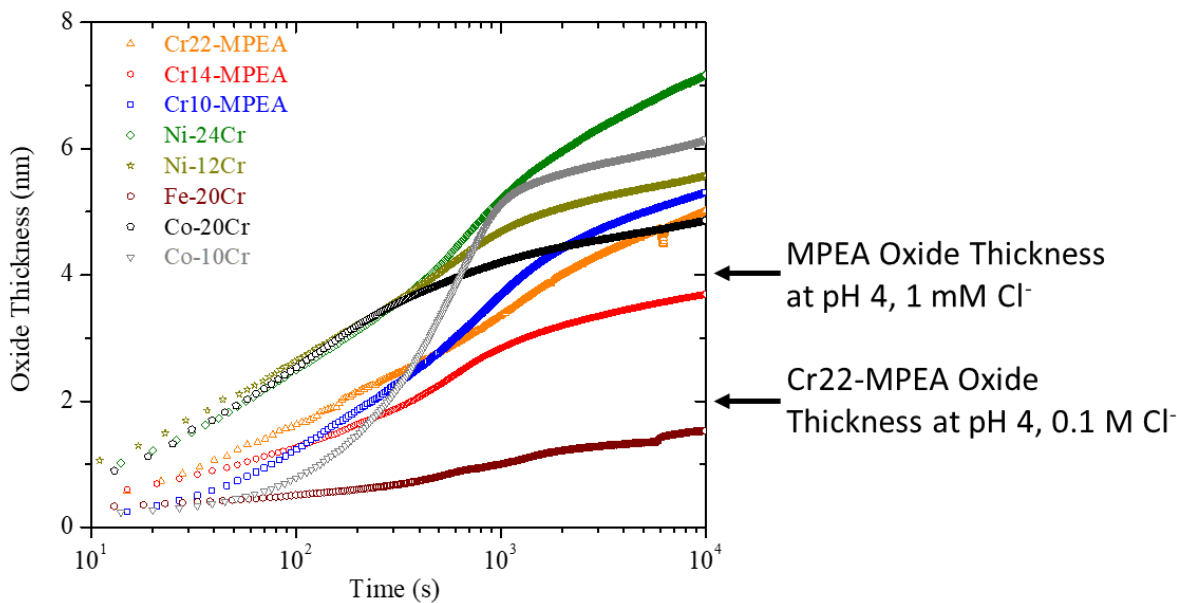


Fig. 4. 7. *In-situ estimation of oxide (passive film) thickness for x Cr-MPEAs, Ni- y Cr, Fe-20Cr, Co- u Cr during potentiostatic hold at $-0.25 V_{SCE}$ for 10 ks in deaerated 0.1 M NaCl + NaOH at pH 10. Where $x = 22, 14, 10$ at. %, $y = 24, 12$ at. %, and $u = 20, 10$ at.%.*

The total electrochemical charge, ion ejection charge, and charge efficiency associated with passive films formed during potentiostatic passivation at $-0.25 V_{SCE}$ for 10 ks in pH 10 electrolyte as a function of bulk Cr content is shown in **Fig. 4.8**. For each computed parameter, no trend was observed with respect to bulk Cr content for each tested alloy with the exception of the Co-Cr alloys total electrochemical charge, which decreased with increasing bulk Cr content (**Fig. 4.8a**). The Fe-20Cr and Cr22-MPEA had the highest calculated ion ejection charge compared to all other tested alloys (**Fig. 4.8b**). The charge efficiency for each passive film formed was high regardless of bulk Cr content (≥ 0.8) (**Fig. 4.8c**). This result suggests that cations are primarily oxidizing to form a passive film rather than dissolving into solution for each tested alloy in pH 10 electrolyte.

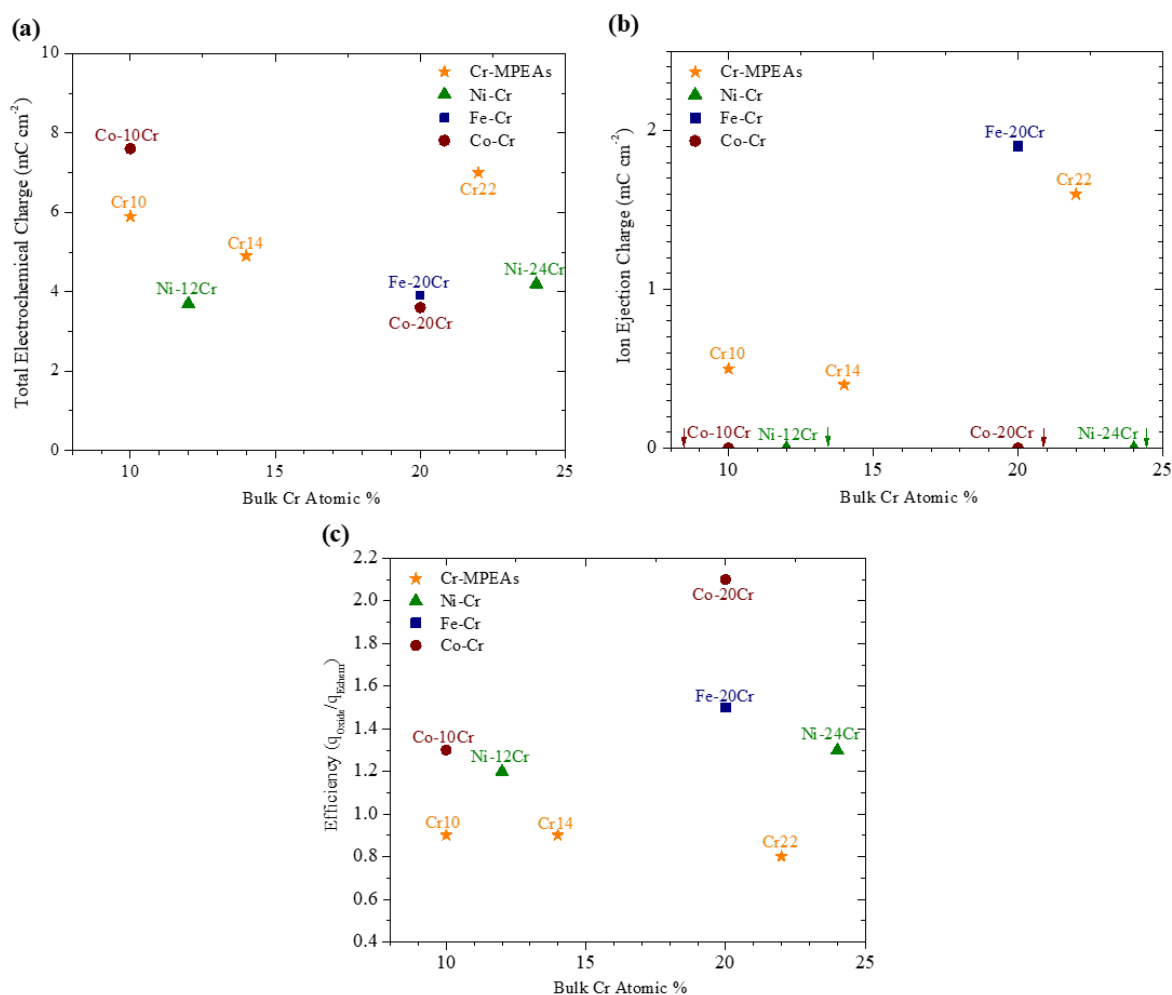


Fig. 4. 8. (a) Total electrochemical charge, (b) ion ejection charge, and (c) efficiency of passive films formed on Cr22-MPEA, Cr14-MPEA, Cr10-MPEA, Ni-24Cr, Ni-12Cr, Fe-20Cr, Co-20Cr, and Co-10Cr during potentiostatic hold at $-0.25 V_{SCE}$ for 10 ks in deaerated $0.1 M NaCl + NaOH$ at pH 10. Values were estimated from measured current density and passive film (oxide) thickness as a function of time.

4.4.3 Passive Film Cation Fractions and Valence State Identified by XPS

The passive film cation fraction and altered zone (i.e., metal/film interface) elemental fraction determined by XPS are summarized in **Table 4.2** for each Cr-MPEA and the binary alloys. All Cr-MPEAs electrochemically passive films were enriched with Ni(II) and Cr(III), relative to the bulk alloy fraction. The Cr10-MPEA had a high Ni(II) cation fraction but was only enriched in Cr (III). The Ni(II) and Cr(III) levels were similar for the Cr22-MPEA passive film. Small amounts of Fe(II) and Co(II) cations were present in each Cr-MPEA passive film but Mn(II) was only found

in the Cr10-MPEAs passive film with a cation fraction of 0.03. It should be noted in pH 4 electrolyte (shown in Ch 2 and 3), the Cr-MPEA passive film contains only a small fraction of Ni (II) and Fe (II) cations but at pH 10 an increase in Ni (II) and Fe (II) cation fraction was observed. The Ni-24Cr and Ni-12Cr passive films were enriched with Ni(II) and Cr(III) cations with greater amounts of Ni(II), as were passive films formed on Fe-20Cr which were enriched in Fe(II) and Fe(III) to a greater extent than Cr(III) cations (**Table 4.2**). This trend was not observed in the case of the binary Co-Cr alloys. Passive films formed on Co-20Cr and Co-10Cr had a low concentration of Cr(III) cations (0.14) near the bulk elemental fraction and were highly enriched with Co(II) cations (0.86). It should be noted, the Cr10-MPEA had a similar Cr(III) cation fraction of 0.47 as passive films formed on Cr22-MPEA and Ni-24Cr binary alloy and more Cr(III) cations than Fe-20Cr.

The elemental fraction within the altered zone just under the oxide/metal interface are shown for each alloy in **Table 4.2**. For each Cr-MPEA, Ni enrichment was observed in the altered zone. The concentration of Cr within the altered zone is relatively the same as the bulk Cr content for the Cr22- and Cr14-MPEA. The Cr10-MPEAs elemental Cr concentration within the altered zone was slightly enriched (0.16) with respect to the bulk Cr content. Low concentrations of Fe, Mn, and $\text{Co} \leq 0.1$ were observed in the altered zone for each Cr-MPEA, suggesting depletion. Compared to the binary alloys, the Cr concentration within the altered zone stayed relatively unchanged as the bulk Cr content for the Ni-24Cr and Co-20Cr binary alloys. In the case of the Ni-12Cr and Co-10Cr binary alloys, an enrichment of Cr was seen within the altered zone. Slight Cr depletion was observed in the case of the Fe-20Cr binary alloy (**Table 4.2**).

Table 4. 2. All cation and elemental fractions detected by XPS for passive films formed at -0.25 V_{SCE} for 10ks in 0.1 M NaCl + NaOH pH 10 N_{2(g)} deaerated solution.

Alloy	Passive Film Cation Fraction					Metal/Film Interface Elemental Fraction				
	Ni(II)	Fe(III)	Cr(III)	Mn(II)	Co(II)	Ni	Fe	Cr	Mn	Co
Cr22-MPEA	0.41	0.10	0.40	0.00*	0.09*	0.57	0.10	0.21	0.08*	0.04*
Cr14-MPEA	0.4	0.17	0.26	0.00*	0.17*	0.68	0.08	0.14	0.05*	0.05*
Cr10-MPEA	0.27	0.14	0.47	0.03*	0.09*	0.64	0.10	0.16	0.01*	0.09*
Ni-24Cr	0.53	--	0.47	--	--	0.79	--	0.21	--	--
Ni-12Cr	0.68	--	0.32	--	--	0.77	--	0.23	--	--
Fe-20Cr	--	0.66**	0.34	--	--	--	0.84	0.16	--	--
Co-20Cr	--	--	0.14	--	0.86	--	--	0.21	--	0.79
Co-10Cr	--	--	0.14	--	0.86	--	--	0.32	--	0.68

*Assuming max allowed Mn and Co fractions consistent with XPS 2p_{1/2} signal.
**Total Fe cation for Fe-20Cr passive film accounts for both Fe(II) and Fe(III) valence state

The deconvolution of the XPS spectra for each alloy passivated at -0.25 V_{SCE} in pH 10 electrolyte are shown in **Figs. 4.9-4.12**. The Cr-MPEAs passive films contained oxidized Ni(II), Fe(II), Cr(III), and Co(II) species (**Fig. 4.9**). The dominant species for each Cr-MPEA passive film were hydrated Ni(II) and Cr(III) compared to other anhydrous oxides and were clearly indicated by joint consideration of the accompanying O1s spectra. Unlike in pH 4 electrolyte (Chapter 1 and 2 [30, 51]), no Cr-spinels were detected in any passive film formed on Cr-MPEAs in pH 10 electrolyte. Instead, a NiFe₂O₄ spinel was detected for each Cr-MPEA passive film. Similar to the Cr-MPEAs, passive films formed on the Ni-24Cr and Ni-12Cr binaries mainly consisted of hydrated Ni(II) and Cr(III) and small amounts of anhydrous Cr(III) (**Fig. 4.10**). Unlike all other tested alloys, the Fe-20Cr passive film contained more anhydrous oxides than hydroxides (**Fig. 4.11**). The passive film formed on Fe-20Cr consisted mainly of anhydrous Fe(II), Fe(III), Cr(III) oxides and hydrated Cr(III). Passive films formed on the Co-20Cr and Co-10Cr binary alloys consisted mainly of hydrated Co(II), Cr(III), along with a small amount of anhydrous Cr(III) species (**Fig. 4.12**). All corresponding oxide fractions for each passive film formed during potentiostatic hold at -0.25 V_{SCE} for 10 ks in pH 10 electrolyte are summarized in **Table 4.3**.

Table 4. 3. Predicted Oxides from XPS and their corresponding fraction for passive films formed at -0.25 V_{SCE} for 10ks in 0.1 M NaCl + NaOH pH 10 N₂(g) deaerated solution.

Alloy	Oxide								
	NiO	Ni(OH) ₂	NiFe ₂ O ₄	Cr ₂ O ₃	Cr(OH) ₃	Mn(II)*	Co(OH) ₂	FeO	Fe ₂ O ₃
Cr22-MPEA	--	0.30	0.17	0.06	0.34	--	0.09*	--	0.04
Cr14-MPEA	0.01	0.32	0.10	0.02	0.24	--	0.17*	--	0.14
Cr10-MPEA	--	0.20	0.10	0.04	0.43	0.03	0.09*	--	0.11
Ni-24Cr	--	0.53	--	0.04	0.43	--	--	--	--
Ni-12Cr	--	0.68	--	0.05	0.27	--	--	--	--
Fe-20Cr	--	--	--	0.02	0.32	--	--	0.35	0.31
Co-20Cr	--	--	--	0.03	0.11	--	0.86	--	--
Co-10Cr	--	--	--	0.02	0.12	--	0.86	--	--

*Assuming max allowed Mn and Co fractions consistent with XPS 2p_{1/2} signal.

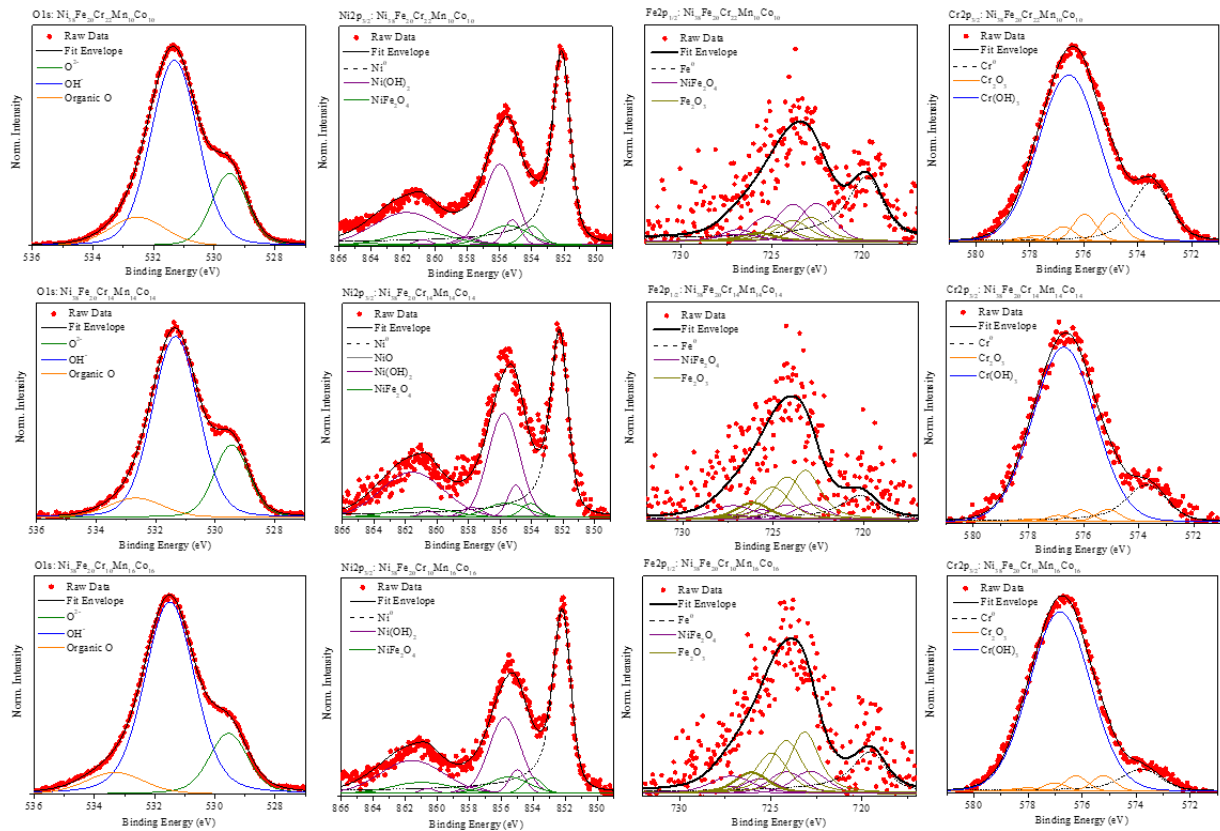


Fig. 4. 9. XPS spectral deconvolution of O 1s, Ni 2p_{3/2}, Fe 2p_{1/2}, and Cr 2p_{3/2} core level for the passive films formed during step-potentiostatic oxide growth at -0.25 V_{SCE} for 10 ks in deaerated 0.1 M NaCl + NaOH at pH 10 on xCr-MPEAs. Where x = 22, 14, 10 at. %.

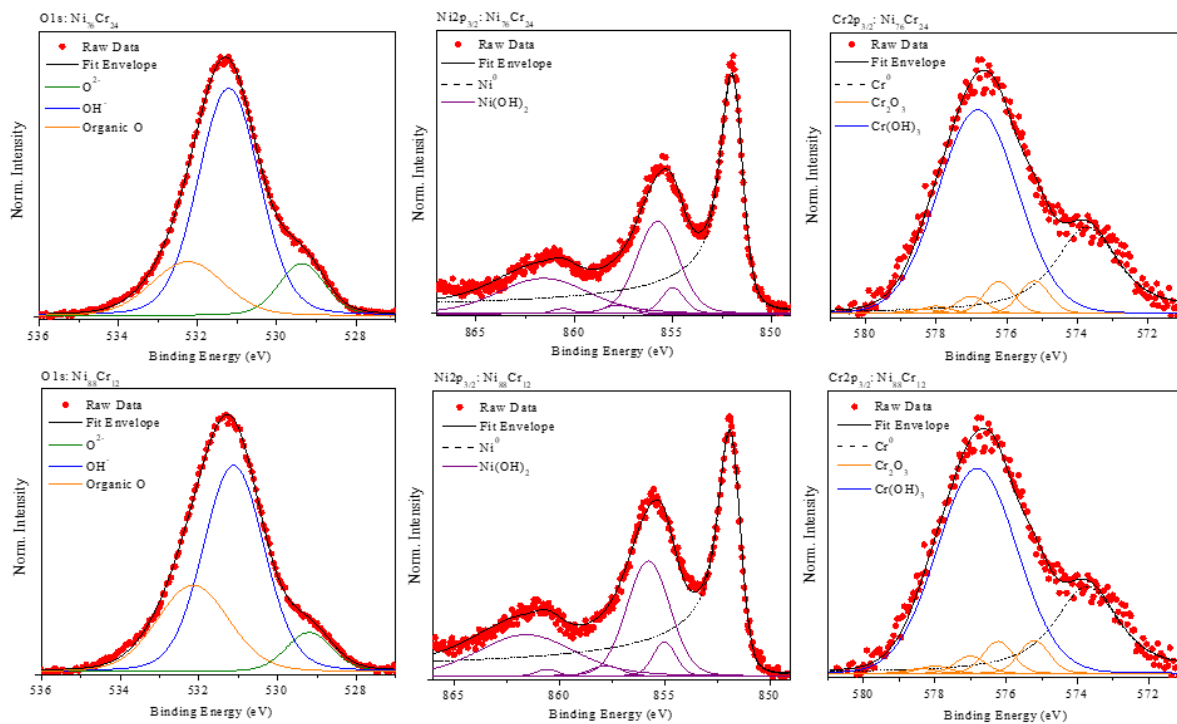


Fig. 4. 10. XPS spectral deconvolution of O 1s, Ni 2p_{3/2}, and Cr 2p_{3/2} core level for the passive films formed during step-potentiostatic oxide growth at -0.25 V_{SCE} for 10 ks in deaerated 0.1 M NaCl + NaOH at pH 10 on Ni-yCr. Where x = 24, 12 at. %

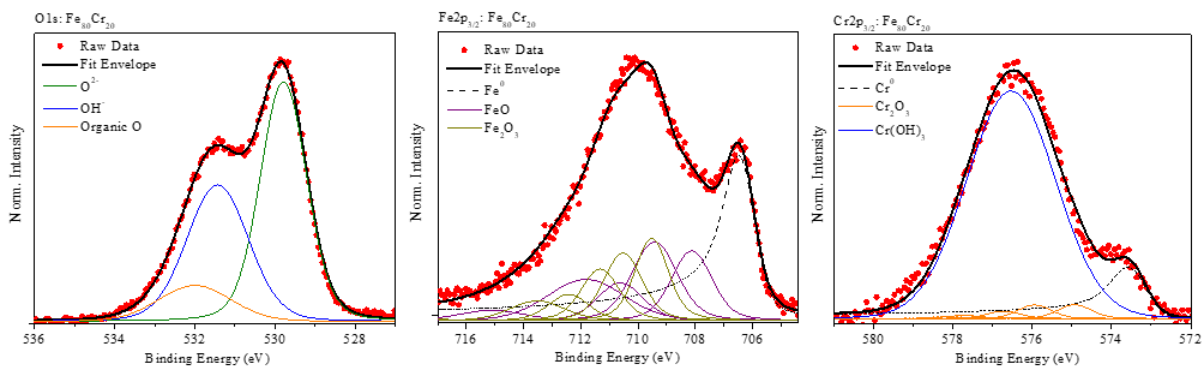


Fig. 4. 11. XPS spectral deconvolution of O 1s, Fe 2p_{3/2}, and Cr 2p_{3/2} core level for the passive films formed during step-potentiostatic oxide growth at -0.25 V_{SCE} for 10 ks in deaerated 0.1 M NaCl + NaOH at pH 10 on Fe-20Cr.

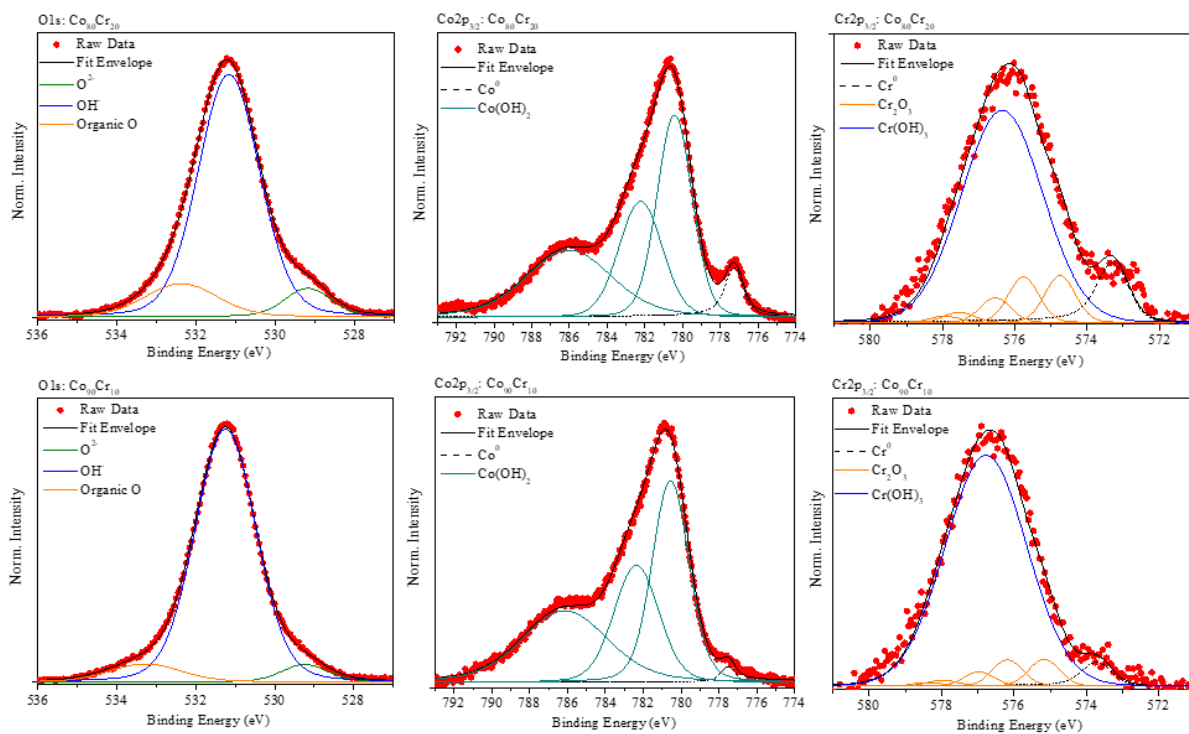


Fig. 4. 12. XPS spectral deconvolution of O 1s, Co 2p_{3/2}, and Cr 2p_{3/2} core level for the passive films formed during step-potentiostatic oxide growth at -0.25 V_{SCE} for 10 ks in deaerated 0.1 M NaCl + NaOH at pH 10 on Co-uCr. Where u = 20, 10 at. %.

Comparisons between the Cr(III) cation % for passive films formed in pH 10 versus pH 4¹ with respect to bulk Cr content are summarized in **Fig. 4.13**. It should be noted, at pH 4 the passive potential used for film formation was 0.0 V_{SCE}, recall Chapter 3. Potential can influence the nature of the passive film but recall Chapter 2, passive films formed on the Cr22-MPEA at a potential of -0.25V_{SCE} were enriched with Cr(III) (64-73 %) and had low concentration of Ni, Fe, Mn, Co cations well below the bulk composition, similar to its film grown at 0.0 V_{SCE} in 1 mM NaCl pH 4 electrolyte (Chapter 3, Cr(III) = 80 %). With this said, comparisons were made between the two different potentials with the assumption passive film cation concentration was independent of potential. A clear difference in passive film Cr concentration can be seen depending on pH (i.e., 4 or 10). In more acidic conditions (pH 4), passive films were dominated by Cr(III) species with a cation fraction ≥ 0.70 (**Fig. 4.13a**). At higher pH levels (pH 10), passive films were still Cr enriched relative to the alloy composition but at much lower cation fraction of ≤ 0.5 (**Fig. 4.13b**). Interestingly, out of the Cr-MPEAs, in pH 4 electrolyte Cr10-MPEA had the lowest Cr(III) enrichment but at pH 10 it had the highest Cr(III) enrichment.

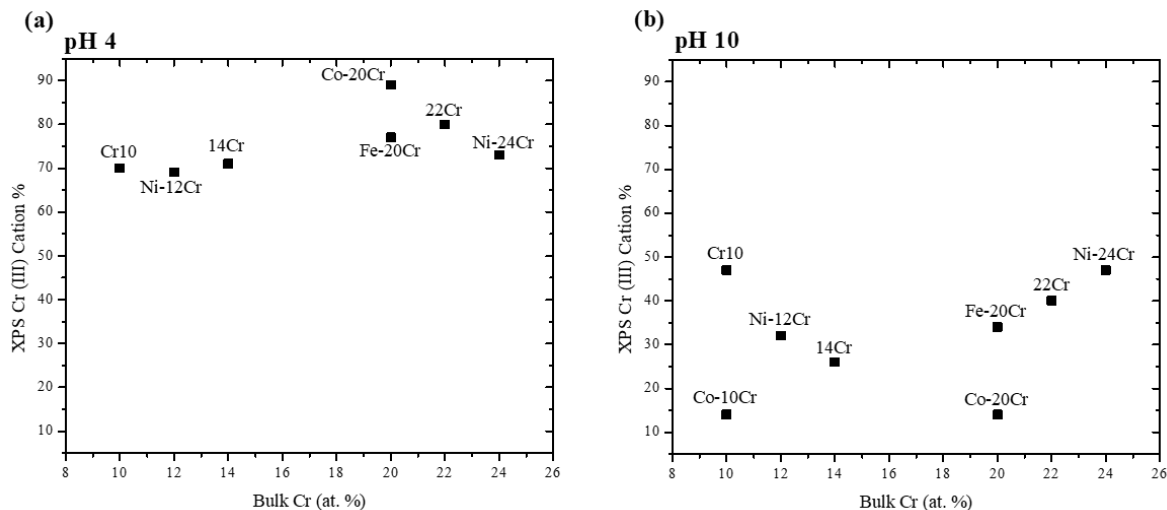


Fig. 4.13. Cr (III) cation % versus Bulk Cr at. % for the passive films formed during step-potentiostatic oxide growth at 10 ks in deaerated (a) 1 mM NaCl + HCl at pH 4 at $-0.0 V_{SCE}$ and (b) 0.1 M NaCl + NaOH at pH 10 at $-0.25 V_{SCE}$ on xCr-MPEAs, Ni-yCr, Fe-20Cr, Co-uCr. Where $x = 22, 14, 10$ at. %, $y = 24, 12$ at. %, and $u = 20, 10$ at. %.

The dominant Cr(III) species for each passive film formed during electrochemical passivation in pH 10 electrolyte vs bulk Cr content is plotted in **Fig. 4.14**, where Cr_2O_3 is indicated by orange squares and $Cr(OH)_3$ as blue dots. For each Cr-MPEA and Cr binary alloy the dominant Cr(III) species was Cr hydroxide. An increase in the amount of hydrated Cr(III) versus bulk Cr content was observed for the Cr22-MPEA, Cr14-MPEA, and the binary Ni-Cr alloys. The Cr10-MPEAs passive film was estimated to have the highest amount of Cr hydroxide compared to all other alloys (**Fig. 4.14**).

Comparisons between different cation species for passive films formed on Cr-MPEAs during potentiostatic passivation at $-0.25 V_{SCE}$ for 10 ks in pH 10 electrolyte are summarized in **Fig. 4.15**. For each Cr-MPEA passive film, a correlation can be observed with the increase in Cr(III) + M(II) cation with increasing bulk Cr + M concentration. All Cr-MPEAs showed the same trend in which the dominant species were Cr(III) + Ni(II) followed by -Fe (II) and then lastly -Co(II). (**Fig. 4.15**).

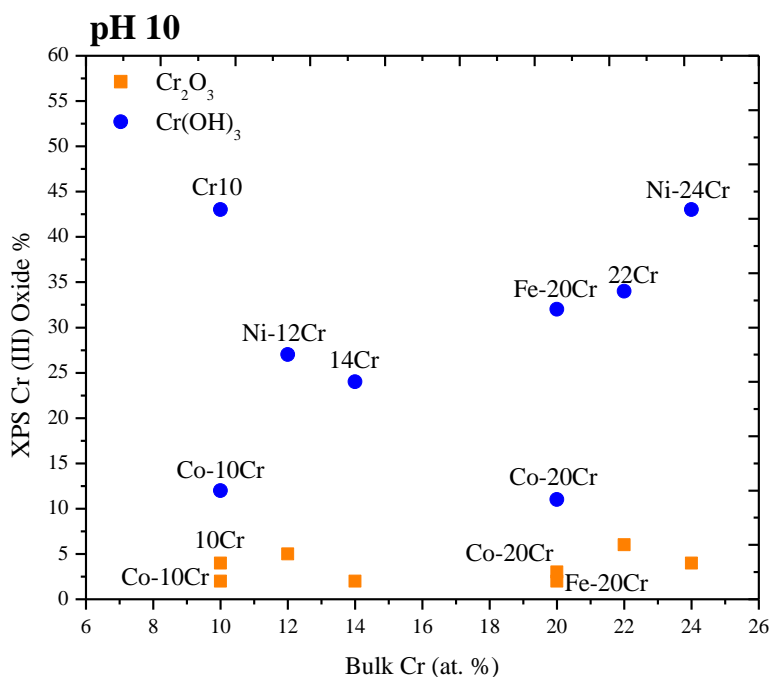


Fig. 4. 14. Cr (III) Oxide % versus Bulk Cr at. % for the passive films formed during step-potentiostatic oxide growth at $-0.25 V_{SCE}$ for 10 ks in deaerated (a) 1 mM NaCl + HCl at pH 4 and (b) 0.1 M NaCl + NaOH at pH 10 on xCr-MPEAs, Ni-yCr, Fe-20Cr, Co-uCr. Where x = 22, 14, 10 at. %, y = 24, 12 at. %, and u = 20, 10 at. %.

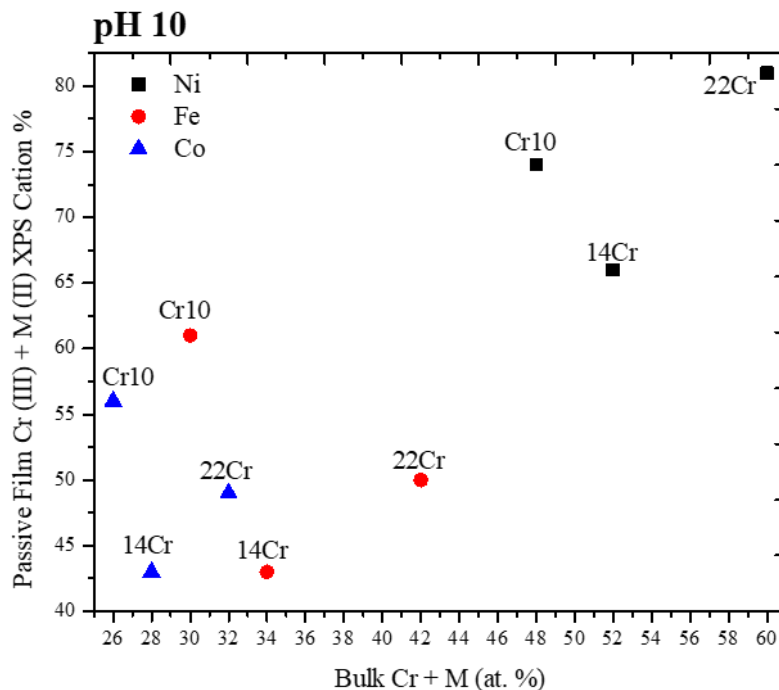


Fig. 4. 15. Cr (III) + M (II) cation % versus Bulk Cr at. % for the passive films formed during step-potentiostatic oxide growth at $-0.25 V_{SCE}$ for 10 ks in deaerated (a) 1 mM NaCl + HCl at pH 4 and (b) 0.1 M NaCl + NaOH at pH 10 on xCr-MPEAs. Where $x = 22, 14, 10$ at. %.

4.4.4 AESEC During 10 ks Potentiostatic hold at $-0.25V_{SCE}$ for Cr22-MPEA in deaerated 0.1 M NaCl + NaOH pH 10

The elemental dissolution rate profiles are presented in equivalent current densities of Ni, Fe, Cr, Mn, and Co for the Cr22-MPEA during passivation at $-0.25 V_{SCE}$ for 10 ks in deaerated 0.1 M NaCl + NaOH pH 10 are shown in **Fig. 4.16**. The dissolution rates of Ni, Fe, Cr, and Co were under the detection limit during electrochemical passivation at $-0.25 V_{SCE}$. In the case of Mn, an initial dissolution transient is observed at $t \sim 500$ s before dropping below the detection limit at longer times (**Fig. 4.16**). Unlike pH 10, in pH 4 electrolyte a dissolution profile was observed for Ni, Fe, and Co, previously shown in Ch 2. This result suggests at high pH levels, the above species are more likely to oxidize into the passive film rather than dissolve into solution, which is predicted by thermodynamic potential-pH stability diagrams [4].

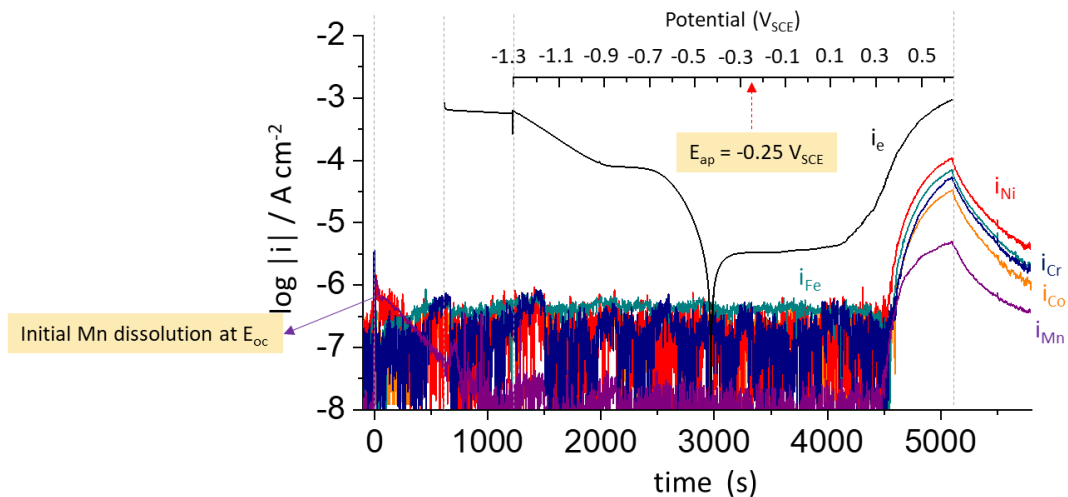


Fig. 4. 16. Atomic emission spectroelectrochemistry of Cr22-MPEA during potentiostatic hold at $-0.25 V_{SCE}$ for 10 ks in deaerated $0.1 M NaCl + NaOH$ at pH 10 after initial cathodic reduction at $-1.3 V_{SCE}$ for 600 s.

4.5 Discussion

4.5.1 Aqueous Passivation in Acidic versus Basic Conditions

Depending on solution pH, a passive films electrochemical properties and chemistry may differ when electrochemically formed in acidic versus basic electrolyte. This phenomenon was observed in the above results for a non-equiatomic $Ni_{38}Fe_{20}Cr_xMn_{21-0.5x}Co_{21-0.5x}$ MPEA, where $x = 22, 14, 10, 6$ at. %. Linear sweep voltammetry showed that passivation of all tested alloys improved when polarized in pH 10 electrolyte compared to pH 4 (**Figs. 4.1 and 4.2**). In particular, the Cr-MPEAs passive behavior showed large improvements in which each MPEA had a stable broad passive region with low passive current densities. This behavior could be attributed to the improved thermodynamic stability of various oxides. At higher pH levels, more oxides/hydroxides become stable and can form, unlike in acidic pH conditions [4]. Consider the potential-pH stability diagrams of pure Ni, Fe, Cr, Mn, and Co, at pH 10 and a potential of $-0.25 V_{SCE}$ ($\sim 0 V_{SHE}$ – versus standard hydrogen electrode), the following oxides/hydroxides are thermodynamically stable: $Ni(OH)_2$, Fe_2O_3 , $Fe(OH)_3$, Cr_2O_3 , $Cr(OH)_3$, Mn_3O_4 , and $Co(OH)_2$; compared to a pH level of 4 only Cr oxide and hydroxide are stable while other elements are metastable [4]. This behavior can also be seen in potentiodynamic polarization of high purity elements in pH 10 versus pH 4

electrolyte. Linear sweep voltammetry in deaerated 0.1 M NaCl + HCl pH 10 shows that pure Ni, Fe, Cr, and Co have clearly defined passive regions suggesting the above oxides are forming shown in **Fig. 4.17**. In pH 4 solutions, only pure Ni and Cr LSV show clearly defined passive regions, unlike in pH 10, (**Thesis Chapter 3**) [51]. According to these thermodynamic predications and comparisons to pure metals it might be expected that such oxides may form during passivation of a NiFeCrMnCo MPEA. Which can be correlated to the observed increase in Ni and Fe cation fractions within the Cr-MPEAs' passive films when formed in pH 10 electrolyte versus pH 4^[30, 51] (**Table 4.2 and Fig. 4.13**). Unfortunately, the above predictions are only of typical stoichiometric oxides and lack information on mixed element oxides and/or non-stoichiometric oxides such as spinels (i.e., NiFe₂O₄ or NiCr₂O₄).

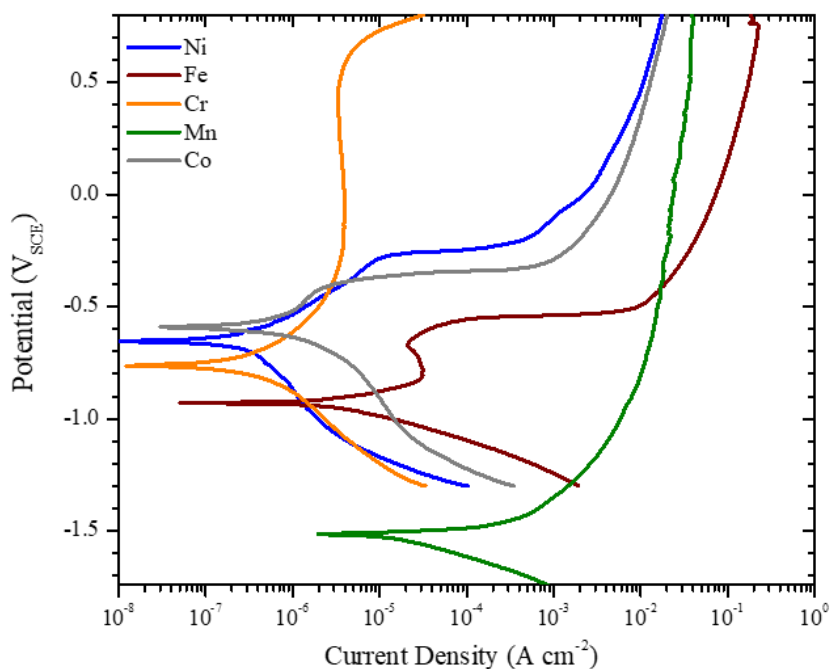


Fig. 4. 17. Linear sweep voltammetry in $N_{2(g)}$ deaerated 0.1 M NaCl + NaOH electrolyte at pH 10 after an initial cathodic reduction at -1.3 VSCE for 600 s for Pure Ni, Fe, Cr, Mn, and Co.

In understanding aqueous passivation of MPEAs, it is necessary to take into account of the formation of possible stoichiometric and/or non-stoichiometric oxides when an alloy contains a high number of alloying elements [5]. Consider the potential-pH stability diagram for the Cr22-MPEA (Ni₃₈Fe₂₀Cr₂₂Mn₁₀Co₁₀) in 1 kg of water with 0.6 m NaCl at ambient conditions at pH 10

and a potential of $-0.25 V_{SCE}$ the following stoichiometric oxides are stable: $CoCr_2O_4$, $MnOOH$, $NiFe_2O_4$, Cr_2O_3 , NiO , $Ni(OH)_2$ and non-stoichiometric: spinel, corundum, M_2O_3 -cubic, NiO , $Ni(OH)_2$, $FeOOH$, and $CoOOH$ [5]. Further predictions can also be made in which the concentration of dissolved ions is considered as a function of potential at pH 10, shown in **Fig. 4.18**. Only ion concentrations above 10^{-6} m were considered, anything below this concentration indicates thermodynamic immunity to corrosion [5, 60-64]. Consider the polarizing potential $-0.25 V_{SCE}$ ($\sim 0.0 V_{SHE}$), at this potential only one species is predicted to dissolve as $Ni(OH)_2$, which is very similar to AESEC dissolution profiles in which only Mn showed an initial dissolution profile at $t = 500$ s (**Figs. 4.18a and 4.16**). This result is also similar to the Mn^{2+} boundaries, where at low polarizing potentials ($-1.5 V_{SHE}$ to $-0.1 V_{SHE}$) Mn^{2+} is predicted to dissolve into solution (**Fig. 4.18a**). When considering stoichiometric oxide phases (**Fig. 4.18b**), many different oxides are predicted to form at $-0.25 V_{SCE}$ ($\sim 0.0 V_{SHE}$), such as spinel, $Ni(OH)_2$, and cubic- M_2O_3 . Similar to the pure metals, at pH 4, the number of predicted oxides to be stable decreases tremendously and are as follows: stoichiometric Cr_2O_3 , $FeCr_2O_4$, and non-stoichiometric spinel [5]. These thermodynamics show the complexity of passive films formed on the surface of MPEAs and is also seen in the results of this study for the tested NiFeCrMnCo MPEAs. The XPS of the passive films formed on MPEAs showed many of these oxides present such as $NiFe_2O_4$, Fe_2O_3 , Cr_2O_3 , and $Cr(OH)_3$ (**Fig. 4.9 and Table 4.3**). These results also correlate with the observed dissolution profiles from AESEC of the Cr22-MPEA during potentiostatic passivation at $-0.25 V_{SCE}$. Dissolution profiles of all alloying elements were below the detection limit, suggesting all elements oxidized directly into the passive film, rather than dissolving into solution (**Fig. 4.16**).

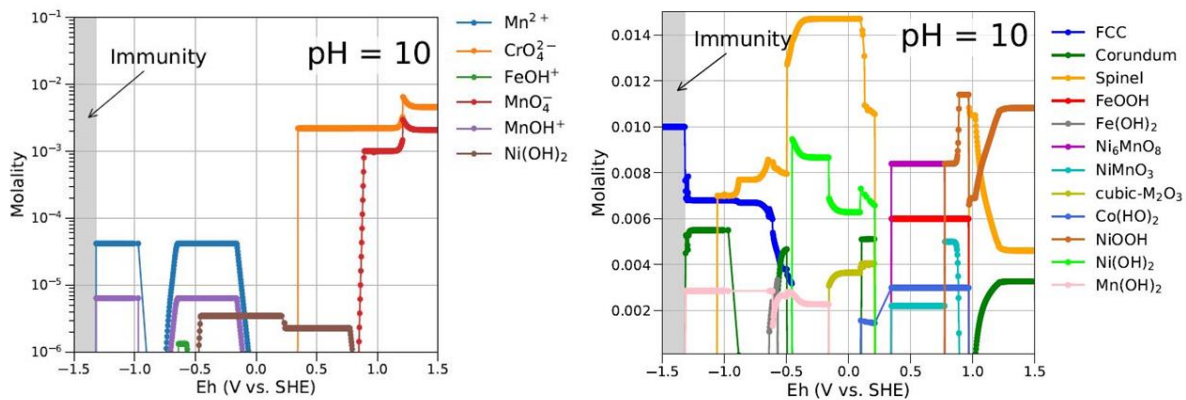


Fig. 4. 18. Ion molality versus potential and phase molality versus potential for the Cr22-MPEA at pH 10. Ion molality refers to reaction products that are dissolved species and phase molality refers to reaction products that are stable solid phase (i.e., precipitate).

4.5.2 Aqueous Passivation of Binary Alloys versus MPEAs

Unlike MPEAs, binary alloys typically do not have such complex passive films form. Commonly, a bilayer passive film will form and consist of an outer hydroxide and inner oxide layer [15-17, 21]. Depending on pH the dominate species can vary between Cr and other alloying elements such as Fe or Ni, when considering stainless steels and Ni-Cr alloys, respectively [19-21, 65, 66]. Wang et. al. investigated the passivation behavior of 316L SS by potentiostatic polarization at 0.1 V_{SCE} for 3600 s in 15g/L NaCl electrolyte adjusted to pH 7, 9, 11, and 13. Researchers found by XPS that the passive films formed on 316L SS at pH 7 consisted of Cr₂O₃, Cr(OH)₃, Fe₂O₃, Fe₃O₄, and FeOOH. As the pH level became more alkaline, Cr₂O₃ became less prominent until no longer being present at pH 13. An increase in Fe oxides and hydroxides was observed when pH level increased [21]. Compared to the Cr-MPEAs in this study, similar oxides were observed with the exception of Fe. Passive films formed on Cr22-, Cr14-, and Cr10-MPEA consisted of Fe₂O₃, and NiFe₂O₄ species. Unlike the above study in which only Fe oxides and hydroxides such as Fe₂O₃, Fe₃O₄, and FeOOH were detected.

Lutton et. al. investigated the passive film growth at 0.2 V_{SCE} on Ni-24Cr alloys in 0.1 M NaCl solution at pH 4 and 10 [66]. XPS analysis of Ni-24Cr passive film at pH 4 after a 10 ks hold were dominate and enriched in Cr oxides and hydroxides compared to Ni. At a pH level 10 the reverse was observed in passive film composition. Passive films formed in pH 10 were enriched in Ni(II)

and consisted mainly of NiO and Ni(OH)₂ [66]. Another study conducted by Mishra et. al. on passive films formed on a commercial Ni-Cr-Mo alloy (Hybrid-BC1) at 0.335 V_{SCE} in 1 M NaCl adjusted to pH 9.7 at 60 °C showed similar results [20]. XPS of passive films formed in pH 10 electrolyte did not detect Cr or Mo species but rather only Ni oxides and hydroxides. Compared to passive films formed on the Cr-MPEAs within this study, Cr22- and Cr14-MPEA were enriched in Ni(II) and Cr(III) species but Cr10-MPEA was more enriched in Cr, even though the Ni concentration increased compared to pH 4 electrolyte (**Fig. 4.13** and **Chapter 3 [51]**). These similarities and differences observed between passive films formed on typically stainless steels and Ni-Cr alloys compared to MPEAs, demonstrates the increased complexity of MPEA passive films. Thermodynamics can help predict the formation of many of these oxides but if predictions were perfect, then differences would not be observed such as in the Cr10-MPEA.

4.6 Conclusions

The electrochemical passivation of a Ni₃₈Fe₂₀Cr_xMn_{21-0.5x}Co_{21-0.5x} MPEA (where x = 22, 14, 10, 6 – at. %) and the effect of alkaline pH was investigated and compared to binary Ni-Cr, Fe-Cr, and Co-Cr alloys. The following conclusions can be drawn:

- LSV showed improved passive behavior for the Cr-MPEAs, Fe-Cr, Ni-Cr and Co-Cr alloys in pH 10 electrolyte. Each alloy exhibited a stable defined passive region exhibiting low passive current densities compared to polarization in pH 4 electrolyte. A dependence in bulk Cr concentration and passive current density was only observed in the Co-Cr and Fe-Cr binary alloys, in which a decrease in current density (10⁻³ to 10⁻⁶ A cm⁻²) was observed with increase in Cr concentration. The Cr-MPEAs and Ni-Cr alloys all had low passive current densities of ~10⁻⁶ A cm⁻² regardless of bulk Cr concentration.
- Passive films formed on the Cr-MPEAs during potentiostatic passivation at -0.25 V_{SCE} in pH 10 electrolyte were all enriched with Ni(II) and Cr(III) and also contained small amounts of Fe(II) and Co(II). Passive films formed on Ni-Cr and Fe-Cr binary alloys were

also enriched with Cr(III) and the other corresponding principle alloying element (ex. Ni). The Cr10-MPEA and Ni-24Cr had similar Cr enrichment and was also the highest in Cr concentration. The Co-Cr binary alloys were not enriched in Cr(III) but rather Co(II).

- Elemental Ni enrichment was observed within the altered zone for the Cr-MPEAs and Ni-Cr binary alloys. Cr depletion was not observed but rather stayed relatively the same as the bulk Cr content. The Cr10-MPEA, Ni-12Cr, and Co-10Cr binary alloys showed slight Cr enrichment within the altered zone.
- All passive films were dominated by hydroxides with the exception of Fe-20Cr. The dominant Cr(III) species for all alloys was Cr hydroxide. The Cr-MPEAs passive films contained high content of Ni hydroxide and low concentrations NiFe₂O₄ spinel, unlike in pH 4 electrolyte in which NiCr₂O₄ and FeCr₂O₄ forms instead.
- Passive films formed in pH 4 electrolyte showed a higher concentration of Cr(III) species (≥ 0.70) compared to when formed in pH 10 electrolyte (≤ 0.5). An increase in Ni(II) and Fe(II) cation fractions were observed in the Cr-MPEAs passive films formed in pH 10 electrolyte.

4.7 References

1. Taylor, C.D., et al., *Integrated computational materials engineering of corrosion resistant alloys*. npj Materials Degradation, 2018. **2**(1): p. 6.
2. Qiu, Y., et al., *Corrosion of high entropy alloys*. npj Materials Degradation, 2017. **1**(1): p. 15.
3. McCafferty, E., *Introduction to Corrosion Science*. 2010, 233 Spring St, New York, NY 10013 USA: Springer.
4. Pourbaix, M., *Atlas of Electrochemical Equilibria in Aqueous Solutions* 1974, Houston, TX: National Association of Corrosion Engineers.
5. Wang, K., et al., *Potential-pH diagrams considering complex oxide solution phases for understanding aqueous corrosion of multi-principal element alloys*. npj Materials Degradation, 2020. **4**(1): p. 35.
6. Elfström, B.O., *The effect of chloride ions on passive layers on stainless steels*. Materials Science and Engineering, 1980. **42**: p. 173-180.

7. Marcus, P., V. Maurice, and H.H. Strehblow, *Localized corrosion (pitting): A model of passivity breakdown including the role of the oxide layer nanostructure*. Corrosion Science, 2008. **50**(9): p. 2698-2704.
8. Natishan, P.M. and W.E. O'Grady, *Chloride Ion Interactions with Oxide-Covered Aluminum Leading to Pitting Corrosion: A Review*. Journal of The Electrochemical Society, 2014. **161**(9): p. C421-C432.
9. Pardo, A., et al., *Influence of pH and Chloride Concentration on the Pitting and Crevice Corrosion Behavior of High-Alloy Stainless Steels*. CORROSION, 2000. **56**(4): p. 411-418.
10. Samin, A.J. and C.D. Taylor, *First-principles investigation of surface properties and adsorption of oxygen on Ni-22Cr and the role of molybdenum*. Corrosion Science, 2018. **134**: p. 103-111.
11. Soltis, J., *Passivity breakdown, pit initiation and propagation of pits in metallic materials – Review*. Corrosion Science, 2015. **90**: p. 5-22.
12. Szklarska-Smialowska, Z., *Pitting corrosion of aluminum*. Corrosion Science, 1999. **41**(9): p. 1743-1767.
13. Yu, X.-x., et al., *New Insights on the Role of Chloride During the Onset of Local Corrosion: TEM, APT, Surface Energy, and Morphological Instability*. CORROSION, 2019. **75**(6): p. 616-627.
14. Lutton, K., et al., *Passivation of Ni-Cr and Ni-Cr-Mo Alloys in Low and High pH Sulfate Solutions*. Journal of The Electrochemical Society, 2023. **170**(2): p. 021507.
15. Zhang, X., D. Zagidulin, and D.W. Shoesmith, *Characterization of film properties on the NiCrMo Alloy C-2000*. Electrochimica Acta, 2013. **89**: p. 814-822.
16. Lloyd, A.C., et al., *Cr, Mo and W alloying additions in Ni and their effect on passivity*. Electrochimica Acta, 2004. **49**(17): p. 3015-3027.
17. Olefjord, I., B. Brox, and U. Jelvestam, *Surface Composition of Stainless Steels during Anodic Dissolution and Passivation Studied by ESCA*. Journal of The Electrochemical Society, 1985. **132**(12): p. 2854-2861.
18. Gray, J.J. and C.A. Orme, *Electrochemical impedance spectroscopy study of the passive films of alloy 22 in low pH nitrate and chloride environments*. Electrochimica Acta, 2007. **52**(7): p. 2370-2375.
19. LECKIE, H.P., *Effect of pH on the Stable Passivity of Stainless Steels*. CORROSION, 1968. **24**(3): p. 70-74.
20. Mishra, A.K. and D.W. Shoesmith, *The activation/depasivation of nickel–chromium–molybdenum alloys: An oxyanion or a pH effect—Part II*. Electrochimica Acta, 2013. **102**: p. 328-335.
21. Wang, Z., et al., *Effect of pH on the Electrochemical Behaviour and Passive Film Composition of 316L Stainless Steel*. Acta Metallurgica Sinica (English Letters), 2019. **32**(5): p. 585-598.
22. Gray, J.J., et al., *Influence of Solution pH, Anion Concentration, and Temperature on the Corrosion Properties of Alloy 22*. Journal of The Electrochemical Society, 2006. **153**(3): p. B61.
23. Frankel, G.S., T. Li, and J.R. Scully, *Perspective—Localized Corrosion: Passive Film Breakdown vs Pit Growth Stability*. Journal of The Electrochemical Society, 2017. **164**(4): p. C180-C181.

24. Gerard, A.Y., et al., *Progress in Understanding the Origins of Excellent Corrosion Resistance in Metallic Alloys: From Binary Polycrystalline Alloys to Metallic Glasses and High Entropy Alloys*. CORROSION. **0**(0): p. null.
25. Chen, Y.Y., et al., *Microstructure and electrochemical properties of high entropy alloys—a comparison with type-304 stainless steel*. Corrosion Science, 2005. **47**(9): p. 2257-2279.
26. Wang, Z., et al., *Pseudo-passivation mechanism of CoCrFeNiMo0.01 high-entropy alloy in H₂S-containing acid solutions*. Corrosion Science, 2021. **179**: p. 109146.
27. Luo, H., et al., *Corrosion behavior of an equiatomic CoCrFeMnNi high-entropy alloy compared with 304 stainless steel in sulfuric acid solution*. Corrosion Science, 2018. **134**: p. 131-139.
28. Wang, L., et al., *Study of the surface oxides and corrosion behaviour of an equiatomic CoCrFeMnNi high entropy alloy by XPS and ToF-SIMS*. Corrosion Science, 2020. **167**: p. 108507.
29. Zhou, Q., et al., *Corrosion behavior of Hf_{0.5}Nb_{0.5}Ta_{0.5}Ti_{1.5}Zr refractory high-entropy alloy in aqueous chloride solutions*. Electrochemistry Communications, 2019. **98**: p. 63-68.
30. Gerard, A.Y., et al., *Aqueous passivation of multi-principal element alloy Ni₃₈Fe₂₀Cr₂₂Mn₁₀Co₁₀: Unexpected high Cr enrichment within the passive film*. Acta Materialia, 2020. **198**: p. 121-133.
31. Li, T., et al., *Localized corrosion behavior of a single-phase non-equimolar high entropy alloy*. Electrochimica Acta, 2019. **306**: p. 71-84.
32. Sahu, S., et al., *Localized Corrosion Behavior of Non-Equiatomic NiFeCrMnCo Multi-Principal Element Alloys*. Electrochimica Acta, 2020. **354**: p. 136749.
33. Rodriguez, A., J.H. Tyleczak, and M. Ziomek-Moroz, *Corrosion Behavior of CoCrFeMnNi High-Entropy Alloys (HEAs) Under Aqueous Acidic Conditions*. ECS Transactions, 2017. **77**(11): p. 741-752.
34. Dworschak, D., et al., *Bottom-up characterization of electrochemical passivity from simple binary alloys to high entropy alloys*. Electrochimica Acta, 2022. **405**: p. 139804.
35. Jayaraj, J., et al., *Corrosion behavior and surface film characterization of TaNbHfZrTi high entropy alloy in aggressive nitric acid medium*. Intermetallics, 2017. **89**: p. 123-132.
36. Koga, G.Y., et al., *Corrosion resistant and tough multi-principal element Cr-Co-Ni alloys*. Journal of Alloys and Compounds, 2021. **884**: p. 161107.
37. Lee, C.P., et al., *Enhancing pitting corrosion resistance of Al_xCrFe1.5MnNi0.5 high-entropy alloys by anodic treatment in sulfuric acid*. Thin Solid Films, 2008. **517**(3): p. 1301-1305.
38. Nene, S.S., et al., *Corrosion-resistant high entropy alloy with high strength and ductility*. Scripta Materialia, 2019. **166**: p. 168-172.
39. Pang, J., et al., *Oxide MnCr₂O₄ induced pitting corrosion in high entropy alloy CrMnFeCoNi*. Materialia, 2019. **6**: p. 100275.
40. Zhang, Z., T. Yuan, and R. Li, *Corrosion performance of selective laser-melted equimolar CrCoNi medium-entropy alloy vs its cast counterpart in 3.5 wt% NaCl*. Journal of Alloys and Compounds, 2021. **864**: p. 158105.
41. Muangtong, P., et al., *The corrosion behaviour of CoCrFeNi-x (x = Cu, Al, Sn) high entropy alloy systems in chloride solution*. Corrosion Science, 2020. **172**: p. 108740.

42. Wang, Z., et al., *Effect of temperature on the passive film structure and corrosion performance of CoCrFeMoNi high-entropy alloy*. Corrosion Science, 2022. **208**: p. 110661.
43. Choudhary, S., N. Birbilis, and S. Thomas, *Evolution of Passivity for the Multi-Principal Element Alloy CoCrFeNi with Potential, pH and Exposure in Chloride Solution*. Corrosion, 2021.
44. Wang, Z., et al., *Corrosion behavior and surface characterization of an equiatomic CoCrFeMoNi high-entropy alloy under various pH conditions*. Journal of Alloys and Compounds, 2022. **900**: p. 163432.
45. Quiambao, K.F., et al., *Passivation of a corrosion resistant high entropy alloy in non-oxidizing sulfate solutions*. Acta Materialia, 2019. **164**: p. 362-376.
46. Zheng, Z.Y., et al., *Microstructure and corrosion behaviour of FeCoNiCuSnx high entropy alloys*. Materials Science and Technology, 2015. **31**(10): p. 1148-1152.
47. Qiu, X.-W. and C.-G. Liu, *Microstructure and properties of Al2CrFeCoCuTiNix high-entropy alloys prepared by laser cladding*. Journal of Alloys and Compounds, 2013. **553**: p. 216-220.
48. Lu, P., et al., *Computational design and initial corrosion assessment of a series of non-equimolar high entropy alloys*. Scripta Materialia, 2019. **172**: p. 12-16.
49. Kautz, E.J., et al., *Element redistributions during early stages of oxidation in a Ni38Cr22Fe20Mn10Co10 multi-principal element alloy*. Scripta Materialia, 2021. **194**: p. 113609.
50. Han, J., et al., *Potential Dependent Mn Oxidation and Its Role in Passivation of Ni38Fe20Cr22Mn10Co10 Multi-Principal Element Alloy Using Multi-Element Resolved Atomic Emission Spectroelectrochemistry*. Journal of The Electrochemical Society, 2021. **168**(5): p. 051508.
51. Gerard, A.Y., et al., *The role of chromium content in aqueous passivation of a non-equiatomic Ni38Fe20Cr_xMn21-0.5xCo21-0.5x multi-principal element alloy (x = 22, 14, 10, 6 at%) in acidic chloride solution*. Acta Materialia, 2023. **245**: p. 118607.
52. Bruemmer, S.M., et al., *Grain boundary selective oxidation and intergranular stress corrosion crack growth of high-purity nickel binary alloys in high-temperature hydrogenated water*. Corrosion Science, 2018. **131**: p. 310-323.
53. Lutton, K., et al., *Understanding multi-element alloy passivation in acidic solutions using operando methods*. Electrochemistry Communications, 2017. **80**: p. 44-47.
54. Jakupi, P., et al., *The impedance properties of the oxide film on the Ni–Cr–Mo Alloy-22 in neutral concentrated sodium chloride solution*. Electrochimica Acta, 2011. **56**(17): p. 6251-6259.
55. Doniach, S. and M. Sunjic, *Many-electron singularity in X-ray photoemission and X-ray line spectra from metals*. Journal of Physics C: Solid State Physics, 1970. **3**(2): p. 285-291.
56. KOLXPD, <http://kolxpd.kolibrik.net>.
57. Biesinger, M.C., et al., *Resolving surface chemical states in XPS analysis of first row transition metals, oxides and hydroxides: Cr, Mn, Fe, Co and Ni*. Applied Surface Science, 2011. **257**(7): p. 2717-2730.
58. Ogle, K., *Atomic Emission Spectroelectrochemistry: Real-Time Rate Measurements of Dissolution, Corrosion, and Passivation*. CORROSION, 2019. **75**(12): p. 1398-1419.

59. Ogle, K. and S. Weber, *Anodic Dissolution of 304 Stainless Steel Using Atomic Emission Spectroelectrochemistry*. Journal of The Electrochemical Society, 2000. **147**(5): p. 1770-1780.
60. Thompson W. T., K., M.H., Bale, C.W., Pelton, A.D., *Uhlig's Corrosion Handbook, 3rd Edition*. 3 ed, ed. R.W. Revie. 2011, New Jersey: The Electrochemical Society and John Wiley & Sons.
61. Cubicciotti, D., *Flow-assisted corrosion of steel and the influence of Cr and Cu additions*. Journal of Nuclear Materials, 1988. **152**(2): p. 259-264.
62. Cubicciotti, D., *Pourbaix Diagrams for Mixed Metal Oxides — Chemistry of Copper in BWR Water*. Corrosion, 1988. **44**(12): p. 875-880.
63. Cubicciotti, D., *Equilibrium chemistry of nitrogen and potential-pH diagrams for the Fe-Cr-H₂O system in bwr water*. Journal of Nuclear Materials, 1989. **167**: p. 241-248.
64. Cubicciotti, D., *Potential-pH diagrams for alloy-water systems under LWR conditions*. Journal of Nuclear Materials, 1993. **201**: p. 176-183.
65. Sun, M., et al., *Effect of pH on Semiconducting Property of Passive Film Formed on Ultra-High-Strength Corrosion-Resistant Steel in Sulfuric Acid Solution*. Metallurgical and Materials Transactions A, 2013. **44**(10): p. 4709-4717.
66. Cwalina, K.L., et al., *In Operando Analysis of Passive Film Growth on Ni-Cr and Ni-Cr-Mo Alloys in Chloride Solutions*. Journal of The Electrochemical Society, 2019. **166**(11): p. C3241-C3253.

5. Evolution of Multi-Principal Element Alloy $\text{Ni}_{38}\text{Fe}_{20}\text{Cr}_x\text{Mn}_{21-0.5x}\text{Co}_{21-0.5x}$ ($x = 22, 14$ at. %) passive film as a function of exposure time in acidified chloride solution

5.1 Abstract

Electrochemical potentiostatic passivation as a function of exposure time was investigated for passive films formed on a single-phase non-equiatomic $\text{Ni}_{38}\text{Fe}_{20}\text{Cr}_x\text{Mn}_{21-0.5x}\text{Co}_{21-0.5x}$ ($x = 22, 14$ at. %) multi-principal element alloy (MPEAs) and compared to a solid solution Ni-24Cr binary alloy. Various electrochemical methods, such as electrochemical impedance spectroscopy (EIS) and linear sweep voltammetry (LSV), were utilized to evaluate the corrosion characteristics of each passive film formed at all exposure times. The passive film formed at each exposure time was characterized using ex situ angle-resolved X-ray photoelectron spectroscopy (AR-XPS). At each exposure time, passive film formation was observed on all alloy surface's during potentiostatic hold at a passive potential of $-0.25 \text{ V}_{\text{SCE}}$. LSV experiments revealed, the Cr22-, Cr14-MPEA and Ni-24Cr binary alloy passive films exhibited a linear passive region with low passive current densities at all exposure times. Cr(III) enrichment was observed in both Cr-MPEAs and Ni-24Cr passive films at all exposure times. The Cr22-MPEA passive film was enriched with Co(II) at earlier times but was depleted at longer exposure times. At exposure times 100 s and 1 ks, the Cr-MPEA passive films contained a small fraction of Ni(II), Mn(II), Fe(II), less than their bulk fractions. At longer exposure times Mn(II) and Fe(II) increased in concentration within the Cr-MPEA passive films. At early exposure times Cr-MPEA passive films consisted mainly of hydrated Cr(III), suggested to be $\text{Cr}(\text{OH})_3$ but the species decreased in concentration with exposure time. Cr-spinels were not detected in the Cr-MPEA passive films at early exposure times but spinel of Cr with Fe, Ni, Co, Mn were detected at longer exposure times, eventually becoming the dominate oxide molecular species. Passive films formed on the Ni-24Cr surface consisted mainly of hydrated Ni(II) and Cr(III) regardless of exposure time. Cr spinels were not detected in passive films formed on Ni-24Cr surface. How passive films evolve on Cr-MPEA surfaces as a function of exposure time is discussed considering both thermodynamics and kinetic principles. It should be noted that passive films and protection attributes in short term lab experiments are not necessarily representative of long-term behavior. It is further noted that this behavior may be more

pronounced in MPEAs because of possible oxide molecular stabilities, thermodynamic driving forces and kinetic variations brought about by a diversity of elements.

5.2 Introduction

When passive films are formed under aqueous conditions, the resulting film's chemical identity can vary or evolve with time depending on how long it is exposed to the corrosive solution and how harsh that solution is. Typically, kinetics will dominate on how a passive film forms during short term passivation but at longer passivation times already formed oxides will evolve into the most thermodynamically favorable phase [1, 2]. Studies have explored this phenomenon in the case of conventional alloys and have shown interesting results when exposed to both acidic and alkaline solutions [1, 3-5]. Various passive film oxide configurations have been proposed for Ni-Cr corrosion resistant alloys (CRAs) such as, a Cr-rich stoichiometric oxide, a Ni-rich stoichiometric oxide, Ni-Cr spinel, amorphous oxide, or a non-stoichiometric solid solution oxide depending on passivation time [1-3, 5-15]. This high variability is commonly linked to changes in elemental dissolution, oxide stability, and/or non-equilibrium solute capture. One issue that this brings up regarding corrosion protection is the question of which oxide is most protective given the oxide regulates point defect migration, cation solubilization and mitigate instabilities which cause breakdown [16].

Under acidic conditions, passivation of conventional Cr-based CRAs commonly do not initially start with forming a Cr dominated oxide, even though it is thermodynamically more stable than Ni- and Fe- oxides [1, 2, 5, 11, 12, 15]. This behavior has been shown to occur in Ni-Cr and Ni-Cr-Mo alloys [1, 5, 15]. Lutton investigated the passive film growth of a Ni-22Cr and Ni-20Cr-10Mo (wt. %) from 10 s to 10 ks in 0.1 M NaCl pH 4 utilizing both XPS and inductively coupled plasma-mass spectrometry (ICP-MS) [1]. For both alloys at initial oxidation times the passive film was enriched with Ni-oxide species. The formation of Ni-oxide species during early growth times may be a result of favored NiO formation due to its epitaxial relationship with the bulk matrix which is FCC. After 1 ks, enrichment switches to Cr and Ni preferentially dissolves into solution. It was suggested each passive film was a non-stoichiometric solid solution rock-salt and corundum oxide with solute captured cations [1]. It was concluded initial oxide compositions (i.e., at short growth times) were governed by non-equilibrium solute capture and enrichment was promoted by

the dissolution of Ni at longer growth times (i.e., Ni oxide dissolution). This behavior may be governed by the formation rate competing with the chemical dissolution rate at the oxide/electrolyte interface. Other investigations have shown that after exposure at a fixed time, from 300 s to 44 h, a layered passive film forms consisting of stoichiometric anhydrous inner oxides and hydrated outer oxides [7, 10, 17-19]. Ebrahimi et al. characterized passive films formed on Alloy C-22 (22 wt. % Cr) at a passive potential for 8 h in 5 M NaCl solution adjusted to pH 7. After 8 h exposure in 5 M NaCl, the passive film formed on the C-22 alloy surface exhibited a bilayer structure. The inner layer was proposed to be Cr_2O_3 while the outer layer consisted of Mo oxides and hydrated Ni and Cr oxides [10]. Unfortunately, shorter exposure times were not explored and how these layered oxides developed was not discussed.

A number of multi-principal element alloy (MPEAs) corrosion investigations exists in which the passive behavior and resulting chemistry of the passive film have been characterized [20-38]. Typically, these studies explore the electrochemical nature of passive films formed at a fixed time (600 s to 11 h) or rate during aqueous oxidation and in general have shown that when alloyed with Cr, passive films are enriched in oxidized Cr (III) cations [20-22, 25, 28, 34-40]. Some MPEA studies have indicated after a set exposure time passivated films may be either a solid solution oxide or layered oxides consisting of anhydrous oxides and hydroxides [28, 33, 39]. Zhou et al. investigated the passive behavior of a $\text{Hf}_{0.5}\text{Nb}_{0.5}\text{Ta}_{0.5}\text{Ti}_{1.5}\text{Zr}$ alloy by potentiostatic passivation for 600 s at passive potentials of 1.0 V_{SCE} , 1.9 V_{SCE} , 5.0 V_{SCE} in 3.5 wt. % NaCl. After potentiostatic passivation passive films were characterized by X-ray photoelectron spectroscopy (XPS). From XPS it was concluded passive films formed at each potential consisted of a single-phase solid solution oxide containing high concentrations of passivity promoting elements such as, Ti, Zr, Hf, Nb, and Ta [33]. Another potentiostatic passivation study conducted by Quiambao et al. on a $\text{Ni}_{38}\text{Cr}_{21}\text{Fe}_{20}\text{Ru}_{13}\text{Mo}_6\text{W}_2$ alloy showed similar results after passivation for 10 ks at 0.1 M Na_2SO_4 adjusted to pH 4 at a passive potential [28]. Researchers concluded the resulting passive film consisted of a non-equilibrium non-stoichiometric solid solution containing all elements from both XPS and atom probe tomography (ATP). The above studies suggest that after passivation at a passive potential the resulting film will consist of a solid solution oxide both at short (600 s) and relatively longer (10 ks) exposure times [28, 33]. But another study has reported different results for passivation for 1 h compared to the other two. Wang et al. found that after forming a passive film for 1 h at 0 V_{MSE} in 0.05 M H_2SO_4 on the surface of a $\text{Cr}_{15}\text{Fe}_{10}\text{Co}_5\text{Ni}_{60}\text{Mo}_{10}$ MPEA the passive

film consisted of a bilayer structure. The outer layer was composed of Ni and Cr hydroxides and Fe and Mo oxides and the inner layer consisted mainly of Cr oxides [39]. This result is different compared to the passive films formed at 600 s and 10 ks. With such limited information known on how a passive film evolves and which alloying elements enrich or deplete over exposure time, many unknowns exist on how these solid solution or layered oxides form on MPEA surfaces. Moreover, this information is critical to how the oxide regulates anion and cation transmission which effects the passive current density as well as the mechanism of passivation.

A few time dependent investigations have been conducted but are limited [21, 23, 26, 38]. Choudhary et al. investigated the time evolution of passivity in an equiatomic CoCrFeNi MPEA in 0.1 M NaCl solution at three different pH levels: 2, 6, and 10 [38]. The electrochemical behavior of passive films formed on the CoCrFeNi MPEA were characterized by electrochemical impedance spectroscopy (EIS) at the open-circuit potential (OCP) at following time intervals: 1800 s, 1 h, 2 h, and 4 h. The resulting polarization resistance of the passive films and OCP, regardless of pH, increased with exposure time. These results suggest passive films formed on the CoCrFeNi MPEA become more corrosion resistant over time. Element-resolved dissolution analysis was conducted during potentiostatic polarization at 0.350 V_{SHE} (standard hydrogen electrode) for 1500 s. The dissolution profiles of Cr and Co both decreased with exposure time suggesting enrichment of these elements as cations within the passive film. The passive film protectiveness was attributed to an enrichment of Cr(III) species but unfortunately X-ray photoelectron spectroscopy (XPS) characterization was only conducted after a 4 h OCP hold and little is known how Cr(III) evolved at shorter or longer time intervals [38]. Many other time dependent investigations utilize in situ solution analysis during passivation, for example atomic emission spectroelectrochemistry (AESEC), but this is limited information pertaining to the passive film's chemical identity as a function of time [21, 23, 26].

To better understand the electrochemical properties of passive films formed on MPEAs it is important to understand how they initially form and evolve over time when exposed in a corrosive environment. Many uncertainties exist around the nature of oxides formed on MPEAs in aqueous conditions, such as; Do MPEAs behave like CRA Ni-Cr alloys in which a Cr dominate oxide is formed over time but during initial passivation Ni oxides are more favorable to form such as, NiO? Are some oxides more favorable to form at initial exposure times and at longer durations do these

oxides evolve and/or dissolve to form more complex oxides such as spinels? How does the presence of multiple alloying elements effect the evolution of Cr enrichment during aqueous oxidation? These questions are only some of the unknowns revolved around MPEA passivation. With lacking information, it is not well understood how MPEAs form highly enriched solid solution oxides and/or layered oxides during aqueous oxidation. Moreover, passivity mechanisms and protectiveness in short term experiments may not reflect long term behavior.

In this study, the evolution of aqueous oxidation was investigated in for two non-equimolar, single phase, solid solution $\text{Ni}_{38}\text{Fe}_{20}\text{Cr}_x\text{Mn}_{21-0.5x}\text{Co}_{21-0.5x}$ MPEAs, where $x = 22$ and 14 at. %, and compared to a solid solution Ni-24Cr (at. %) binary alloy. The goal of this study is to provide an improved understanding how passive films evolve when formed on MPEAs with one substrate structure (i.e., FCC) and exposed to slightly acidic chloride electrolyte. The electrochemical behavior of passive films formed at a range of exposure times was explored utilizing potentiostatic passivation at a passive potential. Potentiostatic single frequency-EIS and full spectral EIS was utilized for in situ monitoring of passive film formation/growth during potential hold at various exposure times. Angle resolved-XPS characterization was conducted on resulting passive films and comparisons was made between oxide compositions, metallic composition at the oxide/metal interface (i.e., altered zone), valence states, and oxide configurations at various times.

5.3 Experimental

The $\text{Ni}_{38}\text{Fe}_{20}\text{Cr}_x\text{Mn}_{21-0.5x}\text{Co}_{21-0.5x}$ – at. % MPEAs were arc-melted, cast, and homogenized at $1100\text{ }^\circ\text{C}$ for 96 h using methods described previously [41]. The MPEA forms a single-phase FCC solid solution where $x = 22$ and 14 at. %. For simplicity, these MPEAs will be referred to as Cr22- and Cr14-MPEA, respectively. Solid solution Ni-24Cr (at. %) binary alloy was arc-melted, cast, rolled, solutionized at $1100\text{ }^\circ\text{C}$, and recrystallized, resulting in a homogenous single-phase FCC alloy. All testing materials and corresponding chemical composition are listed in **Table 5.1**. Prior to potentiostatic passivation and AR-XPS, sample surfaces were mechanically ground to 1200 grit SiC and then polished with $0.25\text{ }\mu\text{m}$ diamond suspension. Samples were degreased after polishing by sonicating in acetone, 1:1 acetone and isopropanol, isopropanol, and deionized water, each for 1 min, and dried with $\text{N}_{2(g)}$. For XPS characterization of the native air oxide and cathodic pretreated

surfaces of the Cr22-MPEA and Ni-24Cr alloy, samples were mechanically ground to 1200 grit SiC and degreased with the same above procedure.

Table 5. 1. Multiple-Principal Element Alloys and Binary Alloy Nominal Composition

Alloy	Chemical Composition (at. %)
Cr22-MPEA	38Ni-20Fe-22Cr-10Mn-10Co
Cr14-MPEA	38Ni-20Fe-14Cr-14Mn-14Co
Ni-24Cr	76Ni-24Cr

Electrochemical tests were conducted in $N_{2(g)}$ – deaerated 0.1 M NaCl, with the final pH adjusted to 4 using 0.1 M HCl. Experiments were performed with a Gamry Instruments Reference 600+™ potentiostat. A standard three-electrode cell was utilized with a Pt mesh counter electrode, a saturated calomel reference electrode (SCE) and an MPEA or binary alloy sample as the working electrode. Samples were pressed against a rubber O-ring to expose a working area of 0.1 cm². All potentials are reported against SCE.

Electrochemical passivation was investigated within the passive potential region by potentiostatic passivation, where the passive potential was determined from LSV, shown in Task 1 and 3 [20, 34]. Potentiostatic passivation was conducted using the following procedure: (1) cathodic treatment to minimize the effect of the air-formed oxide at -1.3 V_{SCE} for 600 s, (2) potential hold at -0.25 V_{SCE} within the passive potential region for 5 s, 1 ks, 10 ks, and 86.4 ks (24 h) followed by (3) an EIS measurement over a range of frequencies at the same potential as (2). Two different frequency ranges were used for EIS measurements. At potential hold times 5 s and 1000s a frequency range of 100 kHz to 100 mHz was utilized. At potential hold times 10 ks and 86.4 ks, a frequency range of 100 kHz to 1 mHz was utilized. The difference in frequency ranges is due to passive film stability and the time required to characterize films at low frequency ≤ 10 mHz. Potentiostatic passivation times of 5 s and 1 ks were utilized to minimize the amount of time held at -0.25 V_{SCE}, considering EIS potential hold time (this was not an issue at 10 ks and 86.4 ks). The total time each Cr-MPEA is held at the passive applied potential is equal to the potentiostatic hold time plus time required for EIS measurements. The actual time held for each alloy considering both potentiostatic hold and EIS measurements varies from 130 s to 150 s and ~1110 s. For simplicity the nominal time 100s and 1 ks nomenclature will be used throughout the manuscript

but data was reported at actual exposure times at the time of the measurement. On all figure keys actual hold time at the passive potential is indicated in parenthesis (potentiostatic hold + EIS). During the potentiostatic hold experiment, passive film growth was monitored as a function of time using a single-frequency EIS method (SF-EIS) at $f = 1$ Hz and an AC potential magnitude of $20 \text{ mV}_{\text{rms}}$ [5, 20, 28]. All EIS data were analyzed with an equivalent circuit model initially established for alloy C-22 and adapted for MPEAs [20, 28, 42, 43]. Approximate oxide thickness (ℓ_{ox}) as a function of time was calculated (i.e., to monitor oxide growth) based on the relationship between the equivalent circuit model, constant phase element exponential, and $-Z''$, equation and methodology shown in Chapter 2 [5, 20, 28].

Linear sweep voltammetry (LSV) experiments were conducted over a range of applied potentials ($-0.25 \text{ V}_{\text{SCE}}$ to $0.4 \text{ V}_{\text{SCE}}$) with a scan rate of 0.5 mV s^{-1} . Prior to LSV passive films were formed on the alloy surfaces using the above cathodic pretreated and SF-EIS methodology for each exposure time. During LSV, the imaginary impedance component ($-Z''$) was monitored at an applied AC voltage of $20 \text{ mV}_{\text{rms}}$ at $f=1$ Hz.

XPS spectra were acquired of the Cr22-MPEA and Cr14-MPEA native air oxide and cathodic pretreated surfaces using Al K α X-rays (binding energy: 1468.7 eV) with a take-off angle of 45° at a pass energy of 26 eV with a spot size of $100 \mu\text{m}$ and an analysis depth of $< 10 \text{ nm}$ in a PHI VersaProbe IIITM system. AR-XPS spectra were acquired for the potentiostatically grown passive films at $-0.25 \text{ V}_{\text{SCE}}$ on each testing material utilizing AR-XPS with the above XPS parameters with the exception of take-off angle in which 45° and 90° were used. Cation fraction within the passive film and elemental composition below the metal/film interface (relative to all cations or elements detected) were determined by spectral deconvolution of individual core-level spectra with KOLXPDTM analysis software. Spectral deconvolution was implemented with Voigt functions for oxides, asymmetric Doniach Sunjic-like features for metals, and a Shirley background subtraction [44, 45]. For each alloying element, the $2p$ core feature was deconvoluted utilizing reported parameters for multiplet splitting of reference stoichiometric compounds [46]. Due to Ni Auger overlap with Mn $2p_{3/2}$, Co $2p_{3/2}$, and Fe $2p_{2/3}$ spectra, the $2p_{1/2}$ feature was utilized for XPS spectral deconvolution. A peak intensity limit of less than or equal to the intensity of noise was considered for Co and Mn $2p_{1/2}$ spectra, in order to establish an upper limit to the Mn(II) and Co(II) fractions present within the passive film. If XCr_2O_4 ($\text{X} = \text{Fe}, \text{Mn}, \text{Co}$) spinels were detected within the Cr

2p_{3/2} spectrum, then these species were assumed to be the oxide intensity observed within the Fe2p_{1/2}, Mn2p_{1/2}, and Co2p_{1/2} spectra. A more detailed description of XPS spectral deconvolution has been provided previously in Chapter 2 [20, 21, 28, 47].

A surface enrichment-depletion calculation approach, developed by Castle and Asami [48], was utilized to calculate a cation/elemental enrichment or depletion term for each alloying element A, f_A , where A = Ni, Fe, Cr, Mn, and Co within the native air oxide and passive films formed during electrochemical passivation at -0.25 V_{SCE}. Enrichment and depletion terms were determined from all cation fractions ($f_{A,ox}$) as well as separately for the metallic concentration at the metal/film interface, hereafter referred to as the altered zone ($f_{A,az}$), determined from XPS or AR-XPS. A more detail enrichment-depletion methodology has been previously provided in Chapter 2 [20].

5.4 Results

5.4.1 Aqueous Oxidation at an Applied Passive Potential of -0.25 V_{SCE}

The passive current decay during potentiostatic hold at -0.25 V_{SCE} for 100 s, 1 ks, 10 ks, and 86.4 ks in 0.1 M NaCl for Cr22-, Cr14-MPEA, and Ni-24Cr binary alloy is shown in **Fig. 5.1**. At all exposure times each Cr alloy exhibited a low passive current density, which continuously decreased to 10⁻⁷ A cm⁻². At longer exposure times of 10 ks and 86.4 ks each alloy's passive current density exhibited a rapid decrease and became negative (not shown) indicative of cathodic reaction rates exceeding anodic rates. This phenomenon occurred for Cr22 at $t_{10ks} > 1.4$ ks and $t_{86.4ks} > 2$ ks (**Fig. 5.1a**), Cr14-MPEA at $t_{10ks} \approx 8$ ks and $t_{86.4ks} \approx 20$ ks (**Fig. 5.1b**), and Ni-24Cr during 10 ks and 86.4 ks exposure at $t_{10ks} \approx 800$ s and $t_{86.4ks} \approx 7$ ks (**Fig. 5.1c**). The Cr14-MPEA exhibited instantaneous metastable breakdown events during 10 ks and 86.4 ks exposure, indicated by the current density spikes starting at $t \approx 7$ ks.

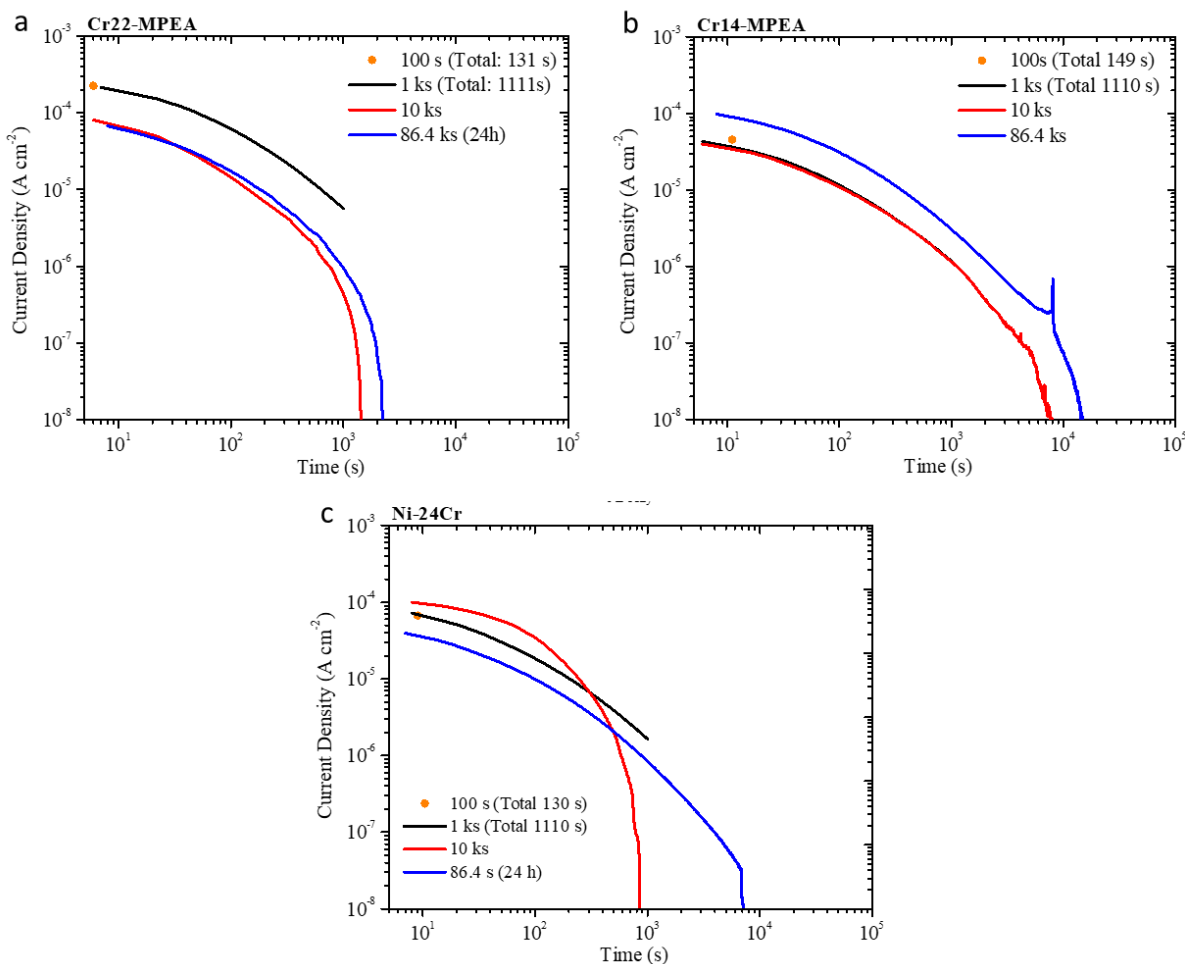


Fig. 5. 1. Measured electrochemical current density during potentiostatic hold at $-0.25 V_{SCE}$ for 100 s, 1ks, 10 ks, and 86.4 ks (24 h) after initial cathodic reduction at $-1.3V_{SCE}$ for 600 s in deaerated 0.1 M NaCl + HCl at pH 4 of (a) Cr22-MPEA, (b) Cr14-MPEA, and (c) Ni-24Cr. Time outside the parathesis is the nominal time and the time within parathesis is the total time held at $-0.25V_{SCE}$ (SFEIS time + EIS time).

The impedance behavior of the passive films and impedance properties of the corroding interface were characterized using potentiostatic EIS at the end of each exposure time at a potential hold of $-0.25 V_{SCE}$. Bode plots for each alloy in 0.1 M NaCl at each exposure time are shown in **Fig. 5.2**. For all alloys, the low-frequency impedance magnitude increased with exposure time. At an impedance frequency of 0.1 Hz, the Cr22-MPEA and Cr14-MPEA exhibited an increase in impedance magnitude with exposure time but the largest difference was observed at exposure times 100 s and 1 ks, shown in **Fig 5.2a and 5.2b**, respectively. At 0.1 Hz and exposure time of 100 s and 86.4 ks, the impedance magnitude increased from $4.8 \times 10^3 \Omega \text{ cm}^2$ to $4.2 \times 10^4 \Omega \text{ cm}^2$

for the Cr22-MPEA passive film and from $1.2 \times 10^4 \Omega \text{ cm}^2$ to $4.4 \times 10^4 \Omega \text{ cm}^2$ for Cr14-MPEA passive film. In the case of the Ni-24Cr binary alloy, at 0.1 Hz an increase in the impedance magnitude was observed at exposure times 100 s, 1ks, and 86.4 ks, shown in **Fig. 5.2c**. At 10 ks a slight decrease in impedance magnitude was observed compared to 1 ks exposure time. At 0.1 Hz and exposure time of 100s and 86.4 ks, the impedance magnitude increased from $1.1 \times 10^4 \Omega \text{ cm}^2$ to $6.0 \times 10^4 \Omega \text{ cm}^2$ for passive films formed on Ni-24Cr. At 1 mHz, the impedance magnitude for each alloys passive film increased to $10^5 \Omega \text{ cm}^2$ (**Fig. 5.2**). The largest difference observed in impedance magnitude at 1 mHz were for passive films formed on Ni-24Cr at duration times of 10 ks and 86.4 ks. The observed increase in impedance magnitude both at 0.1 Hz and 1 mHz from short to long exposure times suggest these passive films are becoming more protective with time. It should be noted the improved passive properties as a function of exposure time are due to passive film composition and structure changes rather than the thickening of the film. Recall in Chapter 2 and 3, potentiostatically formed passive films on MPEA surfaces reached a steady state thickness at $\sim t \geq 3000 \text{ s}$. In summary, the Cr22-, Cr14-MPEA and Ni-24Cr binary alloy formed a passive film at each exposure time indicated by a decrease in current density during potentiostatic hold. The resulting passive film impedance increased with exposure time, suggesting the formation of a more protective passive film.

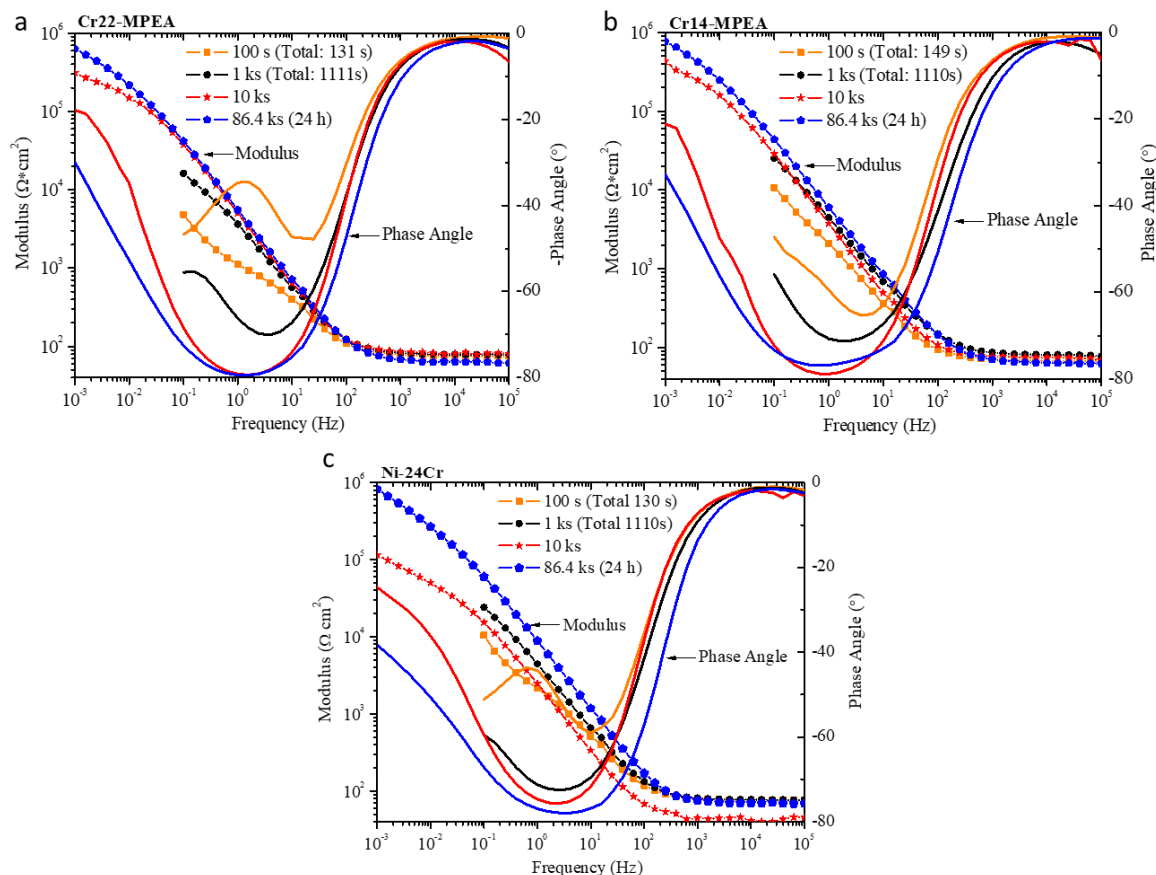


Fig. 5. 2. Bode plot of Cr22-MPEA, Cr14-MPEA, and Ni-24Cr in deaerated 0.1 M NaCl + HCl at pH 4 after potentiostatic hold at $-0.25 V_{SCE}$ for 100s, 1ks, 10 ks, and 86.4 ks (24 h). Time outside the parathesis is the nominal time and the time within parathesis is the total time held at $-0.25V_{SCE}$ (SFEIS time + EIS time).

5.4.2 Electrochemical Behavior of Passive Films Formed During Aqueous Oxidation

The LSV curves and corresponding potential dependence of the imaginary impedance component ($-Z''$) at $f = 1$ Hz of passive films formed during potentiostatic hold at $-0.25 V_{SCE}$ for 100 s, 1 ks, 10 ks, and 86.4 ks in 0.1 M NaCl for Cr22-, Cr14-MPEA, and Ni-24Cr binary alloy are shown in **Fig. 5.3a and 5.3b**, respectively. Each alloy's passive film exhibited a clear linear passive region, low current densities of 10^{-7} to 10^{-6} A cm^{-2} , and an increase in $-Z''$ during LSV (**Fig. 5.3a and 5.3b**), with the exception of Cr22-MPEA passive film formed during 1 ks exposure time. Note that $-Z''$ does not start at zero in Fig. 5.3b typical of previous studies with oxide reduction as the oxide has formed at $-0.25V_{SCE}$ for the times indicated. The Cr22-MPEA's passive film formed at 100 s LSV exhibited a broad passive region comparable to 86.4 ks and wider than

at 10 ks exposure times. This was not observed in Cr14-MPEA and Ni-24Cr in which their passive films formed at 100 s had a narrower passive region compared to all other exposure times (**Fig. 5.3a**). Current-potential spikes and $-Z''$ -potential spikes were observed in the passive regions for both Cr22- and Cr14-MPEAs, indicative of instantaneous metastable breakdown events (**Fig. 5.3a and 5.3b**).

The breakdown potential behavior of the Cr22-MPEA passive films also exhibited interesting behavior compared to Cr14-MPEA and Ni-24Cr. The Cr22-MPEA passive film formed at 100s demonstrated a slightly more positive breakdown potential ($0.15 V_{SCE}$) compared to 10 ks ($0.10 V_{SCE}$) and 86. ks ($0.14 V_{SCE}$) exposure times (**Fig. 5.3a and 5.3b**). In the case of the Cr14-MPEA, the breakdown potential increases with exposure time and at 10 ks and 86.4 ks its breakdown potential is the same ($0.08 V_{SCE}$). The Ni-24Cr passive films showed a more stable and broader passive region at each exposure time compared to the Cr-MPEAs. This is also clearly observed the imaginary impedance component, which was greater in magnitude at all exposure times compared to the Cr-MPEAs $-Z''$ (**Fig. 5.3b**). The breakdown potential at 100 s and 1 ks was also higher than that of the Cr-MPEAs, $0.18 V_{SCE}$ and $0.28 V_{SCE}$, respectively. At exposure times of 10 ks and 86.4 ks the Ni-24Cr passive films did not exhibit a clear breakdown potential but rather the passive film became transpassive (i.e., Cr^{3+} to Cr^{6+}) (**Fig. 5.3a and 5.3b**). The imaginary impedance component exhibits the same trends as the current-potential plots, in which each alloy's $-Z''$ magnitude increases with time from $-0.25V_{SCE}$ to breakdown potential. Once at the breakdown potential $-Z''$ rapidly decreases, corresponding to passive film breakdown by crevice corrosion (**Fig. 5.3b**). In summary, the Cr-MPEAs and Ni-24Cr LSV at all exposure times showed a clear passive potential region with a low passive current density. The Cr22-MPEA passive film formed at 100s exhibited a similar passive region as 86.4 ks exposure time and higher breakdown potential compared to 10 ks exposure time. In the case of the Cr14-MPEA and Ni-24Cr binary alloy, the passive region became broader and its breakdown potential increased as exposure time increased. Compared to the Cr-MPEAS, the Ni-24Cr passive films exhibited better stability and broader passive regions.

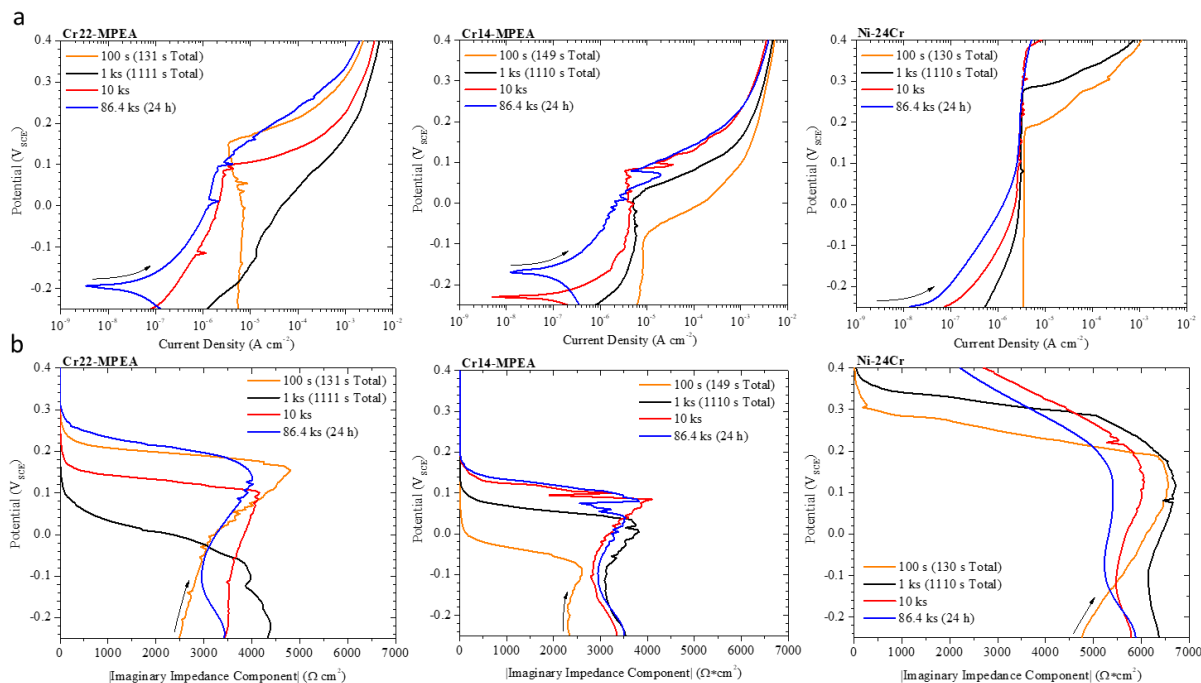


Fig. 5. 3. Cr22-MPEA, Cr14-MPEA, and Ni-24 Cr (a) Linear sweep voltammetry and (b) potential vs. imaginary component of impedance ($-Z''$) at $f = 1$ Hz during LSV with 0.5 mV s^{-1} scan rate in $N_2(g)$ deaerated $0.1 \text{ M NaCl} + \text{HCl}$ at pH 4 after initial cathodic reduction at -1.3 V_{SCE} for 600 s and potentiostatic hold at -0.25 V_{SCE} at each exposure time. Time outside the parathesis is the nominal time and the time within parathesis is the total time held at -0.25 V_{SCE} (SFEIS time + EIS time).

5.4.3 Oxide Valence and Cation Fraction Identified by AR-XPS

The valence state and chemical composition of the electrochemically formed passive films on each alloy at all exposure times were determined by AR-XPS and are summarized in **Table 5.2** and **Fig. 5.4**. The Cr22- and Cr14-MPEA native air oxide showed initial Cr(III) enrichment, which slightly increased during the initial cathodic pretreatment at -1.3 V_{SCE} for the Cr22-MPEA (**Fig. 5.4a and 5.4b**). In the case of the Ni-24Cr native air oxide³, Cr (III) was slightly enriched at AR-XPS take-off angle 45° but equaled the bulk concentration at 90° take-off angle. After an initial cathodic pretreatment, Cr (III) becomes more enriched and Ni is depleted with respect to the bulk concentrations (**Fig. 5.4c**). A larger Cr (III) enrichment was observed in the Ni-24Cr native air oxide compared to the Cr-MPEAs after initial cathodic pretreatment. Overall, at each exposure

³ Sample preparation and AR-XPS procedure the same as listed in experimental section. Experiments were conducted separately from this thesis.

time, the Cr22-, Cr14-MPEA, and Ni-24Cr passive films consisted mainly of Cr(III) cations at both take-off angles. A difference in cation concentration is observed between AR-XPS take-off angles, suggesting a layered passive film formation. At a more surface sensitive AR-XPS take-off angle of 45°, the Cr(III) composition is higher than that of the 90° take-off angle, suggesting the outer layer is slightly more enriched in Cr(III) compared to the inner layer.

Overall, differences in cation concentration are observed for each element as a function of exposure time. The 22Cr-MPEA passive films at exposure times of 100 s and 1 ks mainly consist of Cr(III) cations ≥ 0.76 and small amounts of Fe(II) and Co(II) cations. It should be noted at 1 ks exposure time, no Ni(II) cations were detected at the 45° take-off angle (**Fig. 5.4a**) but a low concentration of 0.03 Ni(II) cation fraction was detected at 90° (**Fig. 5.4a**). At exposure times of 10 ks and 86.4 ks, the Cr22-MPEA passive films consisted of small amounts of Ni(II), Fe(II), Mn(II), Co(II) and a high concentration of Cr(III), regardless of AR-XPS take-off angle. Unlike Cr22-MPEA, the passive films formed on the Cr14-MPEA consisted of each oxidized alloying element with the exception of Mn at 86.4 ks exposure time (**Table 5.2 and Fig. 5.4b**). At a 45° take-off angle, the Cr14-MPEA passive films Cr(III) and Ni(II) cation concentration decreased from exposure time of 100 s to 10 ks and all other cations increased in concentration. At 86.4 ks the Cr(III) cations increased to 0.71 cation fraction, which is higher than any other exposure time. In the case of the Ni-24Cr passive films, both Cr(III) and Ni(II) were detected at all exposure times (**Table 5.2 and Fig. 5.4c**). At exposure times of 100 s and 1 ks, the Cr(III) concentration increases at both take-off angles and Ni (II) cation fraction decreases. At 10 ks and 86.4 ks and a 45° take-off angle the Cr cation fraction decreases to a relatively constant value (0.59) while Ni(II) increases to a constant value of 0.41 cation fraction (**Fig. 5.4c**). At 90° take-off angle, Cr(III) slightly decreases from 0.56 to 0.50 while Ni(II) cation fraction increases from 0.44 to 0.50 at exposure times of 10 ks and 86.4 ks (**Fig. 5.4c**). In summary, the Cr22-, Cr14-MPEA, and Ni-224Cr alloy passive films at each exposure time were enriched with Cr(III) cations. Small amounts of Ni(II), Fe(II), Mn(II) are present in the Cr-MPEA passive films at all exposure times at cation fractions less than the bulk fraction in the substrate; with the exception of Ni(II) in Cr22-MPEA passive film formed for 100 s which was 0. The Cr14-MPEA passive film formed at 100 s had the highest Ni(II) cation fraction but decreased with exposure time. An increase in Fe(II) and Mn(II) cations was observed at longer times for both Cr-MPEA passive films. Co(II) enrichment is observed within the Cr-MPEA passive films at exposure times of 100 s and 1 ks.

Table 5. 2. All cation and elemental fractions detected by AR-XPS for passive films formed at $-0.25 V_{SCE}$ in 0.1 M NaCl + HCl pH 4 $N_{2(g)}$ deaerated solution for Cr22-MPEA, Cr14-MPEA, and Ni-24Cr binary alloy.

Cr22-MPEA											
Take-off Angle	Time	Passive Film Cation Fraction					Metal/Film Interface Elemental Fraction				
		Ni (II)	Fe (II)	Cr (III)	*Mn (II)	*Co (II)	Ni	Fe	Cr	Mn	Co
45° (Surface)	100 s SFEIS (131s)	0.00	0.08	0.76	0.00	0.15	0.56	0.16	0.17	0.05	0.06
	1 ks SFEIS (1111s)	0.00	0.02	0.81	0.00	0.17	0.56	0.17	0.18	0.05	0.04
	10 ks	0.11	0.1	0.73	0.02	0.03	0.67	0.04	0.22	0.04	0.03
	86.4 ks	0.04	0.13	0.68	0.09	0.06	0.52	0.09	0.23	0.13	0.02
90° (Bulk)	100 s SFEIS (131s)	0.00	0.06	0.74	0.00	0.20	0.56	0.15	0.18	0.05	0.06
	1 ks SFEIS (1111s)	0.03	0.13	0.58	0.00	0.26	0.52	0.19	0.18	0.05	0.05
	10 ks	0.1	0.07	0.77	0.03	0.03	0.65	0.06	0.22	0.04	0.03
	86.4 ks	0.08	0.08	0.66	0.12	0.06	0.53	0.07	0.23	0.14	0.04
Cr14-MPEA											
Take-off Angle	Time	Passive Film Cation Fraction					Metal/Film Interface Elemental Fraction				
		Ni (II)	Fe (II)	Cr (III)	*Mn (II)	*Co (II)	Ni	Fe	Cr	Mn	Co
45° (Surface)	100 s SFEIS (149s)	0.16	0.05	0.63	0.00	0.16	0.62	0.12	0.12	0.07	0.07
	1 ks SFEIS (1110s)	0.11	0.04	0.56	0.05	0.24	0.57	0.16	0.13	0.08	0.06
	10 ks	0.13	0.14	0.58	0.04	0.1	0.56	0.17	0.12	0.09	0.07
	86.4 ks	0.04	0.17	0.71	0	0.07	0.5	0.11	0.14	0.12	0.14
90° (Bulk)	100 s SFEIS (149s)	0.36	0.02	0.38	0.04	0.21	0.57	0.15	0.12	0.08	0.08
	1 ks SFEIS (1110s)	0.14	0.05	0.55	0.04	0.22	0.57	0.15	0.13	0.08	0.07
	10 ks	0.11	0.1	0.53	0.08	0.18	0.56	0.16	0.12	0.1	0.07
	86.4 ks	0.09	0.14	0.65	0	0.12	0.61	0.07	0.15	0.11	0.07
Ni-24Cr											
Take-off Angle	Time	Passive Film Cation Fraction					Metal/Film Interface Elemental Fraction				
		Ni (II)	Fe (II)	Cr (III)	Mn (II)	Co (II)	Ni	Fe	Cr	Mn	Co
45° (Surface)	100 s SFEIS (130s)	0.28	--	0.72	--	--	0.77	--	0.23	--	--
	1 ks SFEIS (1110s)	0.18	--	0.82	--	--	0.77	--	0.23	--	--
	10 ks	0.41	--	0.59	--	--	0.79	--	0.21	--	--
	86.4 ks	0.41	--	0.59	--	--	0.76	--	0.24	--	--
90° (Bulk)	100 s SFEIS (130s)	0.30	--	0.70	--	--	0.77	--	0.23	--	--
	1 ks SFEIS (1110s)	0.29	--	0.71	--	--	0.79	--	0.21	--	--
	10 ks	0.44	--	0.56	--	--	0.8	--	0.20	--	--
	86.4 ks	0.5	--	0.5	--	--	0.76	--	0.24	--	--

*At 100 s and 1 ks: Mn2p1 signal assumed to be MnO and Co2p1 as CoO. At 10 ks and 86.4 ks: Mn2p1 assumed to be MnCr₂O₄ and Co2p1 as either CoCr₂O₄ or CoO/Co(OH)₂.

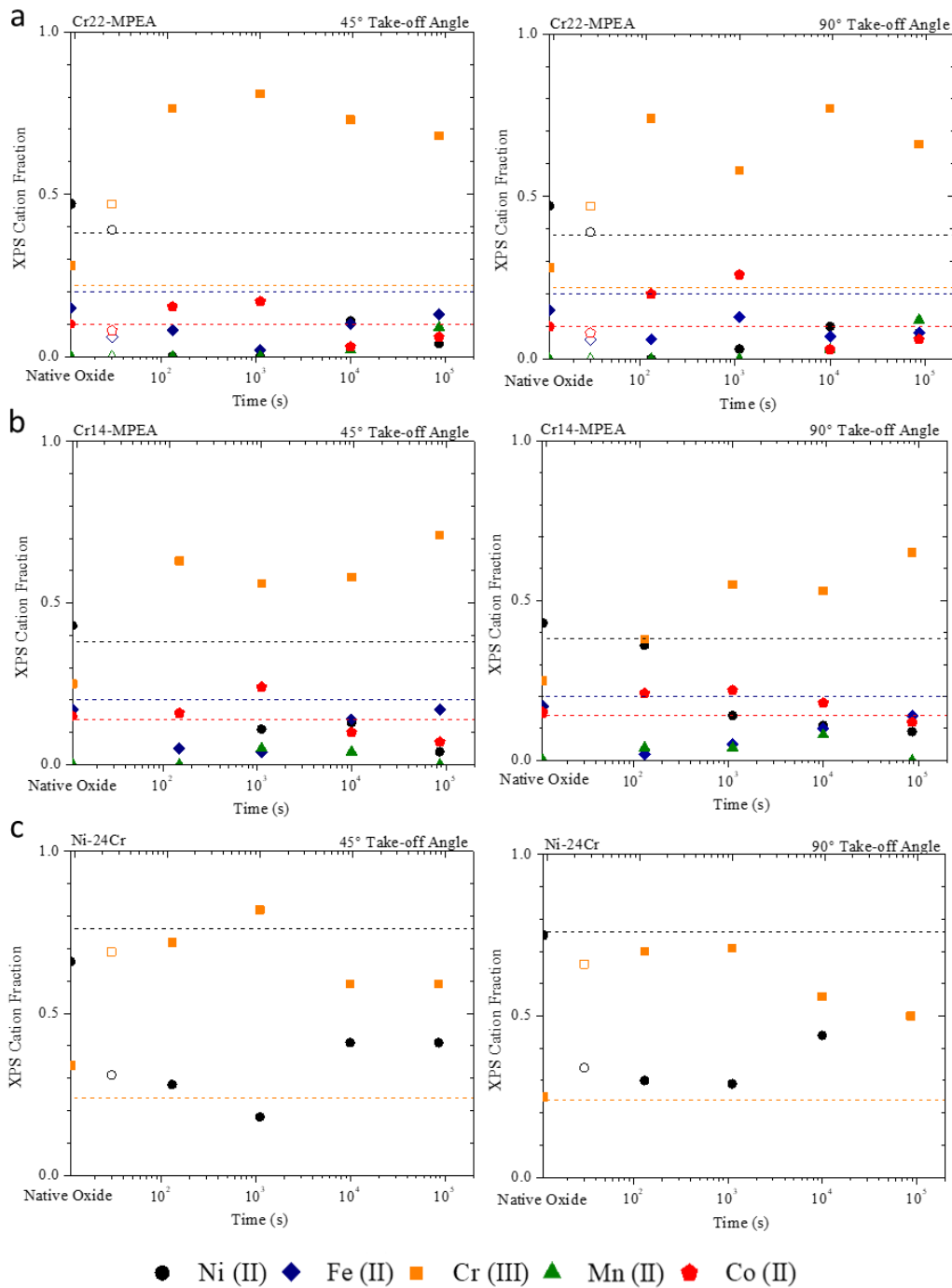


Fig. 5. 4. Cation fractions detected by AR-XPS at 45° and 90 ° take-off angle for (a) Cr22-MPEA and (b) Cr14-MPEA passive films potentiostatically formed at $-0.25 V_{SCE}$ for 100 s, 1ks, 10 ks, and 86.4 ks (24 h) after initial cathodic reduction at $-1.3V_{SCE}$ for 600 s in deaerated 0.1 M NaCl + HCl at pH 4. The bulk atomic fraction for each alloying element is indicated by the horizontal dashed lines. Native air oxide XPS cation fraction is shown on the y-axis. Cation fractions of Cr22-MPEA and Ni-24Cr cathodically pretreated surface is indicated by the colored outline data points at time = 30 s.

Due to the low concentration of oxidized cations within passive films formed on the Cr-MPEAs relative to the Cr cation fraction; Ni(II), Fe(II), Mn(II), and Co(II) cation fractions were summed together and compared to Cr(III) cation fractions as a function of exposure time, shown in **Fig. 5.5**. At a take-off angle of 45°, passive films formed on the Cr22-MPEA exhibit a decrease in Cr cation fraction while all other cations increase with exposure time (**Fig. 5.5a**). At a take-off angle of 90°, the above trend is not observed but rather fluctuation in cation concentration is observed at each exposure time (**Fig. 5.5a**). In the case of the Cr14-MPEA at 45°, the passive film initially decreases in Cr(III) concentration but then begins to increase while all other cations decrease with $t \geq 10$ ks (**Fig. 5b**). Unlike at 45°, at a take-off angle of 90° the Cr14-MPEA passive film initially started out enriched in Ni(II) + Fe(II) + Mn(II) + Co(II) cations compared to Cr(III) at 100 s exposure time (**Fig. 5b**). As the exposure time duration increases the Cr(III) cations become the dominate cation within the passive film.

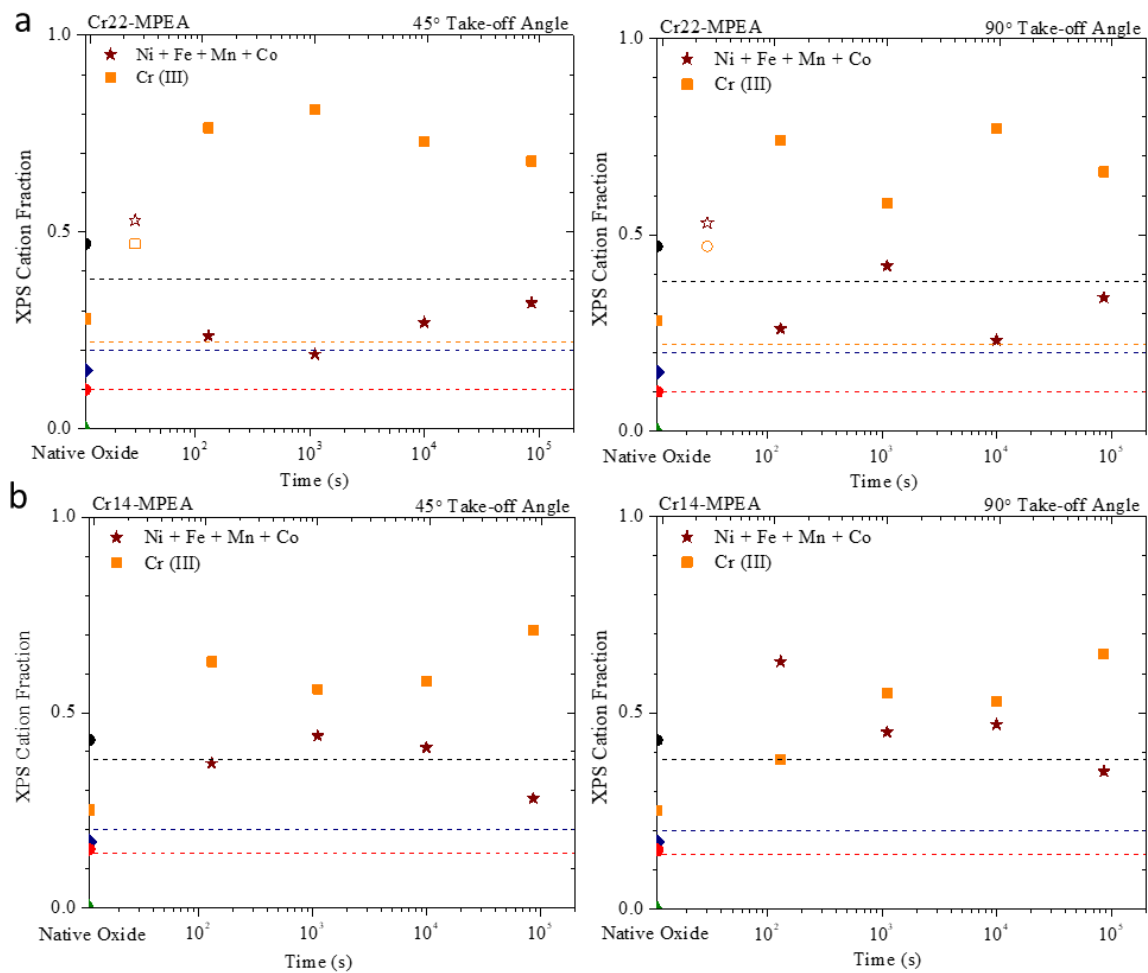


Fig. 5. 5. Cation fractions detected by AR-XPS at 45° and 90 ° take-off angle for (a) Cr22-MPEA and (b) Cr14-MPEA passive films potentiostatically formed at $-0.25 V_{SCE}$ for 100 s, 1ks, 10 ks, and 86.4 ks (24 h) after initial cathodic reduction at $-1.3V_{SCE}$ for 600 s in deaerated 0.1 M NaCl + HCl at pH 4. The bulk atomic fraction for each alloying element is indicated by the horizontal dashed lines. Native air oxide XPS cation fraction is shown on the y-axis. Cation fractions of Cr22-MPEA and Ni-24Cr cathodically pretreated surface is indicated by the colored outline data points at time = 30 s.

Deconvolution of XPS spectra was performed and the detected oxidized species are summarized in **Fig. 6**. At 100 s and 1 ks exposure time the dominant species in passive films formed on both Cr-MPEAs are Cr(III) and/or Ni(II) hydroxides, regardless of take-off angle. But an increase in XO and X₂O₃, where x = Ni, Fe, Cr, Mn, and/or Co, oxide fraction is observed from 45° to 90° take-off angle (**Fig. 6a and 6b**). As exposure time increases to 10 ks and 86.4 ks, the hydrated oxide fraction decreases and spinels (i.e., XCr₂O₃) becomes the dominant species present, with the exception of Cr14-MPEA at 90° (**Fig. 6b**). At a take-off angle of 90°, the Cr14-MPEAs passive film consists of equal parts spinel and hydroxide species at both 10 ks and 86.4 ks. Unlike the Cr-MPEAs, Ni-Cr spinels were not detected within passive films formed on the Ni-24Cr binary alloy (**Fig. 6c**). Only hydrated and anhydrous Ni(II) and Cr(III) species were present, regardless of exposure time. At 100 s and 45° take-off angle, Ni-24Cr passive film had the highest hydroxide fraction compared to the Cr-MPEAs. This in part may be due to the cathodic pretreatment in which an increase in oxidized Cr(III) was detected on the Ni-24Cr surface (**Fig. 4c**). As time increases to 10 ks the hydroxide fraction continues to decrease and in return the anhydrous oxide fraction increases. However, the hydroxide fraction increases and anhydrous oxide fraction decreases at 86.4 ks. Unlike at 45°, the Ni-24Cr passive films at 90° take-off angle exhibited similar behavior until 10 ks in which a slight increase in hydroxide was observed but then decreased again at 86.4 ks to equal amounts of anhydrous oxide (**Fig 6c**). In summary, all passive films formed on the Cr alloy surfaces contained high concentrations of hydrated Cr(III) assigned to Cr(OH)₃ at all exposure times. Cr spinels began to form at longer exposure times of 10 ks and 86.4 ks for passive films formed on the Cr-MPEAs. In contrast, no Cr spinels formed in the Ni-24Cr passive films at any exposure time but an increase in concentration of anhydrous oxides was observed.

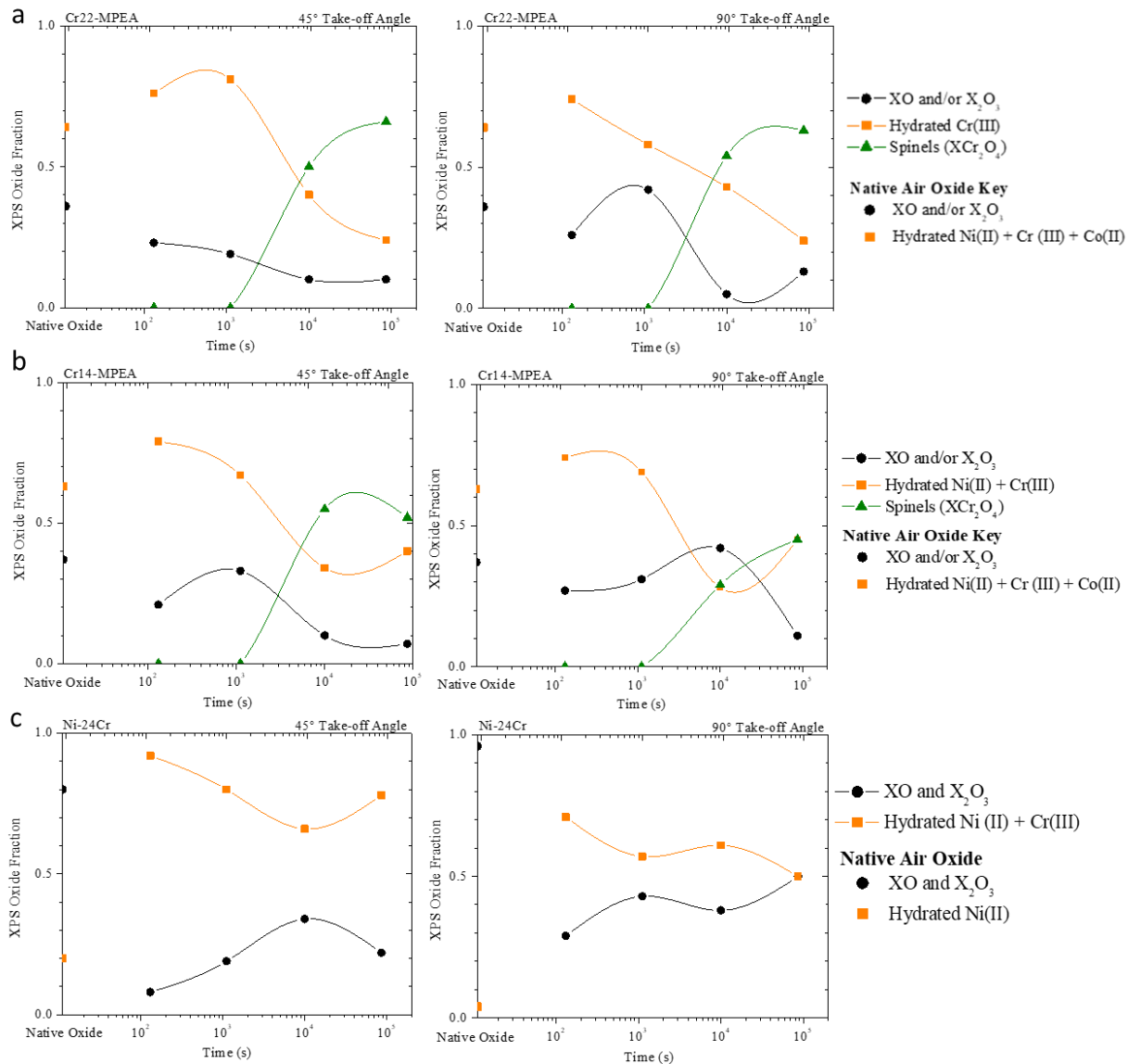


Fig. 5. 6. Oxide fractions detected by AR-XPS at 45° and 90 ° take-off angle of (a) Cr22-MPEA, (b) Cr14-MPEA, and (c) Ni-24Cr passive films potentiostatically formed at $-0.25 V_{SCE}$ for 100 s, 1ks, 10 ks, and 86.4 ks (24 h) after initial cathodic reduction at $-1.3V_{SCE}$ for 600 s in deaerated 0.1 M NaCl + HCl at pH 4. Native air oxide XPS oxide fraction is shown on the y-axis.

5.4.4 Passive Film and Altered Zone Enrichment and Depletion Term

Enrichment and depletion terms were computed for alloying element “A”, where A = Ni, Fe, Cr, Mn, Co, within the native air oxide, electrochemically formed passive film ($f_{A,ox}$) and altered zone beneath the oxide metal interface ($f_{A,az}$) at each exposure time for the Cr22-MPEA, Cr14-MPEA, and Ni-24Cr are summarized in **Figs. 5.7-5.9**, respectively. Enrichment of element “A” is indicated by a $f_{A,ox} > 1$ (i.e., above the horizontal line) and depletion of “A” is indicated by a $f_{A,ox} < 1$. Both Ni and Cr within the Cr-22 MPEA’s native oxide showed slight enrichment with $f_{Ni,ox} = 1.24$ and $f_{Cr,ox} = 1.28$ (**Fig. 5.7**). Within the altered zone Ni was the only element to exhibited enrichment with an $f_{Ni,az} = 1.95$. All other elements within the altered zone for the native air oxide were depleted with an $f_{A,az} < 1$.

As exposure time increases, a large jump in Cr enrichment was observed in the Cr22-MPEA passive film and its $f_{Cr,ox}$ ranged from 3.1 to 3.7 and 2.6 to 3.5 at take-off angles 45° and 90° , respectively (**Fig. 5.7**). At take-off angle 45° , a decrease in $f_{Cr,ox}$ is observed from short exposure times (100 s to 1 ks) to longer exposure times (10 ks to 86.4 ks). This decrease in $f_{Cr,ox}$ could be connected to the decrease in hydrated Cr(III) and increase in XCr_2O_4 spinel species at longer exposure times (**Fig. 5.7 and 5.6**). Co also showed enrichment at exposure times of 100 s and 1 ks. The $f_{Co,ox}$ was 1.5 and 2 for take-off angles 45° and 90° at 100 s, respectively. At 1 ks exposure its $f_{Co,ox}$ increased to 1.7 and 2.6 for take-off angles 45° and 90° , respectively (**Fig. 5.7**). The larger $f_{Co,ox}$ observed at take-off angle 90° , suggests Co cations are more enriched within the bulk of the passive film, rather than at the surface. At longer exposure times, 10 ks and 86.4 ks, Co was depleted within the Cr22-MPEA passive film with a $f_{Co,ox}$ of 0.3 and 0.6 at both take-off angles, respectively. All other alloying elements (i.e., Ni, Fe, and Mn) were depleted within the Cr22-MPEA passive film with a $f_{A,ox}$ of less than one, with the exception of Mn at exposure time 86.4 ks. At exposure time 86.4 ks and take-off angle 90° Mn was slightly enriched with a $f_{A,ox}$ of 1.2 (**Fig. 5.7**). Mn showed slight enrichment within the altered zone with a $f_{Mn,az}$ of 1.3 and 1.4 at take-off angles 45° and 90° , respectively. Within the altered zone for the Cr22-MPEA passive film, Ni was the only element to be enriched at all exposure times and its $f_{Ni,az}$ ranged from 1.4 to 1.8 and 1.4 to 1.7 at take-off angles 45° and 90° , respectively (**Fig. 5.7**).

Cr14-MPEA showed similar enrichment and depletion profiles to the Cr22-MPEA for each element within its native air oxide and altered zone, with the exception of Co (**Fig. 5.8**). Co exhibited enrichment within the Cr14-MPEA native air oxide with a $f_{Co,ox}$ of 1.5. Slight differences are observed between the Cr14-MPEA and Cr22-MPEA alloying element enrichment and depletion as a function of exposure time (**Fig. 5.8 and 5.7**). At all exposure times Cr was enriched within the Cr14-MPEA passive film and its $f_{Cr,ox}$ ranged from 2.5 to 3.2 and 1.7 to 3.0 at take-off angles 45° and 90° , respectively (**Fig. 5.8**). A larger Cr depletion is observed within the altered zone of the Cr14-MPEA compared to Cr22-MPEA. Its $f_{Cr,az}$ ranged from 0.5 to 0.6 at both take-off angles 45° and 90° . Co enrichment and depletion profile was also different for the Cr14-MPEA compared to the Cr22-MPEA. At a take-off angle of 45° Co exhibited a high $f_{Co,ox}$ of 1.6 and 2.4 at exposure times 100 s and 1 ks, respectively but decreased to ≤ 1 at 10ks and 86.4 ks (**Fig. 5.8**). Unlike at 45° , at a take-off angle of 90° Co remained enriched at all exposure times. Its $f_{Co,ox}$ did decrease with exposure time from 2.2 to 1.2. These results suggest Co was more enriched within the Cr14-MPEA passive film at earlier times and stays enriched within the bulk of the film at all exposure times (**Fig. 5.8**). In the case of Ni, Fe, and Mn within the Cr14-MPEA passive film each showed depletion profiles with a $f_{A,ox} \leq 1$ at all exposure times. Ni initially at 100s had a $f_{Ni,ox}$ of 0.94 but continues to decrease to 0.23 at 86.4 ks at a take-off angle 90° . Similar Ni trends were observed at a take-off angle 45° where $f_{Ni,ox}$ decreased from 0.43 to 0.11. Fe had the opposite $f_{Fe,ox}$ trend compared to Ni, in which it continually increased from 0.27 to 0.87 and 0.09 to 0.69 at take-off angles 45° and 90° , respectively (**Fig. 5.8**). Ni was the only element to show a $f_{Ni,az}$ enrichment profile at all exposure times within the Cr14-MPEA altered zone. At take-off angle 45° , $f_{Ni,az}$ slightly decreases with exposure time from 1.6 to 1.3. At take-off angle 90° , Ni $f_{Ni,az}$ stays relatively constant (~ 1.5). At an exposure time of 86.4 ks, Mn and Co are slightly enriched within Cr14-MPEA altered zone with a $f_{A,ox}$ of 1.2 and 1.4, respectively.

Compared to the MPEAs f_A , Ni-24Cr binary alloy also exhibited Cr enrichment within the passive film at all exposure times (**Fig. 5.9**). At a 45° take-off angle, $f_{Cr,ox}$ increased from 1.9 to 2.2 from 100 s to 1 ks. At exposure time 10 ks and 86.4 ks $f_{Cr,ox}$ decreases to 1.6 and remains constant. At 90° take-off angle and 100 s and 1 ks exposure time $f_{Cr,ox}$ is relatively constant at 1.9. As exposure time increases to 10 ks and 86.4 ks $f_{Cr,ox}$ decreases to 1.5 and 1.3, respectively. The opposite trend was observed for Ni $f_{Ni,ox}$ compared to Cr within the Ni-24Cr passive film. At both take-off angles Ni was depleted within the passive film but an increase was observed at exposure

times of 10 ks and 86.4 ks. At 45° take-off angle, $f_{Ni,ox}$ slightly decreases from 0.45 to 0.29 at 100s and 1 ks, respectively, but increase to 0.64 and remains constant at 10 ks and 86.4 ks. At 90° take-off angle and 100 s and 1 ks exposure times $f_{Ni,ox}$ is relatively constant (~0.4) but then increases to 1.5 and 1.4 at 10 ks and 86.4 ks, respectively. Similar to the MPEAs Ni and Cr $f_{A,az}$ enrichment and depletion profiles within the altered zone a slight enrichment of Ni and Cr depletion is observed for the Ni-24Cr altered zone at all exposure times. Both $f_{Ni,az}$ (1.2) and $f_{Cr,az}$ (0.6) remains relatively constant at all exposure times for each take-off angle. In summary, Cr is enriched within the passive film at all exposure times for all alloys and slightly depleted or equal to the bulk Cr concentration within the altered zone. Cr22- and Cr14-MPEA passive film exhibits Co enrichment at exposure times 100 s and 1 ks. Ni enrichment is observed within the altered zone for all Cr alloys at all exposure times. The Cr22- and Cr14-MPEA altered zones were depleted on Fe, Co, and Mn at all exposure times. Slight Mn enrichment was observed in the altered zone for the MPEAs at exposure times of 86.4 ks.

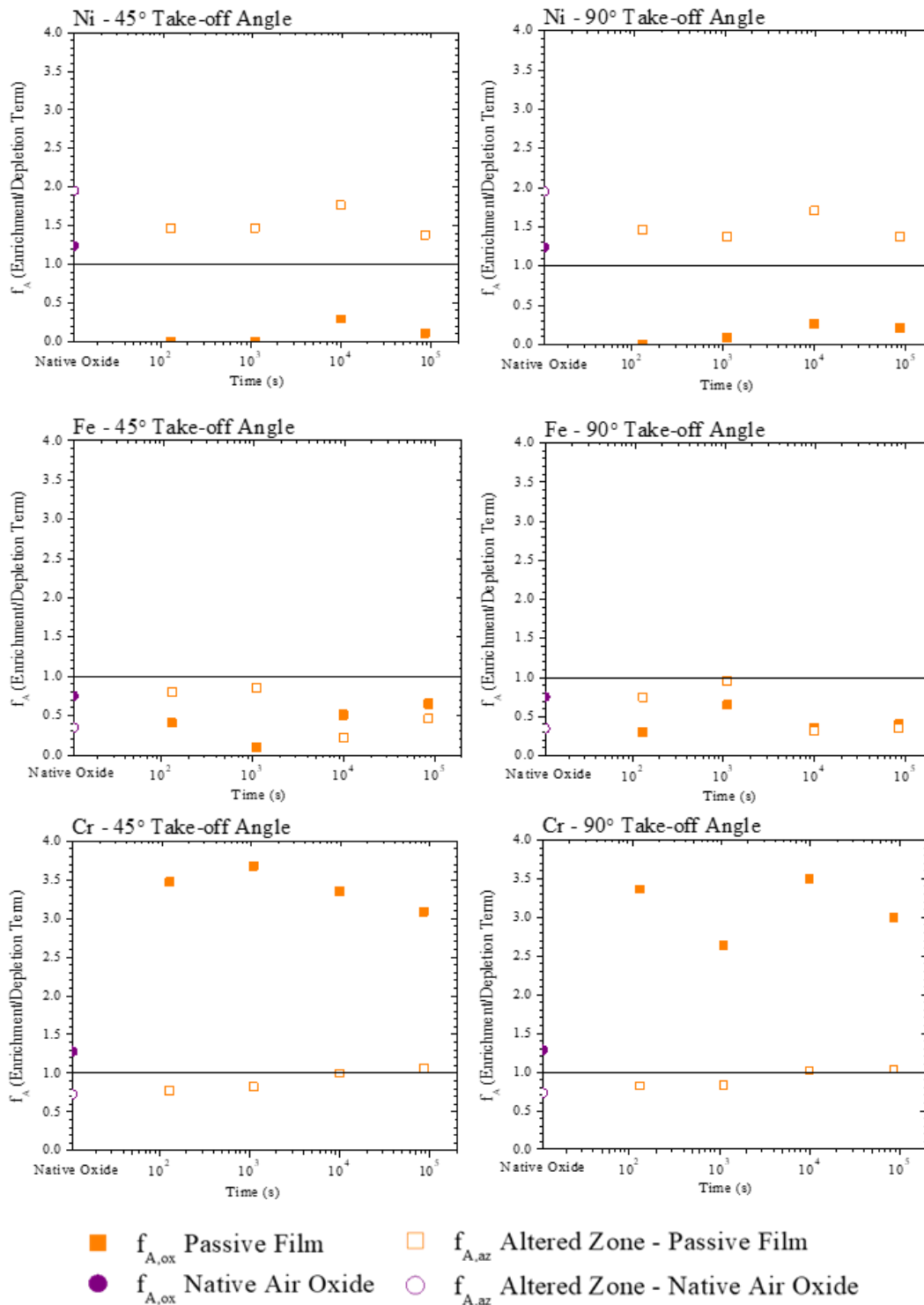


Fig. 5. 7. Cr22-MPEA XPS enrichment/depletion term (f_A) where $A = Ni, Fe, Cr, Mn,$ and Co for both A cations within native air oxide (y-axis), the passive film ($f_{A,ox}$) and elemental “ A ” within the altered zone ($f_{A,az}$) (i.e., metal/oxide interface) formed during potentiostatic passivation at $-0.25 V_{SCE}$ for 100 s, 1ks, 10 ks, and 86.4 ks (24 h) after initial cathodic reduction at $-1.3V_{SCE}$ for 600 s in deaerated 0.1 M NaCl + HCl at pH 4.

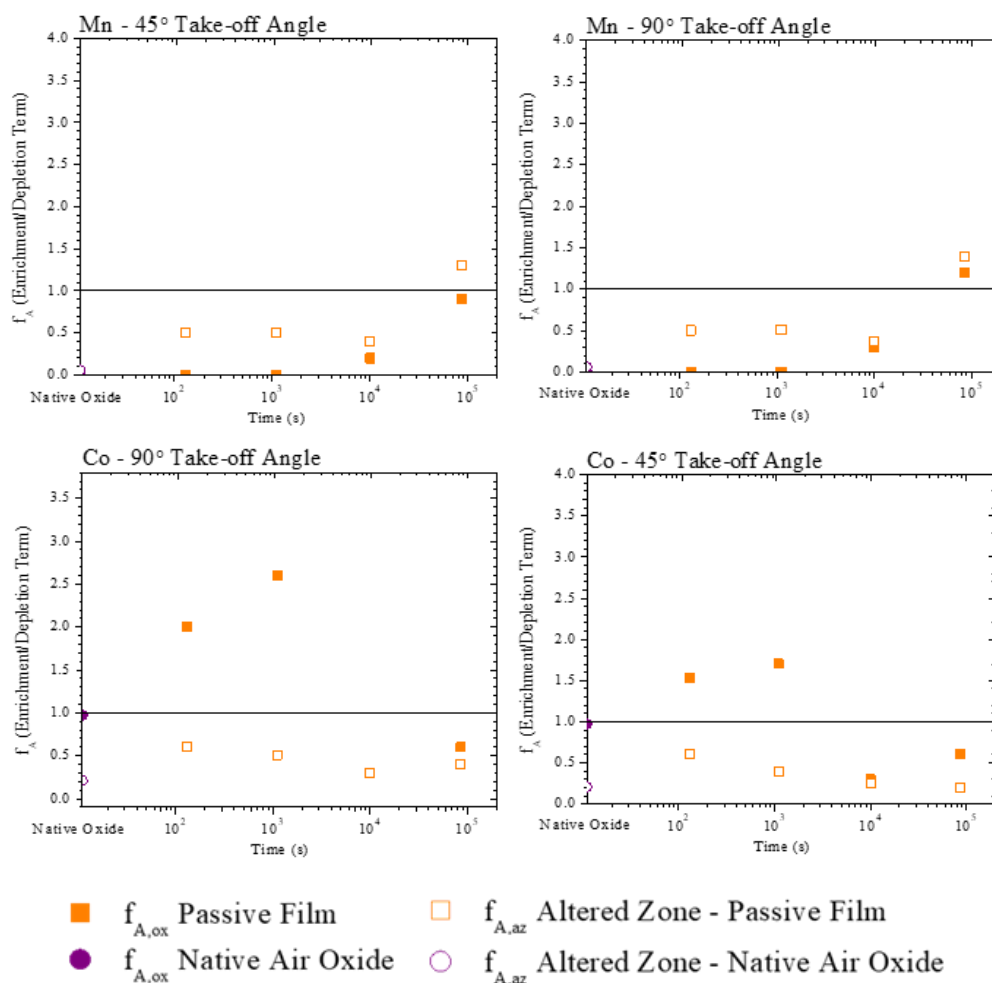


Fig. 5.7 continued. Cr22-MPEA XPS enrichment/depletion term (f_A) where $A = Ni, Fe, Cr, Mn,$ and Co for both A cations within native air oxide (y -axis), the passive film ($f_{A,ox}$) and elemental “ A ” within the altered zone ($f_{A,az}$) (i.e., metal/oxide interface) formed during potentiostatic passivation at $-0.25 V_{SCE}$ for 100 s, 1 ks, 10 ks, and 86.4 ks (24 h) after initial cathodic reduction at $-1.3V_{SCE}$ for 600 s in deaerated 0.1 M NaCl + HCl at pH 4.

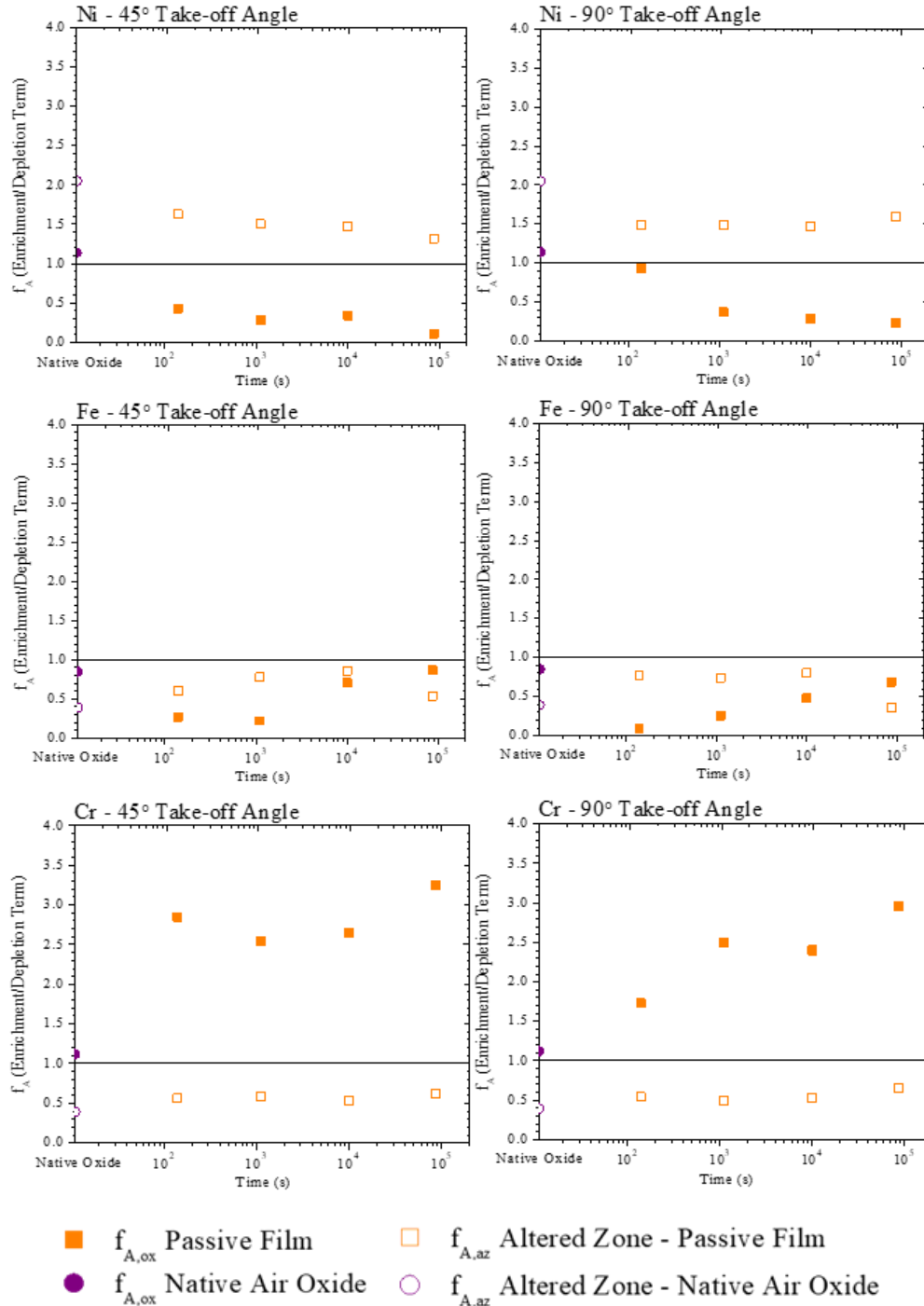


Fig. 5. 8. Cr14-MPEA XPS enrichment/depletion term (f_A) where $A = Ni, Fe, Cr, Mn,$ and Co for both “ A ” cations within the passive film ($f_{A,ox}$) and elemental “ A ” within the altered zone ($f_{A,az}$) (i.e., metal/oxide interface) formed during potentiostatic passivation at $-0.25 V_{SCE}$ for 100 s, 1ks, 10 ks, and 86.4 ks (24 h) after initial cathodic reduction at $-1.3V_{SCE}$ for 600 s in deaerated $0.1 M NaCl + HCl$ at pH 4.

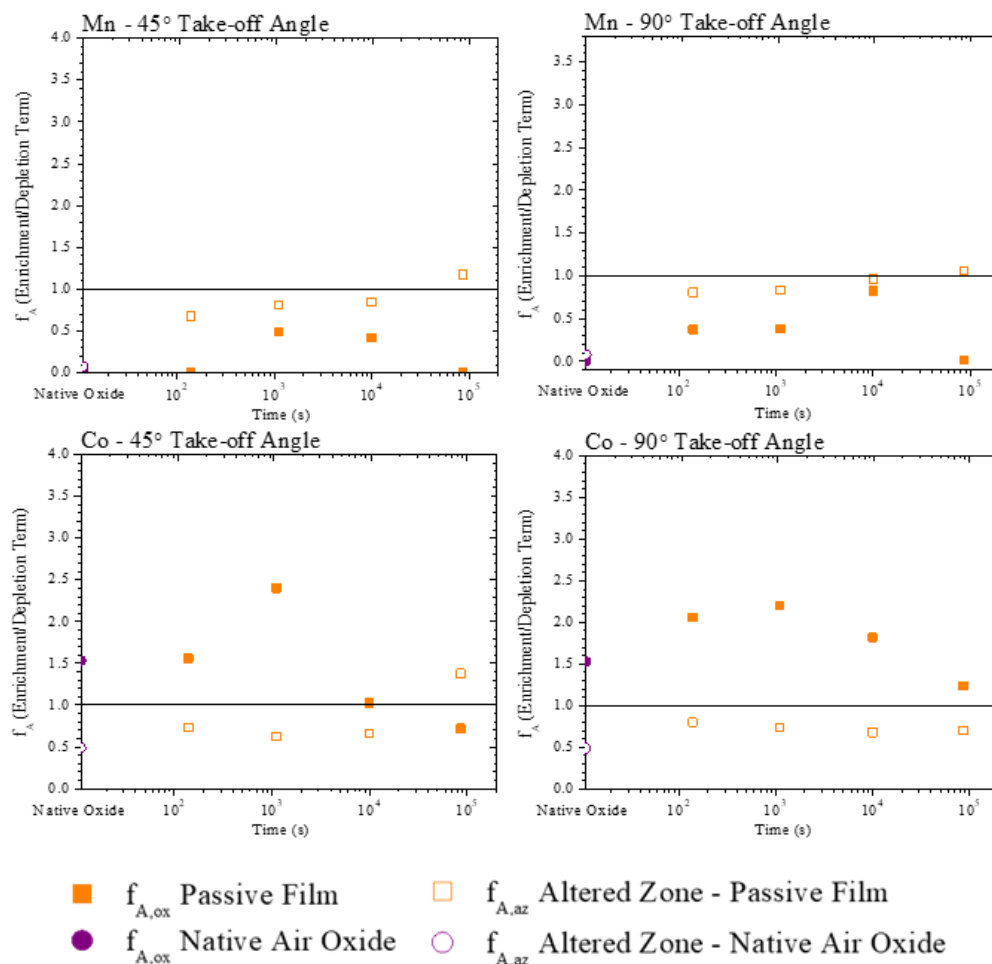


Fig. 5.8 continued. Cr14-MPEA XPS enrichment/depletion term (f_A) where $A = \text{Ni}, \text{Fe}, \text{Cr}, \text{Mn}, \text{and Co}$ for both “ A ” cations within the passive film ($f_{A,ox}$) and elemental “ A ” within the altered zone ($f_{A,az}$) (i.e., metal/oxide interface) formed during potentiostatic passivation at -0.25 V_{SCE} for 100 s, 1ks, 10 ks, and 86.4 ks (24 h) after initial cathodic reduction at -1.3 V_{SCE} for 600 s in deaerated 0.1 M NaCl + HCl at pH 4.

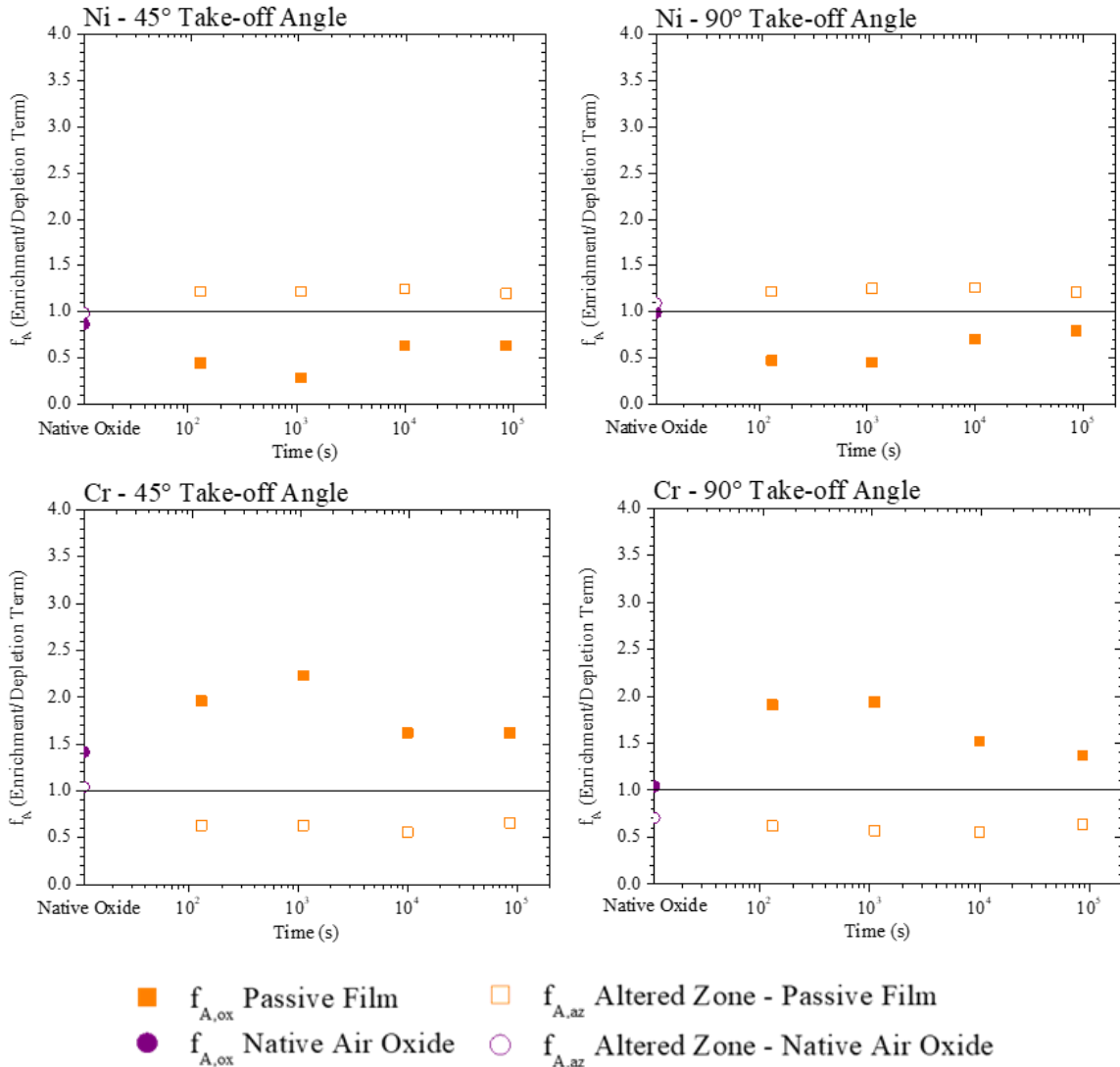


Fig. 5. 9. Ni-24Cr binary alloy XPS enrichment/depletion term (f_A) where $A = \text{Ni, Fe, Cr, Mn, and Co}$ for both “ A ” cations within the passive film ($f_{A,ox}$) and elemental “ A ” within the altered zone ($f_{A,az}$) (i.e., metal/oxide interface) formed during potentiostatic passivation at $-0.25 \text{ V}_{\text{SCE}}$ for 100 s, 1ks, 10 ks, and 86.4 ks (24 h) after initial cathodic reduction at $-1.3 \text{ V}_{\text{SCE}}$ for 600 s in deaerated 0.1 M NaCl + HCl at pH 4

5.5 Discussion

5.5.1 What is Known About Oxide Exposure Aging

A passive film's oxide chemistry, valence state, and configuration (i.e., layered phase separated oxides, oxide islands, flasks or disks typical of phase separated near stoichiometric oxides with near equilibrium solid solubilities, and complex solid solutions mixture) will have a large influence on the film's protective qualities [49, 50]. Depending on exposure time and environment, these properties can vary and change if the nature of the passive film changes due to rapidly forming compared to forming for long periods of time during aqueous oxidation (**Fig. 5.2-5.6 and Table 5.2**). For conventional corrosion resistant Cr-containing alloys, different passive film configurations have been reported for a range of exposure times (1 to 44 h) such as, amorphous, layered oxides, non-equilibrium solute capture, non-stoichiometric oxides like corundum $\text{Cr}_{2-x}\text{Ni}_x\text{O}_3$ and/or a solid solution oxide where x can vary more or less continuously [1, 2, 6-14]. Solid solutions can be both non-equilibrium or stable thermos phases. Fe-Cr hematite and corundum are completely soluble in the solid state as are Cr_2O_3 as corundum and Al_2O_3 and are thermodynamically stable. Solute capture is representative of non-equilibrium solid solution [12]. Yu et al. characterized passive films by transmission electron microscopy (TEM) on Ni-24Cr (at. %) in 0.1 M NaCl adjusted to pH 4 with HCl for 10 ks using H_2O_2 as an oxidizing agent. High-resolution TEM revealed that the passive film contained a non-conventional Cr corundum oxide (Cr_2O_3) with solute captured Ni atoms [11]. The formation of these non-equilibrium oxides occurs during rapid oxidation, in which all oxidized cations are trapped within the matrix of a pre-existing stoichiometric oxide's matrix during passive film growth [11, 12].

5.5.2 Observations in this Study

Compared to the experimental results presented here, at exposure times 100 s and 1 ks we see the formation of typically stoichiometric oxides and hydroxides enriched in Cr for both the Cr-MPEAs and Ni-24Cr binary (**Fig. 5.6**), based on assignments relying on XPS binding energies but lacking in structural conformation. At 10 ks the fraction of these oxides and hydroxides decreases within the Cr-MPEAs passive films due to the formation of Cr-spinels (XCr_2O_4 , where X= Ni, Fe, Mn) (**Fig. 5.6a and 5.6b**). As exposure time increases to 86.4 ks, a continued increase in spinel oxide fraction is observed. Spinel were not detected in passive films formed on Ni-24Cr surfaces

at any exposure time. It is possible the formed spinels within Cr-MPEA passive films at longer exposure times is a non-stoichiometric solid solution oxide, with the following spinel structure XY_2O_4 , where X and Y can be Ni, Fe, Cr, Mn, or Co [29]. If we consider the cation fraction of each element in the Cr-MPEA passive film, Cr stays enriched at all exposure times but a slight decrease is observed while other cations such as Fe, and Mn increase with exposure time (**Fig. 5.4a, 5.4b, and 5.5**). Unfortunately, other high-resolution characterization techniques like TEM are needed to differentiate experimentally between the two oxides. Some XPS studies have investigated the difference in binding energy between stoichiometric and non-stoichiometric oxides, in which very small differences are observed in core level binding energy spacing [47, 51]. Consider the $FeCr_2O_4$ spinel and its $Cr2p_{3/2}$ photoelectron peak, depending on the stoichiometry of Fe and Cr the binding energy will change slightly, for example $FeCr_2O_4$ binding energy is 576.2 eV and $Fe_{1.4}Cr_{1.6}O_4$ is 576.4 eV. These two binding energies differ only by 0.2 eV [47]. Therefore, given a sample which can contain both species it would be difficult to differentiate the two alone with XPS.

5.5.3 Kinetic versus Thermodynamic Factors

Many different initiation processes have been proposed for passive film formation on Ni-Cr based alloy surfaces for both air and aqueous oxidation [2, 11, 12, 52-55]. Consider air oxidation at a constant temperature and $O_{2(g)}$ partial pressure of Ni-Cr binary alloys, studies have shown utilizing scanning tunneling microscopy (STM) during the initial stages of oxidation, NiO forms quickly followed by the nucleation of Cr-rich particles. As exposure time increases NiO continues to grow and the Cr-rich particles develop into a Cr passive film [52-55]. Another air oxidation investigation by Yu et al. of Ni-Cr and Ni-Cr-Mo alloys showed similar in situ TEM results but instead of a pure NiO layer forming initially, a non-stoichiometric rock-salt ($Ni_{1-x}Cr_xO_{1+y}$) layer formed [2]. As exposure time increased, oxidation resulted in the following oxide formation rock-salt, spinel, and corundum. From chemical analysis, solute atoms were initially captured in the rock-salt phase but would diffuse out and transform into more thermodynamically stable phase separated conventional oxides [2]. Consider passive films formed on Cr-MPEAs surfaces during aqueous oxidation, at short exposure times small amounts of NiO and FeO form and then at later times the composition of these oxides decreases in concentration while that of spinels increases, suggesting at longer exposure times the more thermodynamically favorable oxide (**Fig. 5.6a and**

5.6b). This behavior could be predicted from the oxide standard free energy of formation in which, spinels typically have a more negative free energy compared to common stoichiometric oxides (i.e., NiO, FeO, etc.). For example, the standard free energy formation of FeO is $-251.4 \text{ kJ mol}^{-1}$ and compared to FeCr_2O_4 it is $-1343.8 \text{ kJ mol}^{-1}$ [56]. It is interesting that one would suspect FeCr_2O_4 would form first but this is not what we observe in the Cr-MPEA passive films (**Fig. 5.6a and 5.6b**) [56]. Due to rapid dissolution of cations into the electrolyte, which can influence passive film composition and structure, thermodynamics alone cannot predict how passive films form on alloy surfaces during aqueous oxidation. Passive films grown electrochemically at $0.2 \text{ V}_{\text{SCE}}$ on Ni-24Cr surfaces in 0.1 M NaCl pH 4 adjusted with HCl exhibited Ni and Cr cation concentrations equal to the bulk concentration at an initial exposure time of 100 s. As exposure time increased from 1 ks to 10 ks, the passive film became more enriched with Cr and instead of distinct oxide layers forming after 10 ks, the passive film consisted of a non-stoichiometric solid solution [1]. In the case of the Cr-MPEAs electrochemically grown passive films at 100 s and 1 ks, small amounts of rock-salt oxides and Cr-enriched hydroxide are detected based on XPS binding energies. The large Cr-enrichment can partially be due to the cathodic pretreatment but regardless an observed increase in Cr (III) cations was seen from cathodic pretreatment to 100 s exposure time (**Fig. 5.4 and 5.5**). If we consider chemical stability diagrams for $\text{Ni}^{2+}/\text{NiO}$, $\text{Fe}^{2+}/\text{FeO}$, $\text{Cr}^{3+}/\text{Cr}_2\text{O}_3\text{-Cr}(\text{OH})_3$, Mn/MnO , and Co/CoO species, only Cr species are predicated to be stable at pH 4 and a ion concentration of 10^{-3} to 10^{-6} M [57]. This could explain the high concentration of Cr hydroxide observed at all exposure times (**Fig. 5.6**). These predictions correlate with previous observations observed for the electrochemical passivation of the Cr22-MPEA, in which preferential dissolution of Ni, Fe, and Co were observed by AESEC [20]. The low concentration of oxides other than Cr(III) at short exposure times could also be due to the increase in Cr in the passive film enhancing the resistance against Cl^- adsorption compared to other oxides [50]. As exposure time increases Fe and Mn cation content increases compared to that of Ni cation which decreases within the Cr-MPEA passive films at 10 ks to 86.4 ks exposure time. This behavior could be a result of differences in diffusion coefficients. Consider the inter-diffusion of Ni, Fe, Cr, Mn, and Co in a solid solution equiatomic Co-Cr-Fe-Mn-Ni alloy at a temperature range of 1173 to 1373 K [58, 59]. In ranking order, the diffusion rates were $\text{Mn} > \text{Cr} > \text{Fe} > \text{Co} > \text{Ni}$ and will assume it is the same under these aqueous conditions. Similarly in another study focused on diffusion in Cr_2O_3 the following cations were ranked fastest to slowest: Mn^{2+} , Fe^{2+} , Ni^{2+} , and Cr^{2+} [60]. The increase in

Mn and Fe cation compared to Ni could be a result of Fe and Mn diffusing faster from the altered zone through the passive film compared to Ni cations. Similarly, if we compare to the elemental concentrations within the altered zone, Ni was enriched at all exposure times while Fe and Mn decrease in concentration (**Table 5.2 and Fig. 5.4**) suggesting both these elements are being oxidized and are joining the passive film and/or dissolving into solution.

The resulting protective passive properties of a passive film will depend on the type of oxide present. Commonly, passive film properties will be different compared to bulk oxides because they are typically thin and contain an amorphous or highly disordered structure [61, 62]. The more alloying elements present, the more the electrochemical properties may change compared to their pure counterparts. This behavior is illustrated in the LSV curves of passive films formed on the Cr-MPEAs and Ni-24Cr binary alloy (**Fig. 5.3**). Each Cr alloys passive film showed a passive region during LSV experiments but the Ni-24Cr at all exposure times exhibited a broader and more stable region compared to the Cr-MPEAs (**Fig. 5.3**). The Ni-24Cr LSV curves had less pronounced metastable breakdown events compared to the Cr-MPEAs passive film. Unlike passive films formed on the Cr-MPEAs which contain multiple oxides and spinels, the Ni-24Cr only contains Ni and Cr oxides and hydroxides. This difference in composition could explain the observed differences in potentiodynamic polarization. The Cr-MPEAs passive films contain extra cations with varies valence states that theoretically creates a large positive charge within the passive film. To charge balance, electrons must be present and as a result passive films should have a high passive current density. Overall, it appears the high cation concentration of passive films formed on the Cr-MPEA's surfaces have similar protective qualities as the Cr-dominate passive film formed on Ni-24Cr (**Fig. 5.2 and 5.3**). Another example of similar protectiveness can be seen in comparisons with the Cr concentration of each oxide within the passive films formed on each alloy (i.e., Cr22-, Cr14-MPEA, and Ni-24Cr) and their low-frequency impedance modulus and passive current density at $-0.1 V_{SCE}$ as a function of exposure time, shown in **Fig. 5.10**. At exposure times 100 s and 1 ks the Cr-MPEAs passive film consist only of hydrated Cr(III) with an impedance modulus magnitude between 10^3 to $10^4 \Omega \text{ cm}^2$ and passive current density of 10^{-6} to $10^{-5} \text{ A cm}^{-2}$. At longer exposure times (10 ks and 86.4 ks) the percentage of hydrated Cr(III) decreases and an increase in Cr(III) spinels were observed. The corresponding impedance modulus increased to $10^5 \Omega \text{ cm}^2$ and passive current density either decreased to $10^{-7} \text{ A cm}^{-2}$ or remained the same magnitude as 1 ks exposure time (**Fig. 5.2, 5.3, and 5.10**). The Ni-24Cr passive film did not contain any Cr-

spinel species at any exposure time. At 100 s exposure time the Ni-24Cr passive film was dominated in hydrated Cr(III) but as exposure time increased to 1 ks to 86.4 ks small amounts of anhydrous Cr(III) formed. The low-frequency impedance magnitude and passive current density of each exposure time for the Ni-24Cr were at similar magnitudes as the Cr-MPEAs (Fig. 5.2, 5.3, and 5.10). These results suggest the Cr-MPEA passive films with a high number of mixed Cr-spinels share similar protective qualities as passive films consisting of only Cr(III) oxide and/or hydroxide.

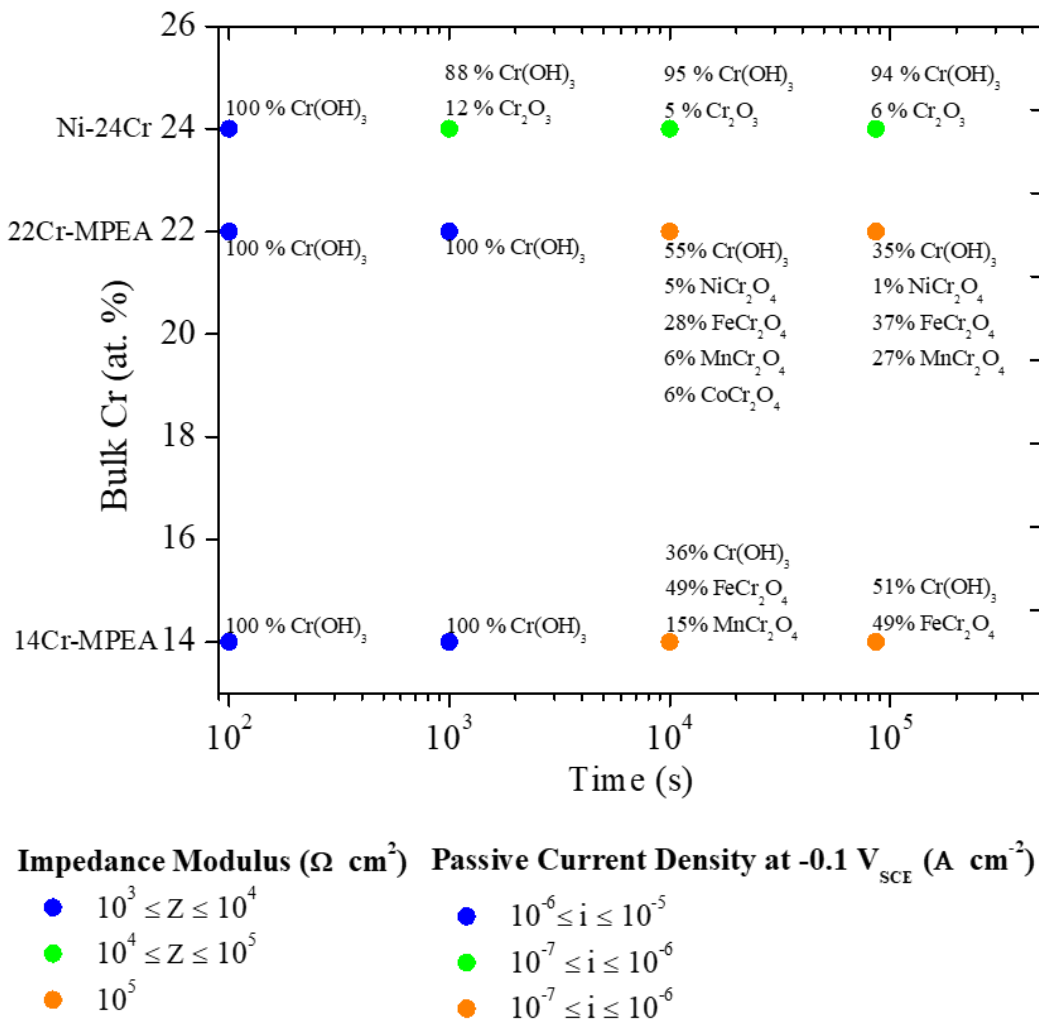


Fig. 5. 10. Cr(III) oxide fractions detected by AR-XPS at 45° take-off angle at each bulk Cr at. % concentration versus exposure time (100 s, 1 ks, 10 ks, and 86.4 ks) of passive films potentiostatically formed at -0.25 V_{SCE} after initial cathodic reduction at -1.3 V_{SCE} for 600 s in deaerated 0.1 M NaCl + HCl at pH 4 of Ni-24Cr, Cr22-MPEA and Cr14-MPEA. The low-frequency impedance modulus for each exposure time is indicated by data point color. The low-frequency impedance for 100 s and 1 ks was 0.1 Hz and was 1 mHz for 10 ks and 86.4 ks. Passive current densities were obtained from LSV curves shown in Fig. 5.3.

5.5.4 Ramifications Towards Corrosion Protection

Figures 2 and 3 as well as the summary figure in 10 indicate improvements in passive current density and impedance with time. This study indicates that passive films and protection attributes in short term exposure experiments are not necessarily representative of long-term behavior. It is further noted that this behavior may be more pronounced in MPEAs because of possible oxide molecular stabilities, thermodynamic driving forces and kinetic variations brought about by a diversity of elements. It is also posited that the most superior oxides for corrosion protection improved with exposure time in Cl⁻. This is a distinguishing factor.

5.5 Conclusion

Electrochemical passivation as a function of short and long exposure times of Cr22- and Cr14-MPEA was investigated and compared to a binary Ni-24Cr alloy. In particular, how the passive film evolved and its corresponding passive properties at exposure times 100 s, 1 ks, 10 ks, and 86.4 ks were explored in deaerated 0.1 M NaCl adjusted to pH 4 using HCl. The following conclusions can be drawn:

- During potentiostatic passivation at $-0.25 V_{SCE}$ each Cr alloy exhibited passive film formation with a low current density that continuously decreased from 10^{-3} - 10^{-4} to $10^{-7} A cm^{-2}$ over the exposure times used. The low-frequency impedance magnitude for each Cr alloy passive film increased with exposure time from 10^3 to $10^5 \Omega cm^2$, indicative of the formation of a more protective passive film. It should be noted this was not due to passive film thickening which reached steady state after $\sim t \geq 3000 s$.
- Upward LSV experiments of each Cr alloy's potentiostatically formed passive film at all exposure times, each exhibited a passive region with low passive current densities (10^{-7} to $10^{-6} A cm^{-2}$).
- The cation concentration for each Cr alloy's passive film was enriched in Cr(III) cations at all exposure times. The Cr22-MPEA passive film (both at the surface and bulk film) was enriched with Co at exposure times of 100 s and 1 ks but was depleted at longer exposure times of 10 ks and 86.4 ks. The concentration of Fe(II) and Mn(II) cations increased with exposure time. Ni(II) cations were not detected at 100 s exposure time but increased in concentration at 10 ks before decreasing in concentration at 86.4 ks.

- The Cr14-MPEA passive films at all exposure times were enriched in Cr(III) and contained small amounts of Ni(II), Fe(II), and Mn(II) with the exception of Mn(II) at 86.4 ks. A decrease in Ni(II) was observed at all exposure times. Fe(II) and Mn(II) increased with exposure time for the Cr14-MPEA passive films. Co enrichment was observed at early exposure times and remained enriched within the bulk of the film at all exposure times.
- Ni enrichment was observed within the altered zone for all alloys at all exposure times, while Cr was either slightly depleted or near bulk Cr concentration. The Cr22- and Cr14-MPEA altered zones were depleted of Fe, Co, and Mn at all exposure times. Slight Mn enrichment was observed in the altered zone for the MPEAs at exposure times of 86.4 ks.
- The dominate species in passive films formed on the Cr-MPEA surfaces at exposure times 100 s and 1 ks was hydrated Cr (III) regardless of take-off angle. At 10 ks and 86.4 ks exposure times the dominate species within the passive film was Cr (III) spinels, with the exception of Cr14-MPEA which had equal amounts of hydrated Cr (III) and spinels at 86.4 ks exposure time.
- Cr spinels were not detected in passive films formed on the Ni-24Cr surface, rather only hydrated and anhydrous Ni(II) and Cr(III) had formed.

5.6 References

1. Cwalina, K.L., et al., *In Operando Analysis of Passive Film Growth on Ni-Cr and Ni-Cr-Mo Alloys in Chloride Solutions*. Journal of The Electrochemical Society, 2019. **166**(11): p. C3241-C3253.
2. Yu, X.-x., et al., *In Situ Observations of Early Stage Oxidation of Ni-Cr and Ni-Cr-Mo Alloys*. CORROSION, 2018. **74**(9): p. 939-946.
3. Jabs, T., P. Borthen, and H.H. Strehblow, *X-Ray Photoelectron Spectroscopic Examinations of Electrochemically Formed Passive Layers on Ni-Cr Alloys*. Journal of The Electrochemical Society, 1997. **144**(4): p. 1231-1243.
4. Li, X. and K. Ogle, *The Passivation of Ni-Cr-Mo Alloys: Time Resolved Enrichment and Dissolution of Cr and Mo during Passive-Active Cycles*. Journal of The Electrochemical Society, 2019. **166**(11): p. C3179-C3185.
5. Lutton, K., et al., *Understanding multi-element alloy passivation in acidic solutions using operando methods*. Electrochemistry Communications, 2017. **80**: p. 44-47.
6. Jeng, S.-P., P.H. Holloway, and C.D. Batich, *Surface passivation of Ni/Cr alloy at room temperature*. Surface Science, 1990. **227**(3): p. 278-290.
7. Olefjord, I., B. Brox, and U. Jelvestam, *Surface Composition of Stainless Steels during Anodic Dissolution and Passivation Studied by ESCA*. Journal of The Electrochemical Society, 1985. **132**(12): p. 2854-2861.
8. Zagidulin, D., et al., *Characterization of surface composition on Alloy 22 in neutral chloride solutions*. Surface and Interface Analysis, 2013. **45**(6): p. 1014-1019.

9. Zhang, X., D. Zagidulin, and D.W. Shoesmith, *Characterization of film properties on the NiCrMo Alloy C-2000*. *Electrochimica Acta*, 2013. **89**: p. 814-822.
10. Ebrahimi, N., et al., *The influence of chromium and molybdenum on the repassivation of nickel-chromium-molybdenum alloys in saline solutions*. *Surface and Interface Analysis*, 2017. **49**(13): p. 1359-1365.
11. Yu, X.-x., et al., *New Insights on the Role of Chloride During the Onset of Local Corrosion: TEM, APT, Surface Energy, and Morphological Instability*. *CORROSION*, 2019. **75**(6): p. 616-627.
12. Yu, X.-x., et al., *Nonequilibrium Solute Capture in Passivating Oxide Films*. *Physical Review Letters*, 2018. **121**(14): p. 145701.
13. Lin, A.Y.W., et al., *Early-stage NiCrMo oxidation revealed by cryo-transmission electron microscopy*. *Ultramicroscopy*, 2019. **200**: p. 6-11.
14. Oh, K., et al., *Observation of passive films on Fe–20Cr–xNi (x=0, 10, 20wt.%) alloys using TEM and Cs-corrected STEM–EELS*. *Corrosion Science*, 2014. **79**: p. 34-40.
15. Lutton, K., et al., *Passivation of Ni-Cr and Ni-Cr-Mo Alloys in Low and High pH Sulfate Solutions*. *Journal of The Electrochemical Society*, 2023. **170**(2): p. 021507.
16. Ramanathan, R. and P.W. Voorhees, *Morphological stability of steady-state passive oxide films*. *Electrochimica Acta*, 2019. **303**: p. 299-315.
17. Zhang, Z., et al., *Role of Alloying Elements in Passive and Transpassive Behavior of Ni–Cr-Based Alloys in Borate Buffer Solution*. *Journal of The Electrochemical Society*, 2021. **168**(8): p. 081503.
18. Karri, M., et al., *Role of Chromium in Anomalous Behavior of the Passive Layer in Ni-Cr-Mo Alloys in 1 M HCl Solution*. *Corrosion*, 2022. **78**(3): p. 228-238.
19. Wang, Z., et al., *XPS and ToF-SIMS Investigation of Native Oxides and Passive Films Formed on Nickel Alloys Containing Chromium and Molybdenum*. *Journal of The Electrochemical Society*, 2021. **168**(4): p. 041503.
20. Gerard, A.Y., et al., *Aqueous passivation of multi-principal element alloy Ni₃₈Fe₂₀Cr₂₂Mn₁₀Co₁₀: Unexpected high Cr enrichment within the passive film*. *Acta Materialia*, 2020. **198**: p. 121-133.
21. Han, J., et al., *Potential Dependent Mn Oxidation and Its Role in Passivation of Ni₃₈Fe₂₀Cr₂₂Mn₁₀Co₁₀ Multi-Principal Element Alloy Using Multi-Element Resolved Atomic Emission Spectroelectrochemistry*. *Journal of The Electrochemical Society*, 2021. **168**(5): p. 051508.
22. Inman, S.B., et al., *Effect of Mn Content on the Passivation and Corrosion of Al_{0.3}Cr_{0.5}Fe₂Mn_xMo_{0.15}Ni_{1.5}Ti_{0.3} Compositionally Complex Face-Centered Cubic Alloys*. *Corrosion*, 2021. **78**(1): p. 32-48.
23. Li, X., et al., *Communication—Dissolution and Passivation of a Ni-Cr-Fe-Ru-Mo-W High Entropy Alloy by Elementally Resolved Electrochemistry*. *Journal of The Electrochemical Society*, 2020. **167**(6): p. 061505.
24. Luo, H., et al., *Corrosion behavior of an equiatomic CoCrFeMnNi high-entropy alloy compared with 304 stainless steel in sulfuric acid solution*. *Corrosion Science*, 2018. **134**: p. 131-139.
25. Panindre, A.M., et al., *Corrosion of Ni-Fe-Cr-Mo-W-X Multi-Principal Element Alloys*. *Journal of The Electrochemical Society*, 2021. **168**(3): p. 031513.
26. Qiu, Y., et al., *Real-time dissolution of a compositionally complex alloy using inline ICP and correlation with XPS*. *npj Materials Degradation*, 2020. **4**(1): p. 7.

27. Qiu, Y., et al., *A Surface Study of the Native Oxide upon a Compositionally Complex Alloy*. CORROSION, 2018. **74**(12): p. 1312-1317.
28. Quiambao, K.F., et al., *Passivation of a corrosion resistant high entropy alloy in non-oxidizing sulfate solutions*. Acta Materialia, 2019. **164**: p. 362-376.
29. Wang, K., et al., *Potential-pH diagrams considering complex oxide solution phases for understanding aqueous corrosion of multi-principal element alloys*. npj Materials Degradation, 2020. **4**(1): p. 35.
30. Wang, L., et al., *Study of the surface oxides and corrosion behaviour of an equiatomic CoCrFeMnNi high entropy alloy by XPS and ToF-SIMS*. Corrosion Science, 2020. **167**: p. 108507.
31. Wang, Z., et al., *Effect of temperature on the passive film structure and corrosion performance of CoCrFeMoNi high-entropy alloy*. Corrosion Science, 2022. **208**: p. 110661.
32. Zhang, B., Y. Zhang, and S.M. Guo, *A thermodynamic study of corrosion behaviors for CoCrFeNi-based high-entropy alloys*. Journal of Materials Science, 2018. **53**(20): p. 14729-14738.
33. Zhou, Q., et al., *Corrosion behavior of Hf_{0.5}Nb_{0.5}Ta_{0.5}Ti_{1.5}Zr refractory high-entropy in aqueous chloride solutions*. Electrochemistry Communications, 2019. **98**: p. 63-68.
34. Gerard, A.Y., et al., *The role of chromium content in aqueous passivation of a non-equiatomic Ni₃₈Fe₂₀Cr_xMn_{21-0.5x}Co_{21-0.5x} multi-principal element alloy (x = 22, 14, 10, 6 at%) in acidic chloride solution*. Acta Materialia, 2023. **245**: p. 118607.
35. Yang, J., et al., *Effects of Mn on the electrochemical corrosion and passivation behavior of CoFeNiMnCr high-entropy alloy system in H₂SO₄ solution*. Journal of Alloys and Compounds, 2020. **819**: p. 152943.
36. Raza, A., et al., *Corrosion resistance of weight reduced Al_xCrFeMoV high entropy alloys*. Applied Surface Science, 2019. **485**: p. 368-374.
37. Hsu, K.-M., S.-H. Chen, and C.-S. Lin, *Microstructure and corrosion behavior of FeCrNiCoMn_x (x = 1.0, 0.6, 0.3, 0) high entropy alloys in 0.5 M H₂SO₄*. Corrosion Science, 2021. **190**: p. 109694.
38. Choudhary, S., N. Birbilis, and S. Thomas, *Evolution of Passivity for the Multi-Principal Element Alloy CoCrFeNi with Potential, pH and Exposure in Chloride Solution*. Corrosion, 2021.
39. Wang, X., et al., *Origin of enhanced passivity of Cr–Fe–Co–Ni–Mo multi-principal element alloy surfaces*. npj Materials Degradation, 2023. **7**(1): p. 13.
40. Lu, Q., et al., *Corrosion behavior of a non-equiatomic CoCrFeNiTi high-entropy alloy: A comparison with 304 stainless steel in simulated body fluids*. Journal of Alloys and Compounds, 2022. **897**: p. 163036.
41. Lu, P., et al., *Computational design and initial corrosion assessment of a series of non-equimolar high entropy alloys*. Scripta Materialia, 2019. **172**: p. 12-16.
42. Li, T., et al., *Localized corrosion behavior of a single-phase non-equimolar high entropy alloy*. Electrochimica Acta, 2019. **306**: p. 71-84.
43. Jakupi, P., et al., *The impedance properties of the oxide film on the Ni–Cr–Mo Alloy-22 in neutral concentrated sodium chloride solution*. Electrochimica Acta, 2011. **56**(17): p. 6251-6259.

44. Doniach, S. and M. Sunjic, *Many-electron singularity in X-ray photoemission and X-ray line spectra from metals*. Journal of Physics C: Solid State Physics, 1970. **3**(2): p. 285-291.
45. KOLXPD, <http://kolxpd.kolibrik.net>.
46. Biesinger, M.C., et al., *Resolving surface chemical states in XPS analysis of first row transition metals, oxides and hydroxides: Cr, Mn, Fe, Co and Ni*. Applied Surface Science, 2011. **257**(7): p. 2717-2730.
47. Allen, G.C., et al., *A study of a number of mixed transition metal oxide spinels using X-ray photoelectron spectroscopy*. Applied Surface Science, 1989. **37**(1): p. 111-134.
48. Castle, J.E. and K. Asami, *A more general method for ranking the enrichment of alloying elements in passivation films*. Surface and Interface Analysis, 2004. **36**(3): p. 220-224.
49. Frankel, G.S., T. Li, and J.R. Scully, *Perspective—Localized Corrosion: Passive Film Breakdown vs Pit Growth Stability*. Journal of The Electrochemical Society, 2017. **164**(4): p. C180-C181.
50. Gerard, A.Y., et al., *Progress in Understanding the Origins of Excellent Corrosion Resistance in Metallic Alloys: From Binary Polycrystalline Alloys to Metallic Glasses and High Entropy Alloys*. CORROSION, 2020. **76**(5): p. 485-499.
51. Prince, A.A.M., et al., *Characterization of ferrites and chromites prepared by solid-state methods: XRD, XPS and Moessbauer study*. Power Plant Chemistry, 2007. **9**(7): p. 432-440.
52. Blades, W.H., M.R. Barone, and P. Reinke, *Initial atomic-scale oxidation pathways on a Ni–15Cr(100) alloy surface*. npj Materials Degradation, 2021. **5**(1): p. 17.
53. Blades, W.H. and P. Reinke, *From Alloy to Oxide: Capturing the Early Stages of Oxidation on Ni–Cr(100) Alloys*. ACS Applied Materials & Interfaces, 2018. **10**(49): p. 43219-43229.
54. Blades, W.H. and P. Reinke, *Early-stage evolution of nanoscale oxides on Ni(111) and Ni–Cr(111) surfaces*. Corrosion Science, 2022. **209**: p. 110755.
55. Ramanathan, R., et al., *Evolution of NiO Island Size Distributions during the Oxidation of a Ni–5Cr Alloy: Experiment and Modeling*. ACS Applied Materials & Interfaces, 2018. **10**(10): p. 9136-9146.
56. Lange, J.G.S.a.N.A., *Lange's Handbook of Chemistry* ed. 17. 2017, New York: McGraw-Hill Education.
57. Pourbaix, M., *Atlas of Electrochemical Equilibria in Aqueous Solutions* 1974, Houston, TX: National Association of Corrosion Engineers.
58. Tsai, K.Y., M.H. Tsai, and J.W. Yeh, *Sluggish diffusion in Co–Cr–Fe–Mn–Ni high-entropy alloys*. Acta Materialia, 2013. **61**(13): p. 4887-4897.
59. Kulkarni, K. and G.P.S. Chauhan, *Investigations of quaternary interdiffusion in a constituent system of high entropy alloys*. AIP Advances, 2015. **5**(9): p. 097162.
60. Lobnig, R.E., et al., *Diffusion of cations in chromia layers grown on iron-base alloys*. Oxidation of Metals, 1992. **37**(1): p. 81-93.
61. Dean, M.H. and U. Stimming, *The electronic properties of disordered passive films*. Corrosion Science, 1989. **29**(2): p. 199-211.
62. Ter-Ovanessian, B. and B. Normand, *Passive films growth on different Ni–Cr alloys from the migration of cation vacancies*. Journal of Solid State Electrochemistry, 2016. **20**(1): p. 9-18.

6. Conclusions

This dissertation enhanced the understanding of the fate of each alloying element during aqueous passivation of $\text{Ni}_{38}\text{Fe}_{20}\text{Cr}_x\text{Mn}_{21-0.5x}\text{Co}_{21-0.5x}$ ($x = 22, 14, 10, 6$ at. % - i.e., Cr_x-MPEAs) MPEAs and how they affect the resulting electrochemical passive behavior when exposed to a Cl^- electrolyte. Many different experimental factors were considered in order to remove unknowns about MPEA passivity such as, solution pH level, bulk alloy Cr concentration, and exposure time. Improved insights were gained on MPEA passive film's chemistry such as, valence state, cation fraction, elemental fraction at the oxide/metal interface, and cation/elemental distribution throughout the passive film and at the oxide/metal interface. Furthermore, elemental dissolution was tracked to account for lost cations to solution rather than joining the passive film and/or at the oxide/metal interface (i.e., altered zone). Electrochemical and passive film properties were compared to conventional binary Cr alloys. An in-depth analysis of the electrochemical properties, passive film characteristics and elemental dissolution was conducted by utilizing various in situ and ex situ characterization techniques. Listed below are the key findings of this dissertation:

The passive behavior of a $\text{Ni}_{38}\text{Fe}_{20}\text{Cr}_{22}\text{Mn}_{10}\text{Co}_{10}$ MPEA was explored for electrochemically formed passive films in acidic Cl^- solution. The electrochemical passive behavior was characterized by EIS and LSV experiments. Potentiostatically formed passive film was monitored by SF-EIS for 10 ks assuming an equivalent circuit model with a constant phase element. The passive film chemistry and cation/elemental distribution throughout the film and at the oxide/metal interface was explored by XPS and APT. Elemental dissolution during passive film formation was monitored by AESEC. The electrochemical behavior of the MPEA was similar to that of the binary Ni-24Cr alloy. Each had a broad passive region with low passive current densities and exhibited crevice corrosion at high anodic potentials. Electrochemical passivation at a constant passive potential of the Cr₂₂-MPEA resulted in a Cr-rich passive film with a low concentration of Ni, Fe, Mn, and Co cations. The Cr₂₂-MPEA had a higher Cr(III) enrichment compared to passive film formed on the Ni-24Cr binary alloy. The MPEA passive film valence state was investigated and found to consist of hydrated Cr(III) and a small concentration of Cr spinels such as, NiCr_2O_4 and FeCr_2O_4 . The oxide/metal interface was enriched with Ni, with a slight enrichment of Cr. Mn, Fe, and Co were all depleted within the oxide/metal interface. Cr enrichment is attributed to a

combination of thermodynamics and kinetic factors as well as depletion of Ni, Fe, Co, and Mn governed by chemical dissolution kinetics exacerbated by the NaCl environment.

The role of Cr in MPEA passivity was explored for a series of Cr-MPEAs in which the bulk Cr concentration was varied, $\text{Ni}_{38}\text{Fe}_{20}\text{Cr}_x\text{Mn}_{21-0.5x}\text{Co}_{21-0.5x}$ ($x = 22, 14, 10, 6$ at. % - i.e., Cr_x-MPEAs) and compared to binary Fe-Cr, Ni-Cr, and Co-Cr binary alloys. The same techniques used above were utilized in this investigation. In general, all Cr-MPEAs and Cr binary alloys showed improved corrosion resistance with increasing bulk Cr concentration such as, wider passive region, decrease in passive current density, and increase in breakdown potential. Clear passive regions were exhibited by Cr-MPEAs with bulk Cr concentration ≥ 10 at. % and for Ni-Cr $\geq 12\%$ Cr. Limited passivity and localized crevice corrosion was observed in the Cr₆-MPEA, Fe- x Cr, Ni- x Cr, and Co- x Cr ($x \leq 10$ at. %). The Cr₁₀-MPEA was shown to have lower sustained passive current densities compared to Fe-10Cr and Co-10Cr binary alloys. Alloys that demonstrated significant passivation behavior at 0.0 V_{SCE} for 10 ks, underwent electrochemical passivation and the resulting film was characterized. Passive films formed on both Cr-MPEAs and Cr binary alloys were enriched in Cr(III) cations, at concentrations above the bulk Cr concentration. The highest Cr enrichment was observed for passive films formed on the Cr₁₀-MPEA surface but was also the only alloy to be Cr depleted in the altered zone (i.e., oxide/metal interface). The dominate species in all Cr-MPEA and Cr binary alloy passive films was hydrated Cr(III). A small fraction of Cr spinels with Ni and Fe were detected in the MPEAs but was not seen in any binary Cr alloy. Cr enrichment within the potentiostatically formed passive films was attributed to the selective dissolution of Ni, Fe, Mn, and Co. Cr enrichment terms could not be uniquely associated to third element effects based on Ni, Co, Mn, or Fe alloying elements. Limiting factors for Cr(III) enrichment within the passive film should consider the Cr depletion in the altered zone and Cr solid state diffusion rates.

An investigation of the electrochemical passive behavior of a $\text{Ni}_{38}\text{Fe}_{20}\text{Cr}_x\text{Mn}_{21-0.5x}\text{Co}_{21-0.5x}$ MPEA (where $x = 22, 14, 10, 6$ - at. %) and the effect of alkaline pH was investigated and compared to binary Ni-Cr, Fe-Cr, and Co-Cr alloys. The same techniques discussed for acidic conditions were utilized in this study. The passive behavior of the Cr-MPEAs and binary Cr alloys in alkaline Cl⁻ electrolyte improved when compared to acidic Cl⁻ electrolytes. When polarized in alkaline conditions, the Cr-MPEAs exhibited improved passive behavior demonstrated by a broad

passive region with a low passive current density of $\sim 10^{-6}$ A cm⁻². The passive current density was found to be independent of bulk Cr content when polarized in alkaline pH level versus an acidic pH level. A dependence of bulk Cr concentration and passive current density was only observed in the Co-Cr and Fe-Cr binary alloys in which passive current density decreased from 10^{-3} to 10^{-6} A cm⁻² with increase in bulk Cr content. All Cr-MPEAs and Ni-Cr alloys had a low passive current density of $\sim 10^{-6}$ A cm⁻² regardless of bulk Cr concentration. Passive films formed on the Cr-MPEA surfaces under alkaline conditions were enriched with both Ni(II) and Cr(III) cations and a low concentration of Fe(II) and Co(II) cations. A slight increase in Fe(III) cations were observed in Cr-MPEA passive films formed in alkaline conditions versus acidic pH levels. Passive films formed on the Ni-Cr and Fe-Cr alloys were enriched with Cr(III) and the corresponding principle alloying element (i.e., Ni and Fe). The Cr10-MPEA and Ni-24Cr binary had similar Cr enrichment and their passive films were the highest in Cr concentration. Passive films formed in alkaline pH level had a lower concentration of Cr(III) cations compared to passive films formed in acidic pH levels. Ni enrichment was observed within the altered zone (i.e., oxide/metal interface) for the Cr-MPEAs and Ni-Cr binary alloys. Cr depletion was not observed in the high Cr containing alloys instead the Cr concentration within the altered zone stayed relatively constant with the bulk Cr content. Slight Cr depletion was seen in the altered zone for the Cr10-MPEA, Ni-12Cr, and Co-10Cr binary alloy. The dominate valence state for all passive films were hydroxide species with the exception of passive films formed on the Fe-20Cr binary alloy. The valence state of the Cr-MPEA passive films consisted mainly of hydrated Ni(II) and Cr(III) species. A small fraction of NiFe₂O₄ spinel was detected, which is different compared to passive films formed at acidic pH levels which contain only Cr spinels only. The dominate Cr(III) species was Cr hydroxide for all passive films.

Finally, the Cr22-, Cr14-MPEA, and Ni-24Cr passive film formation was investigated as a function of exposure time when passivated in slightly acidic Cl⁻ solution for 100 s, 1 ks, 10 ks, and 86.4 ks using the same electrochemical characterization techniques discussed previously. The cation, elemental, and oxide distribution of passive films were investigated by AR-XPS. During potentiostatic passivation all alloys exhibited passive film formation with a low current density that continuously decreased from 10^{-3} to 10^{-4} to 10^{-7} A cm⁻² over all exposure times. At all exposure times, the passive films low-frequency impedance increased from 10^3 to 10^5 Ω cm², indicative of the formation of a more protective passive film. Anodic LSV experiments of formed passive films at each exposure time for all alloys exhibited passive region with a low passive current density

(10^{-7} to 10^{-6} A cm⁻²). It should be noted the improved passive behavior was not due to passive film thickening which reached steady state after $\sim t \geq 3000$ s. At all exposure times the Cr22-MPEA passive films were enriched with Cr(III) cations. As exposure time increases from 100 s to 86.4 ks an increase in Fe(II) and Mn(II) cations is observed. The Cr22-MPEA was also enriched in Co(II) cations (both at the surface and bulk film) at exposure times of 100 s and 1 ks but then decreased in concentration becoming depleted at exposure times of 10 ks and 86.4 ks. At 100 s Ni(II) cations were not detected but increased in concentration at exposure time of 10 ks before decreasing in concentration at 86.4 ks. Passive films formed on the Cr14-MPEA were also enriched in Cr(III) cations at all exposure times. Co enrichment was also observed at all exposure times within the bulk of the film and only on the surface at exposure times of 100 s and 1 ks. At all exposure times the Cr14-MPEA contained a low concentration of Ni(II), Fe(II), and Mn(II) cations, with the exception of Mn(II) at 86.4 ks. At exposure time increased Fe(II) cations increased and Ni(II) cations decreased. An increase in Mn(II) cation was observed at exposure times of 100 s to 10 ks. Ni enrichment was observed in the altered zone (i.e., oxide/metal interface) at all exposure times for the Cr22-, Cr14-MPEA, and Ni-24Cr binary alloy, while Cr was either slightly depleted or near bulk Cr concentration. The Cr22- and Cr14-MPEA altered zones were depleted of Fe, Co, and Mn at all exposure times. Slight Mn enrichment was observed only at exposure time of 86.4 ks in the MPEA altered zones. At relatively early exposure times, the MPEA passive films consisted mainly of hydrated Cr(III) oxide and a small fraction of XO, X₂O₃ oxides where X = Ni, Fe, Cr, Mn, Co. As exposure time increases to 10 ks and 86.4 ks, the fraction of hydrated Cr(III) decreases and Cr spinels form. As exposure times increased the concentration of spinels increased eventually becoming the dominate oxide species. With the exception of Cr14-MPEA passive film bulk composition, which has equal parts hydroxide and spinels. Compared to a Ni-24Cr binary alloy, no spinels were detected at any exposure time. Only hydrated and anhydrous Cr and Ni oxides.

7. Suggested Future Work

The research presented in this dissertation only provides some in-sight on MPEA passivity and the fate of the alloying elements. With limited time only so many investigations can be conducted that explore MPEA passivity. Due to the high complexity of MPEAs and the limited corrosion research known to date many unknowns still exist, such as MPEA passive film's crystal

structure and its correlating dielectric constant (ϵ) and electronic properties such as, n-type vs p-type semiconductor.

The passive film characterization techniques, XPS and APT, used within this dissertation are only able to give information about the passive film's valence state, cation fraction, elemental fraction, and their corresponding distribution within the film and at the oxide/metal interface. Further structure characterization will need to be conducted such as, transmission electron microscopy (TEM) and/or grazing incidence X-ray diffraction (GIXRD) to determine whether a passive film is a non-equilibrium corundum or rock salt solid solution versus phase separated oxides. With such information an improved understanding can be developed on the fate of each alloying element during MPEA passivity. This includes but are not limited to, if there are solute-trapped cations residing within a certain oxide phase, the distribution of cations if a solid solution oxide forms, and how the oxide structure initially forms and evolves over time.

Passive film growth was monitored by thickness calculations by SF-EIS assuming a constant phase element. The calculation requires knowing ϵ of the particular oxide being analyzed. MPEAs are a relatively new class of material with limited known about their properties compared to conventional alloys. Due to this limitation, assumptions must be made in order to composite for the unknowns. Thickness calculations conducted within each chapter used the same rule of mixtures assumption in which a weighted average of known dielectric constants was used of oxides detected by XPS. Due to limited information on passive film structure this assumes the detected oxides by XPS are indeed present and are contributing to the dielectric properties. With so many assumptions on the nature of the MPEA passive film, it is difficult to report a thickness with a high degree of accuracy using SF-EIS. A more precise ϵ for MPEA passive films would resolve such an issue. Future research should include considerations in the ϵ of MPEA passive films which can be obtained from ellipsometry experiments.

Understanding the semiconducting properties, such as n-type vs. p-type, of a passive film formed on MPEA surface will provide more insights on its ability to inhibit electron transfer through the film. Many processes in corrosion depend on the transfer of electrons such as passive film formation and breakdown. To better understand the protective qualities of MPEA passive films, one must first determine whether it behaves as an n-type semiconductor or a p-type semiconductor. Mott-Schottky has shown to be a powerful tool in corrosion science in which the

tests provides the ability to analyze the semiconducting properties in situ by measuring the capacitance as a function of potential. Future testing should consider Mott-Schottky experiments on passive films formed on MPEA surfaces and compared to their pure metal counterparts. Such analysis should provide insights on MPEA passive films ability to inhibit electron transfer into reducible aqueous species and how it compares to simpler oxides.

8. Appendix: Thermal oxidation of Multi-Principal Element Alloy $\text{Ni}_{38}\text{Fe}_{20}\text{Cr}_{22}\text{Mn}_{10}\text{Co}_{10}$ and the Nature of its Passive Film: Phase Separated versus Solid Solution Oxides.

8.1 Introduction

Depending on the alloy, environment, and testing conditions a variety of oxide configurations and compositions have been observed on multi-principal element alloys (MPEAs), for example: layering of complex or stoichiometric oxides (or other shapes dictated at equilibrium by surface energy and interface energy minimization), complex oxide mixtures, and non-stoichiometric multi-element solid solution oxides [1-22]. The oxidation behavior of $\text{NbCrMoTiAl}_{0.5}$, $\text{NbCrMoVAl}_{0.5}$, $\text{NbCrMoTiVAl}_{0.5}$ and $\text{NbCrMoTiVAl}_{0.5}\text{Si}_{0.3}$ alloys was investigated at 1200 °C for 20 hours in air by X-ray diffraction (XRD) and backscattered electron imaging (BSE). Oxides formed on each $\text{NbCrMoTiAl}_{0.5}$ –based MPEA exhibited similar behavior with only slight changes in oxide product, due to the alloying element variations. The MPEA oxide products exhibited a layered profile consisting of an inner complex oxide (CrNbVO_6 , $(\text{TiCrNb})\text{O}_2$, or $(\text{TiCrNbV})\text{O}_2$) and outer stoichiometric oxide (Al_2O_3) [10]. The mechanisms involved in the formation of these complex layered oxides were not discussed. Similar observations have been observed on solid solution Hf-Ta binary alloys, in which after air oxidation a superstructure oxide consistent with $\text{Hf}_6\text{Ta}_2\text{O}_{17}$ had formed [14]. It was suggested this $\text{Hf}_6\text{Ta}_2\text{O}_{17}$ superstructure was a result of a reaction between HfO_2 and metastable Ta_2O_5 oxides.

Many of these reported complex oxides form after a relatively long exposure time and may not be seen during the early stages of oxidation. Typically, during the initial stages of oxidation kinetics will largely influence an oxides composition and structure. While thermodynamics will play a weaker role due to the constraint of element diffusion and inefficient time to form thermodynamically stable complex oxides[21, 23, 24]. Kautz et al. investigated the early stages of oxidation of a $\text{Ni}_{38}\text{Cr}_{22}\text{Fe}_{20}\text{Mn}_{10}\text{Co}_{10}$ MPEA by atom probe tomography (APT) at two different conditions: 10 mbar $\text{O}_{2(g)}$ at 120 °C for 5 minutes and 300 °C for 2 minutes [21]. At both conditions, the resulting nm thick oxide consisting of an inner Cr-rich oxide and outer Fe, Mn, Co, and Ni-rich oxide. At 300 °C a larger Ni enrichment was observed at the oxide/metal interface compared to at 120 °C. Unfortunately, the valence state of the oxide was not investigated but it was concluded

due to the low temperatures and short exposure times used stoichiometric oxides and complex oxides likely had not formed but rather the oxide consisted of a mixture of metastable oxide phases [21]. To further explore the oxides composition and oxide configuration, other characterization techniques are necessary such as angle-resolved X-ray photoelectron spectroscopy (AR-XPS).

In this study a non-equimolar, single phase, solid solution $\text{Ni}_{38}\text{Fe}_{20}\text{Cr}_{22}\text{Mn}_{10}\text{Co}_{10}$ MPEA was heat treated at 300 °C for 2 minutes to form a nm thick oxide and the resulting films chemistry was investigated. The aim of this study was to establish an improved understanding of the nature of the oxide including its chemistry, valence state, configuration, cation and elemental distribution when formed on a MPEA. The atomic distribution and profiles of each alloying element and potentially formed oxides within the passive film will be explored by AR-XPS and APT.

8.2 Experimental

The $\text{Ni}_{38}\text{Fe}_{20}\text{Cr}_{22}\text{Mn}_{10}\text{Co}_{10}$ – at. % MPEA were arc-melted, cast, and homogenized at 1100 °C for 96 h using methods described previously in Task 1 [25]. For simplicity, the MPEA will be referred to as Cr22-MPEA. Sections of the Cr22-MPEA with approximate surface area of 10 mm by 10 mm and thickness of 2 mm were prepared using metallographic polishing methods to a final mechanical polish/chemical etching step of 0.05 μm colloidal silica suspension. In preparation for thermal oxidation treatments, flat, polished sections (i.e., coupons) of Cr22-MPEA were mounted onto SEM stubs using Ag paste. The coupons were sputtered at an angle of 45° using 2kV monatomic Ar^+ rastered over a 4 mm² area. Five equally spaced locations over the sample surface were sputtered to remove any surface contaminants prior to thermal oxidation. APT sample preparation was performed using an FEI Helios dual beam focused ion beam-scanning electron microscope (FIB-SEM) according to details given in Thompson et al. [26]. The APT microtip array contained specimens of both alloys and was mounted in a stainless-steel micro-array mount (Oxford Atomic).

Thermal oxidation treatments were performed in a chemical reactor chamber attached to the XPS instrument under UHV (10^{-7} to 10^{-8} mbar). The reactor chamber was preheated to a temperature of 300 °C at a rate of ≈ 20 C/min, then XPS and APT coupons were inserted into the reactor, and O_2 was leaked into the chamber until the desired pressure level of 10 mbar was achieved, after which samples were held at 300 °C-10 mbar O_2 gas for 2 minutes. After the 2-

minute exposure was completed, the reactor was evacuated and samples were cooled under He gas to room temperature at a cooling rate of $\approx 5 \text{ C min}^{-1}$. Samples were transferred back to the analysis chamber under UHV. The exposure conditions of $300 \text{ }^\circ\text{C} - 10 \text{ mbar O}_2 \text{ gas} - 2 \text{ minutes}$ were selected to form a nanoscale oxide film [21].

A CAMECA local electrode atom probe (LEAP) 4000X HR APT system equipped with a 355 nm wavelength UV laser was used for APT data collection with the following user-selected parameters: 60 pJ/pulse laser energy, 125 kHz pulse repetition rate, 40 K specimen base temperature, and 0.003 detected ions/pulse detection rate. Data were reconstructed and analyzed using the Interactive Visualization and Analysis Software (IVAS), version 3.8.8 by CAMECA. Elemental composition profiles were determined using 1D concentration profiles with a bin width of 0.3 nm. Representative mass spectra for oxide film/alloy substrates analyzed via APT (Cr22-MPEA), with prominent peaks labelled are shown in **Fig. 8.1**. Each mass spectra contains signal from the base alloy and oxide film. Peak deconvolution based on natural isotopic abundances were done for overlaps at 27 Da ($^{56}\text{Fe}^{2+}/^{56}\text{Cr}^{2+}$) and 56 Da ($^{56}\text{Fe}^+ / ^{56}\text{Cr}^+$) for the MPEA.

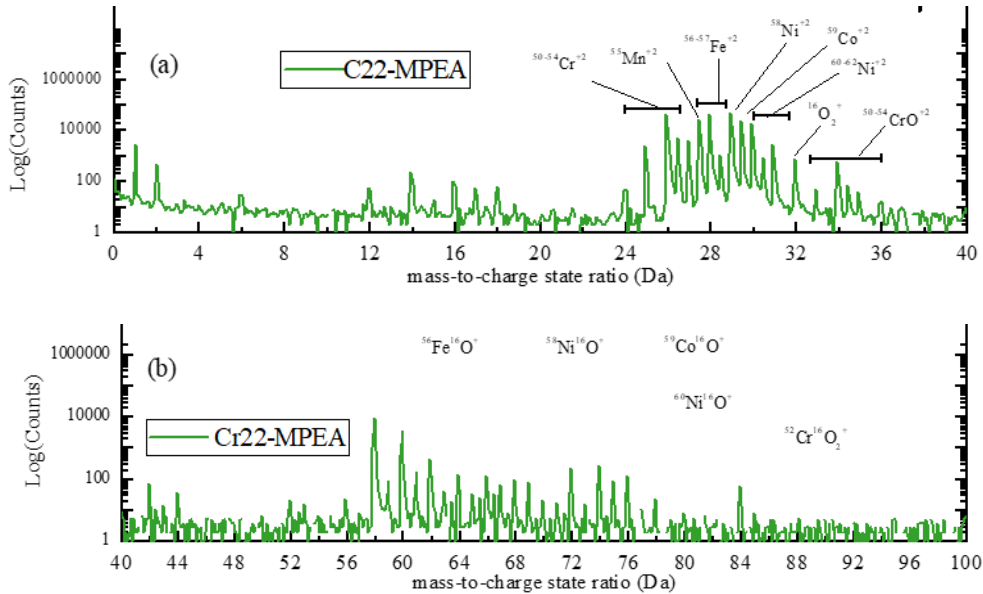


Fig. 8. 1. Ranging criteria for APT mass spectrum analysis for the base alloy and oxide film for from (a) 0-40 Da and (b) from 40-100 Da for Cr22-MPEA. A bin width of 0.1 Da was used.

XPS measurements were performed with a Physical Electronics Quantera Scanning X-ray Microprobe (SXM). This system uses a focused monochromatic Al K α X-ray (1486.7 eV) source for excitation and a spherical section analyzer at a take-off angle of 30°, 45°, 75°, 90°. The instrument has a 32-element multichannel detection system. High energy resolution spectra were collected using a pass-energy of 69.0 eV with a step size of 0.125 eV. For the Ag 3d5/2 line, these conditions produced a FWHM of 0.92 eV \pm 0.05 eV. The binding energy (BE) scale is calibrated using the Cu 2p3/2 feature at 932.62 \pm 0.05 eV and Au 4f7/2 at 83.96 \pm 0.05 eV. Cation fraction within the passive film and elemental composition just below the metal/oxide interface (i.e., altered zone) (relative to all cations or elements detected) were determined by spectral deconvolution of individual core-level spectra with KOLXPDTM analysis software. A more detailed description of XPS spectral deconvolution has been provided previously in Chapter 2 [16, 27, 28]. From hereafter the metal/oxide interface will be referred to as the altered zone.

Theoretical XPS cation fractions were computed from XPS intensity expressions assuming exponential attenuation in a homogenous thin overlayer shown in **Eq. 8.1**;

$$I_i = I_i^\infty \left[1 - \exp\left(\frac{-l_{iox}}{\lambda_{i,iox} \sin\theta}\right) \right] \times \exp\left(\frac{1}{\sin\theta} \sum_{j=1}^{j=i-1} \frac{-l_j}{\lambda_{i,j}}\right) \quad (8.1)$$

where I_i is the XPS core level intensity of element/oxide of i , I_i^∞ is the relative sensitivity factor (RSF) for element i , l_{iox} is the oxide thickness of i , θ is AR-XPS take-off angle, $\lambda_{i,iox}$ is the electron attenuation length (EAL) of element i being attenuated by i oxide, l_{jox} is the oxide thickness of overlay j on i , and $\lambda_{i,jox}$ is the EALS of element i being attenuated by j overlayer [29, 30]. The EAL values were obtained from NIST Standard Reference Database 82, assuming Ni2p3/2, Cr2p3/2, Fe2p1/2, Mn2p1/2, and Co2p1/2 XPS spectra [31]. The following elements and oxides (i.e., i and j) were considered: Cr/Cr₂O₃, Fe/Fe₂O₃, and Ni/NiO, corundum solid solution assuming X-Cr₂O₃, where X = Ni, Fe, Cr, Mn, Co, and a rock-salt solid solution assuming X-NiO, where X = Ni, Fe, Cr, Mn, Co, summarized in **Fig. 8.2**. For the solid solution models X is the same as i . Three different phase separated oxide configurations were modeled and consisted of (from outer to inner most layer) (1) Fe₂O₃-Cr₂O₃-NiO, (2) Fe₂O₃-NiO-Cr₂O₃, and (3) Cr₂O₃-Fe₂O₃-NiO (**Fig. 8.2**).

Example intensity expressions are provided for phase separated model (1) Fe₂O₃-Cr₂O₃-NiO, shown in **Eqs. 8.2-8.5**;

$$\text{Top: Fe2p - Fe}_2\text{O}_3 \quad I_{Fe} = I_{Fe}^{\infty} \left[1 - \exp\left(\frac{-I_{Fe2O3}}{\lambda_{Fe,Fe2O3} \sin\theta}\right) \right] \quad (2)$$

$$\text{Middle: Ni2p - NiO} \quad I_{Ni} = I_{Ni}^{\infty} \left[1 - \exp\left(\frac{-I_{NiO}}{\lambda_{Ni,NiO} \sin\theta}\right) \right] \times \exp\left[\frac{1}{\sin\theta} \left(\frac{-I_{Fe2O3}}{\lambda_{Ni,Fe2O3}}\right)\right] \quad (3)$$

$$\text{Bottom: Cr2p - Cr}_2\text{O}_3 \quad I_{Cr} = I_{Cr}^{\infty} \left[1 - \exp\left(\frac{-I_{CrO}}{\lambda_{Cr,CrO} \sin\theta}\right) \right] \times \exp\left[\frac{1}{\sin\theta} \left(\frac{-I_{Fe2O3}}{\lambda_{Cr,Fe2O3}} + \frac{-I_{NiO}}{\lambda_{Cr,NiO}}\right)\right] \quad (4)$$

$$\text{Concentration:} \quad C_{Fe} = \frac{\frac{I_{Fe2O3}}{RSF_{Fe}}}{\sum \frac{I_j}{RSF_j}} \quad C_{Ni} = \frac{\frac{I_{NiO}}{RSF_{Ni}}}{\sum \frac{I_j}{RSF_j}} \quad C_{Cr} = \frac{\frac{I_{Cr2O3}}{RSF_{Cr}}}{\sum \frac{I_j}{RSF_j}} \quad (5)$$

Model (1) oxide configuration was determined from APT concentration profiles obtained from thermal treatment of Cr22-MPEA. Model (2) oxide configuration was determined from free energy of formation for each oxide at 300 °C, utilizing Ellingham diagrams. Model (3) configuration was based on APT concentration profiles of Cr22-MPEA passive film formed during aqueous oxidation that was previously discussed in Chapter 2. All oxide thicknesses were 1 nm. A summary of EALs and RSF values are shown in **Table 8.1**.

Table 8. 1. EALS for elements in Cr₂O₃, NiO, and Fe₂O₃ oxides obtained from NIST

Cr ₂ O ₃ (1 nm)			NiO (1 nm)			Fe ₂ O ₃ (1 nm)		
Angle	Element	EAL	Angle	Element	EAL	Angle	Element	EAL
30	Ni	1.058	30	Ni	0.884	30	Ni	1.076
	Fe	1.233		Fe	1.027		Fe	1.254
	Cr	1.424		Cr	1.184		Cr	1.447
	Mn	1.325		Mn	1.103		Mn	--
	Co	1.137		Co	0.948		Co	--
45	Ni	1.052	45	Ni	0.871	45	Ni	1.07
	Fe	1.233		Fe	1.02		Fe	1.254
	Cr	1.428		Cr	1.182		Cr	1.452
	Mn	1.327		Mn	1.098		Mn	--
	Co	1.134		Co	0.938		Co	--
75	Ni	1.11	75	Ni	0.913	75	Ni	1.13
	Fe	1.308		Fe	1.077		Fe	1.332
	Cr	1.515		Cr	1.25		Cr	1.543
	Mn	1.408		Mn	1.16		Mn	--
	Co	1.2		Co	0.987		Co	--
90	Ni	1.131	90	Ni	0.928	90	Ni	1.152
	Fe	1.335		Fe	1.097		Fe	1.36
	Cr	1.547		Cr	1.274		Cr	1.576
	Mn	1.438		Mn	1.183		Mn	--
	Co	1.224		Co	1.005		Co	--

RSF Values: Ni2p3 (2.309), Fe2p1 (1.623), Cr2p3 (0.972), Mn2p1 (0.923), and Co2p1 (1.056)

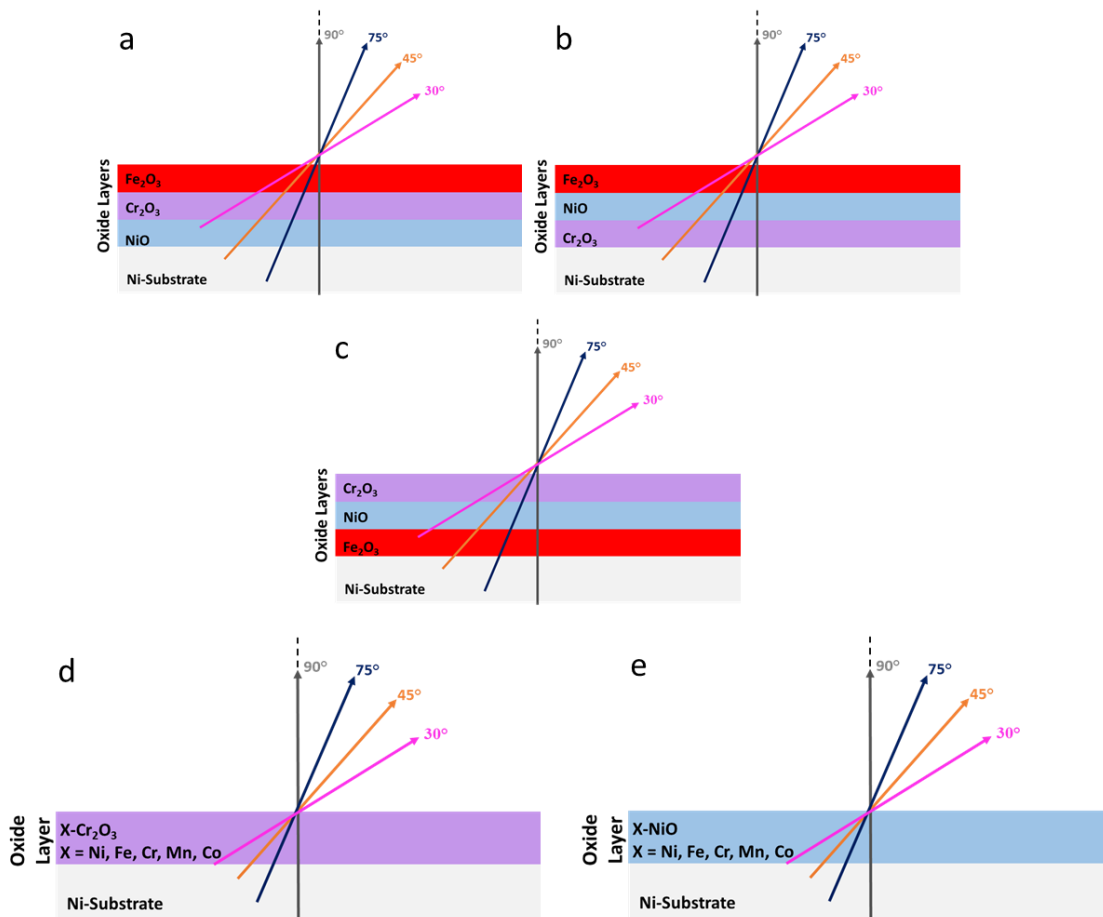


Fig. 8. 2. Theoretical oxide layer configurations (top-bottom) (a) Fe_2O_3 - Cr_2O_3 - NiO , (b) Fe_2O_3 - NiO - Cr_2O_3 , (c) Cr_2O_3 - Fe_2O_3 - NiO , (d) corundum solid solution assuming X - Cr_2O_3 , and (e) rock-salt solid solution assuming X - NiO , where $X = Ni, Fe, Cr, Mn, Co$. All oxide thicknesses were 1 nm.

8.3 Results

8.3.1 APT cation and elemental distribution within oxide and altered zone

APT concentration profiles of Cr22-MPEA after thermal treatment at 300 °C-10 mbar O₂ gas for 2 minutes is shown in **Fig. 8.3**. Ni enrichment is observed within the altered zone (i.e., oxide/film interface) and initially enriched within the inner oxide but decreases in concentration eventually becoming depleted (fractions were < nominal bulk fractions). Mn and Co depletion was also observed within the altered zone but concentration does increase within the inner oxide. Cr enrichment was observed throughout the inner oxide but became depleted within the outer oxide. The outer oxide was highly enriched with Fe and slightly enriched in Mn and Co species.

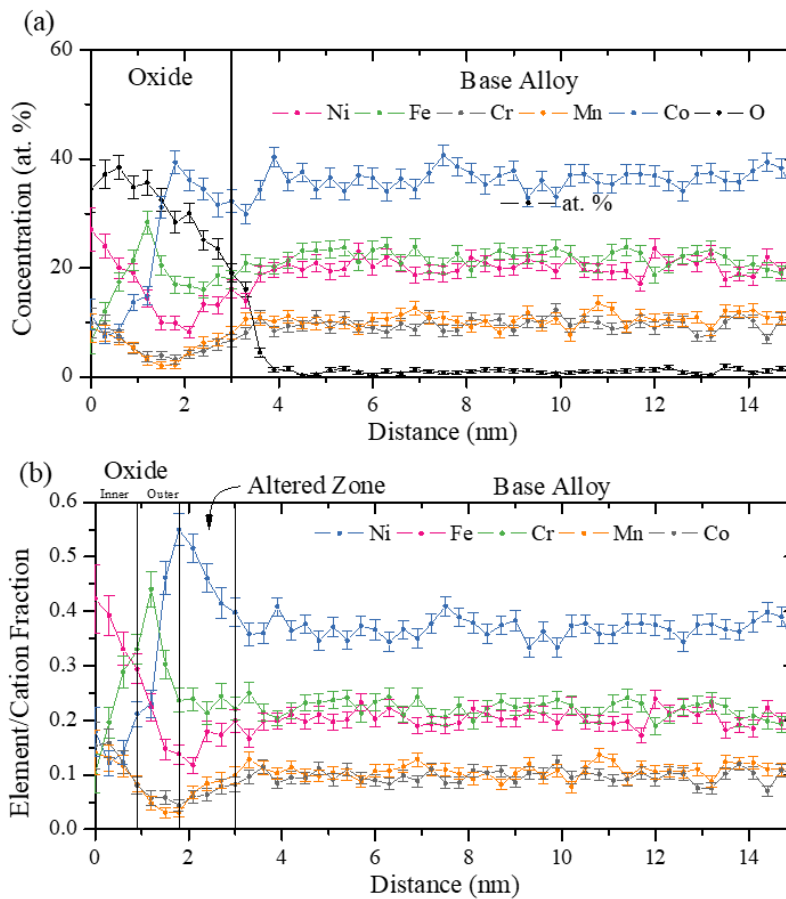


Fig. 8. 3. APT concentration profile of Cr22-MPEA oxide formed at 300 °C-10 mbar O_{2(g)} for 2 minutes. Concentration profile (a) was determined using proximity histogram across a 20 at. % O iso-concentration surface with a bin width of 0.3 nm. Concentration profile (b) only shows the elemental/cation fraction of principle alloying elements and was calculated from (a). Plots were from a 10 nm thick region of interest through the center of the reconstructed volume.

8.3.2 Oxide Valence, Cation, and Elemental Fraction Identified by AR-XPS

The valence state and chemical composition of the thermally treated Cr22-MPEA oxide were determined by AR-XPS and are summarized in **Fig. 8.4**. The bulk alloying concentration of each principal element is indicated by the horizontal dotted lines. There is good agreement between observations in APT and XPS. Similar to APT, Ni enrichment is observed in the altered zone and depletion of Fe, Mn, and Co at all XPS take-off angles (**Fig. 8.4a**). Cr stays relatively constant with its bulk alloy concentration (0.22 at. fraction) regardless of XPS take-off angle. Unlike in the altered zone, the oxide is enriched in Cr (III) cations but increases with XPS take-off angle (**Fig. 8.3b**). At a surface sensitive take-off angle of 30°, enrichment of Mn (IV), Co (II), and Fe (II) + (III) was exhibited but decreased toward bulk alloy concentrations as the take-off angle increased (i.e., bulk sensitive). This is in good agreement with APT concentration profiles in which, Fe, Mn, and Co enrichment was observed within the outer oxide and high Cr enrichment was observed within the inner oxide. Ni (II) was depleted within the oxide at take-off angles of 30° and 45° but increased to bulk alloy concentrations at 75° and 90° take-off angles (**Fig. 8.3b**). The oxide fraction is summarized in **Fig 8.4c** and **8.4d**. **Fig. 8.4c** shows all detected oxides within the thermally treated Cr22-MPEA oxide. **Fig. 8.4d** illustrates a summarized plot of oxide fractions in which spinels and Mn/Co oxides were summed and shown as individual species for simplicity. In both figures Cr-spinels are the dominate species with a large fraction being associated with FeCr₂O₄ spinel at all take-off angles (**Fig. 8.4c**). A large amount of Mn (IV) and Co (II) oxides were detected but a larger fraction was observed at a take-off angle of 30°. Small amount of NiO was detected at all take-off angles but increased in fraction as the take-off angle increased. No Cr₂O₃ oxide was detected at take-off angle of 30° but a small fraction was observed when take-off angle increased from 45° to 90°. A small fraction of Fe₂O₃ had formed but stayed relatively constant at all take-off angles. These results suggest the following oxide configuration: an outer oxide enriched in Fe, Cr, Mn, and Co species, an inner oxide consisting of Cr, Ni, and Fe species, and an altered zone enriched in Ni.

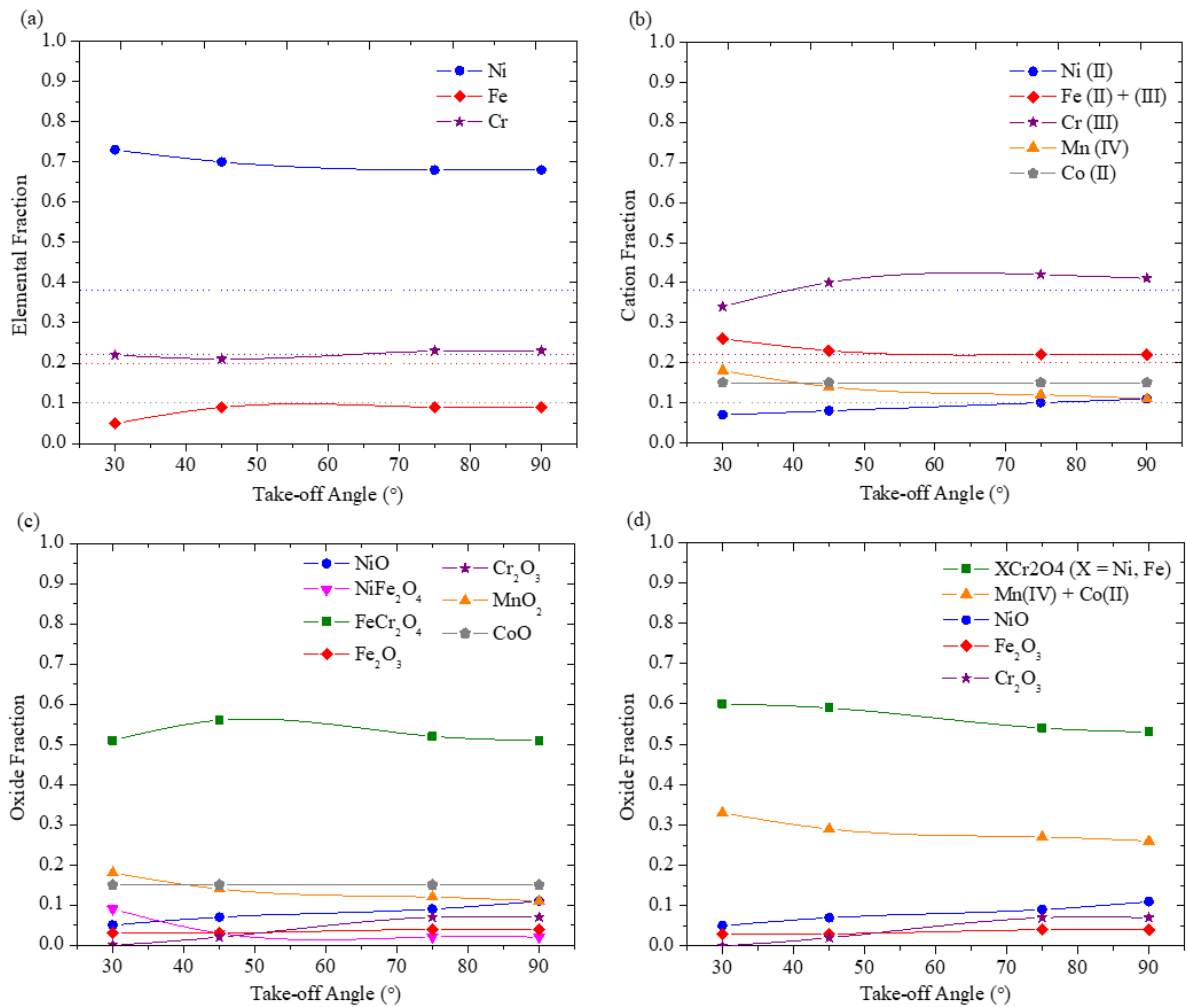


Fig. 8. 4. (a) elemental fractions, (b) Cation fractions (c, d) oxide fractions detected by AR-XPS at 30° to 90 ° take-off angle of Cr22-MPEA oxide formed at 300 °C-10 mbar $O_{2(g)}$ for 2 minutes. The bulk atomic fraction for each alloying element is indicated by the horizontal dotted lines in (a) and (b). Plot (c) exhibits all detect oxides by AR-XPS. Plot (d) illustrates the sum oxide fraction of XCr_2O_4 ($X=Ni, Fe$) oxide and $Mn(II) + Co(II)$ oxides produced from plot (c).

8.3.3 Theoretical XPS Models of Phase Separated and Solid Solution Oxides

The phase separated oxide models consisting of different configurations of Fe_2O_3 , Cr_2O_3 , and NiO oxide phases are shown in **Fig. 8.5**. For simplicity, only these valence states (i.e., Fe (III), Cr (III), and Ni (II)) were considered to better illustrate the effect of oxide layering versus a solid solution oxide on cation fractions. In all configurations the top layer (Fe_2O_3 and Cr_2O_3) exhibited a high Fe (III) and Cr (III) cation fraction at surface sensitive take-off angles of 30° and 45° (**Fig. 8.5**). As take-off angle increased to 75° and 90° a decrease in outer oxide cation fraction and increase in inner oxide cation fraction was observed (**Fig. 8.5**). In general, for all oxide configurations as take-off angle increased from 75° to 90° the cation fraction of each oxide layer approached a relatively constant value, with the exception of Ni (II) when assumed as the middle layer. When NiO is the middle layer between Fe_2O_3 and Cr_2O_3 phases, a different cation fraction trend is observed compared to oxide configurations with NiO as the bottom layer. As take-off angle increases from 30° to 75° , Ni (II) cation fractions increase but then decreases at a take-off angle of 90° . For each oxide configuration, each overlay exhibited a higher cation fraction compared to the layer below it, at all take-off angles. Interesting, for oxide configurations with NiO as the bottom layer and the outer oxide consisting of either Fe_2O_3 and Cr_2O_3 exhibited very similar cation fractions (**Fig. 8.5a and 8.5c**). For example, regardless of the outer oxide being Cr_2O_3 or Fe_2O_3 the same cation fraction for Fe (III) and Cr (III) was observed at all take-off angles (0.8 to 0.6 cation fraction) (**Fig. 8.5a and 8.5c**). Differences in Cr (III) cation fraction was also observed in each model. The lowest Cr (III) fraction was observed when Cr_2O_3 was made the bottom layer of the inner oxide (**Fig. 8.5b**). When Cr_2O_3 was configured closer to the outer oxide, its cation fraction increased. The largest Cr (III) cation fraction was observed when the Cr_2O_3 phase was assumed to be the outer oxide (**Fig. 8.5c**).

The solid solution models, assuming corundum and rock-salt phases, exhibited different cation trends compared to the phase separated models (**Fig. 8.5**) and are shown in **Fig. 8.6**. Unlike in the phase separated models where cation fractions either increased or decreased with take-off angle (depending on layer configuration), the cation fraction for each principal alloying element remained relative constant at all take-off angles for both solid solution models. Regardless of what phase was considered as the solid solution (i.e., corundum vs. rock-salt), the same cation trends were observed. In both the corundum and rock-salt solid solution models the cation fraction of

each principal alloying elements was the same fraction (Ni (II) = Fe (III) = Cr (III) = Mn (II) = Co (II)).

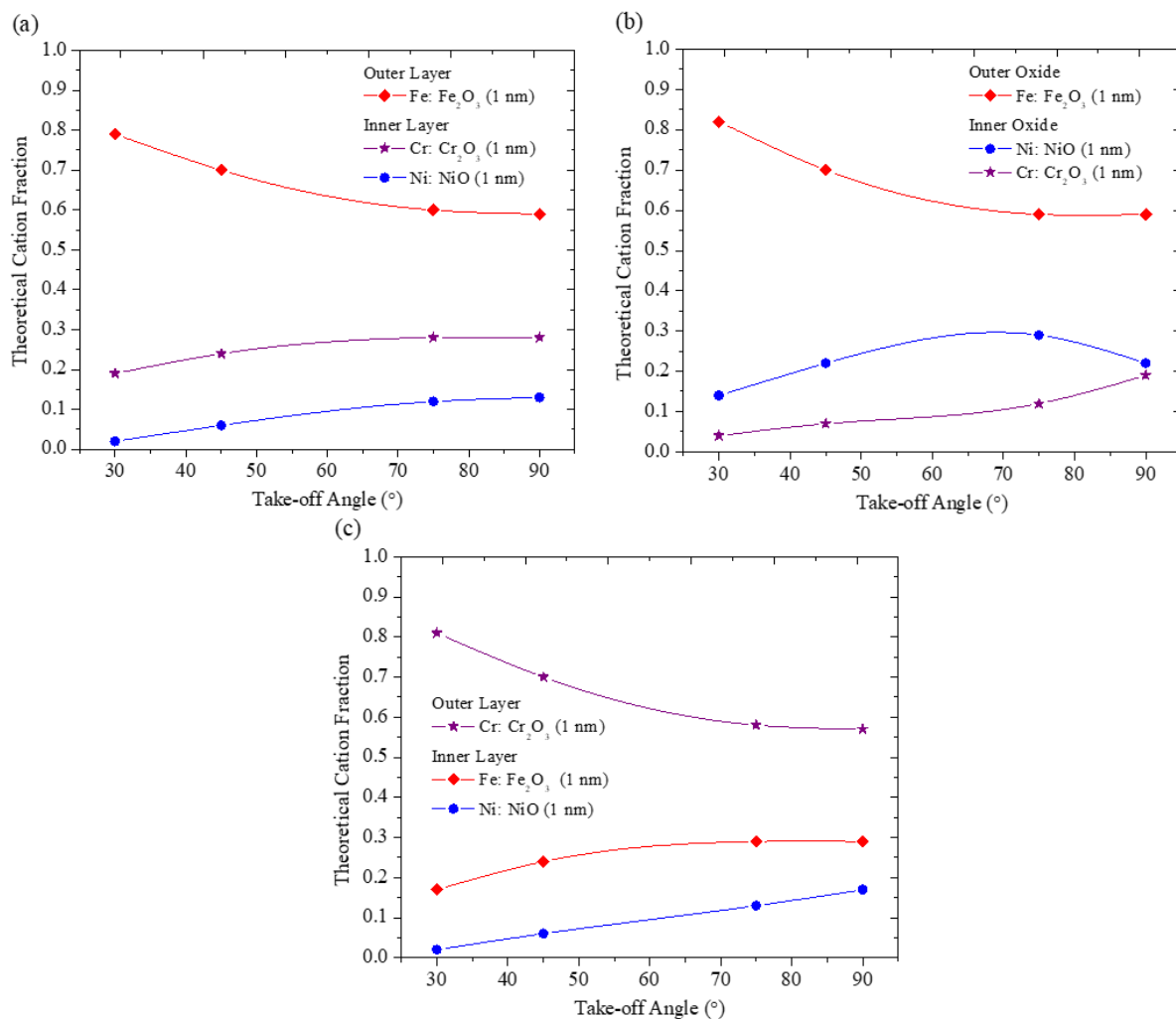


Fig. 8. 5. Theoretical XPS cation fraction of various oxide layer configurations (top-bottom) (a) $Fe_2O_3-Cr_2O_3-NiO$, (b) $Fe_2O_3-NiO-Cr_2O_3$, and (c) $Cr_2O_3-Fe_2O_3-NiO$. Cation fractions were calculated from XPS intensity expressions assuming exponential attenuation in a homogenous thin overlayer.

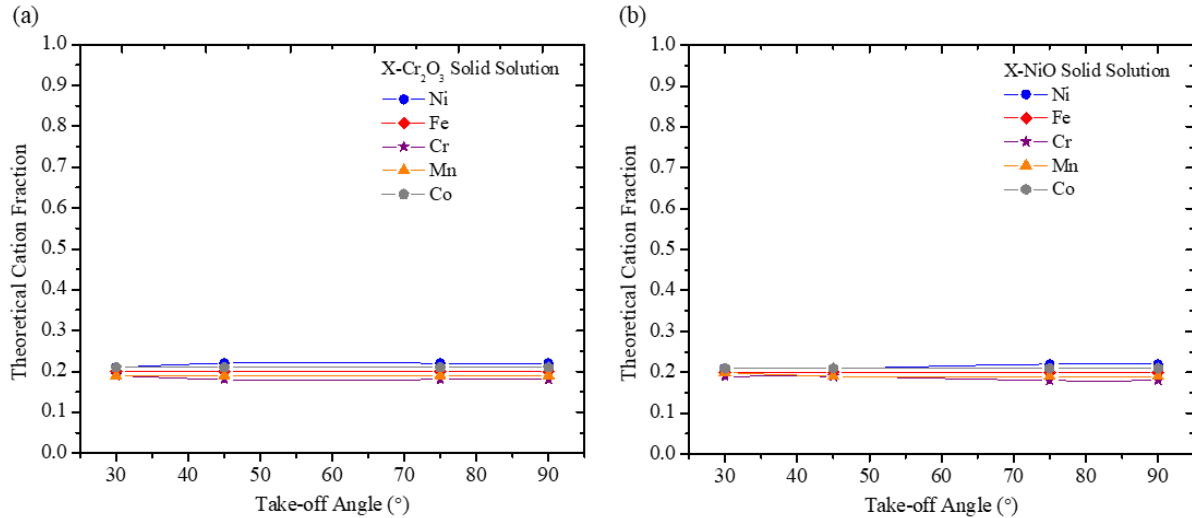


Fig. 8. 6. Theoretical XPS cation fraction of (a) Corundum solid solution assuming $X\text{-Cr}_2\text{O}_3$ and (b) rock-salt solid solution assuming $X\text{-NiO}$, where $X = \text{Ni}, \text{Fe}, \text{Cr}, \text{Mn},$ and Co . Cation fractions were calculated from XPS intensity expressions assuming exponential attenuation in a homogenous thin overlayer.

8.4 References

1. Butler, T.M., et al., *High temperature oxidation behaviors of equimolar NbTiZrV and NbTiZrCr refractory complex concentrated alloys (RCCAs)*. Journal of Alloys and Compounds, 2017. **729**: p. 1004-1019.
2. Butler, T.M. and M.L. Weaver, *Oxidation behavior of arc melted AlCoCrFeNi multi-component high-entropy alloys*. Journal of Alloys and Compounds, 2016. **674**: p. 229-244.
3. Chang, C.-H., M.S. Titus, and J.-W. Yeh, *Oxidation Behavior between 700 and 1300 °C of Refractory TiZrNbHfTa High-Entropy Alloys Containing Aluminum*. Advanced Engineering Materials, 2018. **20**(6): p. 1700948.
4. Daoud, H.M., et al., *Oxidation Behavior of Al₈Co₁₇Cr₁₇Cu₈Fe₁₇Ni₃₃, Al₂₃Co₁₅Cr₂₃Cu₈Fe₁₅Ni₁₅, and Al₁₇Co₁₇Cr₁₇Cu₁₇Fe₁₇Ni₁₇ Compositionally Complex Alloys (High-Entropy Alloys) at Elevated Temperatures in Air*. Advanced Engineering Materials, 2015. **17**(8): p. 1134-1141.
5. Gorr, B., et al., *Phase equilibria, microstructure, and high temperature oxidation resistance of novel refractory high-entropy alloys*. Journal of Alloys and Compounds, 2015. **624**: p. 270-278.
6. Gorr, B., et al., *High temperature oxidation behavior of an equimolar refractory metal-based alloy 20Nb20Mo20Cr20Ti20Al with and without Si addition*. Journal of Alloys and Compounds, 2016. **688**: p. 468-477.
7. Gorr, B., et al., *High-Temperature Oxidation Behavior of Refractory High-Entropy Alloys: Effect of Alloy Composition*. Oxidation of Metals, 2017. **88**(3): p. 339-349.
8. Holcomb, G.R., J. Tylczak, and C. Carney, *Oxidation of CoCrFeMnNi High Entropy Alloys*. JOM, 2015. **67**(10): p. 2326-2339.

9. Jayaraj, J., et al., *Microstructure, mechanical and thermal oxidation behavior of AlNbTiZr high entropy alloy*. Intermetallics, 2018. **100**: p. 9-19.
10. Liu, C.M., et al., *Microstructure and oxidation behavior of new refractory high entropy alloys*. Journal of Alloys and Compounds, 2014. **583**: p. 162-169.
11. Otto, F., et al., *Decomposition of the single-phase high-entropy alloy CrMnFeCoNi after prolonged anneals at intermediate temperatures*. Acta Materialia, 2016. **112**.
12. Senkov, O.N., et al., *Oxidation behavior of a refractory NbCrMo_{0.5}Ta_{0.5}TiZr alloy*. Journal of Materials Science, 2012. **47**(18): p. 6522-6534.
13. Waseem, O.A., et al., *A combinatorial approach for the synthesis and analysis of Al_xCr_yMo_zNbTiZr high-entropy alloys: Oxidation behavior*. Journal of Materials Research, 2018. **33**(19): p. 3226-3234.
14. Yang, Y., J.H. Perepezko, and C. Zhang, *Oxidation synthesis of Hf₆Ta₂O₁₇ superstructures*. Materials Chemistry and Physics, 2017. **197**: p. 154-162.
15. Zheng, J., et al., *Isothermal oxidation mechanism of a newly developed Nb–Ti–V–Cr–Al–W–Mo–Hf alloy at 800–1200°C*. International Journal of Refractory Metals and Hard Materials, 2016. **54**: p. 322-329.
16. Quiambao, K.F., et al., *Passivation of a corrosion resistant high entropy alloy in non-oxidizing sulfate solutions*. Acta Materialia, 2019. **164**: p. 362-376.
17. Wang, L., et al., *Study of the surface oxides and corrosion behaviour of an equiatomic CoCrFeMnNi high entropy alloy by XPS and ToF-SIMS*. Corrosion Science, 2020. **167**: p. 108507.
18. Luo, H., et al., *Corrosion behavior of an equiatomic CoCrFeMnNi high-entropy alloy compared with 304 stainless steel in sulfuric acid solution*. Corrosion Science, 2018. **134**: p. 131-139.
19. Qiu, Y., et al., *A Surface Study of the Native Oxide upon a Compositionally Complex Alloy*. CORROSION, 2018. **74**(12): p. 1312-1317.
20. Zhou, Q., et al., *Corrosion behavior of Hf_{0.5}Nb_{0.5}Ta_{0.5}Ti_{1.5}Zr refractory high-entropy in aqueous chloride solutions*. Electrochemistry Communications, 2019. **98**: p. 63-68.
21. Kautz, E.J., et al., *Element redistributions during early stages of oxidation in a Ni₃₈Cr₂₂Fe₂₀Mn₁₀Co₁₀ multi-principal element alloy*. Scripta Materialia, 2021. **194**: p. 113609.
22. Schreiber, D.K., et al., *Revealing the complexity of high temperature oxide formation in a 38Ni-21Cr-20Fe-13Ru-6Mo-2W (at. %) multi-principal element alloy*. Scripta Materialia, 2022. **210**: p. 114419.
23. Yu, X.-x., et al., *Nonequilibrium Solute Capture in Passivating Oxide Films*. Physical Review Letters, 2018. **121**(14): p. 145701.
24. Yu, X.-x., et al., *New Insights on the Role of Chloride During the Onset of Local Corrosion: TEM, APT, Surface Energy, and Morphological Instability*. CORROSION, 2019. **75**(6): p. 616-627.
25. Lu, P., et al., *Computational design and initial corrosion assessment of a series of non-equimolar high entropy alloys*. Scripta Materialia, 2019. **172**: p. 12-16.
26. Thompson, K., et al., *In situ site-specific specimen preparation for atom probe tomography*. Ultramicroscopy, 2007. **107**(2): p. 131-139.
27. Gerard, A.Y., et al., *Aqueous passivation of multi-principal element alloy Ni₃₈Fe₂₀Cr₂₂Mn₁₀Co₁₀: Unexpected high Cr enrichment within the passive film*. Acta Materialia, 2020. **198**: p. 121-133.

28. Han, J., et al., *Potential Dependent Mn Oxidation and Its Role in Passivation of Ni₃₈Fe₂₀Cr₂₂Mn₁₀Co₁₀ Multi-Principal Element Alloy Using Multi-Element Resolved Atomic Emission Spectroelectrochemistry*. Journal of The Electrochemical Society, 2021. **168**(5): p. 051508.
29. Vitchev, R.G., et al., *X-ray photoelectron spectroscopy characterisation of high-k dielectric Al₂O₃ and HfO₂ layers deposited on SiO₂/Si surface*. Applied Surface Science, 2004. **235**(1): p. 21-25.
30. Suzuki, S., et al., *Effect of the surface segregation of chromium on oxidation of high-purity Fe-Cr alloys at room temperature*. Applied Surface Science, 1996. **103**(4): p. 495-502.
31. Jablonski, C.J.P.a.A., *NIST Electron Effective-Attenuation-Length Database Verision 1.3*. 2011, Gaithersburg, MD: National Institute of Standards and Technology.

